TECHNISCHE UNIVERSITÄT
CHEMNITZ

Beeinflussung der Metall-Metall-Interaktionen in Ferrocenyl-funktionalisierten Phospholen

von der Fakultät für Naturwissenschaften der Technischen Universität Chemnitz

genehmigte Dissertation zur Erlangung des akademischen Grades

doctor rerum naturalium

(Dr. rer. nat.)

vorgelegt von Dipl.-Chem. Dominique Miesel

geboren am 17.02.1988 in Karl-Marx-Stadt, jetzt Chemnitz

eingereicht am 29.10.2015

Gutachter: Prof. Dr. Heinrich Lang

Prof. Dr. Stefan Spange

Tag der Verteidigung: 01.03.2016

Bibliografische Beschreibung und Referat

Dominique Miesel

Beeinflussung der Metall-Metall-Interaktionen in Ferrocenyl-funktionalisierten Phospholen

Technische Universität Chemnitz, Fakultät für Naturwissenschaften
Dissertation, 2015, 168 Seiten

Die vorliegende Arbeit beschreibt die Synthese Ferrocenyl-funktionalisierter Phosphole und deren elektrochemische sowie spektroelektrochemische Charakterisierung zur Bestimmung der Stärke der Metall-Metall-Wechselwirkungen. Aufgrund der mangelnden Aromatizität stehen das freie Elektronenpaar am Phosphoratom und das dienische System für weitere Reaktionen zur Verfügung. Somit konnten gezielt Modifikationen am heterozyklischen Grundgerüst vorgenommen werden, um dessen elektronische Eigenschaften zu beeinflussen.

Ein Schwerpunkt der Arbeit lag im Aufbau eines Phospholsystems mit Ferrocenyl-substituenten in 2- und 5-Position des Heterozyklus. Weiterhin wurden die Auswirkungen auf die elektronischen Eigenschaften des Moleküls nach chemischer Oxidation des Phosphoratoms von P^{III} zu P^{V} mit Schwefel und Selen untersucht. Ein weiterer Schwerpunkt lag in der Synthese von Übergangsmetallkomplexen des 2,5-Diferrocenyl-1-phenyl-1*H*-phosphols, um den Einfluss des Phosphoratoms und des dienischen Systems auf die elektronische Wechselwirkung der Ferrocenylgruppen genauer zu untersuchen und die elektronischen Eigenschaften gezielt zu beeinflussen. In weiteren Arbeiten wurden räumlich anspruchsvolle Substituenten am Phosphoratom zur Veränderung der Geometrie der pyramidalen Phosphorumgebung und somit zur Erhöhung der Delokalisierung im Heterozyklus eingeführt. Die Phosphole mit räumlich anspruchsvollen Gruppen zeigten die größte Metall-Metall-Wechselwirkung der Fc/Fc^{+}-Gruppen über den Phospholring.

Stichworte: Heterozyklen, Phosphole, Carbonyle, Ferrocen, Elektronentransfer, Cyclovoltammetrie, Spektroelektrochemie

Die vorliegende Arbeit wurde in der Zeit von September 2011 bis Oktober 2015 unter Leitung von Herrn Prof. Dr. Heinrich Lang am Lehrstuhl für Anorganische Chemie der Technischen Universität Chemnitz durchgeführt.

Herrn Prof. Dr. Heinrich Lang

danke ich für das mir entgegengebrachte Vertrauen, die stete Unterstützung und hilfreichen Diskussionen während der Arbeit sowie die Freiheiten bei der Bearbeitung des Themas.

Präambel

Während der im Zeitraum von September 2011 bis Oktober 2015 durchgeführten Promotionsarbeit wurden für die vorliegende Dissertationsschrift vier, die Promotion betreffende, Publikationen selbstständig unter Anleitung von Prof. Dr. Heinrich Lang und Dr. Alexander Hildebrandt verfasst. Dabei sind die Publikationen entweder bereits in den entsprechenden Fachzeitschriften veröffentlicht oder zur Veröffentlichung eingereicht, worauf am Anfang eines jeden Kapitels verwiesen wird. Die dazugehörigen Kurzbeschreibungen der einzelnen Publikationen sind als Anhänge A bis D in englischer Sprache zu finden.

Die Publikationen sind als Kapitel B bis E in englischer Sprache und in inhaltlich unveränderter Form dieser Schrift eingefügt. Die Kapitel „Einleitung und Kenntnisstand“ (Kapitel A) sowie „Zusammenfassung“ (Kapitel F) sind in deutscher Sprache verfasst. Für die Nummerierung der Verbindungen der einzelnen Kapitel wurden dem jeweiligen Kapitel entsprechend die Großbuchstaben **B**, **C**, **D** oder **E** den Nummern der Verbindungen vorangestellt. Vereinzelte Verbindungen werden dabei in mehreren Publikationen erwähnt, wodurch es vorkommt, dass eine Verbindung mehrere Nummerierungen erhält. Ausgewählte Abbildungen aus den Supporting Information der einzelnen Publikationen sind in den entsprechenden Anhängen gezeigt.

Inhalt

Formelzeichen und Abkürzungen

Ar	Aryl
BI	Bird-Index
Bu	Butyl
Calcd.	berechnet (calculated)
Cp	Cyclopentadienyl
decomp.	Zersetzung (decomposition)
dia.	Durchmesser (diameter)
DIPA	Diisopropylamin
Et	Ethyl
equiv.	Äquivalent (equivalent)
Fc	Ferrocenyl
HOMO	Highest Occupied Molecular Orbital
IUPAC	International Union of Pure and Applied Chemistry
LF	Ligandenfeld
LUMO	Lowest Unoccupied Molecular Orbital
m	*meta*-Position
M	Metall
Me	Methyl
MLCT	Metall-zu-Ligand-Charge-Transfer
Mp	Schmelzpunkt (melting point)
o	*ortho*-Position
OLED	Organische Leuchtdiode (organic light-emitting device)
ORTEP	Oak Ridge Thermal Ellipsoid Plot
p	*para*-Position
Ph	Phenyl
ppm	parts per million
R	funktionelle Gruppe
rms	Root mean square
TD-DFT	Time-dependent density functional theory
Thf	Tetrahydrofuran

IR	**Infrarot-Spektroskopie**
m	mittlere Intensität (middle)
s	starke Intensität (strong)
w	schwache Intensität (weak)

NMR	**Kernresonanzspektroskopie (Nuclear Magnetic Resonance)**
δ	Chemische Verschiebung
${}^{n}J_{XY}$	Kopplungskonstante über n Bindungen zwischen den Kernen X und Y
d	Dublett
m	Multiplett
pt	Pseudotriplett
s	Singulett
$\Delta H^{\ddagger}$	Aktivierungsenthalpie
$\Delta S^{\ddagger}$	Aktivierungsentropie

Elektrochemie

CV	Cyclovoltammetrie
SWV	Square-Wave-Voltammetrie
$E^{\circ\prime}$	Potential eines Redoxprozesses
$\Delta E^{\circ\prime}$	Separation zweier Redoxprozesse
ΔE_{p}	Differenz zwischen Oxidation und Reduktion eines Redoxprozesses
E_{pa}	anodisches Peakpotential
K_{c}	Komproportionierungskonstante
ΔG_{c}	Freie Energie des Komproportionierungsgleichgewichtes
ΔG_{e}	elektrostatischer Beitrag
ΔG_{i}	induktiver Beitrag
ΔG_{r}	Resonanzbeitrag

Spektroelektrochemie

IVCT	Intervalence-Charge-Transfer
NIR	Nah-Infrarot
OTTLE	Optically Transparent Thin-Layer Electrochemical
UV/Vis	Ultraviolett/sichtbarer Bereich

H_{ab}	Elektronischer Kopplungsparameter
ε_{max}	Extinktionskoeffizient
ν_{max}	Energie der Absorptionsbande bei maximaler Intensität
$\Delta\nu_{1/2}$	Breite der Bande bei halber Höhe (Halbwertsbreite)
$(\Delta\nu_{1/2})_{theo}$	theoretisch berechnete Halbwertsbreite
r_{ab}	effektiver Elektronentransferabstand
f	Oszillatorstärke
λ	Wellenlänge

HRMS	**Hochauflösende Massenspektrometrie (High Resolution Mass Spectrometry)**
ESI-TOF	Elektrospray-Ionisation-Time-Of-Flight
M	Molpeak
m/z	Masse-zu-Ladungsverhältnis

A Einleitung und Kenntnisstand

1. Einleitung

Die fortschreitende Miniaturisierung von elektronischen Bauelementen führt zur Entwicklung von immer leistungsfähigeren, kleiner werdenden, elektronischen Komponenten, wie beispielsweise Transistoren oder Schaltern, für den Einsatz in neuen Geräten.[A1–A4] 1965 sagte Gordon Moore voraus, dass sich in Silizium-basierenden Bauelementen die Anzahl der Transistoren pro cm² alle 18 – 24 Monate verdoppeln wird.[A5] Die Grenzen der Miniaturisierung in der Elektronik werden mit der Verwendung einzelner Moleküle erreicht. Die Herausforderung besteht damit in der Entwicklung von Transistoren, Schaltern, Speichern und Drähten auf molekularer Ebene.[A6–A10]

Eine Möglichkeit zur Miniaturisierung im Bereich der Elektronik stellt das „top-down" Verfahren dar, welches die Verkleinerung von etablierten Bauelementen umfasst.[A1,A11] Diese Methode stößt jedoch bei Größenordnungen weit oberhalb der Größe eines Moleküls an ihre Grenzen.[A7] Die sogenannte molekulare Elektronik liefert hierbei eine interessante Alternative. Durch das „bottom-up" Verfahren werden einzelne Moleküle, die als elektronische Bauelemente dienen können, verwendet oder ausgehend von diesen Nanostrukturen aufgebaut.[A1,A12,A13] Gewünschte physikalische und elektronische Eigenschaften können dabei gezielt durch Modifikationen der funktionellen Gruppen eingestellt werden.[A11]

Besonders in den letzten zwei Jahrzehnten hat die Forschung auf dem Gebiet der molekularen Elektronik an Bedeutung gewonnen.[A6,A14] Großen Anteil daran haben Aviram und Ratner, welche 1974 von dem theoretischen Konzept einer molekularen Gleichrichterdiode, bestehend aus Donor- und Akzeptorteil, berichteten (Abbildung A1).[A15] Anknüpfend an diese Arbeiten entstanden viele Untersuchungen für die potentielle Verwendung von Molekülen zur Umsetzung in molekularen Bauelementen.[A16–A19]

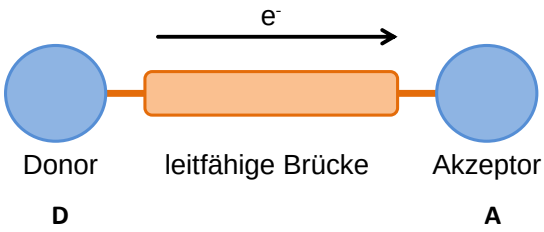

Abbildung A1. Schematische Darstellung eines molekularen Bauelementes.

Maßgebend für eine erfolgreiche Entwicklung molekularer Elektronik ist das Verständnis der ablaufenden Prozesse in den Einzelmolekülen.[A10,A20] Ein molekularer Draht, in welchem Ladung von **D** nach **A** durch eine Brücke transportiert werden soll (Abbildung A1), stellt ein einfaches Beispiel eines molekularen Bauelementes dar.[A21,A22] Um dies zu realisieren ist es zunächst wichtig, Modellverbindungen zu synthetisieren und zu verstehen, welche Faktoren den Ladungstransport durch das Molekül beeinflussen.[A23]

Um Untersuchungen zu Elektronentransferprozessen in Molekülen im Labor zu gewährleisten, können Metalle als Donoren und Akzeptoren an den terminalen Positionen des Moleküls angebracht werden. Durch einfache Oxidation oder Reduktion dieser Verbindungen ist es möglich, Moleküle zu erhalten, in denen die Redoxeinheiten formal in unterschiedlichen Oxidationsstufen vorliegen. Das bekannteste Beispiel für diese Verbindungsklasse ist das Creutz-Taube-Ion (**A-1**), bei dem zwei Rutheniumionen über eine Pyrazineinheit verbrückt vorliegen (Abbildung A2).[A24]

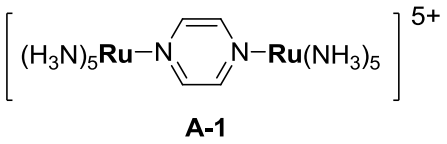

A-1

Abbildung A2. Creutz-Taube-Ion (**A-1**).[A24]

Die Forschung auf dem Gebiet der Elektronentransferreaktionen über einen Brückenliganden wurde besonders von Henry Taube vorangetrieben,[A25] der im Jahr 1983 den Nobelpreis für Chemie „*für seine Arbeiten über die Reaktionsmechanismen der Elektronenübertragung, insbesondere bei Metallkomplexen*“ erhielt.[A26] Die Untersuchungen an dieser Verbindung gaben Anstoß zur Synthese und Elektronentransferuntersuchungen zahlreicher Verbindungen, bei denen zwei Redoxgruppen über einen Brückenliganden miteinander verbunden sind.[A27]

2. Kenntnisstand

2.1 Gemischt-valente Verbindungen

Verbindungen, bei denen zwei oder mehr redox-aktive Gruppen in unterschiedlichen Oxidationsstufen über eine π-konjugierte Brückeneinheit verknüpft sind, werden gemischt-valente Verbindungen genannt.[A28–A36] Zu den „klassischen“ gemischt-valenten Verbindungen zählen Moleküle mit Übergangsmetallatomen als Redoxgruppen.[A31] Aber auch Systeme mit organischen Redoxeinheiten, wie z. B. Triarylamin-Gruppen, sind für diese Verbindungsklasse bekannt.[A37] Eine der ältesten gemischt-valenten Verbindungen ist das Berliner Blau $Fe_4[Fe(CN)_6]_3$, welches bereits um 1704 synthetisiert wurde[A38] und auch heute noch durch seine Verwendung als Farbstoff von großem Interesse ist.[A39] Die intensiven Farben gemischt-valenter Verbindungen basieren nicht auf den Farben der Einzelkomponenten, sondern entstehen durch kooperative Wechselwirkungen zwischen diesen.[A39,A40] Die tiefblaue Farbe des Berliner Blau kann durch die Anwesenheit von Eisenionen in zwei unterschiedlichen Oxidationsstufen (Fe^{II}, Fe^{III}) und den photoinduzierten Elektronentransfer zwischen diesen erklärt werden.[A41]

Zusätzlich zu den intensiven Farben ergibt sich das Interesse an gemischt-valenten Verbindungen aus den starken Änderungen der physikalischen Eigenschaften im Vergleich zu denen der einzelnen Molekülbausteine.[A23,A28,A42–A45] So ist es möglich, dass die entsprechenden gemischt-valenten Systeme als elektrische Leiter dienen können, wohingegen die Einzelkomponenten isolierenden Charakter aufweisen.[A28] Da die interessanten Eigenschaften der gemischt-valenten Verbindungen von den elektronischen Wechselwirkungen zwischen den einzelnen Redoxeinheiten abhängen, hat die Stärke der Metall-Metall-Wechselwirkungen einen großen Einfluss auf diese Eigenschaften.[A32,A41]

Weiterhin können gemischt-valente Verbindungen als Modellsysteme für molekulare Drähte angesehen werden.[A27] Deren Modifikationen helfen somit zu verstehen, wie Elektronentransferprozesse ablaufen und welche Faktoren einen Einfluss auf den Elektronentransfer haben.[A32,A46–A55] Im Fokus der Forschung stehen daher die Variation der π-konjugierten Brückeneinheit, der redox-aktiven Endgruppen oder zusätzlich gebundener Liganden und die daraus resultierende Änderung der Stärke der Wechselwirkungen.[A48,A56]

Zum Verständnis der Theorie von Elektronentransferreaktionen haben besonders die Arbeiten von Marcus und Hush beigetragen.[A57–A61] Die Elektronentransferreaktionen können mit Hilfe von Potentialenergiekurven (Abbildung A3) beschrieben werden. Dabei wird ein

symmetrischer, bimetallischer Komplex typischerweise mit Hilfe von Potentialhyperflächen beschrieben.[A23] Die Metalle M_1 und M_2 liegen in unterschiedlichen Oxidationsstufen n und n+1 vor und sind über einen Brückenliganden miteinander verbunden. Des Weiteren ist das Molekül von Lösungsmittelmolekülen umgeben. In Abbildung A3 beschreibt die dimensionslose Reaktionskoordinate eine Kombination von Metall-Ligand- und Lösungsmittel-Streckschwingungen.

Eine Klassifizierung für gemischt-valente Verbindungen basierend auf der Stärke der Wechselwirkungen zwischen M_1 und M_2 und den resultierenden physikalischen Eigenschaften wurde erstmalig 1967 von Robin und Day vorgenommen.[A28,A41] Die Einteilung in Klasse I (keine Wechselwirkungen), Klasse II (schwache bis moderate Wechselwirkungen) und Klasse III (starke Wechselwirkungen) basiert auf dem Grad der Delokalisierung des ungepaarten Elektrons zwischen M_1 und M_2.[A28,A62]

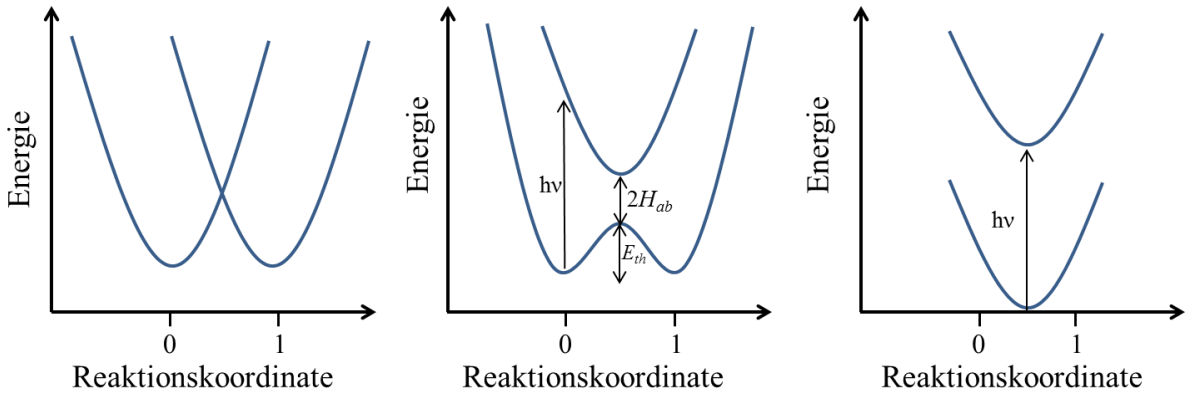

Abbildung A3. Potentialenergiekurven eines dinuklearen Komplexes (geändert nach D'Alessandro & Keene).[A63]

Für ein lokalisiertes System (Abbildung A3, links) sind die Potentialkurven der zwei Zustände $[M_1^{n}M_2^{n+1}]_0$ und $[M_1^{n+1}M_2^{n}]_0$ als zwei diabatische Parabeln gezeigt. Dabei sind keine Wechselwirkungen zwischen den beiden Zuständen möglich.[A37,A63] Die Ladungen liegen lokalisiert vor und es kann kein intramolekularer Elektronentransfer zwischen Donor- und Akzeptorseite stattfinden.[A27] Eine derartige Verbindung wird der Klasse I nach Robin und Day zugeordnet.

Am Schnittpunkt (0.5) der beiden diabatischen Flächen führt die Mischung der Wellenfunktionen zu zwei neuen adiabatischen Flächen (Abbildung A3, Mitte).[A32] Die Ladung ist zwar lokalisiert, aber durch thermische oder photochemische Anregung kann ein Ladungstransfer stattfinden. Die Verbindung zählt zu Klasse II nach Robin und Day und in

den gemischt-valenten Verbindungen wird eine Intervalence-Charge-Transfer- (IVCT)-Bande während der UV/Vis-NIR-Messung beobachtet, welche in den vollständig oxidierten bzw. reduzierten Spezies nicht auftritt. Die Aufspaltung der beiden Flächen repräsentiert den elektronischen Kopplungsparameter H_{ab}. Der optisch induzierte Übergang vom adiabatischen Grundzustand $[M_1^{n}M_2^{n+1}]_0$ in den angeregten Zustand $[M_1^{n+1}M_2^{n}]^*$ repräsentiert den IVCT-Übergang. Die optische Anregung resultiert in einer nahezu Gauß-förmigen Bande.[A37] Da gemäß dem Franck-Condon-Prinzip der Elektronenübergang schneller ist als die Kernbewegung, befindet sich das Metall M_1^{n+1} direkt nach dem Übergang in einer Umgebung eines Metalls M^n und entsprechend Metall M_2^{n} in einer Metall M^{n+1} Umgebung. Die Energie, welche für die optische Anregung benötigt wird, wird „Marcus Reorganisationsenergie" genannt und besteht aus einer inneren und einer äußeren Reorganisationsenergie.[A63] Die äußere Reorganisationsenergie ist die Energie, welche für die Reorganisation der umgebenden Lösungsmittelmoleküle nach erfolgtem Elektronentransfer benötigt wird. Die innere Reorganisationsenergie stellt die benötigte Energie für die Reorganisation der Metall-Ligand- und Ligand-Bindungslängen und -winkel dar. Da es bei einem IVCT-Übergang ebenfalls zu einer Änderung des Dipolmomentes kommt, ist in Klasse II Verbindungen die Lage, ν_{max}, der IVCT-Bande stark lösungsmittelabhängig. Die IVCT-Banden von Klasse II Verbindungen sind typischerweise von geringer Intensität und breit. Die thermische Anregung erfolgt entlang der Reaktionskoordinate vom Minimum des Zustandes A zum Minimum des Zustandes B.

Wenn die beiden Metalle M_1 und M_2 stark miteinander wechselwirken, verschwindet die Barriere für die thermische Anregung und im Grundzustand liegt nur noch ein Minimum vor (Abbildung A3, rechts). Solche Systeme werden der Klasse III nach Robin und Day zugeordnet, wobei beide Metallionen formal eine gemittelte Oxidationsstufe $n^{1/2}$ besitzen. Die Ladung ist über das gesamte System delokalisiert und es wird eine intensive, schmale Absorption beobachtet.[A64] Für Verbindungen zwischen delokalisiertem und lokalisiertem Zustand werden intensive, asymmetrische Banden beobachtet. In Klasse III Verbindungen sind die beiden Metalle durch spektroskopische Methoden nicht voneinander unterscheidbar.[A62]

Um die Stärke der Kopplung der redox-aktiven Endgruppen über ein Brückensystem genau zu bestimmen, gibt es verschiedene spektroskopische Möglichkeiten. Elektrochemische Messungen (meist Cyclovoltammetrie und Square-Wave-Voltammetrie) können helfen, erste Einblicke in die elektronischen Eigenschaften einer Verbindung zu erhalten. Bei Vorliegen

einer elektronischen Wechselwirkung der beiden Redoxeinheiten können zwei Redoxprozesse im Cyclovoltammogramm beobachtet werden. Die Größe der Separation zwischen den beiden Redoxprozessen, $\Delta E°'$, kann dabei erste Auskünfte über die Stärke der Wechselwirkung geben. Die Freie Energie der Komproportionierung ΔG_c und die Komproportionierungskonstante K_c (Gleichung A1, Gleichung A2) erlauben eine Abschätzung der Stärke der Metall-Metall-Wechselwirkung.[A65]

$$M^nM^n + M^{n+1}M^{n+1} \rightleftharpoons 2\,M^nM^{n+1}$$

$$K_c = \frac{[M^nM^{n+1}]^2}{[M^nM^n][M^{n+1}M^{n+1}]} = e^{\frac{\Delta E°' \cdot F}{R \cdot T}} \qquad \text{(Gl. A1)}$$

Der Wert für K_c lässt sich aus der Redoxseparation der verschiedenen Redoxprozesse nach Gleichung A1 berechnen und stellt die thermodynamische Stabilität der gemischt-valenten Verbindung (M^nM^{n+1}) im Vergleich zu neutralem (M^nM^n) und komplett oxidiertem System ($M^{n+1}M^{n+1}$) dar.[A66] Zumeist weisen die gemischt-valenten M^nM^{n+1} Verbindungen im Gegensatz zu den homovalenten Spezies M^nM^n und $M^{n+1}M^{n+1}$ eine geringe thermodynamische Stabilität auf, wodurch K_c einen kleinen Wert annimmt.[A27,A42]

$$\Delta G_c = -RT \cdot lnK_c = -\Delta E°' \cdot F \qquad \text{(Gl. A2)}$$

$$\Delta G_c = RTln\frac{1}{4} + \Delta G_e + \Delta G_i + \Delta G_r \qquad \text{(Gl. A3)}$$

Eine genaue Aussage über den Grad der Metall-Metall-Interaktion ist durch elektrochemische Methoden jedoch nicht möglich, da die Redoxseparation von zusätzlichen Faktoren abhängt.[A67] ΔG_c steht dabei in Zusammenhang mit $\Delta E°'$ (Gleichung A2) und setzt sich gemäß Gleichung A3 aus einem statistischen Faktor ($RT\ln\frac{1}{4}$), einem elektrostatischen Faktor ΔG_e, welcher durch die Abstoßung zweier gleich geladener Redoxgruppen entsteht, einem induktiven Faktor ΔG_i basierend auf Metall-Ligand-Rückbindungen und einem Resonanzfaktor ΔG_r zusammen.[A63,A65] Die Delokalisierung findet nur im letzten Term ΔG_r Ausdruck und trägt somit nicht allein zur Redoxseparation bei. Bei kompletter Abwesenheit von Wechselwirkungen zwischen beiden Redoxeinheiten werden diese im Cyclovoltammogramm als ein Prozess beobachtet. Die Redoxseparation entsteht in diesem Fall allein durch statistische Faktoren und beträgt bei Raumtemperatur etwa 36 mV.[A35]

Eine sehr nützliche Methode zur Charakterisierung der gemischt-valenten Verbindungen ist die Spektroelektrochemie.[A42] Diese ist eine Kombination aus Elektrochemie und

spektroskopischen Methoden, wie IR-, Raman- oder UV/Vis-NIR-Spektroskopie und erlaubt eine Identifizierung von Zwischenprodukten und Produkten während der Oxidation der Verbindungen.[A68,A69] Dabei erfolgt die Aufnahme der spektroskopischen Daten *in situ*, während die Verbindungen schrittweise oxidiert werden. Somit ist eine Isolierung der gemischt-valenten Verbindung zu deren Charakterisierung nicht notwendig.

Die am häufigsten verwendete spektroelektrochemische Methode zur genauen Klassifizierung gemischt-valenter Verbindungen ist die *in situ* UV/Vis-NIR-Untersuchung, da die gemischt-valenten Spezies typischerweise im energiearmen Nahen-Infrarot-Bereich (NIR, 800–2500 nm) eine Absorptionsbande zeigen. Diese Bande entsteht durch einen „Intervalence-Charge-Transfer“ (IVCT)-Übergang, einem Elektronenübergang zwischen den Metallen unterschiedlicher Oxidationsstufe über einen Brückenliganden.[A42]

Die *in situ* UV/Vis-NIR-Messung findet in einer sogenannten OTTLE (Optically Transparent Thin-Layer Electrochemical)-Zelle statt.[A42,A70] Die OTTLE-Zelle erlaubt die Aufnahme von UV/Vis-NIR-Spektren bei sukzessiver Oxidation der Verbindung durch schrittweise Erhöhung des Potentials. Während der schrittweisen Oxidation wird im Falle einer elektronischen Wechselwirkung das Entstehen einer Bande im NIR-Bereich aufgrund der Bildung der gemischt-valenten Spezies und der elektronischen Wechselwirkung der unterschiedlich valenten Redoxgruppen beobachtet. Bei weiterer Oxidation zu den höher oxidierten Spezies verschwindet diese Absorption wieder. Da die IVCT-Bande meist von anderen, verschieden intensiven Übergängen, wie beispielsweise Metall-Ligand- oder Ligand-Metall-Übergängen, begleitet ist, muss eine Spektren-Dekonvolution durchgeführt werden. Dabei wird das experimentelle Spektrum in Gauß-förmige Banden zerlegt.[A37,A55] Nach Dekonvolution des experimentellen Spektrums können die Energie ν_{max}, die Intensität ε_{max} und die Halbwertsbreite $\Delta\nu_{1/2}$ (die Breite der Bande bei halber Höhe) der IVCT-Bande Aufschluss über die Stärke der elektronischen Wechselwirkung der beiden Redoxeinheiten geben.

Anhand der Größe des elektronischen Kopplungsparameters H_{ab} lässt sich eine Klassifizierung für gemischt-valente Verbindungen vornehmen. Für Klasse II Systeme lässt sich H_{ab} nach Gleichung A4 berechnen.

$$H_{ab} = \left(\frac{0.0206}{r_{ab}}\right) \cdot (\nu_{max} \cdot \Delta\nu_{1/2} \cdot \varepsilon_{max})^{1/2} \qquad \text{(Gl. A4)}$$

Dabei können $\Delta\nu_{1/2}$, ε_{max} und ν_{max} aus den nach der Dekonvolution erhaltenen Daten der IVCT-Bande entnommen werden. Für den effektiven Elektronentransferabstand r_{ab} wird meist der Abstand der Redoxgruppen durch den Raum genommen, welcher z. B. durch Einkristallröntgenstrukturanalyse ermittelt werden kann. Der effektive Elektronentransferabstand ist dabei aber meist deutlich geringer. Für Klasse III Systeme lässt sich H_{ab} direkt aus der Energie des Übergangs nach Gleichung A5 berechnen.

$$H_{ab} = \frac{\nu_{max}}{2} \qquad \text{(Gl. A5)}$$

Die Berechnung der theoretischen Halbwertsbreite nach Hush (Gleichung A6) und der Vergleich mit den experimentell gefundenen Halbwertsbreiten der IVCT-Banden lassen weitere Aussagen über die Stärke der Wechselwirkung zu. Banden von Klasse III Verbindungen weisen typischerweise schmalere Halbwertsbreiten als die theoretisch berechneten auf, während die IVCT-Banden der Klasse II Systeme typischerweise breiter als die theoretischen sind.[A27]

$$(\Delta\nu_{1/2})_{theo} = (2310 \cdot \nu_{max})^{1/2} \qquad \text{(Gl. A6)}$$

Neben elektrochemischen Methoden und *in situ* UV/Vis-NIR-Spektroelektrochemie gibt es noch weitere Möglichkeiten eine Klassifizierung betreffend Delokalisation/Lokalisation vorzunehmen. Mit Hilfe der Einkristallröntgenstrukturanalyse können wichtige Informationen bezüglich der Struktur gemischt-valenter Verbindungen im Festkörper erhalten werden. Während Verbindungen mit Metallen in unterschiedlichen Oxidationsstufen verschiedene M-C-Bindungslängen aufweisen, sind in Systemen mit Metallen gemittelter Oxidationsstufen gleichwertige M-C-Bindungslängen zu finden.[A35]

Die Mößbauerspektroskopie, welche auf wenige Kerne beschränkt ist, findet vor allem in gemischt-valenten Verbindungen mit Eisenionen als redox-aktive Endgruppen Anwendung.[A52] Dabei werden typischerweise zwei Signale gefunden, bei denen der Abstand voneinander und die Breite der Aufspaltung stark abhängig von der Elektronendichte am Kern ist. Je nach Vorhandensein von Fe^{II}/Fe^{III} in lokalisierten Verbindungen bzw. dem Vorliegen gemittelter Oxidationsstufen in delokalisierten Systemen können so verschiedene, charakteristische Mößbauerspektren erhalten werden.

Die IR-Spektroskopie ist auf Verbindungen mit funktionellen Gruppen beschränkt. IR-Spektren lokalisierter gemischt-valenter Verbindungen zeigen die charakteristischen Banden der Redoxeinheiten der zwei verschiedenen Oxidationsstufen, während diese Banden in IR-

Spektren delokalisierter Verbindungen verschwinden und neue Schwingungsbanden für die gemittelten Einheiten gefunden werden.[A52] Verbindungen mit Carbonylgruppen sind dabei gut zur Klassifizierung geeignet, da die intensiven Schwingungsbanden der Carbonyl-Funktionalitäten eine Unterscheidung zwischen symmetrischen Zuständen für Ladungs-delokalisation bzw. unterschiedlichen Carbonylgruppen in lokalisierten Verbindungen erlauben.[A42] Nichtsdestotrotz kann eine genaue Klassifizierung von gemischt-valenten Verbindungen in manchen Fällen nicht eindeutig vorgenommen werden und hängt stark von den verschiedenen experimentellen Methoden ab.

2.2 Ausgewählte Vertreter gemischt-valenter Verbindungen

Die ersten Untersuchungen zu molekular aufgebauten, gemischt-valenten Spezies und eine mögliche elektronische Kommunikation zwischen terminal gebundenen Redoxgruppen wurden auf dem Gebiet der Creutz-Taube analogen Ruthenium-Systeme durchgeführt. Für das Creutz-Taube-Ion **A-1**, bei welchem die Rutheniumionen formal in der Oxidationsstufe +2.5 vorliegen, kann während *in situ* UV/Vis-NIR-Spektroskopie im Nah-Infrarot-Bereich bei 6370 cm^{-1} eine schmale, intensive Bande beobachtet werden.[A24] Bei dieser Absorption handelt es sich um eine IVCT-Bande mit einer Intensität von ε_{max} = 5000 $L \cdot mol^{-1} \cdot cm^{-1}$ und einer Halbwertsbreite von $\Delta\nu_{1/2}$ = 1400 cm^{-1}[A71], welche in der neutralen [$Ru^{II}Ru^{II}$] und komplett oxidierten [$Ru^{III}Ru^{III}$] Spezies nicht auftritt.

Verbindung **A-1** stand lange im Fokus der Forschung auf dem Gebiet der gemischt-valenten Verbindungen, da in der Literatur kontroverse Ergebnisse diskutiert wurden, ob die Ladung über das komplette Molekül delokalisiert oder lokalisiert vorliegt.[A72–A75] Zahlreiche Untersuchungen belegen jedoch, dass im Grundzustand eine vollständige Delokalisation vorhanden ist und die Verbindung in die Klasse III nach Robin und Day eingeordnet werden kann.[A75–A79]

Aufbauend auf diesen Ergebnissen wurden analoge Ruthenium-Systeme mit modifizierten Brückensystemen synthetisiert, um den Einfluss des veränderten Brückenfragments auf die elektronische Interaktion der Redoxeinheiten zu untersuchen (Abbildung A4, Tabelle A1).

Bei Verlängerung des Ru-Ru-Abstandes durch Verwendung von 4,4'-Bipyridin als π-konjugierte Brückeneinheit (**A-2**) kann eine IVCT-Bande bei 9710 cm^{-1} beobachtet werden, jedoch ist diese im Vergleich zu **A-1** signifikant schwächer und breiter (Tabelle A1).[A71] Die Wechselwirkung der Rutheniumionen nimmt im Vergleich zu **A-1** deutlich ab.[A71,A80,A81]

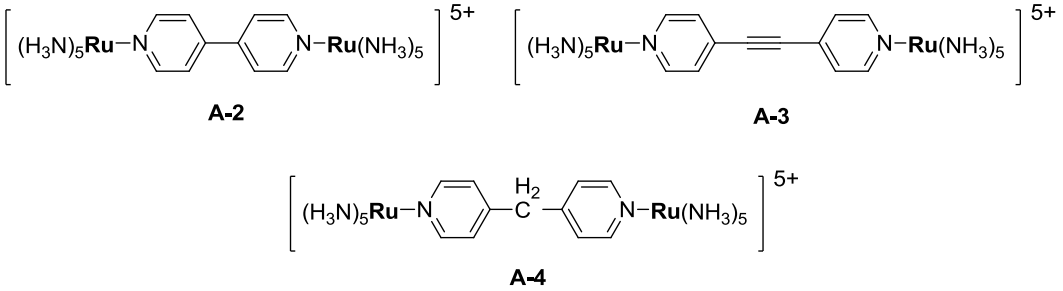

Abbildung A4. Verbrückte Pentaamin-Rutheniumkomplexe mit den Brückenliganden 4,4'-Bipyridin (**A-2**, Fleischer **1972**)[A80], 4,4'-(1,2-Ethindiyl)bipyridin (**A-3**, Sutton, **1981**)[A81] und 4,4'-Methylen-bipyridin (**A-4**, Rieder, **1977**)[A82].

Tabelle A1. Daten der IVCT-Banden für Verbindungen [A-1]$^+$–[A-4]$^+$.[A71]

	ν_{max} [cm^{-1}]	ε_{max} [L ·mol^{-1} ·cm^{-1}]	$\Delta\nu_{1/2}$ [cm^{-1}]
[**A-1**]$^+$	6370	5000	1400
[**A-2**]$^+$	9710	920	5200
[**A-3**]$^+$	10870	640	5400
[**A-4**]$^+$	12350	30	7100

Eine weitere Verlängerung der π-konjugierten Brückeneinheit um eine Acetyleneinheit im 4,4'-(1,2-Ethindiyl)bipyridin verbrückten Molekül **A-3** führt zu einer weiteren Abnahme der Intensität der IVCT-Bande und einer Zunahme der Halbwertsbreite (Tabelle A1).[A81] Die Bedeutung einer vorhandenen Konjugation des Brückensystems wird bei Einbringen eines sp^3-hybridisierten Kohlenstoffatoms zwischen die Pyridineinheiten deutlich. Verbindung **A-4** zeigt im NIR-Bereich lediglich eine sehr kleine, breite IVCT-Bande (Tabelle A1), wodurch die sehr geringe Metall-Metall-Interaktion deutlich wird.[A81,A82] Die Verbindungen **A-2**–**A-4** können in schwach koppelnde Klasse II Systeme nach Robin und Day eingeordnet werden.

Neben den Ruthenium-basierten Systemen existieren zahlreiche Untersuchungen zu Elektronentransferprozessen in Molekülen mit Ferrocenyleinheiten als redox-aktive Endgruppe. Die Vorteile der Ferrocenylgruppen als Redoxeinheiten liegen in der hohen Stabilität des Ferrocen/Ferrocenium-Redoxpaares und der einfachen chemischen Modifizierbarkeit.[A55] Nahezu gleichzeitig mit der Synthese des Creutz-Taube-Ions erfolgte die Synthese einer Reihe verbrückter Ferrocenylverbindungen von der Gruppe um Cowan.[A45,A83–A86] Das Biferrocen, bei dem die beiden Ferrocenyleinheiten direkt über die Cyclopentadienyle verbunden sind, stellt dabei den einfachsten Fall zweier miteinander verbundener Ferrocene dar (Abbildung A5).[A83] Oxidation mit Benzochinon in Anwesenheit von Pikrinsäure führt zum Biferroceniumpikrat **A-5**. Diese gemischt-valente Verbindung weist bei der UV/Vis-NIR-spektroskopischen Untersuchung in CH_2Cl_2 eine IVCT-Bande bei

5555 cm^{-1} mit einer Intensität von 750 $L \cdot mol^{-1} \cdot cm^{-1}$ auf. Die Form der IVCT-Bande lässt auf eine schwache Kopplung der Eisenionen schließen. Des Weiteren ist die elektrische Leitfähigkeit des Biferroceniumpikrates im Festkörper um sechs Größenordnungen größer als die des Ferrocens oder des Ferroceniumpikrates. Die Verbindung kann der Klasse II nach Robin und Day zugeordnet werden.

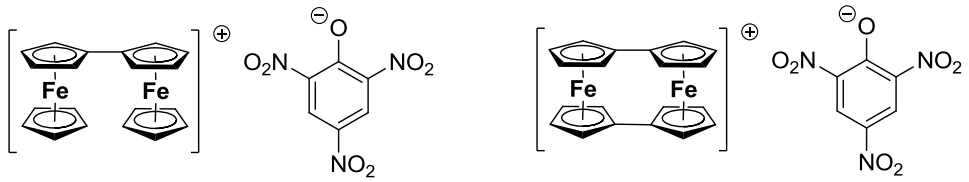

A-5 Cowan, 1970 **A-6** Cowan, 1972

Abbildung A5. Biferroceniumpikrat (**A-5**)[A83] und Bisfulvalendieisenpikrat (**A-6**)[A85].

Im Bisfulvalendieisen (**A-6**) führt die zusätzliche Bindung zwischen den Cyclopentadienylliganden zu einer Einschränkung der freien Drehbarkeit der Ferrocenylsubstituenten, wodurch es zu einer besseren Orbitalüberlappung kommt. Dies hat zur Folge, dass die elektronische Wechselwirkung im Bisfulvalendieisen deutlich stärker ist als die des Biferrocens **A-5**.[A85,A87] Die größere Metall-Metall-Interaktion wird durch Vergleich der Eigenschaften der IVCT-Banden deutlich. Die mono-oxidierte Spezies **A-6** weist in Acetonitril eine IVCT-Bande bei 6451 cm^{-1} mit einer deutlich höheren Intensität von 2100 $L \cdot mol^{-1} \cdot cm^{-1}$ im Vergleich zu **A-5** auf.[A88] Die starke Metall-Metall-Wechselwirkung wird weiterhin durch Mößbauerspektroskopie der beiden Verbindungen belegt. Das Mößbauerspektrum des Biferrocens **A-5** zeigt Quadrupolaufspaltungen für Fe^{II} und Fe^{III}, wodurch das gleichzeitige Vorliegen von Ferrocen- und Ferrocenium-Spezies im Molekül nachgewiesen werden konnte. Die Ladung liegt demzufolge auf der Mößbauer-Zeitskala lokalisiert vor. Im Gegensatz dazu deutet das Spektrum von Bisfulvalendieisen **A-6** auf eine delokalisierte Ladung und äquivalente Eisenionen auf der Mößbauer-Zeitskala hin.[A89]

Analog zu den verbrückten Ruthenium-Systemen wurden auf dem Gebiet der Ferrocenylverbindungen zahlreiche Untersuchungen unternommen, wie sich die elektronische Kommunikation der Fc/Fc^{+}-Gruppen bei Modifikation der konjugierten Brückeneinheiten verändert (Abbildung A6).

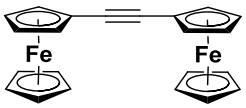

A-7

LeVanda, 1974

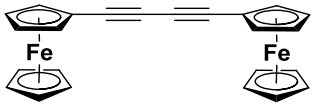

A-8

LeVanda, 1976

Abbildung A6. Verbrückte Biferrocene; Diferrocenylacetylen (**A-7**)[A86] und 1,4-Diferrocenylbutadiin (**A-8**)[A88].

Ein erstes Beispiel für ein über eine reine Kohlenstoffbrücke verbrücktes Biferrocen ist das Diferrocenylacetylen **A-7**.[A86] Das Cyclovoltammogramm (CH_2Cl_2, [N^{n}Bu$_4$][BF_4]) zeigt zwei reversible Redoxprozesse mit einer Redoxseparation von 135 mV. Die geringe Redoxseparation gibt Hinweise auf eine schwache elektronische Interaktion der Ferrocenyl-substituenten. Im UV/Vis-NIR-Spektrum der gemischt-valenten Verbindung [**A-7**]$^+$ kann eine breite Absorption bei 6410 cm^{-1} mit einer Intensität von 670 L $\cdot$mol^{-1} $\cdot$cm^{-1} gefunden werden, welche in der neutralen und zweifach oxidierten Spezies nicht auftritt und somit einem IVCT-Übergang zugeordnet werden kann. Eine Verlängerung der Kettenlänge um eine weitere Acetyleneinheit zum 1,4-Diferrocenylbutadiin (**A-8**) führt zu einer Abnahme der Redoxseparation der Redoxprozesse auf etwa 100 mV (CH_2Cl_2, [N^{n}Bu$_4$][BF_4]) und zu einer geringeren Intensität der IVCT-Bande (ε_{max} = 570 L $\cdot$mol^{-1} $\cdot$cm^{-1}) der mono-oxidierten Verbindung [**A-8**]$^+$.[A88] Die Zunahme der Kettenlänge und somit ein größerer Eisen-Eisen-Abstand führt demzufolge zu einer geringeren elektronischen Interaktion.

Der Schwerpunkt der Forschung auf dem Gebiet der gemischt-valenten Ferrocenyl-verbindungen liegt besonders in der Variation der π-konjugierten Brückensysteme zur Beeinflussung der Metall-Metall-Interaktion und auf dem Verstehen des ablaufenden Ladungstransfers. Interessante Ergebnisse konnten dabei bei Verwendung von Heterozyklen als π-konjugierte Brückeneinheit erzielt werden. Es konnte gezeigt werden, dass die Position der Ferrocenylgruppen am heterozyklischen Brückenfragment, die Art des Heteroatoms sowie zusätzliche funktionelle Gruppen einen großen Einfluss auf die Metall-Metall-Interaktion haben.[A90–A92]

Der Einfluss des Substitutionsmusters auf die elektronische Wechselwirkung wurde am Beispiel diferrocenylsubstituierter Thiophene untersucht (Abbildung A7).[A90] Dazu wurden 2,5-Fc_2-^{c}C_4H_2S (**A-9**), 3,4-Fc_2-^{c}C_4H_2S (**A-10**), 2,3-Fc_2-^{c}C_4H_2S (**A-11**) und 2,4-Fc_2-^{c}C_4H_2S (**A-12**) synthetisiert und elektrochemisch und spektroelektrochemisch untersucht. Die Separationen der Redoxprozesse der Ferrocenylsubstituenten in den Cyclovoltammogrammen (CH_2Cl_2, [N^{n}Bu$_4$][B(C_6F_5)]) liegen zwischen 169 mV (**A-12**) und 283 mV (**A-11**), wobei

besonders in den Verbindungen **A-10** und **A-11** die große Redoxseparation durch starke elektrostatische Wechselwirkungen der direkt benachbarten Ferrocenylgruppen erklärt werden kann.

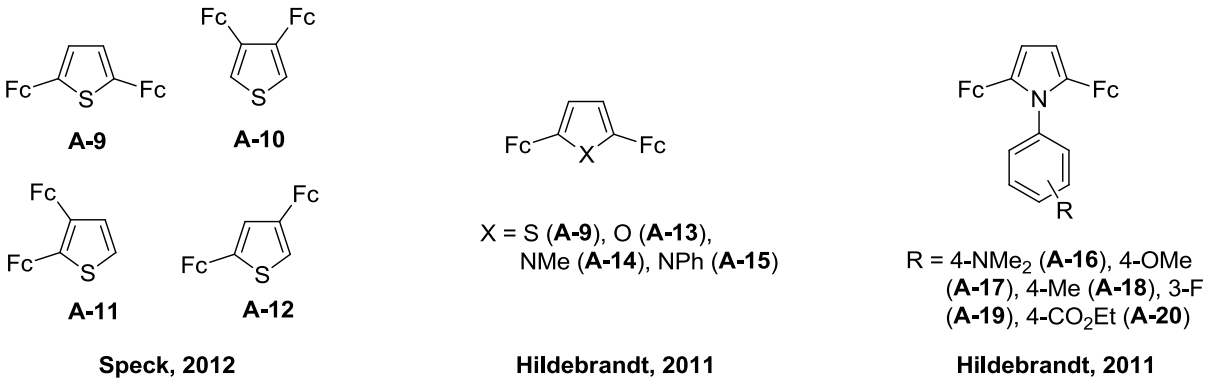

Abbildung A7. Beispiele Ferrocenyl-funktionalisierter Heterozyklen, Variation des Substitutionsmusters[A90], des Heteroatoms[A91] und der Substituenten.[A92]

Tabelle A2. Daten der IVCT-Banden für Verbindungen [A-9]$^+$–[A-12]$^+$.[A90]

	ν_{max} [cm^{-1}]	ε_{max} [L ·mol^{-1} ·cm^{-1}]	$\Delta\nu_{1/2}$ [cm^{-1}]
[**A-9**]$^+$[A91]	5490	821	2519
[**A-10**]$^+$	5405	70	7761
[**A-11**]$^+$	5300	401	5492
[**A-12**]$^+$	6098	151	5620

Um die Stärke der elektronischen Wechselwirkungen über den Heterozyklus genau zu klassifizieren, wurden UV/Vis-NIR-Messungen durchgeführt (Tabelle A2). Für das 2,5-Diferrocenylthiophen **A-9** konnte eine IVCT-Bande mit einer Intensität von 821 L ·mol^{-1} ·cm^{-1}[A91] und einer Halbwertsbreite von 2519 cm^{-1}[A91] beobachtet werden, wohingegen die IVCT-Absorption des 3,4-Diferrocenylthiophen **A-10** eine deutlich geringere Intensität (70 L ·mol^{-1} ·cm^{-1}) und eine größere Halbwertsbreite (7761 cm^{-1}) aufweist. Die Stärke der Wechselwirkung sinkt in der Reihenfolge **A-9**>**A-11**>**A-12**>**A-10**. Der Grad der elektronischen Interaktion ist am größten, wenn die Ferrocenylsubstituenten in den *α*-Positionen des Thiophenringes vorliegen.

Neben dem Substitutionsmuster hat auch die Variation des Heteroatoms in fünfgliedrigen Heterozyklen einen Einfluss auf die Metall-Metall-Wechselwirkung, was in der Reihe 2,5-Diferrocenyl-substituierter Heterozyklen von Thiophen (**A-9**), Furan (**A-13**), *N*-Methylpyrrol

(**A-14**) und *N*-Phenylpyrrol (**A-15**) untersucht wurde.[A91] Elektrochemische Messungen (CH_2Cl_2, $[N^nBu_4][B(C_6F_5)_4]$) ergaben, dass die Redoxseparationen der Ferrocenylgruppen in der Reihe Thiophen **A-9** ($\Delta E^{\circ\prime}$ = 260 mV), Furan **A-13** ($\Delta E^{\circ\prime}$ = 290 mV), *N*-Methylpyrrol **A-14** ($\Delta E^{\circ\prime}$ = 410 mV) und *N*-Phenylpyrrol **A-15** ($\Delta E^{\circ\prime}$ = 450 mV) ansteigen. Aufgrund ähnlicher Geometrien und somit ähnlicher elektrostatischer Anteile an der Redoxseparation sind die Ergebnisse der elektrochemischen Messungen ein Indiz für eine steigende elektronische Interaktion von Thiophen bis hin zu *N*-Phenylpyrrol. Ein Vergleich der Potentiale des ersten Redoxprozesses zeigt, dass **A-9** ($E_1^{\circ\prime}$ = -94 mV) und **A-13** ($E_1^{\circ\prime}$ = -152 mV) eine geringere Elektronendichte am Eisen aufweisen und somit schwerer zu oxidieren sind als die elektronenreicheren Heterozyklen **A-14** ($E_1^{\circ\prime}$ = -206 mV) und **A-15** ($E_1^{\circ\prime}$ = -238 mV).

Tabelle A3. Daten der IVCT-Banden für Verbindungen [A-9]$^+$,[A-13]$^+$–[A-15]$^+$.[A91]

	ν_{max} [cm^{-1}]	ε_{max} [$L \cdot mol^{-1} \cdot cm^{-1}$]	$\Delta\nu_{1/2}$ [cm^{-1}]
[**A-9**]$^+$	5490	821	2519
[**A-13**]$^+$	5060	1496	2364
[**A-14**]$^+$	4750	3145	2314
[**A-15**]$^+$	4820	4200	2369

Während spektroelektrochemischer *in situ* Messungen konnte für alle Verbindungen das Auftreten einer IVCT-Bande beobachtet werden, wobei die stärkste Wechselwirkung im *N*-Phenylpyrrol **A-15** vorliegt (Tabelle A3). Die Stärke der Wechselwirkung sinkt in der Reihe NPh>NMe>O>S. Auch die Berechnung der Oszillatorstärke f nach Gleichung A7 ermöglicht eine Klassifizierung der Stärke der Metall-Metall-Interaktion. Dabei konnte für die Reihe der untersuchten Heterozyklen eine lineare Abhängigkeit zwischen der Oszillatorstärke f und der Redoxseparation $\Delta E^{\circ\prime}$ beobachtet werden. Der Zusammenhang zwischen f und $\Delta E^{\circ\prime}$ erlaubt weiterhin eine Berechnung des effektiven Elektronentransferabstandes r_{ab} nach Gleichung A8. Für die untersuchten Systeme **A-9** und **A-13**–**A-15** beträgt r_{ab} 2.0±0.1 Å.

$$f = 4.6 \cdot 10^{-9} \cdot \varepsilon_{max} \cdot \Delta\nu_{1/2} \qquad \text{(Gl. A7)}$$

$$r_{ab} = \sqrt{\frac{m \cdot 8.49 \cdot 10^{-4}}{F \cdot 4.6 \cdot 10^{-9}}} \qquad \text{(Gl. A8)}$$

Anknüpfend an diese Arbeiten und die Erkenntnisse, dass in elektronenreichen Pyrrolen die Wechselwirkung der redox-aktiven Endgruppen über den heterozyklischen Kern stärker ist als

z. B. bei elektronenarmen Thiophenen, wurde eine Reihe Phenyl-substituierter 2,5-Diferrocenyl-1-phenyl-1*H*-pyrrole synthetisiert (**A-16**–**A-20**).[A92] Dabei wurden am Phenylsubstituenten elektronenziehende und elektronenschiebende Gruppen eingeführt und der Einfluss dieser auf die Metall-Metall-Wechselwirkung untersucht. Durch elektrochemische Untersuchungen konnte gezeigt werden, dass die Substituenten am Phenylring die Elektronendichte am Eisen stark beeinflussen, da für elektronenschiebende Substituenten am Phenylring (**A-16**–**A-18**) der erste Redoxprozess für die Eisenoxidation schon in einem Bereich von -305 bis -250 mV beobachtet werden konnte. Für Verbindungen mit elektronenziehenden Substituenten (**A-19** und **A-20**) am Phenylring wird der erste Redoxprozess bei höheren Potentialen zwischen -210 und -190 mV gefunden. Im Vergleich zum unsubstituierten Phenylpyrrol **A-15** wird die Redoxseparation für elektronenschiebende Substituenten erhöht, wohingegen elektronenziehende Gruppen zu einer Verringerung der Redoxseparation führen. Für die Reihe der untersuchten Systeme **A-16** bis **A-20** konnte eine lineare Abhängigkeit zwischen der Redoxseparation und der σ-Hammett-Konstante gefunden werden. Die Hinweise auf eine stärkere Metall-Metall-Interaktion bei Verwendung elektronenschiebender Substituenten konnte mittels *in situ* UV/Vis-NIR-Spektroskopie bestätigt werden (Tabelle A4).

Tabelle A4. Daten der IVCT-Banden für Verbindungen [A-15]$^+$–[A-20]$^+$.[A91,A92]

	ν_{max} [cm^{-1}]	ε_{max} [L ·mol^{-1} ·cm^{-1}]	$\Delta\nu_{1/2}$ [cm^{-1}]
[**A-15**]$^+$	4820	4200	2369
[**A-16**]$^+$	5055	4678	2358
[**A-17**]$^+$	4870	4296	2360
[**A-18**]$^+$	4825	4279	2337
[**A-19**]$^+$	4586	3584	2413
[**A-20**]$^+$	4554	3445	2438

Verbindung **A-16** weist eine IVCT-Bande mit einer Intensität von 4678 L ·mol^{-1} ·cm^{-1} und einer Halbwertsbreite von 2358 cm^{-1} auf. Eine Verringerung der Elektronendichte durch elektronenziehende Substituenten, wie in **A-20**, führt zu einer Abnahme der Intensität und einer Zunahme der Halbwertsbreite (Tabelle A4), wodurch eine geringere elektronische Wechselwirkung verdeutlicht wird. Die Verbindungen können der Klasse II nach Robin und Day zugeordnet werden.[A28]

Zusammenfassend kann gesagt werden, dass die Veränderung der Elektronendichte der Heterozyklen einen großen Einfluss auf die elektronische Kommunikation der

Ferrocenylsubstituenten in 2- und 5-Position hat. In vielen Arbeiten zu fünfgliedrigen Heterozyklen werden jedoch die Phosphor-analogen Verbindungen kaum erwähnt. Die sogenannten Phosphole verhalten sich aufgrund mangelnder Aromatizität sehr verschieden im Vergleich zu Furan, Thiophen und Pyrrol und bieten somit weitere, neue Möglichkeiten, wie Komplexierung oder Oxidation des Phosphoratoms, zur Beeinflussung der elektronischen Interaktion. Im folgenden Kapitel werden daher die Eigenschaften und das Reaktionsverhalten der Phosphole kurz erläutert.

2.3 Phosphole

Das erste bekannte, monozyklische Phosphol ist das 1,2,3,4,5-Pentaphenyl-1*H*-phosphol **A-21**, welches im Jahr 1959 beschrieben wurde (Abbildung A8).[A93] Die Stammverbindung **A-22**, das 1*H*-Phosphol, wurde erst 1983 charakterisiert, da es nur bei tiefen Temperaturen stabil ist und bei Raumtemperatur dimerisiert.[A94]

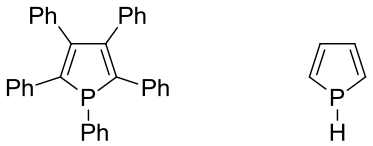

A-21 **A-22**

Abbildung A8. Beispiele erster, monozyklischer Phosphole; 1,2,3,4,5-Pentaphenyl-1*H*-phosphol (**A-21**)[A93] und 1*H*-Phosphol (**A-22**)[A94].

Im Gegensatz zu den analogen Vertretern Furan, Thiophen und Pyrrol, welche industriell leicht zugänglich sind und einfach durch Substitutionsreaktionen am Ringsystem modifiziert werden können, ist die Synthese der Phosphole komplexer. Zum Aufbau der Phospholstrukturen haben sich drei Synthesewege besonders bewährt. Funktionelle Gruppen werden am besten bei Aufbau des Ringes eingeführt, da sich nachträgliche Substitution aufgrund des geringen aromatischen Charakters als schwierig erweist.[A95] Elektrophile sowie nukleophile Angriffe erfolgen ausschließlich am Phosphoratom und nicht an den Ring-Kohlenstoffen.[A96] Die Synthese von 1,2,3,4,5-pentasubstituierten Phospholen gelingt über eine Dehydrohalogenierung von 2,5-Dihydrophospholiumsalzen (Schema A1), welche einfach über eine McCormack Reaktion[A97] zwischen konjugierten Dienen und Dihalophosphinen zugänglich sind. Von Vorteil ist, dass direkt RPX_2-Verbindungen eingesetzt werden können, welche meist einfach zugänglich sind bzw. käuflich erworben werden können.

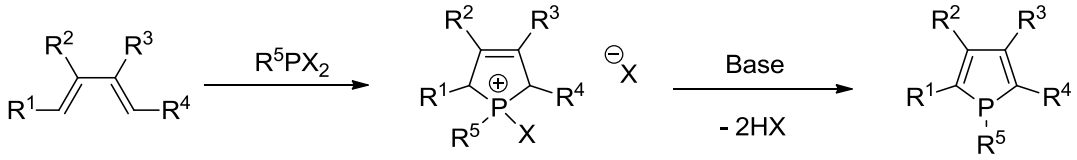

Schema A1. Synthese 1,2,3,4,5-pentasubstituierter Phosphole.[A98]

Eine weitere Möglichkeit zur Synthese von 1,2,5-trisubstituierten Phospholen ist die Reaktion von Butadiinen mit Phosphinen (Schema A2).[A98] Die Reaktion verläuft dabei basenkatalysiert, meist unter Verwendung von *n*-Butyllithium. Vorteil dieser Methode ist, dass nur ein Reaktionsschritt zum Aufbau des Phospholrings durchgeführt werden muss. Nachteil der Reaktion ist, dass keine funktionellen Gruppen in 3- und 4-Position angebracht werden können.

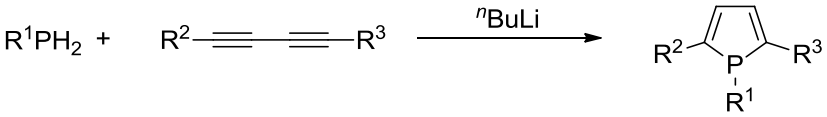

Schema A2. Synthese 1,2,5-trisubstituierter Phosphole.[A98]

Die dritte Syntheseroute beinhaltet die Reaktion von Dihalophosphinen mit Zirconacyclopentadienen (Schema A3), welche aus einer Cycloaddition zwischen den Alkinen und Zirconocen dargestellt werden.[A98] Ein Nachteil dieser Methode ist der zusätzliche Syntheseschritt, bei dem zunächst aus Zirconocendichlorid *in situ* Zirconocen gebildet werden muss, welches dann mit den Alkinen zu den entsprechenden Zirconacyclopentadienen reagiert.

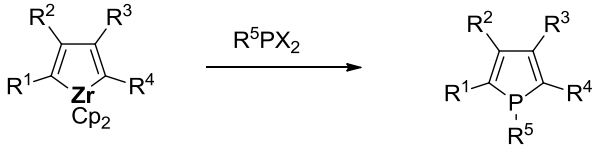

Schema A3. Syntheseweg für Phosphole über Zirconacyclopentadiene.[A98]

Eine weitere Herausforderung in der Synthese von Phospholen stellt die erschwerte Handhabung aufgrund der geringen Stabilität dar. Manche Phosphole neigen zu Dimerisierung, wobei zunächst durch 1,5-sigmatrope Umlagerungen der Substituenten am Phosphoratom das 2*H*-Phosphol erhalten wird (Schema A4).[A96] Anschließende [4+2]-Cycloaddition resultiert in der Bildung des entsprechenden Dimers. Die Migrationswahrscheinlichkeit der Phosphor-gebundenen Funktionalität hängt stark von der

Art der funktionellen Gruppe ab. Beispielsweise werden für R = Ph Temperaturen ab 150 °C benötigt[A99], wohingegen für R = H schon bei Raumtemperatur Dimerisierungsreaktionen beobachtet werden können.[A96,A100]

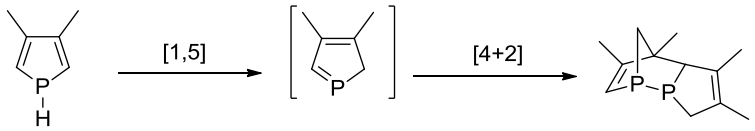

Schema A4. 1,5-Sigmatrope Umlagerung vom 1*H*-Phosphol zu 2*H*-Phosphol und anschließende [4+2]-Cycloaddition.[A98]

Innerhalb der Reihe fünfgliedriger Heterozyklen nehmen die Phosphole im Vergleich zu Furan, Thiophen und Pyrrol eine besondere Position ein, da sie meist keine oder nur eine geringe Aromatizität aufweisen.[A98] Untersuchungen zum aromatischen Charakter in Phospholen stellen ein breites Forschungsfeld innerhalb dieser Verbindungsklasse dar.[A98,A101–A105] Das Phosphoratom in Phospholen weist einen pyramidalen Bau und eine hohe Inversionsbarriere auf, wohingegen beim analogen Vertreter Pyrrol durch die hohe aromatische Stabilisierungsenergie die Energie zur Planarisierung überwunden wird und eine planare Geometrie vorliegt.[A106] Aufgrund der pyramidalen Anordnung der Umgebung am Phosphoratom kann keine Wechselwirkung des freien Elektronenpaares am Phosphor mit dem dienischen System stattfinden.

Da der Phospholring meist als klassisches Phosphan oder als Dien reagiert, können Modifikationen am reaktiven Phosphoratom bzw. dienischen System vorgenommen werden.[A98] Die Oxidationsstufe des Phosphors kann durch Oxidation von P^{III} zu P^{V} zum Oxid, Sulfid bzw. Selenid geändert werden. Reaktionen der Phosphole mit Übergangsmetall-fragmenten führen zur Komplexierung durch das dienische System, das Phosphoratom oder durch beide, wodurch vielfältige Strukturen erhalten werden können.[A107–A109] Eine nachträgliche Funktionalisierung an den Kohlenstoffatomen des Ringes ist zwar kaum möglich, jedoch können besonders durch Komplexierungsreaktionen die Elektronendichte des Phospholringes so verändert werden, dass gewünschte Eigenschaften eingestellt werden können. Diese Vorteile der Phosphole wurden besonders in der Herstellung von Materialien mit photophysikalischen Eigenschaften für eine potentielle Anwendung als organische Leuchtdioden genutzt.[A110] Das Einbetten bestimmter Phosphole in konjugierte Systeme und nachträglicher Reaktionen am Phosphoratom erlaubt so das Feineinstellen gewünschter photophysikalischer Eigenschaften.[A110,A111]

Theoretische Berechnungen zur Aromatizität in Phospholringen zeigen, dass durch π-Akzeptor- oder räumlich anspruchsvolle Substituenten in 1-, 2- oder 5-Position am Phospholring die Aromatizität erhöht werden kann.[A101,A112] Mit dem Konzept der sterisch anspruchsvollen Substituenten zur Planarisierung des Phospholringes beschäftigten sich intensiv in den letzten 20 Jahren die Gruppen um Quin, Keglevich und Nyulászi.[A106,A113–A117] Um die Auswirkungen der sterisch anspruchsvollen P-Substituenten auf die Geometrie des Phospholrings abzuschätzen, erfolgten zunächst theoretische Berechnungen.[A114] Dabei konnten Hinweise erhalten werden, dass mit steigendem sterischen Anspruch der Substituenten der Grad der Planarität erhöht werden kann. Um eine Planarisierung experimentell zu erreichen, wurden Phosphole mit verschiedenen, sterisch anspruchsvollen Substituenten am Phosphoratom synthetisiert und mit sterisch ungehinderten Phospholen verglichen (Abbildung A9).

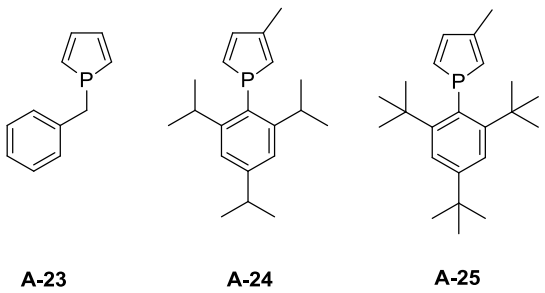

Abbildung A9. Beispiele für Phosphole mit verschiedenen sterisch anspruchsvollen Substituenten in 1-Position; 1-Benzyl-1*H*-phosphol (**A-23**)[A118], 3-Methyl-1-(2,4,6-tri-*iso*-propylphenyl)-1*H*-phosphol (**A-24**)[A119] und 3-Methyl-1-(2,4,6-tri-*tert*-butylphenyl)-1*H*-phosphol (**A-25**).[A120]

Dazu erfolgte die Synthese von 3-Methyl-1-(2,4,6-tri-*iso*-propylphenyl)-1*H*-phosphol (**A-24**) und 3-Methyl-1-(2,4,6-tri-*tert*-butylphenyl)-1*H*-phosphol (**A-25**) und die experimentelle Überprüfung der Planarisierung aus den Ergebnissen der Einkristallröntgenstrukturanalyse (Tabelle A5) und der Vergleich mit dem sterisch ungehinderten 1-Benzyl-1*H*-phosphol (**A-23**).[A119]

Tabelle A5. Geometrische Kriterien zum Abschätzen der Aromatizität der Phosphole A-23–A-25.[A120]

	A-23	**A-24**	**A-25**
α	8.6	12.7	12.9
β	66.9	58.2	44.2
BI	35.5	40.4	56.6
$\sum$ Bindungswinkel um das Phosphoratom	302.7	314.5	331.6

Die Auswirkungen auf eine erhöhte Planarität der Phosphorumgebung werden dabei besonders mit Hilfe der Winkel α und β beschrieben (Abbildung A10). Der Winkel α beschreibt die Abwinkelung des Phosphoratoms aus der C_4-Ebene, also die Planarität des Phospholringes selbst. Der Winkel β erläutert die Abwinkelung des *ipso*-Kohlenstoffatoms des Phenylsubstituenten von der C-P-C-Ebene, also die Planarisierung der pyramidalen Umgebung des Phosphoratoms, wobei letzterer einen größeren Einfluss auf eine höhere Delokalisierung hat.

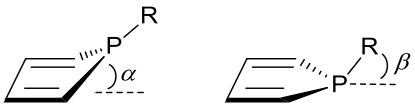

Abbildung A10. Schematische Darstellung der Winkel α und β.

Die Verwendung der sterisch anspruchsvollen Substituenten führt zwar zu einer leicht größeren Verzerrung des Phospholrings in **A-24** und **A-25** ($\alpha \approx 13$ °) im Vergleich zum 1-Benzyl-1*H*-phosphol **A-23** ($\alpha \approx 9$ °), jedoch wird die pyramidale Umgebung des Phosphoratoms signifikant planarer. Durch die Verwendung der 2,4,6-Tri-*tert*-butylphenyl-Gruppe kann der Winkel β von 66.9 ° in **A-23** auf 44.2 ° in **A-25** gesenkt werden, wodurch eine planarere Umgebung für das Phosphoratom aufgezeigt wird.

Ein weiteres Kriterium zur Einschätzung einer erhöhten Delokalisierung im Phospholring ist die Bestimmung der Summe der Winkel um das Phosphoratom nach Schmidpeter.[A121] Dabei resultiert eine Planarisierung in einer erhöhten Bindungswinkelsumme. Diese steigt in der Reihe **A-23** < **A-24** < **A-25**, was verdeutlicht, dass in **A-25** das Phosphoratom am wenigsten pyramidal umgeben ist. Zur Einschätzung einer erhöhten Delokalisierung kann des Weiteren die Berechnung des Bird-Index (BI, Gleichung A9) angewendet werden.[A122] Dieser gilt für zyklische Systeme und beruht auf geometrischen Kriterien. Benzol mit einem Maximalwert von 100 gilt als Bezugssystem.

$$\mathrm{BI} = 100\left(1 - \frac{V}{V_K}\right) \qquad \text{(Gl. A9)}$$

V = Koeffizient der Variation der Bindungsordnungen, berechnet nach Bird[A122]; V_K = Konstante in Abhängigkeit der Ringgröße, für fünfgliedrige Heterozyklen gilt $V_K = 35$.

Für die Verwendung der stark räumlich anspruchsvollen 2,4,6-Tri-*tert*-butylphenyl-Gruppe kann eine signifikante Erhöhung (BI = 56.6) im Vegleich zu **A-23** (BI = 35.5) beobachtet werden.[A120] All diese geometrischen Kriterien belegen eine erfolgreiche Planarisierung des Phosphoratoms mit Verwendung sterisch anspruchsvoller Substituenten. An der Verbindung

A-25 konnte erstmalig für Phosphole eine aromatische, elektrophile Substitutionsreaktion beobachtet werden. Die Reaktion von 3-Methyl-1-(2,4,6-tri-*tert*-butylphenyl)-1*H*-phosphol mit Acetylchlorid und Aluminiumtrichlorid führt mit einer Ausbeute von 51 % zur Bildung vom 2-Acetylderivat.[A120] Durch die erhöhte Planarität konnte somit die Aromatizität erfolgreich gesteigert werden.

Zusammenfassend kann gesagt werden, dass die Phosphole interessante Möglichkeiten bieten, die elektronischen Wechselwirkungen über heterozyklische Brückenfragmente weiter zu beeinflussen. Durch das vielfältige Reaktionsverhalten und das reaktive Phosphoratom sowie das dienische System können die elektronischen Eigenschaften gezielt an verschiedenen Stellen des Ringes verändert werden. Weiterhin ist es möglich, durch die Wahl geeigneter Substituenten am Phosphoratom einen Einfluss auf die Delokalisierung im Ring auszuüben.

2.4 Motivation

Die besonderen Eigenschaften der Phosphole geben Anlass, diese Verbindungsklasse analog zu Thiophen, Furan und Pyrrol in Untersuchungen zum Elektronentransfer einzusetzen. Somit sollen die Ziele dieser Dissertation die Synthese Ferrocenyl-funktionalisierter Phosphole und die Untersuchung der Stärke der Metall-Metall-Wechselwirkung der Ferrocenylgruppen über den Phospholring im Vergleich zu analogen Heterozyklen sein.

Der Vorteil der Phosphole liegt insbesondere im reaktiven dienischen System bzw. Phosphoratom und damit in der einfachen chemischen Modifizierung zum Einstellen gewünschter elektronischer Eigenschaften. Somit kann gezielt Einfluss auf die Metall-Metall-Wechselwirkung der Ferrocenylgruppen über das heterozyklische Brückenfragment genommen werden.

Dazu soll der Einfluss der Oxidationsstufe des Phosphors (Kapitel B), die Komplexierung am dienischen System (Kapitel C) sowie am Phosphoratom (Kapitel C, Kapitel D) und eine Variation des Substituenten am Phosphoratom zur Erhöhung der Delokalisation im Phospholring (Kapitel E) untersucht werden.

2.5 Literaturverzeichnis

[A1] V. Balzani, *Photochem. Photobiol. Sci.* **2003**, *2*, 459–476.

[A2] R. M. Metzger, in *Intell. Mater.* (Hrsg.: M. Shahinpoor, H.-J. Schneider), Royal Society Of Chemistry, Cambridge, **2007**, 205–230.

[A3] P. S. Peercy, *Nature* **2000**, *406*, 1023–1026.

[A4] A. Aviram, *Mol. Cryst. Liq. Cryst. Sci. Technol., Sect. A* **1993**, *234*, 13–28.

[A5] G. E. Moore, *Electronics* **1965**, *38*, 114–117.

[A6] J. de Rosnay, *Thin Solid Films* **1992**, *210-211*, 1–3.

[A7] V. Balzani, A. Credi, M. Venturi, *ChemPhysChem* **2003**, *4*, 49–59.

[A8] A. H. Flood, E. W. Wong, J. F. Stoddart, *Chem. Phys.* **2006**, *324*, 280–290.

[A9] L. Fu, L. Cao, Y. Liu, D. Zhu, *Adv. Colloid Interface Sci.* **2004**, *111*, 133–157.

[A10] R. L. McCreery, *Chem. Mater.* **2004**, *16*, 4477–4496.

[A11] J. Chen, M. A. Reed, S. M. Dirk, D. W. Price, A. M. Rawlett, J. M. Tour, D. S. Grubisha, D. W. Bennett, in *Adv. Semicond. Org. Nano-Tech., Part III* (Hrsg.: H. Morkoç), Academic Press, Amsterdam, **2003**, 43–187.

[A12] N. A. Zimbovskaya, M. R. Pederson, *Phys. Rep.* **2011**, *509*, 1–87.

[A13] H. Nishihara, K. Kanaizuka, Y. Nishimori, Y. Yamanoi, *Coord. Chem. Rev.* **2007**, *251*, 2674–2687.

[A14] K. H. Khoo, Y. Chen, S. Li, S. Y. Quek, *Phys. Chem. Chem. Phys.* **2015**, *17*, 77–96.

[A15] A. Aviram, M. A. Ratner, *Chem. Phys. Lett.* **1974**, *29*, 277–283.

[A16] G. Jiang, Y. Song, X. Guo, D. Zhang, D. Zhu, *Adv. Mater.* **2008**, *20*, 2888–2898.

[A17] J. G. Kushmerick, A. S. Blum, D. P. Long, *Anal. Chim. Acta* **2006**, *568*, 20–27.

[A18] R. L. McCreery, A. J. Bergren, *Adv. Mater.* **2009**, *21*, 4303–4322.

[A19] M. Tsutsui, M. Taniguchi, *Sensors* **2012**, *12*, 7259–7298.

[A20] F. Chen, J. Hihath, Z. Huang, X. Li, N. J. Tao, *Annu. Rev. Phys. Chem.* **2007**, *58*, 535–564.

[A21] P. J. Low, *Dalton Trans.* **2005**, 2821–2824.

[A22] N. Robertson, C. A. McGowan, *Chem. Soc. Rev.* **2003**, *32*, 96–103.

[A23] A. Ceccon, S. Santi, L. Orian, A. Bisello, *Coord. Chem. Rev.* **2004**, *248*, 683–724.

[A24] C. Creutz, H. Taube, *J. Am. Chem. Soc.* **1969**, *91*, 3988–3989.

[A25] C. Creutz, P. C. Ford, T. J. Meyer, *Inorg. Chem.* **2006**, *45*, 7059–7068.

[A26] The Royal Swedish Academy of Sciences, "The Nobel Prize in Chemistry 1983," verfügbar unter http://www.nobelprize.org/nobel_prizes/chemistry/laureates/1983/, abgerufen am 12.10.2015.

[A27] P. Aguirre-Etcheverry, D. O'Hare, *Chem. Rev.* **2010**, *110*, 4839–4864.

[A28] M. B. Robin, P. Day, *Adv. Inorg. Chem. Radiochem.* **1967**, *10*, 247–422.

[A29] D. F. Watson, A. B. Bocarsly, *Coord. Chem. Rev.* **2001**, *211*, 177–194.

[A30] H. Taube, *Ann. N. Y. Acad. Sci.* **1978**, *313*, 481–495.

[A31] M. Parthey, M. Kaupp, *Chem. Soc. Rev.* **2014**, *43*, 5067–5088.

[A32] K. D. Demadis, C. M. Hartshorn, T. J. Meyer, *Chem. Rev.* **2001**, *101*, 2655–2685.

[A33] P. Day, *Int. Rev. Phys. Chem.* **1981**, *1*, 149–193.

[A34] P. Day, *Comments Inorg. Chem.* **1981**, *1*, 155–167.

[A35] S. Barlow, D. O'Hare, *Chem. Rev.* **1997**, *97*, 637–670.

[A36] M. D. Ward, *Chem. Soc. Rev.* **1995**, *24*, 121–134.

[A37] A. Heckmann, C. Lambert, *Angew. Chem. Int. Ed.* **2012**, *51*, 326–392.

[A38] H. M. Powell, *Proc. Chem. Soc.* **1959**, 73–108.

[A39] A. Ludi, *Chem. Unserer Zeit* **1988**, *22*, 123–127.

[A40] M. B. Robin, *Inorg. Chem.* **1962**, *1*, 337–342.

[A41] C. Creutz, *Prog. Inorg. Chem.* **1983**, *30*, 1–73.

[A42] W. Kaim, B. Sarkar, G. K. Lahiri, in *Spectroelectrochemistry* (Hrsg.: W. Kaim, A. Klein), Royal Society Of Chemistry, Cambridge, **2008**, 68–90.

[A43] W. Kaim, A. Klein, M. Glöckle, *Acc. Chem. Res.* **2000**, *33*, 755–763.

[A44] R. J. H. Clark, *Chem. Soc. Rev.* **1984**, *13*, 219–244.

[A45] D. O. Cowan, C. LeVanda, J. Park, F. Kaufman, *Acc. Chem. Res.* **1973**, *6*, 1–7.

[A46] D. Astruc, *Acc. Chem. Res.* **1997**, *30*, 383–391.

[A47] D. E. Richardson, H. Taube, *Coord. Chem. Rev.* **1984**, *60*, 107–129.

[A48] M. Kaupp, M. Renz, M. Parthey, M. Stolte, F. Würthner, C. Lambert, *Phys. Chem. Chem. Phys.* **2011**, *13*, 16973–16986.

[A49] W. Kaim, G. K. Lahiri, *Angew. Chem. Int. Ed.* **2007**, *46*, 1778–1796.

[A50] M. H. Chisholm, N. J. Patmore, *Acc. Chem. Res.* **2007**, *40*, 19–27.

[A51] P. V. Bernhardt, F. Bozoglián, B. P. Macpherson, M. Martínez, *Coord. Chem. Rev.* **2005**, *249*, 1902–1916.

[A52] D. E. Richardson, *Comments Inorg. Chem.* **1985**, *3*, 367–384.

[A53] F. Barigelletti, L. Flamigni, *Chem. Soc. Rev.* **2000**, *29*, 1–12.

[A54] F. Paul, C. Lapinte, *Coord. Chem. Rev.* **1998**, *178-180*, 431–509.

[A55] J.-P. Launay, *Chem. Soc. Rev.* **2001**, *30*, 386–397.

[A56] D. N. Hendrickson, S. M. Oh, T.-Y. Dong, T. Kambara, M. J. Cohn, M. F. Moore, *Comments Inorg. Chem.* **1985**, *4*, 329–349.

[A57] N. S. Hush, *Electrochim. Acta* **1968**, *13*, 1005–1023.

[A58] N. S. Hush, *Coord. Chem. Rev.* **1985**, *64*, 135–157.

[A59] R. A. Marcus, N. Sutin, *Comments Inorg. Chem.* **1986**, *5*, 119–133.

[A60] R. A. Marcus, *J. Chem. Phys.* **1957**, *26*, 867–871.

[A61] J. R. Reimers, N. S. Hush, *Chem. Phys.* **1996**, *208*, 177–193.

[A62] C. Lapinte, *J. Organomet. Chem.* **2008**, *693*, 793–801.

[A63] D. M. D'Alessandro, F. R. Keene, *Chem. Soc. Rev.* **2006**, *35*, 424–440.

[A64] D. M. D'Alessandro, F. R. Keene, *Chem. Rev.* **2006**, *106*, 2270–2298.

[A65] B. S. Brunschwig, N. Sutin, *Coord. Chem. Rev.* **1999**, *187*, 233–254.

[A66] J.-P. Launay, *Mol. Cryst. Liq. Cryst. Sci. Technol., Sect. A* **1994**, *255*, 1–6.

[A67] R. F. Winter, *Organometallics* **2014**, *33*, 4517–4536.

[A68] P. J. Low, S. Bock, *Electrochim. Acta* **2013**, *110*, 681–692.

[A69] W. Kaim, J. Fiedler, *Chem. Soc. Rev.* **2009**, *38*, 3373–3382.

[A70] M. Krejčik, M. Daněk, F. Hartl, *J. Electroanal. Chem.* **1991**, *317*, 179–187.

[A71] M. Tanner, A. Ludi, *Inorg. Chem.* **1981**, *20*, 2348–2350.

[A72] U. Fürholz, H.-B. Bürgi, F. E. Wagner, A. Stebler, J. H. Ammeter, E. Krausz, R. J. H. Clark, M. J. Stead, A. Ludi, *J. Am. Chem. Soc.* **1984**, *106*, 121–123.

[A73] V. Petrov, J. T. Hupp, C. Mottley, L. C. Mann, *J. Am. Chem. Soc.* **1994**, *116*, 2171–2172.

[A74] S. P. Best, R. J. H. Clark, R. C. S. McQueen, S. Joss, *J. Am. Chem. Soc.* **1989**, *111*, 548–550.

[A75] T. Todorova, B. Delley, *Inorg. Chem.* **2008**, *47*, 11269–11277.

[A76] L.-T. Zhang, J. Ko, M. J. Ondrechen, *J. Am. Chem. Soc.* **1987**, *109*, 1666–1671.

[A77] D. H. Oh, S. G. Boxer, *J. Am. Chem. Soc.* **1990**, *112*, 8161–8162.

[A78] S. B. Piepho, *J. Am. Chem. Soc.* **1990**, *112*, 4197–4206.

[A79] A. Bencini, I. Ciofini, C. A. Daul, A. Ferretti, *J. Am. Chem. Soc.* **1999**, *121*, 11418–11424.

[A80] E. B. Fleischer, D. K. Lavallee, *J. Am. Chem. Soc.* **1972**, *94*, 2599–2601.

[A81] J. E. Sutton, H. Taube, *Inorg. Chem.* **1981**, *20*, 3125–3134.

[A82] K. Rieder, H. Taube, *J. Am. Chem. Soc.* **1977**, *99*, 7891–7894.

[A83] D. O. Cowan, F. Kaufman, *J. Am. Chem. Soc.* **1970**, *92*, 219–220.

[A84] D. O. Cowan, R. L. Collins, F. Kaufman, *J. Phys. Chem.* **1971**, *75*, 2025–2030.

[A85] D. O. Cowan, C. LeVanda, *J. Am. Chem. Soc.* **1972**, *94*, 9271–9272.

[A86] C. LeVanda, D. O. Cowan, C. Leitch, K. Bechgaard, *J. Am. Chem. Soc.* **1974**, *96*, 6788–6789.

[A87] D. L. Lichtenberger, H.-J. Fan, N. E. Gruhn, *J. Organomet. Chem.* **2003**, *666*, 75–85.

[A88] C. LeVanda, K. Bechgaard, D. O. Cowan, *J. Org. Chem.* **1976**, *41*, 2700–2704.

[A89] D. O. Cowan, C. LeVanda, R. L. Collins, G. A. Candela, U. T. Mueller-Westerhoff, P. Eilbracht, *J. Chem. Soc. Chem. Commun.* **1973**, 329–330.

[A90] J. M. Speck, R. Claus, A. Hildebrandt, T. Rüffer, E. Erasmus, L. van As, J. C. Swarts, H. Lang, *Organometallics* **2012**, *31*, 6373–6380.

[A91] A. Hildebrandt, D. Schaarschmidt, R. Claus, H. Lang, *Inorg. Chem.* **2011**, *50*, 10623–10632.

[A92] A. Hildebrandt, H. Lang, *Dalton Trans.* **2011**, *40*, 11831–11837.

[A93] F. C. Leavitt, T. A. Manuel, F. Johnson, *J. Am. Chem. Soc.* **1959**, *81*, 3163–3164.

[A94] C. Charrier, H. Bonnard, G. de Lauzon, F. Mathey, *J. Am. Chem. Soc.* **1983**, *105*, 6871–6877.

[A95] M. Clochard, M. P. Duffy, B. Donnadieu, F. Mathey, *Organometallics* **2008**, *27*, 567–570.

[A96] F. Mathey, *Chem. Rev.* **1988**, *88*, 429–453.

[A97] W. B. McCormack, *Org. Synth.* **1963**, *43*, 73–76.

[A98] F. Mathey, in *Mod. Heterocycl. Chem.* (Hrsg.: J. Alvarez-Builla, J.J. Vaquero, J. Barluenga), Wiley-VCH Verlag GmbH & Co. KGaA, Weinheim, Germany, **2011**, 2071–2116.

[A99] K. Maitra, V. J. Catalano, J. H. Nelson, *J. Am. Chem. Soc.* **1997**, *119*, 12560–12567.

[A100] F. Mathey, *Acc. Chem. Res.* **2004**, *37*, 954–960.

[A101] L. Nyulászi, L. Soós, G. Keglevich, *J. Organomet. Chem.* **1998**, *566*, 29–35.

[A102] M. K. Cyrański, P. v. R. Schleyer, T. M. Krygowski, H. Jiao, G. Hohlneicher, *Tetrahedron* **2003**, *59*, 1657–1665.

[A103] L. Nyulászi, *Chem. Rev.* **2001**, *101*, 1229–1246.

[A104] S. Noorizadeh, M. Dardab, *Chem. Phys. Lett.* **2010**, *493*, 376–380.

[A105] L. Nyulászi, O. Hollóczki, C. Lescop, M. Hissler, R. Réau, *Org. Biomol. Chem.* **2006**, *4*, 996–998.

[A106] G. Keglevich, in *Phosphorus Heterocycles II* (Hrsg.: R.K. Bansal), Topics in Heterocyclic Chemistry, Springer, Berlin, Heidelberg, **2010**, 149–173.

[A107] E. H. Braye, W. Hübel, I. Caplier, *J. Am. Chem. Soc.* **1961**, *83*, 4406–4413.

[A108] R. C. Cookson, G. W. A. Fowles, D. K. Jenkins, *J. Chem. Soc.* **1965**, 6406–6409.

[A109] K. W. Muir, F. Y. Pétillon, R. Rumin, P. Schollhammer, J. Talarmin, *J. Organomet. Chem.* **2001**, *622*, 297–301.

[A110] Y. Dienes, M. Eggenstein, T. Kárpáti, T. C. Sutherland, L. Nyulászi, T. Baumgartner, *Chem. Eur. J.* **2008**, *14*, 9878–9889.

[A111] H. Chen, W. Delaunay, J. Li, Z. Wang, P.-A. Bouit, D. Tondelier, B. Geffroy, F. Mathey, Z. Duan, R. Réau, M. Hissler, *Org. Lett.* **2013**, *15*, 330–333.

[A112] L. Nyulászi, *J. Phys. Chem.* **1995**, *99*, 586–591.

[A113] L. Nyulászi, G. Keglevich, L. D. Quin, *J. Org. Chem.* **1996**, *61*, 7808–7812.

[A114] L. D. Quin, G. Keglevich, A. S. Ionkin, R. Kalgutkar, G. Szalontai, *J. Org. Chem.* **1996**, *61*, 7801–7807.

[A115] G. Keglevich, R. Farkas, T. Imre, K. Ludányi, A. Szöllösy, L. Töke, *Heteroat. Chem.* **2003**, *14*, 316–319.

[A116] L. D. Quin, A. S. Ionkin, R. Kalgutkar, G. Keglevich, *Phosphorus, Sulfur Silicon Relat. Elem.* **1996**, *109-110*, 433–436.

[A117] G. Keglevich, R. Farkas, K. Ludányi, V. Kudar, M. Hanusz, K. Simon, *Heteroat. Chem.* **2005**, *16*, 104–110.

[A118] P. Coggon, A. T. McPhail, *J. Chem. Soc., Dalton Trans.* **1973**, 1888–1891.

[A119] G. Keglevich, L. D. Quin, Z. Böcskei, G. M. Keserü, R. Kalgutkar, P. M. Lahti, *J. Organomet. Chem.* **1997**, *532*, 109–116.

[A120] G. Keglevich, Z. Böcskei, G. M. Keserü, K. Újszászy, L. D. Quin, *J. Am. Chem. Soc.* **1997**, *119*, 5095–5099.

[A121] G. Jochem, H. Nöth, A. Schmidpeter, *Chem. Ber.* **1996**, *129*, 1083–1086.

[A122] C. W. Bird, *Tetrahedron* **1985**, *41*, 1409–1414.

B The Synthesis and (Spectro)electrochemical Behavior of 2,5-Diferrocenyl-1-phenyl-1*H*-phosphole

Dominique Miesel, Alexander Hildebrandt, Marcus Korb, Paul J. Low, and Heinrich Lang*

Veröffentlicht in *Organometallics* **2013**, *32*, 2993–3002.

Die in Kapitel B präsentierten Ergebnisse wurden selbstständig unter Anleitung von Prof. Dr. Heinrich Lang und Dr. Alexander Hildebrandt erstellt. Die kristallografischen Messungen erfolgten von Marcus Korb. Von Prof. Dr. Paul J. Low wurden die theoretischen Berechnungen durchgeführt.

B1 Introduction

Compounds with two redox-active transition metal fragments connected *via* a π-conjugated spacer unit are of considerable interest as they can be regarded as model compounds for molecular wires.[B1–B14] In the last years huge efforts in the development of molecules in which the two redox-active metal centers exhibit a pronounced electronic communication across the spacer unit have been made. During the course of these investigations, a wide variety of π-conjugated spacers have been explored including systems based on all-carbon chains, vinylogous moieties, aromatic hydrocarbons, metallacycles or heteroatom-containing groups.[B15–B24] An equally wide variety of metal fragments have been used as redox-active termini, including half-sandwich, five- and six-coordinate metal centers, metallocenyl groups, bimetallic complexes and clusters, with the degree of electronic interaction between them in the mixed-valence state assessed by drawing on electrochemical and spectroscopic (UV/Vis-NIR, IR, EPR) data, often supported by quantum chemical calculations.[B2,B11,B12,B25] While it is well-known that the electronic structure of such linear arrays, and hence the 'intermetallic communication' or coupling in the mixed-valence state, depends on the nature of both the metal termini and the spacer unit, predicting these *a priori* is not always a simple task.

Within recent studies of our research group it could be demonstrated on the example of di-, tri- and tetra-ferrocenyl heterocycles (thiophenes, furans and pyrroles)[B22,B24] and metallacycles featuring a Cp^*_2M (M = Ti, Zr)[B17,B18] moiety that the electronic characteristics (conjugation and electron balance) greatly influence the intermetallic communication between the mixed-valent termini. In continuation of this work we herein present the synthesis and characterization of diferrocenyl phosphole as well as its chalcogenides. While neglected for decades, phospholes have gained increasing levels of interest during the last years.[B26–B31] Its successful application in metal-containing organic light-emitting devices (OLEDs) accelerated the research on this topic furthermore.[B32,B33] The phosphole ring shows a degree of aromaticity depending on the substituents in 1-, 2- and 5-position, as bulky substituents force the phosphorus to adopt a planar environment. However, blocking the phosphorus lone pair by coordination or oxidation reactions, for example, prevents the extended conjugation around the ring system and removes the aromaticity. Hence, the phosphole motif may offer a tool to fine-tune the electronic nature of the π-conjugated connector unit and hence the electronic effects that may be transmitted across it. This potential electronic flexibility prompted us to study the mixed-valence behavior of diferrocenyl phospholes as a function of the chemical nature of the phosphorus atom.

B2 Results and Discussion

Synthesis and characterization

2,5-Diferrocenyl-1-phenyl-1*H*-phosphole (**B-3**) was synthesized by cyclization of phenylphosphine with diferrocenyl butadiyne according to a reaction procedure firstly described by Märkl and Potthast.[B34] Phenylphosphine (**B-1**) was reacted with 0.8 equiv. of *n*-butyllithium and the resulting solution was added slowly to 1,4-diferrocenyl butadiyne (**B-2**) giving 2,5-diferrocenyl-1-phenyl-1*H*-phosphole (**B-3**) (Scheme B1). Treatment of **B-3** with elemental sulfur or selenium resulted in the formation of the corresponding phosphole chalcogenides **B-4** and **B-5** (Scheme B1).

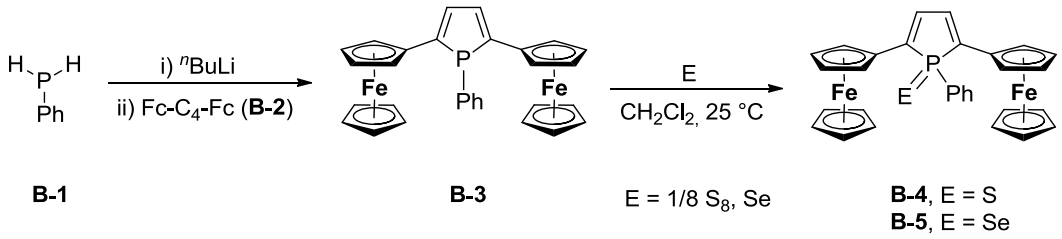

Scheme B1. Synthesis of phospholes **B-3**–**B-5**. (i) benzene/thf (1:1, v/v), 0 °C, 1 h; (ii) thf, 25 °C, 12 h, Fc = Fe(η^5-C_5H_5)(η^5-C_5H_4).

Compounds **B-3**–**B-5** are stable towards air and moisture both in the solid state and in solution. They have been characterized by elemental analysis, IR and NMR (^{1}H, ^{13}C{^{1}H}, ^{31}P{^{1}H}) spectroscopy and ESI-TOF mass spectrometry. The electrochemical and spectroelectrochemical behavior was investigated by cyclic voltammetry (CV), square wave voltammetry (SWV) as well as *in situ* UV/Vis-NIR and IR spectroelectrochemistry.

For the ^{1}H NMR spectra of all three diferrocenyl phospholes **B-3**–**B-5** one singlet for the C_5H_5 rings and four multiplets for the C_5H_4 protons of the ferrocenyl substituents appear as the α- and β-protons are diastereotopic, which is due to the prochiral nature of the phosphorus atom. The signals of the CH phosphole protons appear almost at the same chemical shift (**B-3**: 6.87 ppm; **B-4**: 6.87 ppm; **B-5**: 6.90 ppm) as doublets with $^{3}J_{PH}$ = 11.4 Hz (**B-3**), $^{3}J_{PH}$ = 36.5 Hz (**B-4**) and $^{3}J_{PH}$ = 35.9 Hz (**B-5**). The respective carbon atoms in the ^{13}C{^{1}H} NMR spectra of these species are observed at ca. 130.5 ppm, which indicates that the electronic character of the carbons (and attached protons) in 3- and 4-position of the heterocycle remain unchanged upon oxidation of the phosphorus atom, while the J_{PH} coupling constants change upon oxidation ($J_{P(III)H} < J_{P(V)H}$). The signals of the *meta*- and *para*-protons of the phenyl group in **B-3** appear as an unresolved multiplet at 7.4 ppm (Experimental Section). For the respective *ortho*-protons a multiplet at 7.6 ppm could be observed. In contrast, the *ortho*-protons in **B-4** and **B-5** appear as doublet-of-doublets-of-doublets at 8.02 ppm (**B-4**) and 8.04 ppm (**B-5**) with $^{4}J_{HH}$ = 1.6 Hz, $^{3}J_{HH}$ = 7.9 Hz and $^{3}J_{HP}$ = 14.0 Hz for **B-4** and $^{4}J_{HH}$ = 1.7 Hz, $^{3}J_{HH}$ = 7.8 Hz and $^{3}J_{HP}$ = 14.3 Hz for **B-5**. After oxidation of P(III) in **B-3** to P(V) in **B-4** and **B-5** the signals of the ferrocenyl and phenyl protons in **B-4** and **B-5** are shifted to lower field. In the ^{31}P{^{1}H} NMR spectrum of phosphole **B-3** a singlet at 5.1 ppm is characteristic. After oxidation with sulfur and selenium, respectively, a shift to lower field (46.6 ppm (**B-4**), 33.2 ppm (**B-5**)) occurred.

For selenide **B-5** the characteristic selenium satellites with a $^{1}J_{^{31}P^{77}Se}$ coupling constant of 745 Hz could be found. Typically, the $^{1}J_{^{31}P^{77}Se}$ values allow a quantification of the donor abilities of phosphines PR_3.[B35–B38] An electron-withdrawing group results in increased values for the coupling constants indicating an increased *s* character for the phosphorus orbital involved in the phosphorus-selenium bond. ^{31}P{^{1}H} NMR data and $^{1}J_{^{31}P^{77}Se}$ coupling constants for several seleno phosphines are summarized in Table B1. A comparison with other P(III) species showed that phosphole **B-3** can be characterized as a weak donor.[B36–B38]

Table B1. ^{31}P NMR chemical shifts and ^{31}P-^{77}Se coupling constants for B-5 and several phosphine selenides.

Compd.	δ (ppm)	$^{1}J(^{31}P\text{-}^{77}Se)$ (Hz)
B-5	33.2	745
$Se{=}PPh_3$ [B35]	35.9	732
$Se{=}P(4\text{-}Cl\text{-}C_6H_4)_3$ [B39]	2.21	753
$Se{=}P(2,4,6\text{-}(MeO)_3\text{-}C_6H_2)_3$ [B35]	-16.8	703
$Se{=}P(4\text{-}NMe_2\text{-}C_6H_4)_3$ [B40]	41.6	683

The molecular structures of **B-4** and **B-5** in the solid state have been determined by single crystal X-ray diffraction analysis. Suitable crystals were obtained by diffusion of *n*-hexane into a dichloromethane solution of either **B-4** or **B-5** at ambient temperature. The ORTEP diagrams with selected bond lengths, bond angles and torsion angles are shown in Figures B1 and B2.

Compounds **B-4** and **B-5** both crystallize in the orthorhombic space group $P2_12_12_1$. The ferrocenyl groups are antiparallel oriented and are almost coplanar to the heterocyclic core (torsion of the plane of the C_5H_4 unit to the plane of the phosphole core: **B-4**: -4.4(18) ° for Fe1, 3.0(19) ° for Fe2; **B-5**: 3.3(12) ° for Fe1, -1.7(11) ° for Fe2).

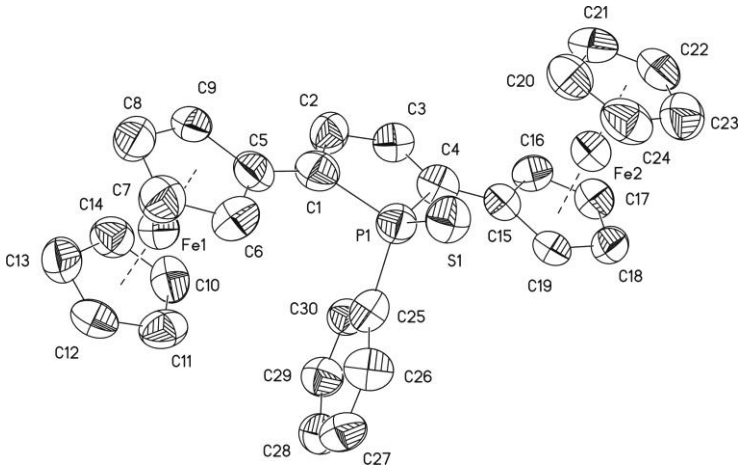

Figure B1. ORTEP diagram (50 % probability level) of the molecular structure of **B-4** with the atom-numbering scheme. All hydrogen atoms have been omitted for clarity. Selected bond distances (Å), angles (deg), and torsion angles (deg): D1–Fe1 = 1.6417(15), D2–Fe1 = 1.6542(15), D3–Fe2 = 1.6487(16), D4–Fe2 = 1.6504(16), P1–C1 = 1.815(12), C1–C2 = 1.363(15), C2–C3 = 1.450(14), C3–C4 = 1.337(14), C4–P1 = 1.851(10), C1–C5 = 1.431(15), C4–C15 = 1.411(15), P1–C25 = 1.834(11), P1–S1 = 1.951(4), C2–C1–P1 = 106.6(8), C1–P1–C4 = 93.8(5), C3–C4–P1 = 105.6(8), C2–C1–C5 = 128.0(11), C3–C4–C15 = 130.2(9), D1–Fe1–D2 = 177.88(11), D3–Fe2–D4 = 179.78(12), C1–P1–C25 = 104.1(5), C25–P1–C4 = 106.2(5), C1–P1–S1 = 116.9(4), C25–P1–S1 = 114.7(4), C4–P1–S1 = 118.4(4), C3–C4–C15–C16 = 3.0(19), C2–C1–C5–C9 = -4.4(18), C2–C3–C4–P1 = 1.5(11), P1–C1–C2–C3 = -0.5(12), C5–D1–D2–C10 = -8.73(81), C15–D3–D4–C20 = 5.33(75) (D = denotes the centroids of C_5H_4 or C_5H_5).

The conformation of the cyclopentadienyl ligands in individual ferrocenyl units is almost eclipsed (**B-4**: -8.73(81) ° for Fe1, 5.33(75) ° for Fe2; **B-5**: 2.79(53) ° for Fe1, -4.00(47) ° for Fe2). The P1-C1-C2-C3-C4 arrangement is planar (**B-4**: rms deviation 0.0025 Å, highest deviation from planarity observed for P1 with -0.0302(158) Å; **B-5**: rms deviation 0.0078 Å, highest deviation from planarity observed for P1 with 0.0280(101) Å). The phosphorus atom possesses, as expected, a tetrahedral environment (Figure B1). The structural features found in phosphole chalcogenides **B-4** and **B-5** resemble those typically found in other examples of this family of molecules.[B41,B42]

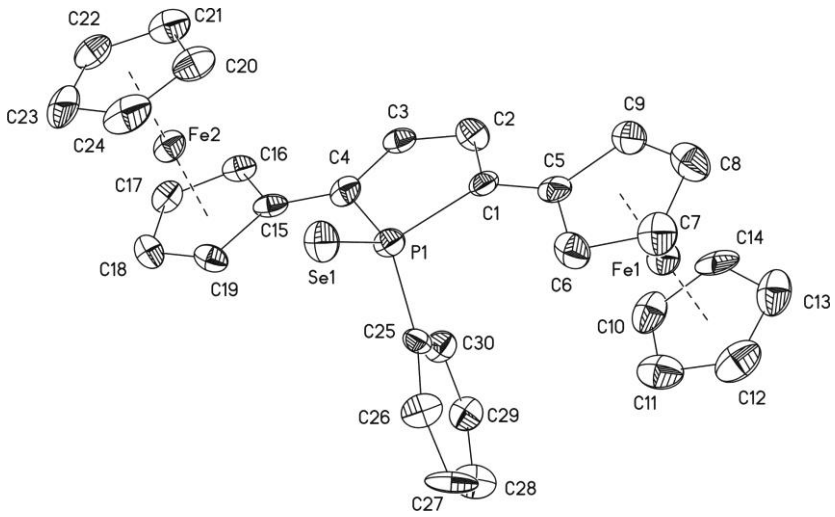

Figure B2. ORTEP diagram (50 % probability level) of the molecular structure of **B-5** with the atom-numbering scheme. All hydrogen atoms have been omitted for clarity. Selected bond distances (Å), angles (deg), and torsion angles (deg): D1–Fe1 = 1.6420(10), D2–Fe1 = 1.6496(10), D3–Fe2 = 1.6406(10), D4–Fe2 = 1.6411(10), P1–C1 = 1.827(7), C1–C2 = 1.349(9), C2–C3 = 1.443(9), C3–C4 = 1.358(9), C4–P1 = 1.819(8), C1–C5 = 1.415(10), C4–C15 = 1.439(10), P1–C25 = 1.807(7), P1–Se1 = 2.1047(15), C2–C1–P1 = 106.4(6), C4–P1–C1 = 93.8(4), C3–C4–P1 = 106.3(6), C2–C1–C5 = 128.2(7), C3–C4–C15 = 127.8(7), D1–Fe1–D2 = 177.45(8), D3–Fe2–D4 = 179.97(10), C25–P1–C1 = 104.5(3), C25–P1–C4 = 106.8(3), C1–P1–Se1 = 116.3(2), C25–P1–Se1 = 115.0(2), C4–P1–Se1 = 117.8(2), C3–C4–C15–C16 = -1.7(11), C2–C1–C5–C9 = 3.3(12), C2–C3–C4–P1 = -2.5(7), P1–C1–C2–C3 = -0.6(8), C5–D1–D2–C10 = 2.79(53), C15–D3–D4–C20 = -4.00(47) (D = denotes the centroids of C_5H_4 or C_5H_5).

Electrochemistry and Spectroelectrochemistry

The redox properties of heterocycles **B-3**–**B-5** were investigated by cyclic voltammetry, square wave voltammetry and spectroelectrochemistry (UV/Vis-NIR, IR). As supporting electrolyte a dry dichloromethane solution containing 0.1 mol·L^{-1} of $[N^nBu_4][B(C_6F_5)_4]$ or $[N^nBu_4][PF_6]$ was used, allowing effects of ion-pairing on the stability of the redox products

to be assessed in a qualitative fashion.[B43–B45] The cyclic voltammetry measurements were performed at 20 °C at a scan rate of 100 mV·s^{-1}. All potentials are referenced to the FcH/FcH$^+$ redox couple.[B46] The data of the cyclic voltammetry experiments are summarized in Table B2. The voltammograms of **B-3**–**B-5** measured in the presence of [N^{n}Bu$_4$][B(C$_6$F$_5$)$_4$] are shown in Figure B3 and the ones measured using [N^{n}Bu$_4$][PF$_6$] as supporting electrolyte are depicted in Figure SI1.

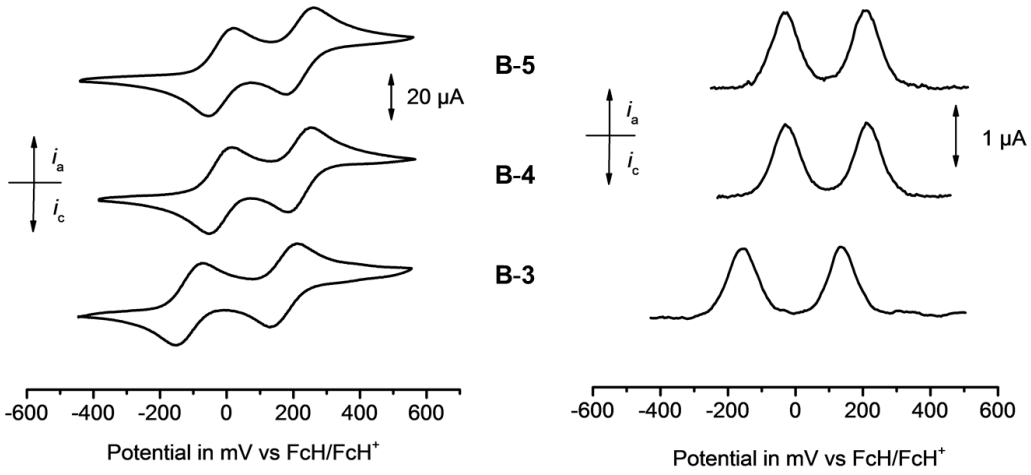

Figure B3. Left: Cyclic voltammograms of **B-3**–**B-5**; scan rate: 100 mV·s^{-1}. Right: Square wave voltammograms of **B-3**–**B-5** in dichloromethane solutions (1.0 mmol·L^{-1}) at 20 °C, supporting electrolyte 0.1 mol·L^{-1} [N^{n}Bu$_4$][B(C$_6$F$_5$)$_4$], working electrode: glassy carbon electrode (surface area 0.031 cm²).

The ferrocenyl groups of compounds **B-3**–**B-5** could be oxidized separately showing two reversible redox events in each electrolyte system with differences between cathodic peak potential and the anodic peak potential (ΔE_p) falling between 68 and 80 mV (Table B2), and peak currents proportional to $\nu^{1/2}$ being observed confirming the essentially reversible character of these ferrocenyl-based oxidation events. The electron-withdrawing character of the P(V) center in **B-4** and **B-5** leads to a shift of the $E_1^{\circ\prime}$ values to more positive potentials relative to the P(III) species **B-3**. The more electron-rich P(III) center also leads to an enhanced thermodynamic stability of the mono-oxidized complex [**B-3**]$^+$ evidenced by the greater comproportionation constant (K_c) (Table B2). Due to the higher ion-pairing capability (spherical diameter [PF$_6$]$^-$, 3.3 Å; [B(C$_6$F$_5$)$_4$]$^-$, 10 Å), the use of dichloromethane and [N^{n}Bu$_4$][PF$_6$] as solvent/supporting electrolyte results in a lower resolution and hence the redox splitting ($\Delta E^{\circ\prime}$) decreases (Table B2).[B47] The difference between $\Delta E^{\circ\prime}_{[PF_6]^-}$ to

$\Delta E^{\circ\prime}_{[B(C_6F_5)_4]^-}$ of about 75–100 mV mostly reflects the electrostatic contribution to the stability of mixed-valent mono-cationic molecules [**B-3**]$^+$–[**B-5**]$^+$. A comparison of phospholes **B-3**–**B-5** with analogous bis(ferrocenes) featuring thiophene-, furan- and pyrrole-derived bridges, reveal similar trends in the first oxidation potential, $E_1^{\circ\prime}$, and $\Delta E^{\circ\prime}$ under identical conditions, with the more readily oxidized complexes bearing the more electron donating heteroatoms giving rise to the larger $\Delta E^{\circ\prime}$ values and hence larger K_c. For example, $\Delta E^{\circ\prime}$ for **B-3**–**B-5** and other 2,5-diferrocenyl substituted heterocycles fall in the sequence NPh (450 mV) > NMe (410 mV) > O (290 mV) ≈ **B-3** (280 mV) > S (260 mV) > **B-4** (240 mV) = **B-5** (235 mV).[B22] The significant $\Delta E^{\circ\prime}$ values indicate considerable stability of the mono-cations with respect to disproportionation to the neutral and dicationic forms. Assuming that the oxidation processes are ferrocene-based, which seems eminently reasonable given the chemical composition, and given the robustness of the ferrocene/ferrocenium redox states, the formally mixed-valence mono-cations [**B-3**]$^+$–[**B-5**]$^+$ were viewed likely to be sufficiently stable to permit spectroscopic observation using spectroelectrochemical methods and further characterization to address the underlying electronic structures and influence of the bridging ligand on the electronic properties.

Table B2. Cyclic voltammetry data of complexes B-3–B-5.

Compd.	$E_1^{\circ\prime}$ in mV (ΔE_p in mV)	$E_2^{\circ\prime}$ in mV (ΔE_p in mV)	$\Delta E^{\circ\prime}$ in mV	K_c / 10^4
B-3, [N^{n}Bu$_4$][PF$_6$]	-135 (76)	50 (62)	185	0.14
B-4, [N^{n}Bu$_4$][PF$_6$]	-65 (76)	100 (76)	165	0.05
B-5, [N^{n}Bu$_4$][PF$_6$]	-60 (80)	100 (78)	160	0.05
B-3, [N^{n}Bu$_4$][B(C$_6$F$_5$)$_4$]	-110 (72)	170 (80)	280	5.4
B-4, [N^{n}Bu$_4$][B(C$_6$F$_5$)$_4$]	-15 (68)	225 (74)	240	1.1
B-5, [N^{n}Bu$_4$][B(C$_6$F$_5$)$_4$]	-15 (74)	220 (80)	235	0.9

Potentials *vs* FcH/FcH$^+$, scan rate 100 mV·s^{-1} at glassy carbon electrode of 1.0 mmol·L^{-1} solutions of **B-3**–**B-5** in dry dichloromethane; 0.1 mol·L^{-1} [N^{n}Bu$_4$][B(C$_6$F$_5$)$_4$] or [N^{n}Bu$_4$][PF$_6$] as supporting electrolyte at 20 °C.

The UV/Vis-NIR spectroelectrochemical measurements of dichloromethane solutions containing **B-3**–**B-5** (2.0 mmol·L^{-1}) and [N^{n}Bu$_4$][B(C$_6$F$_5$)$_4$] (0.1 mol·L^{-1}) as supporting electrolyte were performed in an OTTLE (OTTLE = Optically Transparent Thin-Layer Electrochemical) cell.[B48] The compounds were oxidized by stepwise increments in the applied potential (step width: 25 mV, 50 mV or 100 mV). During the measurements, oxidation of the neutral compounds to mixed-valence mono-cationic [**B-3**]$^+$, [**B-4**]$^+$ and

[**B-5**]$^{+}$, and finally to the dicationic species [**B-3**]$^{2+}$–[**B-5**]$^{2+}$ could be observed. To proof the reversibility after full oxidation, each compound was reduced and the resulted UV/Vis-NIR spectra are identical with the starting compound. The UV/Vis-NIR spectra of phospholes **B-3**–**B-5** measured in dichloromethane are depicted in Figures B4 (**B-3**), SI2 (**B-4**) and SI3 (**B-5**) and the spectra measured in acetonitrile are shown in Figures SI4 (**B-3**), SI5 (**B-4**) and SI6 (**B-5**). Phospholes **B-3**–**B-5** show, as expected, no absorptions in the NIR region (1000–3000 nm). Upon oxidation of these molecules mixed-valence [**B-3**]$^{+}$–[**B-5**]$^{+}$ are formed, resulting in the appearance of a broad band enveloping between 1500 nm and 2500 nm (Figures B4 and SI2). A further potential increase above 500 mV *vs* Ag/AgCl leads to the disappearance of these absorptions, a behavior typically observed for intervalence charge transfer (IVCT) excitations. The observed spectra can be deconvoluted into three Gaussian-shaped bands, which are assumed to represent the IVCT transition, a LF (ligand field) transition associated with the ferrocenium moiety and a third band simulating the edge to the higher energy absorptions. The sum of these three Gaussian functions allows an almost exact overlay with the experimental spectra. Therefore, the intensity ε_{max}, the full-width-at-half-height $\Delta\nu_{1/2}$ and the ν_{max} values associated with the IVCT component could be determined.

Table B3. NIR data of the IVCT absorptions of phospholes [B-3]$^{+}$–[B-5]$^{+}$.[a]

Solvent	Compd.	ν_{max} (cm^{-1}) (ε_{max} (L·mol^{-1}·cm^{-1}))	$\Delta\nu_{1/2}$ (cm^{-1})	$(\Delta\nu_{1/2})_{theo}$[b] (cm^{-1})
dichloromethane	[**B-3**]$^{+}$	5000 (1750)	3050	3400
	[**B-4**]$^{+}$	4900 (1300)	4200	3360
	[**B-5**]$^{+}$	4850 (1100)	4200	3350
acetonitrile	[**B-3**]$^{+}$	6500 (1600)	3200	3870
	[**B-4**]$^{+}$	6900[c]	3100	3990
	[**B-5**]$^{+}$	6900[c]	3400	3990

[a]In dry dichloromethane or acetonitrile containing 0.1 mol·L^{-1} of [N^{n}Bu$_4$][B(C$_6$F$_5$)$_4$] as supporting electrolyte at 20 °C. [b]Values calculated as $(\Delta\nu_{1/2})_{theo} = (2310\cdot\nu_{max})^{1/2}$ according to the Hush relationships for weakly coupled systems.[B49] [c]Due to the lack of solubility of compounds **B-4** and **B-5** in acetonitrile the extinction coefficients were not determined.

The data derived from deconvoluted IVCT absorption bands from [**B-3**]$^{+}$–[**B-5**]$^{+}$ are summarized in Table B3, although the assignment and interpretation of absorption profiles taken from deconvolution should always be treated with caution as the underlying band-shapes are sensitive to the degree of coupling. To help confirm the IVCT assignment, the spectroelectrochemical UV/Vis-NIR experiments were also carried out in acetonitrile as a solvent, as the IVCT band of a class II compound should display solvatochromic

behavior.[B3,B13,B50] Changing the polarity of the solvent from P = 3.1 (dichloromethane) to P = 5.8 (acetonitrile) resulted in a hypsochromic shift of 1500 cm^{-1} (**B-3**$^+$), 2000 cm^{-1} (**B-4**$^+$, **B-5**$^+$) (Table B3).[B51] This solvatochromic behavior is entirely consistent with the IVCT assignment.

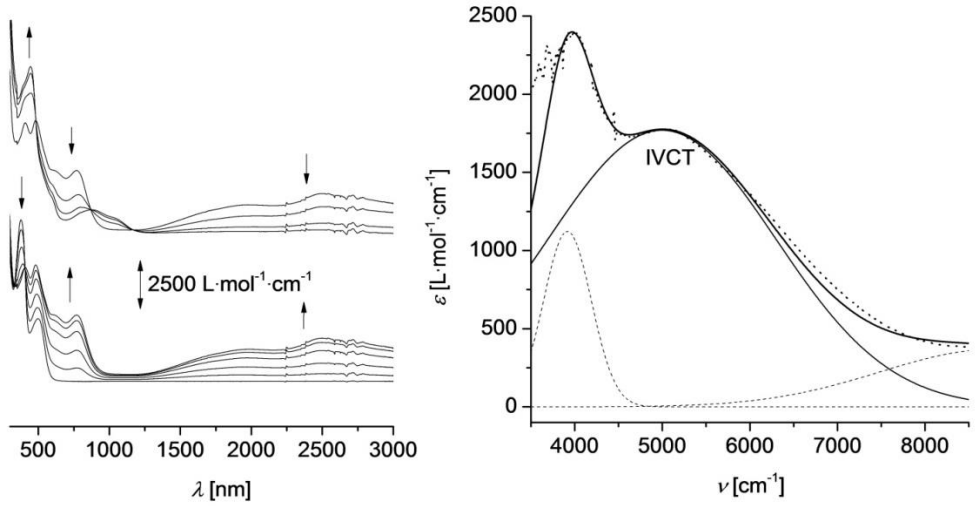

Figure B4. Left: UV/Vis-NIR spectra of **B-3** at 20 °C in dichloromethane (2.0 mmol·L^{-1}) at rising potentials (bottom: -200 to 560 mV; top: 560 to 800 mV vs Ag/AgCl); supporting electrolyte [N^nBu_4][$B(C_6F_5)_4$]. Right: Deconvolution of the NIR absorptions of [**B-3**]$^+$ using three Gaussian shaped bands determined by spectroelectrochemistry in an OTTLE cell.

Analysis of the IVCT absorption allows classification of **B-3** as a moderately coupled class II system within the scheme proposed by Robin and Day.[B5] A comparison of the IVCT absorption of phosphole **B-3** (ε_{max} = 1750 L·mol^{-1}·cm^{-1}, $\Delta\nu_{1/2}$ = 3050 cm^{-1}) with analogous 2,5-diferrocenyl substituted heterocycles shows that regarding to the extinction it can be placed between 2,5-diferrocenyl furan (ε_{max} = 1496 L·mol^{-1}·cm^{-1}) and 2,5-diferrocenyl-1-methyl-1*H*-pyrrole (ε_{max} = 3145 L·mol^{-1}·cm^{-1}).[B22] Nevertheless, the full-width-at-half-height of the IVCT band in **B-3** exceeds those found in all other molecules of the thus mentioned series indicating a weaker interaction. Please note that the Hush two state model is only valid in the weak class II regime while stronger coupling includes partly delocalization and therefore a more narrow bandwidth is observed.[B49,B52] Brunschwig, Creutz and Sutin stated that the quotient between the observed bandwidth and the theoretical bandwidth according to Hush can be taken as a measure for the strength of this coupling.[B50] Nevertheless solvent broadening as observed for [**B-4**]$^+$ and [**B-5**]$^+$ in dichloromethane (Table B3) also contributes to the bandwidth and therefore hinders the direct comparability. A good comparison to other

diferrocenyl heterocycles is complicated because phosphole **B-3** possesses a somewhat different geometry at the $^{c}C_4P$ backbone, as in contrast to other heterocycles the phosphorus lone pair only to some extend involves in the delocalization of the $^{c}C_4E$ ring.[B53,B54] Thus the phosphole behaves similar to a *cis*-diene system rather than an aromatic five membered heterocycle.

The IVCT absorptions of sulfide **B-4** and selenide **B-5** show smaller intensities (**B-4**: 1300 $L \cdot mol^{-1} \cdot cm^{-1}$; **B-5**: 1100 $L \cdot mol^{-1} \cdot cm^{-1}$) (Table B3). This indicates that the occupation of the lone pair slightly decreases the interaction among the $^{c}C_4P$ ring and characterizes those two molecules as weak class II compounds. In generally, the characteristics of the IVCT absorptions resemble those found for 1,4-diferrocenyl butadiene ($\nu_{max} = 5290$ cm^{-1}, $\varepsilon_{max} = 2280$ $L \cdot mol^{-1} \cdot cm^{-1}$, $\Delta\nu_{1/2} = 3900$ cm^{-1}).[B55] One may conclude that the C_4 backbone mainly promotes the electron transfer between the ferrocenyl termini.

B3 Computational studies

To help characterize the redox products and better understand the nature of the electronic transitions, electronic structure calculations were carried out. The computational systems are designated $[\mathbf{B\text{-}3'}]^{n+}$, $[\mathbf{B\text{-}4'}]^{n+}$ and $[\mathbf{B\text{-}5'}]^{n+}$ (n = 0, 1, 2) to distinguish them from the experimental complexes. All geometry optimizations and TD-DFT calculations were undertaken using the B3LYP functional and 3-21G* basis set combination. In the case of the dications, the triplet states were found to be considerably more stable than the analogous singlet states ($\Delta E_{T\text{-}S}$: –134.27 kJ/mol $[\mathbf{B\text{-}3'}]^{2+}$; –81.21 kJ/mol $[\mathbf{B\text{-}4'}]^{2+}$; –76.74 kJ/mol $[\mathbf{B\text{-}5'}]^{2+}$) and the later are not considered further. Selected bond lengths (Å) and angles (°) (Table SI1), orbital energy and composition (Table SI2), calculated and spectroelectrochemically observed IR data (Table B4) and TD-DFT results (Table SI3) are tabulated in the supporting information.

The optimized geometries are in excellent agreement with the available experimentally determined structures of **B-4** and **B-5**, with individual bond lengths being over-estimated by less than 0.03 Å. Within the neutral members of the series, **B-3´**, **B-4´** and **B-5´**, oxidation of the PPh center from P(III) to P(V) leads to a modest increase in the localization of the double bonds in the heterocyclic ring and a small contraction of the Fc-C_4H_2 bond lengths, probably due to increased electrostatic attraction. However, these variations are small and in all cases the phosphole ring system presents a clear alternation in bond lengths consistent with a

description in terms of a cyclic diene. This description is entirely consistent with the distribution and nodal properties of the HOMOs, which are derived from the *cis*-butadiene-like π-system of the C_4H_2 fragment mixed with the ferrocenyl moieties, with vanishingly small contributions from the phosphorus atom and its substituents (Figure SI9, Table SI2).

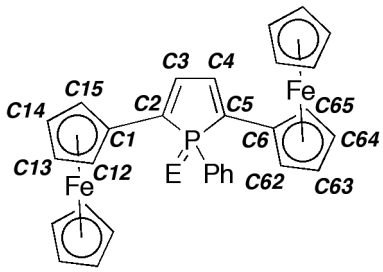

Scheme B2. Numbering scheme for the calculation of phospholes **B-3**–**B-5**.

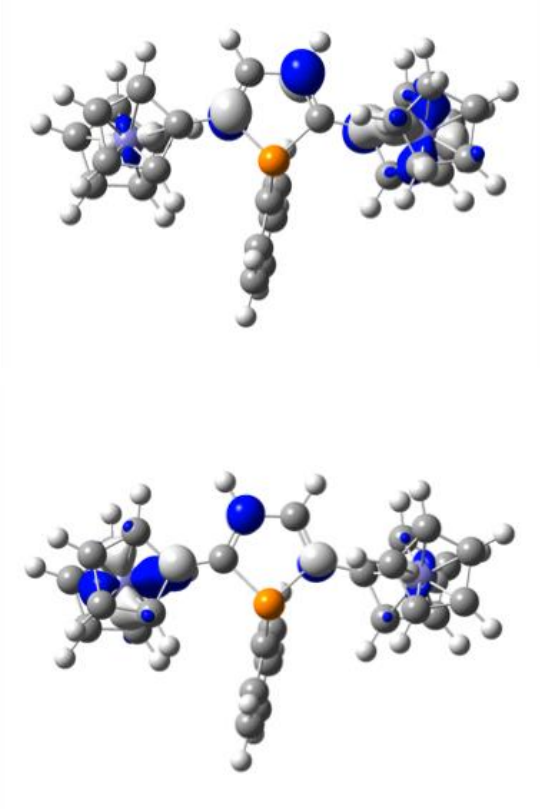

Figure B5. Plots of the β-LUMO (top) and β-HOMO (bottom) of [**B-3´**]$^+$ (isosurface ±0.04 (e bohr^{-3})$^{1/2}$.

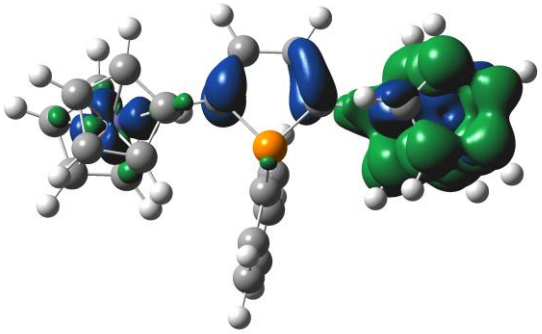

Figure B6. A plot of the spin density for the cation radical [**B-3´**]$^{+}$ (isosurface ±0.04 (e bohr^{-3})$^{1/2}$.

The optimized structures of the radical cations [**B-3´**]$^{+}$, [**B-4´**]$^{+}$ and [**B-5´**]$^{+}$ reflect the depopulation of the parent HOMO, with a subtle (≤0.03 Å) contraction of the Fc-C_4H_2 and C(3)-C(4) bond lengths and concomitant elongation in the C(3)-C(4) bond (Table SI2, Scheme B2). Interestingly, whilst the C(1)-C(2) and C(5)-C(6) bond lengths are arguably different in [**B-3´**]$^{+}$ (C(1)-C(2) 1.4315; C(5)-C(6) 1.4199 Å), and there is little difference in the C(2)-P and C(5)-P bond lengths (1.8337, 1.8255 Å) the opposite is true of the P(V) complexes [**B-4´**]$^{+}$ and [**B-5´**]$^{+}$ (Table SI2).

However, whilst only small structural distortions in the phosphole ring fragment hint at a localized electronic structure, plots of the critical frontier molecular orbitals (Figure B5, Table SI2) and the spin density distributions (Figure B6) are more compelling. Again, the phosphorus group makes little if any contribution to the electronic description, and each of [**B-3´**]$^{+}$, [**B-4´**]$^{+}$ and [**B-5´**]$^{+}$ can be accurately described in terms of a localized oxidation on the ferrocenyl moiety *anti* to the phosphole phenyl ring.

The triplet dications [**B-3´**]$^{2+}$, [**B-4´**]$^{2+}$ and [**B-5´**]$^{2+}$ are also well described in terms of ferrocene-based oxidation processes, and interestingly the structural parameters of the phosphole ring are almost indistinguishable from those of the parent neutral analogues. The *β*-LUMO and *β*-LUMO+1 are each largely localized on a ferrocenyl moiety, with the *β*-LUMO+1 in [**B-4´**]$^{2+}$ and [**B-5´**]$^{2+}$ also containing a small contribution from the C_4H_2 fragment (Figure SI10).

IR spectroscopy and calculated molecular vibrational frequencies provide a useful link between experimentally observable and calculated parameters, allowing the accuracy of the optimized geometries to be assessed. IR spectroelectrochemical methods were employed to obtain experimental IR data, with measurements carried out on solutions of **B-3**–**B-5** in

dichloromethane (10 mmol·L^{-1}) containing 0.1 mol·L^{-1} [N^{n}Bu$_4$][PF$_6$] as supporting electrolyte in an OTTLE cell with CaF_2 windows (Figures B7, SI7 and SI8). The IR spectra of the neutral complexes **B-3**, **B-4** and **B-5** are each characterized by a weak band near 1590 cm^{-1}, which is replicated by calculated frequencies between 1550–1600 cm^{-1} for the computational models **B-3´**, **B-4´** and **B-5´** (Table B4). Analysis of the atomic displacements confirms this feature to be an asymmetric ν(C=C-C=C) stretch associated with the *cis*-butadiene fragment of the phosphole moiety.

The cation radicals [**B-3**]$^+$, [**B-4**]$^+$ and [**B-5**]$^+$ generated by one-electron oxidation in the spectroelectrochemical cell display new vibrational band envelopes between 1400–1500 cm^{-1}. In addition, a degree of decomposition of [**B-3**]$^+$ is also evident by appearance of a new feature near 1700 cm^{-1} in the spectrum that is not sensitive to further changes in redox state (vide infra). The lower frequency feature **(**[**B-3**]$^+$ 1407; [**B-4**]$^+$ 1421; [**B-5**]$^+$ 1419 cm^{-1}) can be assigned to the butadiene-like ν(C=C-C=C) stretch ([**B-3´**]$^+$ 1363; [**B-4´**]$^+$ 1378; [**B-5´**]$^+$ 1376, 1374 cm^{-1}). The shift of this band to lower frequency in the cation radicals when compared with the neutral species is consistent with the structure of the HOMO (**B-3´**, **B-4´** and **B-5´**) and β-LUMO ([**B-3´**]$^+$, [**B-4´**]$^+$ and [**B-5´**]$^+$). The calculations also reveal a relatively strong ν(C-C) stretch for the Fc$^+$-C$_4$H$_2$ moiety ([**B-3´**]$^+$ 1421; [**B-4´**]$^+$ 1423; [**B-5´**]$^+$ 1423 cm^{-1}) and a weaker ν(C-C) stretch for the Fc-C$_4$H$_2$ fragment ([**B-3´**]$^+$ 1398; [**B-4´**]$^+$ 1404; [**B-5´**]$^+$ 1402 cm^{-1}). These calculated bands are consistent with the observed features at 1471, 1413 cm^{-1} ([**B-3**]$^+$); 1486, 1434 cm^{-1} ([**B-4**]$^+$) and 1481, 1434 cm^{-1} ([**B-5**]$^+$).

The IR spectra of the dications [**B-3**]$^{2+}$, [**B-4**]$^{2+}$ and [**B-5**]$^{2+}$ are characterized by a complicated series of bands between 1415 and 1556 cm^{-1}. These complicated band patterns are consistent with the calculated vibrational frequencies (Table B4); the strongest IR active modes have similar ν(C=C-C=C) and ν(C-C) (Fc$^+$-C$_4$H$_2$) character as noted for the mono-cations, admixed with additional aromatic ν(CC) modes from both the ferrocenium moieties and the phosphole phenyl ring.

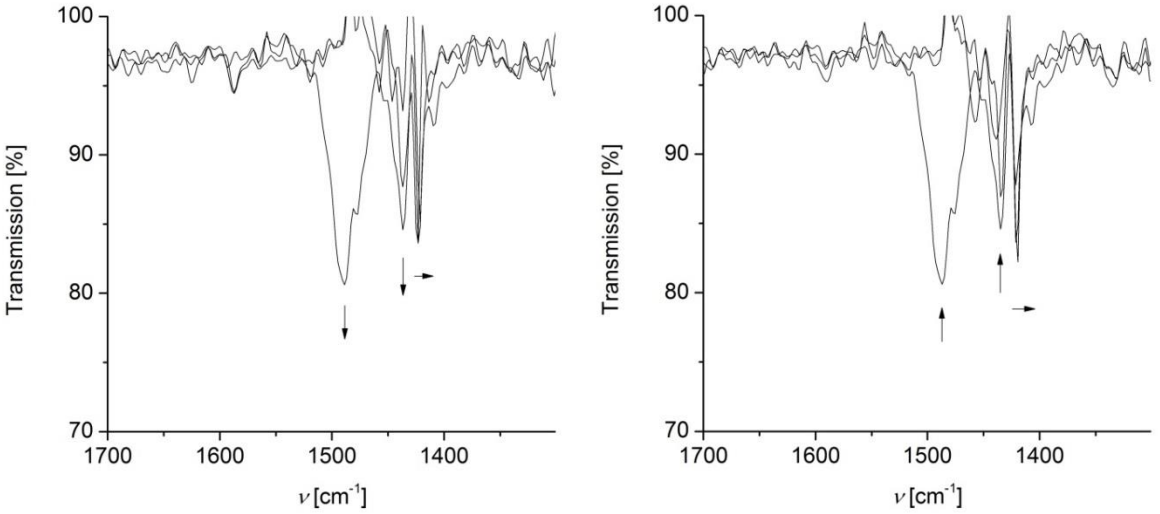

Figure B7. IR spectra of **B-4** at 20 °C in dichloromethane (10 mmol·L^{-1}) at rising potentials (left: -200 to 600 mV (**B-4** → [**B-4**]$^{+}$); right: 600 to 1300 mV ([**B-4**]$^{+}$ → [**B-4**]$^{2+}$) *vs* Ag/AgCl); supporting electrolyte [N^{n}Bu$_4$][PF$_6$].

Table B4. Selected calculated (and observed) IR active ν(C=C) vibrations (cm^{-1}) for [B-3′]$^{n+}$, [B-4′]$^{n+}$ and [B-5′]$^{n+}$ (n = 0, 1, 2).[a]

	n = 0	n = 1	n = 2
[**B-3**′]$^{n+}$ ([**B-3**]$^{n+}$)	1595w (-)[b]	1421s (1471m)	1505m (1556w)
		1398m (1413m)	1430m (1455w)
		1363s (1407m)	1403s (1415w)
[**B-4**′]$^{n+}$ ([**B-4**]$^{n+}$)	1548m (1587w)	1423s (1486m)	1543m (-) [b]
		1404 m (1434m)	1455m (1434w)
		1378s (1421m)	1409s (1419w)
[**B-5**′] $^{n+}$ ([**B-5**]$^{n+}$)	1546m (1585w)	1423s (1481m)	1541m (-) [b]
		1402m (1434m)	1452m (1463w)
		1376m (1419m)	1409s (1434w)
		1374m (-) [b]	1390s (1417)

[a]Correction factor of 0.95 applied to all calculated frequencies. [b]Signal-noise-ratio too low.

TD-DFT calculations can provide a very useful link between the calculated electronic structure and experimentally observable electronic absorption spectra. Whilst pure DFT functionals perform poorly for excitations with considerable charge transfer character, hybrid functionals with increasingly sophisticated treatments of direct exchange can result in much better match, especially when calculations are augmented by a suitable solvent model. In the present case, TD-DFT calculations with even the relatively simple B3LYP functional and small basis set (3-21G*) performed surprisingly well. The UV/Vis-NIR spectra of **B-3**, **B-4** and **B-5** feature two absorption bands near 500 and 400 nm (20000 and 25000 cm^{-1}). TD-DFT

calculations with **B-3′** contain two excitations with significant oscillator strength at 18975 cm^{-1}, which has largely ferrocene-based LF character admixed with ferrocene to C_4H_2 charge transfer character, and 25445 cm^{-1}, which has more clearly defined Fc→C_4H_2 character. For each of **B-4′** and **B-5′** TD-DFT calculations reveal two excitations of similar energy and character that are likely responsible for the lower energy absorption band observed in the experimental spectra (**B-4′** 17921, 18050 cm^{-1}; **B-5′** 17986, 18166 cm^{-1}) and a higher energy transition with Fc→C_4H_2 character (**B-4′** 23255 cm^{-1}; **B-5′** 23584 cm^{-1}). TD-DFT calculations with the cation radicals [**B-3′**]$^+$, [**B-4′**]$^+$ and [**B-5′**]$^+$ reveal two low energy (NIR) excitations arising from the *β*-HOMO→*β*-LUMO transition (*i.e.,* IVCT character, Figure B5, Table SI3) and a lower lying filled ferrocenium orbital (*β*-HOMO-11 ([**B-3′**]$^+$ or *β*-HOMO-12 [**B-4′**]$^+$ and [**B-5′**]$^+$) to the *β*-LUMO and hence offering more intraligand ferrocenium character. It is noteworthy that the calculated oscillator strength of the transition with IVCT character for [**B-3′**]$^+$ is higher, when compared with [**B-4′**]$^+$ and [**B-5′**]$^+$, consistent with the trends in absorptivity observed in the experimental spectra (Table SI3), which may be taken as an indication of increased electronic interaction in the non-oxidized phosphole. Although the relative energies of the IVCT and ferrocenium-based LF transitions in the model cation radicals [**B-3′**]$^+$, [**B-4′**]$^+$ and [**B-5′**]$^+$ are reversed relative to experiment, the results support the general conclusions drawn from initial inspection of the UV/Vis-NIR spectroelectrochemical results. The TD-DFT calculations of [**B-3′**]$^+$, [**B-4′**]$^+$ and [**B-5′**]$^+$ also contain two higher energy excitations near 11000 and 12000 cm^{-1}, with FcC_4H_2→Fc^+ and Fc→$C_4H_2Fc^+$ charge transfer character, which together account for the absorption features observed in the experimental spectra of the radical cations between 1000–650 nm (10000–15380 cm^{-1}). In the case of the triplet dications test calculations with [**B-3′**]$^{2+}$ confirm the absence of transitions with any oscillator strength below 16500 cm^{-1}. The most significant excitation is calculated at 19493 cm^{-1} with considerable C_4H_2→Fc^+ character, consistent with the intense absorption feature near 500 nm in the experimental spectra.

B4 Conclusion

2,5-Diferrocenyl-1-phenyl-1*H*-phosphole (**B-3**) and its chalcogenides **B-4** (P=S) and **B-5** (P=Se) have been successfully prepared by a cyclization reaction of phenylphosphine with 1,4-diferrocenyl butadiyne and subsequent reaction with sulfur and selenium, respectively. NMR spectroscopic studies revealed a tetrahedral environment at phosphorus in **B-3**–**B-5**.

Therefore, the interaction of the phosphorus lone pair with the dienic π system is hindered. Oxidation to P(V) with sulfur or selenium blocks any involvement in the delocalization of the C_4 backbone. Nevertheless, the electronic character at the carbon atoms in 3- and 4-position seems to remain unchanged. Molecules **B-4** and **B-5** have been structurally characterized by single crystal X-ray diffraction showing that they exhibit, as expected, a planar geometry of the heterocyclic core. The ferrocenyl groups are antiparallel oriented and are almost coplanar to the $^{c}C_4P$ setup. Electrochemical measurements revealed that the two ferrocenyl groups in **B-3**–**B-5** undergo two sequential one-electron oxidation processes, with a significant separation of the two waves (280 mV (**B-3**), 240 mV (**B-4**) and 235 mV (**B-5**)) due to a combination of environmental and inherent electronic effects. As observed in spectroelectrochemical investigations, all three compounds **B-3**–**B-5** exhibit IVCT absorptions of weak to moderate strength. Upon oxidation of phosphorus the intensity of the IVCT absorption decreases from ε_{max} = 1750 L·mol^{-1}·cm^{-1} (**B-3**) to ε_{max} = 1300 L·mol^{-1}·cm^{-1} (**B-4**) and ε_{max} = 1100 L·mol^{-1}·cm^{-1} (**B-5**), while the band broadens ($\Delta\nu_{1/2}$ = 3050 cm^{-1} (**B-3**), $\Delta\nu_{1/2}$ = 4200 cm^{-1} (**B-4**, **B-5**)). This indicates that the occupation of the lone pair slightly decreases the interaction among the $^{c}C_4P$ ring. However the electronic characteristics of this series of molecules resemble those of a *cis*-diene structure more than those of an aromatic system and the changes upon oxidation of the phosphorus are therefore small. DFT and TD-DFT calculation in combination with *in situ* IR spectroscopy support the general interpretation of the electrochemical- and *in situ* UV/Vis-NIR data, allocating the main contribution of the electron transfer to the C_4H_2 part of the bridging unit.

B5 Experimental Section

General data

All reactions were carried out under an argon or nitrogen atmosphere using standard Schlenk techniques. Tetrahydrofuran and benzene were purified by distillation from sodium/benzophenone ketyl; dichloromethane was purified by distillation from calcium hydride. For column chromatography silica was used with a particle size of 40–60 µm (230–400 mesh (ASTM), Fa. Macherey-Nagel).

Instruments

FT IR spectra were recorded with a Nicolet IR 200 spectrometer (Fa. Thermo). NMR spectra were recorded with a Bruker Avance III 500 spectrometer (500.3 MHz for ^{1}H,

125.7 MHz for $^{13}C\{^1H\}$ and 202.5 MHz for $^{31}P\{^1H\}$ spectra). Chemical shifts are reported in δ (parts per million) downfield from tetramethylsilane with the solvent as reference signal (^1H NMR: $CHCl_3$, $\delta = 7.26$; $^{13}C\{^1H\}$ NMR: $CDCl_3$, $\delta = 77.16$; CD_2Cl_2, $\delta = 53.8$; $^{31}P\{^1H\}$ NMR: standard external rel. 85% H_3PO_4, $\delta = 0.0$; $P(OMe)_3$, $\delta = 139.0$, respectively). The melting points were determined using a Gallenkamp MFB 595 010 M melting point apparatus. Elemental analyses were measured with a Thermo FlashAE 1112 instrument. High-resolution mass spectra were recorded on a Bruker Daltonik micrOTOF-QII spectrometer.

Electrochemistry

Electrochemical measurements on 1.0 mmol·L^{-1} solutions of compounds **B-3**–**B-5** in dichloromethane were performed in a dried, argon purged cell at 20 °C with a Radiometer Voltalab PGZ 100 electrochemical workstation interfaced with a personal computer. 0.1 mol·L^{-1} $[N^nBu_4][B(C_6F_5)_4]$ or $[N^nBu_4][PF_6]$ were used as supporting electrolyte. For the measurements a three electrode cell containing a Pt auxiliary electrode, a glassy carbon working electrode (surface area 0.031 cm²) and an Ag/Ag^+ (0.01 mmol·L^{-1} $[AgNO_3]$) reference electrode fixed on a Luggin capillary was used. The working electrode was pretreated by polishing on a Buehler microcloth first with 1 micron and then ¼ micron diamond paste. The reference electrode was constructed from a silver wire inserted in a 0.01 mmol·L^{-1} $[AgNO_3]$ and 0.1 mol·L^{-1} $[N^nBu_4][B(C_6F_5)_4]$ or $[N^nBu_4][PF_6]$ acetonitrile solution in a Luggin capillary with a vycor tip. This Luggin capillary was inserted in a second Luggin capillary containing a 0.1 mol·L^{-1} $[N^nBu_4][B(C_6F_5)_4]$ or $[N^nBu_4][PF_6]$ dichloromethane solution and a vycor tip. Experiments under the same conditions showed that all reduction and oxidation potentials were reproducible within 5 mV. Experimental potentials were referenced against an Ag/Ag^+ reference electrode but the presented results are referenced against ferrocene as an internal standard as required by IUPAC.[B46] To achieve this, each experiment was repeated in the presence of 1 mmol·L^{-1} decamethylferrocene (Fc*). Data were processed on a Microsoft Excel worksheet to set the formal reduction potentials of the FcH/FcH^+ couple to 0.0 V. Under our conditions the Fc^*/Fc^{*+} couple was at -619 mV *vs* FcH/FcH^+, ΔE_p = 60 mV, while the FcH/FcH^+ couple itself was at 220 mV *vs* Ag/Ag+, ΔE_p = 61 mV.[B56]

Spectroelectrochemistry

Spectroelectrochemical UV/Vis-NIR measurements of 2.0 mmol·L^{-1} solutions of **B-3**–**B-5** in dry dichloromethane containing 0.1 mol·L^{-1} of $[N^nBu_4][B(C_6F_5)_4]$ as the supporting

electrolyte were performed in an OTTLE (OTTLE = Optically Transparent Thin-Layer Electrochemical)[B48] cell with a Varian Cary 5000 spectrophotometer at 20 °C. Spectroelectrochemical IR measurements of 10 mmol·L^{-1} solutions of **B-3**–**B-5** in dry dichloromethane containing 0.1 mol·L^{-1} [N^{n}Bu$_4$][PF$_6$] as supporting electrolyte were performed in an OTTLE cell with CaF_2 windows. The values obtained by deconvolution could be reproduced within ε_{max}: 100 L·mol^{-1}·cm^{-1}; ν_{max} 50 cm^{-1}; $\Delta\nu_{1/2}$ 50 cm^{-1}.

Single Crystal X-ray Diffraction Analysis

Suitable single crystals of **B-4** and **B-5** for X-ray diffraction analysis were obtained by diffusion of *n*-hexane into a dichloromethane solution containing **B-4** or **B-5** at ambient temperature. Data were collected with an Oxford Gemini S diffractometer at 100 K with graphite monochromated Cu K_α radiation (λ = 1.54184 Å) (**B-4**) or Mo K_α radiation (λ = 0.71073 Å) (**B-5**). The structures were solved by direct methods and refined by full-matrix least-squares procedures on F^2.[B57,B58] All non-hydrogen atoms were refined anisotropically, and a riding model was employed in the treatment of the hydrogen atom positions.

Reagents

All starting materials were obtained from commercial suppliers and used without further purification. Phenylphosphine[B59] and 1,4-diferrocenyl butadiyne[B60] were prepared according to published procedures.

Synthesis of 2,5-Diferrocenyl-1-phenyl-1*H*-phosphole (B-3)

To 0.25 g (2.3 mmol) of **B-1** in 30 mL of a tetrahydrofuran/benzene mixture of ratio 1:1 (v:v) at 0 °C, 0.7 mL (1.8 mmol) of *n*-butyllithium were added drop-wise. The resulting yellow solution was stirred for 10 min at 0 °C and was then added drop-wise to a solution of 0.95 g (2.3 mmol) of 1,4-diferrocenyl butadiyne (**B-2**) in 20 mL of tetrahydrofuran. The deep red solution was stirred overnight at ambient temperature and then all volatiles were removed in vacuum. The remaining solid was purified under argon by column chromatography (column size: 4 × 20 cm) on silica using a mixture of *n*-hexane/dichloromethane 5:1 (v:v) as eluent to give **B-3** as a red solid. Yield 0.61 g (1.2 mmol, 52 % based on **B-1**). Anal. Calcd. for $C_{30}H_{25}Fe_2P$ (528.04 g/mol): C, 68.22; H, 4.77. Found: C, 68.15; H, 4.73. Mp.: 207 °C. IR data (KBr, ν/cm^{-1}): 3086 m, 3037 m, 2954 m, 2920 w, 2847 w, 1714 w, 1635 w, 1562 m, 1477 m, 1433 m, 1408 m. ^{1}H NMR ($CDCl_3$, δ): 3.92 (s, 10 H, C_5H_5), 4.17 (m, 2 H, C_5H_4), 4.18 (m, 2 H, C_5H_4), 4.25 (m, 2 H, C_5H_4), 4.39 (m, 2 H, C_5H_4), 6.87 (d, $^3J_{HP}$ = 11.4 Hz, 2 H, C_4H_2P), 7.38–7.40 (m, 3 H, H^m,H^p/C_6H_5), 7.58–7.62 (m, 2 H, H^o/C_6H_5). ^{13}C{^{1}H} NMR

($CDCl_3$, δ): 65.83 (d, J_{CP} = 3.9 Hz, C_5H_4), 67.18 (d, J_{CP} = 6.8 Hz, C_5H_4), 68.64 (d, J_{CP} = 12.0 Hz, C_5H_4), 69.84 (s, C_5H_5), 82.39 (d, $^2J_{CP}$ = 20.0 Hz, C^i/C_5H_4), 128.92 (d, J_{CP} = 8.7 Hz, C_6H_5), 130.07 (d, $^2J_{CP}$ = 1.7 Hz, CH/C_4H_2P), 130.57 (d, J_{CP} = 9.3 Hz, C_6H_5), 133.05 (d, J_{CP} = 11.7 Hz, C^i/C_6H_5), 134.98 (d, $^4J_{CP}$ = 21.1 Hz, C^o/C_6H_5), 147.96 (d, J_{CP} = 1.5 Hz, C^i/C_4H_2P). $^{31}P\{^1H\}$ NMR ($CDCl_3$, δ): 5.10 (s). HRMS (ESI-TOF) [*m/z*]: calcd for $C_{30}H_{25}Fe_2P$: 528.0388, found: 528.0384 $[M]^+$.

Synthesis of 2,5-Diferrocenyl-1-phenyl-1*H*-phosphole sulfide (B-4)

To 0.10 g (0.19 mmol) of **B-3** in dichloromethane (20 mL) 0.07 g (0.27 mmol) of elemental sulfur was added in a single portion. The deep purple solution was stirred overnight at ambient temperature. All volatiles were removed in vacuum and the remaining solid was purified by column chromatography (column size: 3 × 15 cm) on silica using a mixture of *n*-hexane/dichloromethane of ratio 3:1 (v:v). Compound **B-4** was obtained as a purple solid. Yield 0.097 g (0.17 mmol, 89 % based on **B-3**). Anal. Calcd. for $C_{30}H_{25}Fe_2PS{\cdot}0.5CH_2Cl_2$ (601.99 g/mol): C, 60.78; H, 4.35. Found: C, 60.57; H, 4.33. Mp.: 248 °C. IR data (KBr, ν/cm^{-1}): 3081 w, 3039 w, 2960 m, 2923 m, 2853 w, 1727 w, 1646 w, 1585 m, 1464 m, 1433 m, 1405 m. ^1H NMR ($CDCl_3$, δ): 3.98 (s, 10 H, C_5H_5), 4.27 (m, 2 H, C_5H_4), 4.29 (m, 2 H, C_5H_4), 4.47 (m, 2 H, C_5H_4), 4.62 (m, 2 H, C_5H_4), 5.30 (s, CH_2Cl_2), 6.87 (d, $^3J_{HP}$ = 36.5 Hz, 2 H, C_4H_2P) , 7.48–7.52 (m, 3 H, H^m,H^p/C_6H_5), 8.02 (ddd, $^3J_{HH}$ = 7.9 Hz, $^4J_{HH}$ = 1.6 Hz, $^3J_{HP}$ = 14.0 Hz, 2 H, H^o/C_6H_5). $^{13}C\{^1H\}$ NMR (CD_2Cl_2, δ): 66.45 (d, J_{CP} = 6.3 Hz, C_5H_4), 67.53 (d, J_{CP} = 5.8 Hz, C_5H_4), 69.84 (d, J_{CP} = 12.5 Hz, C_5H_4), 70.58 (s, C_5H_5), 77.65 (d, $^2J_{CP}$ = 22.5 Hz, C^i/C_5H_4), 129.26 (d, J_{CP} = 12.4 Hz, C_6H_5), 129.68 (d, $^1J_{CP}$ = 12.8 Hz, C^i/C_6H_5), 130.61 (d, $^2J_{CP}$ = 24.1 Hz, CH/C_4H_2P), 130.95 (d, $^2J_{CP}$ = 11.6 Hz, C^o/C_6H_5), 132.46 (d, J_{CP} = 3.4 Hz, C_6H_5), 140.49 (d, $^1J_{CP}$ = 81.3 Hz, C^i/C_4H_2P). $^{31}P\{^1H\}$ NMR ($CDCl_3$, δ): 46.61 (s). HRMS (ESI-TOF) [*m/z*]: calcd for $C_{30}H_{25}Fe_2PS$: 560.0109, found: 560.0111 $[M]^+$.

Crystal Data for **B-4**: $C_{30}H_{25}Fe_2PS$, M = 560.23 $g{\cdot}mol^{-1}$, orthorhombic, $P2_12_12_1$, λ = 1.54184 Å, a = 7.5138(6) Å, b = 16.1833(17) Å, c = 19.6680(19) Å, V = 2391.6(4) $Å^3$, Z = 4, ρ_{calcd} = 1.556 mgm^{-3}, μ = 11.300 mm^{-1}, T = 100(2) K, Θ range = 3.54-62.48°, reflections collected: 4528, independent: 3235 (R_{int} = 0.0616), R_1 = 0.0871, wR_2 = 0.2106 [$I > 2\sigma(I)$], absolute structure parameter: 0.001(12).

Synthesis of 2,5-Diferrocenyl-1-phenyl-1*H*-phosphole selenide (B-5)

Using the procedure described above, 0.11 g (0.21 mmol) of **B-3** were reacted with 0.02 g (0.25 mmol) of selenium to give **B-5** as purple solid. Yield 0.109 g (0.18 mmol, 86 % based

on **B-3**). Anal. Calcd. for $C_{30}H_{25}Fe_2PSe$ (607.96 g/mol): C, 59.35; H, 4.15. Found: C, 59.15; H, 4.49. Mp.: 263 °C. IR data (KBr, ν/cm^{-1}): 3074 w, 3048 w, 2958 m, 2923 m, 2853 w, 1738 m, 1653 w, 1582 m, 1461 m, 1433 m, 1407 m. ^{1}H NMR ($CDCl_3$, δ): 3.97 (s, 10 H, C_5H_5), 4.27 (m, 2 H, C_5H_4), 4.29 (m, 2 H, C_5H_4), 4.53 (m, 2 H, C_5H_4), 4.63 (m, 2 H, C_5H_4), 6.90 (d, $^3J_{HP}$ = 35.9 Hz, 2 H, C_4H_2P), 7.47–7.52 (m, 3 H, H^m,H^p/C_6H_5), 8.04 (ddd, $^3J_{HH}$ = 7.8 Hz, $^4J_{HH}$ = 1.7 Hz, $^3J_{HP}$ = 14.3 Hz, 2 H, H^o/C_6H_5). ^{13}C{^{1}H} NMR (CD_2Cl_2, δ): 66.80 (d, J_{CP} = 6.2 Hz, C_5H_4), 67.42 (d, J_{CP} = 6.0 Hz, C_5H_4), 69.81 (d, J_{CP} = 9.3 Hz, C_5H_4), 70.67 (s, C_5H_5), 77.71 (d, $^2J_{CP}$ = 16.3 Hz, C^i/C_5H_4), 129.29 (d, J_{CP} = 12.5 Hz, C_6H_5), 129,51 (d, $^1J_{CP}$ = 12.7 Hz, C^i/C_6H_5), 130.54 (d, $^2J_{CP}$ = 22.5 Hz, CH/C_4H_2P), 131.64 (d, $^2J_{CP}$ = 11.9 Hz, C^o/C_6H_5), 132.59 (d, J_{CP} = 3.1 Hz, C_6H_5), 141.57 (d, $^1J_{CP}$ = 74.4 Hz, C^i/C_4H_2P). ^{31}P{^{1}H} NMR ($CDCl_3$, δ): 33.21 ($^1J_{^{31}P^{77}Se}$ = 745 Hz). HRMS (ESI-TOF) [*m/z*]: calcd for $C_{30}H_{25}Fe_2PSe$: 607.9556, found: 607.9562 $[M]^+$.

Crystal Data for **B-5**: $C_{30}H_{25}Fe_2PSe$, M = 607.13 g·mol^{-1}, orthorhombic, $P2_12_12_1$, λ = 0.71073 Å, a = 7.5250(3) Å, b = 16.0764(13) Å, c = 19.8209(11) Å, V = 2397.8(3) Å^3, Z = 4, ρ_{calcd} = 1.682 mgm^{-3}, μ = 2.813 mm^{-1}, T = 100(2) K, Θ range = 2.90-25.25°, reflections collected: 9898, independent: 4283 (R_{int} = 0.0880), R_1 = 0.0578, wR_2 = 0.0839 [$I > 2\sigma(I)$], absolute structure parameter: -0.017(16).

B6 Acknowledgement

We are grateful to the Fonds der Chemischen Industrie (FCI) and the Deutsche Forschungsgemeinschaft (DFG) for generous financial support. PJL thanks the EPSRC for financial support and the award of a Leadership Fellowship.

B7 Supporting Information Available

Figures giving further (spectro)electrochemical spectra, computational data and CIF files giving crystallographic data for **B-4** and **B-5**. This material is available free of charge via the Internet at http://pubs.acs.org. Crystallographic data of **B-4** and **B-5** are also available from the Cambridge Crystallographic Database as file nos. CCDC 928309 (**B-4**) and 928310 (**B-5**).

B8 Appendix

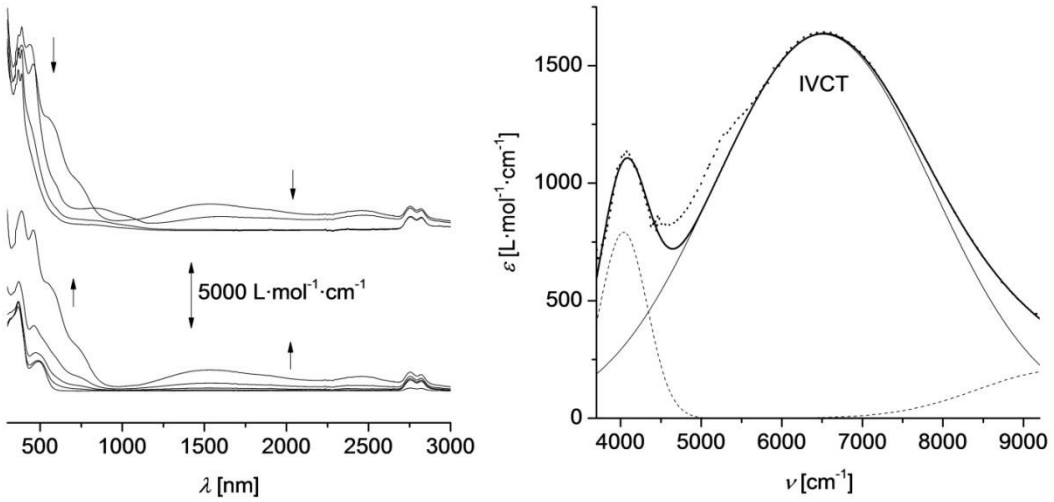

Figure SI4. Left: UV/Vis-NIR spectra of **B-3** at 20 °C in acetonitrile (2.0 mmol·L^{-1}) at rising potentials (bottom: -200 to 490 mV; top: 490 to 800 mV *vs* Ag/AgCl); supporting electrolyte [N^{n}Bu$_4$][B(C$_6$F$_5$)$_4$]. Right: Deconvolution of the NIR absorptions of [**B-3**]$^+$ using three Gaussian shaped bands determined by spectroelectrochemistry in an OTTLE cell.

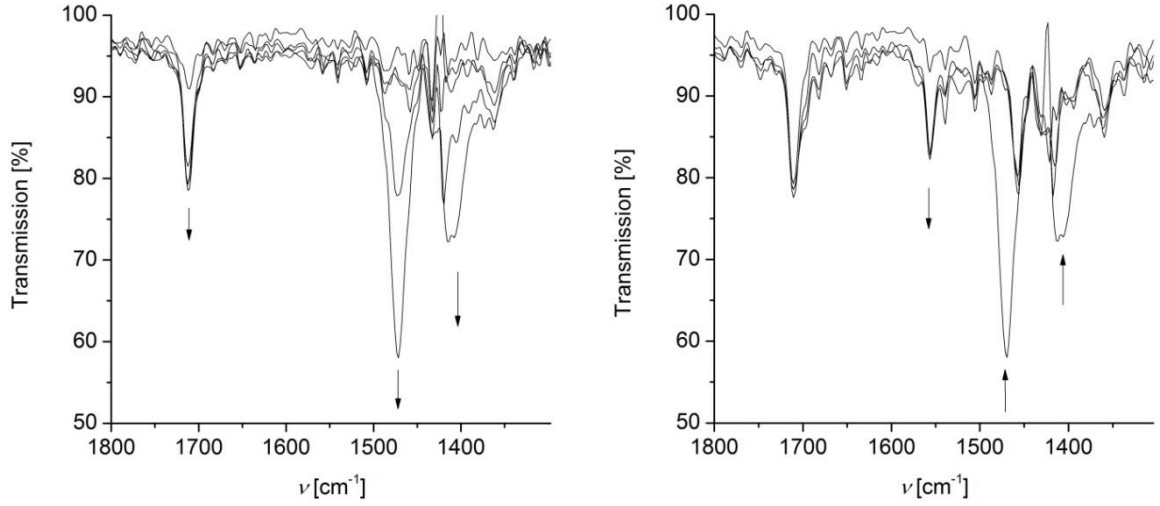

Figure SI7. IR spectra of **B-3** at 20 °C in dichloromethane (10 mmol·L^{-1}) at rising potentials (left: -200 to 520 mV (**B-3** → [**B-3**]$^+$); right: 520 to 1300 mV ([**B-3**]$^+$ → [**B-3**]$^{2+}$) *vs* Ag/AgCl); supporting electrolyte [N^{n}Bu$_4$][PF$_6$].

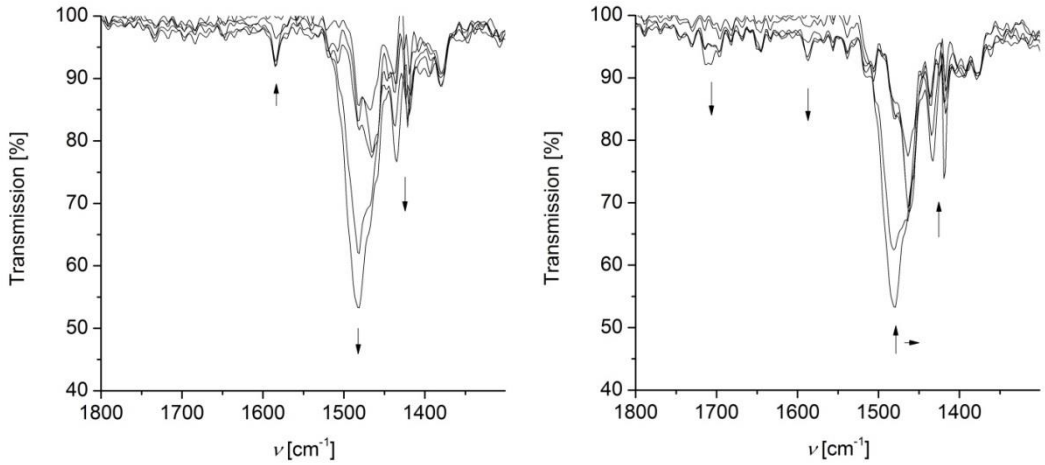

Figure SI8. IR spectra of **B-5** at 20 °C in dichloromethane (10 mmol·L^{-1}) at rising potentials (left: -200 to 500 mV (**B-5** → [**B-5**]$^{+}$); right: 500 to 1300 mV ([**B-5**]$^{+}$ → [**B-5**]$^{2+}$) *vs* Ag/AgCl); supporting electrolyte [$N^{n}Bu_4$][PF_6].

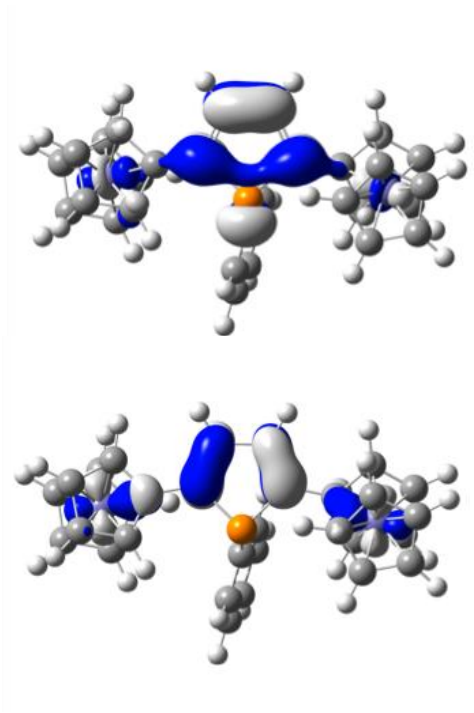

Figure SI9. Plot of the LUMO (top) and HOMO (bottom) of **B-3´** (isosurface ±0.04 (e $bohr^{-3}$)$^{1/2}$.

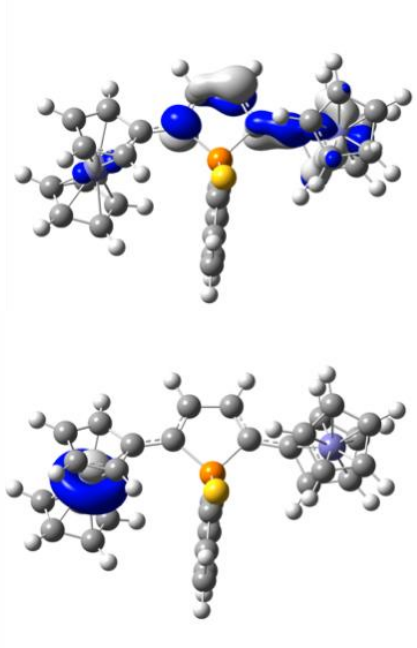

Figure SI10. Plots of the β-LUMO+1 (top) and β-LUMO (bottom) of [**B-4´**]$^{2+}$ (isosurface ±0.04 (e bohr^{-3})$^{1/2}$.

B9 References

[B1] A. Ceccon, S. Santi, L. Orian, A. Bisello, *Coord. Chem. Rev.* **2004**, *248*, 683–724.

[B2] S. Barlow, D. O'Hare, *Chem. Rev.* **1997**, *97*, 637–670.

[B3] P. Aguirre-Etcheverry, D. O'Hare, *Chem. Rev.* **2010**, *110*, 4839–4864.

[B4] M. I. Bruce, *Coord. Chem. Rev.* **1997**, *166*, 91–119.

[B5] P. Mücke, M. Linseis, S. Záliš, R. F. Winter, *Inorg. Chim. Acta* **2011**, *374*, 36–50.

[B6] P. J. Low, *Dalton Trans.* **2005**, 2821–2824.

[B7] P. J. Low, R. L. Roberts, R. L. Cordiner, F. Hartl, *J. Solid State Electrochem.* **2005**, *9*, 717–731.

[B8] P. Mücke, R. F. Winter, I. Novak, K. Kowalski, *J. Organomet. Chem.* **2012**, *717*, 14–22.

[B9] K. Kowalski, R. F. Winter, *J. Organomet. Chem.* **2009**, *694*, 1041–1048.

[B10] M. Lohan, P. Ecorchard, T. Rüffer, F. Justaud, C. Lapinte, H. Lang, *Organometallics* **2009**, *28*, 1878–1890.

[B11] M. Lohan, F. Justaud, H. Lang, C. Lapinte, *Organometallics* **2012**, *31*, 3565–3574.

[B12] A. Jakob, P. Ecorchard, M. Linseis, R. F. Winter, H. Lang, *J. Organomet. Chem.* **2009**, *694*, 655–666.

[B13] D. M. D'Alessandro, A. C. Topley, M. S. Davies, F. R. Keene, *Chem. Eur. J.* **2006**, *12*, 4873–4884.

[B14] F. Paul, C. Lapinte, *Coord. Chem. Rev.* **1998**, *178-180*, 431–509.

[B15] W. Mohr, J. Stahl, F. Hampel, J. A. Gladysz, *Chem. Eur. J.* **2003**, *9*, 3324–3340.

[B16] F. Coat, C. Lapinte, *Organometallics* **1996**, *15*, 477–479.

[B17] K. Kaleta, A. Hildebrandt, F. Strehler, P. Arndt, H. Jiao, A. Spannenberg, H. Lang, U. Rosenthal, *Angew. Chem.* **2011**, *123*, 11444–11448.

[B18] K. Kaleta, F. Strehler, A. Hildebrandt, T. Beweries, P. Arndt, T. Rüffer, A. Spannenberg, H. Lang, U. Rosenthal, *Chem. Eur. J.* **2012**, *18*, 12672–12680.

[B19] U. Pfaff, A. Hildebrandt, D. Schaarschmidt, T. Hahn, S. Liebing, J. Kortus, H. Lang, *Organometallics* **2012**, *31*, 6761–6771.

[B20] J. M. Speck, R. Claus, A. Hildebrandt, T. Rüffer, E. Erasmus, L. van As, J. C. Swarts, H. Lang, *Organometallics* **2012**, *31*, 6373–6380.

[B21] A. Hildebrandt, H. Lang, *Dalton Trans.* **2011**, *40*, 11831–11837.

[B22] A. Hildebrandt, D. Schaarschmidt, R. Claus, H. Lang, *Inorg. Chem.* **2011**, *50*, 10623–10632.

[B23] A. Hildebrandt, U. Pfaff, H. Lang, *Rev. Inorg. Chem.* **2011**, *31*, 111–141.

[B24] A. Hildebrandt, D. Schaarschmidt, H. Lang, *Organometallics* **2011**, *30*, 556–563.

[B25] C. Lapinte, *J. Organomet. Chem.* **2008**, *693*, 793–801.

[B26] Y. Dienes, M. Eggenstein, T. Neumann, U. Englert, T. Baumgartner, *Dalton Trans.* **2006**, 1424–1433.

[B27] Y. Dienes, S. Durben, T. Kárpáti, T. Neumann, U. Englert, L. Nyulászi, T. Baumgartner, *Chem. Eur. J.* **2007**, *13*, 7487–7500.

[B28] D. Carmichael, X. F. Le Goff, E. Muller, *New J. Chem.* **2010**, *34*, 1341–1347.

[B29] T. Möller, M. B. Sárosi, E. Hey-Hawkins, *Chem. Eur. J.* **2012**, *18*, 16604–16607.

[B30] Y. Ren, T. Baumgartner, *Dalton Trans.* **2012**, *41*, 7792–7800.

[B31] H. Chen, W. Delaunay, L. Yu, D. Joly, Z. Wang, J. Li, Z. Wang, C. Lescop, D. Tondelier, B. Geffroy, Z. Duan, M. Hissler, F. Mathey, R. Réau, *Angew. Chem. Int. Ed.* **2012**, *51*, 214–217.

[B32] C. Fave, T. Cho, M. Hissler, C. Chen, T. Luh, C. Wu, R. Réau, *J. Am. Chem. Soc.* **2003**, *125*, 9254–9255.

[B33] H. Su, O. Fadhel, C. Yang, T. Cho, C. Fave, M. Hissler, C. Wu, R. Réau, *J. Am. Chem. Soc.* **2006**, *128*, 983–995.

[B34] G. Märkl, R. Potthast, *Angew. Chem. Int. Ed.* **1967**, *6*, 86.

[B35] D. W. Allen, I. W. Nowell, B. F. Taylor, *J. Chem. Soc. Dalton Trans.* **1985**, 2505–2508.

[B36] D. W. Allen, B. F. Taylor, *J. Chem. Soc. Dalton Trans.* **1982**, 51–54.

[B37] B. Milde, D. Schaarschmidt, T. Rüffer, H. Lang, *Dalton Trans.* **2012**, *41*, 5377–5390.

[B38] A. Jakob, B. Milde, P. Ecorchard, C. Schreiner, H. Lang, *J. Organomet. Chem.* **2008**, *693*, 3821–3830.

[B39] R. P. Pinnell, C. A. Megerle, S. L. Manatt, P. A. Kroon, *J. Am. Chem. Soc.* **1973**, *95*, 977–978.

[B40] D. J. Adams, J. A. Bennett, D. Duncan, E. G. Hope, J. Hopewell, A. M. Stuart, A. J. West, *Polyhedron* **2007**, *26*, 1505–1513.

[B41] M. Clochard, J. Grundy, B. Donnadieu, F. Mathey, *Org. Lett.* **2005**, *7*, 4511–4513.

[B42] O. Fadhel, D. Szieberth, V. Deborde, C. Lescop, L. Nyulászi, M. Hissler, R. Réau, *Chem. Eur. J.* **2009**, *15*, 4914–4924.

[B43] W. E. Geiger, F. Barrière, *Acc. Chem.Res.* **2010**, *43*, 1030–1039.

[B44] F. Barrière, W. E. Geiger, *J. Am. Chem. Soc.* **2006**, *128*, 3980–3989.

[B45] F. Barrière, N. Camire, W. E. Geiger, U. T. Mueller-Westerhoff, R. Sanders, *J. Am. Chem. Soc.* **2002**, *124*, 7262–7263.

[B46] G. Gritzner, J. Kuta, *Pure Appl. Chem.* **1984**, *56*, 461–466.

[B47] H. J. Gericke, N. I. Barnard, E. Erasmus, J. C. Swarts, M. J. Cook, M. A. S. Aquino, *Inorg. Chim. Acta* **2010**, *363*, 2222–2232.

[B48] M. Krejčik, M. Daněk, F. Hartl, *J. Electroanal. Chem.* **1991**, *317*, 179–187.

[B49] N. S. Hush, *Electrochim. Acta* **1968**, *13*, 1005–1023.

[B50] B. S. Brunschwig, C. Creutz, N. Sutin, *Chem. Soc. Rev.* **2002**, *31*, 168–184.

[B51] L. R. Snyder, *J .Chromatogr. Sci.* **1978**, *16*, 223–234.

[B52] D. M. D'Alessandro, F. R. Keene, *Chem. Soc. Rev.* **2006**, *35*, 424–440.

[B53] L. Nyulászi, L. Soós, G. Keglevich, *J. Organomet. Chem.* **1998**, *566*, 29–35.

[B54] L. Nyulászi, *J. Phys.Chem.* **1995**, *99*, 586–591.

[B55] Y. Li, M. Josowicz, L. M. Tolbert, *J. Am. Chem. Soc.* **2010**, *132*, 10374–10382.

[B56] A. Nafady, W. E. Geiger, *Organometallics* **2008**, *27*, 5624–5631.

[B57] G. M. Sheldrick, *Acta Crystallogr., Sect. A* **1990**, *46*, 467–473.

[B58] G. M. Sheldrick, *SHELXL-97, Program for Crystal Structure Refinement* **1997**, University of Göttingen.

[B59] M. Hurtado, M. Yánez, R. Herrero, A. Guerrero, J. Z. Dávalos, J.-L. M. Abboud, B. Khater, J.-C. Guillemin, *Chem. Eur. J.* **2009**, *15*, 4622–4629.

[B60] Z. Yuan, G. Stringer, I. R. Jobe, D. Kreller, K. Scott, L. Koch, N. J. Taylor, T. B. Marder, *J. Organomet. Chem.* **1993**, *452*, 115–120.

C Transition Metal Carbonyl Complexes of 2,5-Diferrocenyl-1-phenyl-1*H*-phosphole

Dominique Miesel, Alexander Hildebrandt, Marcus Korb, Dieter Schaarschmidt and Heinrich Lang*

Veröffentlicht in *Organometallics* **2015**, *34*, 4293–4304.

Die Ergebnisse aus Kapitel B geben Anlass, den Einfluss des dienischen Systems und des Phosphoratoms genauer zu untersuchen. Dazu wurden Metall-Carbonyl-Komplexe hergestellt um den Einfluss der Veränderung der Elektronendichte des Phosphoratoms unter Beibehalten der Oxidationsstufe bzw. Veränderungen am dienischen System auf die Metall-Metall-Interaktion zu bestimmen.

Die in Kapitel C präsentierten Ergebnisse wurden selbstständig unter Anleitung von Prof. Dr. Heinrich Lang und Dr. Alexander Hildebrandt erstellt. Die kristallografischen Messungen erfolgten von Marcus Korb und Dr. Dieter Schaarschmidt.

C1 Introduction

Within the series of five-membered heterocycles, especially the phosphorus-containing heterocycles take an exceptional role because they are non- or only slightly aromatic.[C1–C6] The pyramidal phosphorus environment and the high inversion barrier of phospholes lead to a hindered interaction of the phosphorus lone pair with the dienic system.[C7] This results in a versatile reaction behavior, *e*. *g*. phospholes undergo Diels-Alder reactions of the dienic system, oxidation ($P^{III} \rightarrow P^{V}$) or complexation reactions of the phosphorus atom and/or the dienic system.[C1,C8–C12] Due to the low delocalization within the phosphole ring, they typically behave as a classical diene or phosphine.[C1] In complexation reactions the metal atoms can be coordinated by either the phosphorus atom (= two electron donor), the dienic system (= four electron donor), or by both coordination sites (= six electron donor) resulting in the formation of multimetallic compounds.[C1,C8,C13–C16]

In the development of new materials with promising photophysical properties, phosphorus-based molecules offer the opportunity to modify their features due to their versatile reaction behavior toward numerous transition metals.[C17–C20] For example, incorporation of phospholes into conjugated materials allows to fine-tune their photophysical properties due to modifications on the phosphorus atom.[C18,C21,C22]

Complexation of phospholes with metal carbonyls results in structural motifs with one or more transition metal atoms coordinated by the phosphole unit.[C23–C25] Thereby, reactions of phospholes with chromium, molybdenum, tungsten and iron carbonyls are best studied, whereby the metal fragment is coordinated by the phosphorus atom and/or the dienic system.[C1,C15,C23,C26–C28]

Recently, we investigated the electronic interactions in ferrocenyl functionalized 5- and 6-membered heterocycles and in benzene derivatives.[C29–C44] It could be shown that the metal-metal interaction in mixed-valent 2,5-diferrocenyl-1-phenyl-1*H*-phosphole can be placed between those of 2,5-diferrocenyl furan and 2,5-diferrocenyl-1-methyl-1*H*-pyrrole.[C31] Phospholes offer the opportunity to further influence the metal-metal interaction due to their versatile reaction behavior on the phosphorus atom and the dienic system. It could be shown, that the oxidation of P^{III} to P^{V} resulted in a small decrease of the strength of the electronic interaction *via* the phosphole unit.[C33]

Earlier theoretical studies on 2,5-diferrocenyl-1-phenyl-1*H*-phosphole revealed that the electronic interaction of the ferrocenyl termini is mostly supported by the dienic system.[C33] Therefore, we herein report about the coordination of the phosphorus atom and/or the dienic system to transition metal carbonyl units to study the influence on the electronic interaction of the redox-active end-groups.

C2 Results and Discussion

Synthesis and characterization

Pentacarbonyl-(2,5-diferrocenyl-1-phenyl-1*H*-phosphole) metal complexes **C-3a**–**c** (**C-3a**, M = Cr; **C-3b**, M = Mo; **C-3c**, M = W) were synthesized by reacting 2,5-diferrocenyl-1-phenyl-1*H*-phosphole (**C-1**)[C33] with $M(CO)_5(thf)$[C45–C47] (**C-2**) (thf = tetrahydrofuran) (Scheme C1) of which the latter compound was accessible by irradiation of $M(CO)_6$ in tetrahydrofuran for 4 h.[C48,C49] Further treatment of **C-3a**–**c** with one equiv. of **C-1** under irradiation resulted in the formation of *cis*-tetracarbonyl-bis(2,5-diferrocenyl-1-phenyl-1*H*-

phosphole) metal complexes *cis*-**C-4a–c** (**C-4a**, M = Cr; **C-4b**, M = Mo; **C-4c**, M = W) (Scheme C1).

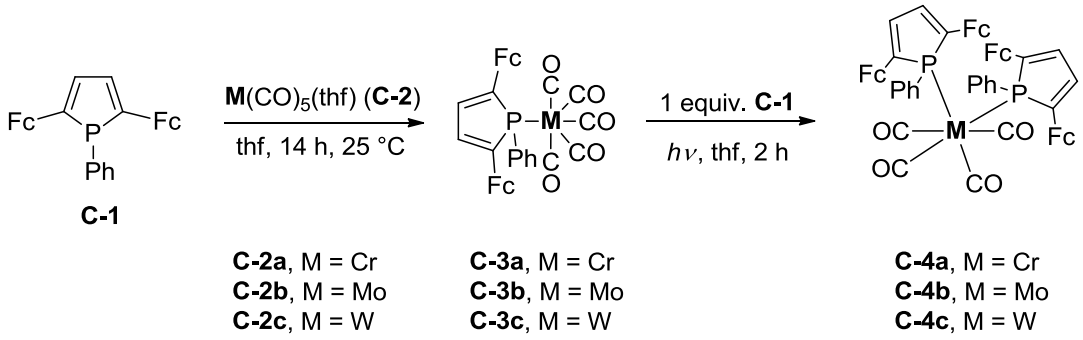

Scheme C1. Synthesis of metal carbonyl compounds **C-3a–c** and **C-4a–c** (Fc = Fe(η^5-C_5H_5)(η^5-C_5H_4).

The reaction of **C-1** with a two to three fold excess of $Fe_2(CO)_9$ (**C-5**) afforded the tetracarbonyliron complex **C-6** and the heptacarbonyldiiron complex **C-7**, which could be separated by column chromatography (Experimental Section). For electrochemical and spectroelectrochemical measurements (*vide infra*), 2,5-diferrocenyl-1-phenyl-1*H*-phosphole sulfide (**C-8**)[C33] was reacted with $Fe_2(CO)_9$ in toluene to give tricarbonyl-[(2,3,4,5,-η)-(2,5-diferrocenyl-1-phenyl-1*H*-phosphole 1-sulfide) iron (**C-9**) in which the dienic system is η^4-coordinated to a $Fe(CO)_3$ building block (Scheme C2).

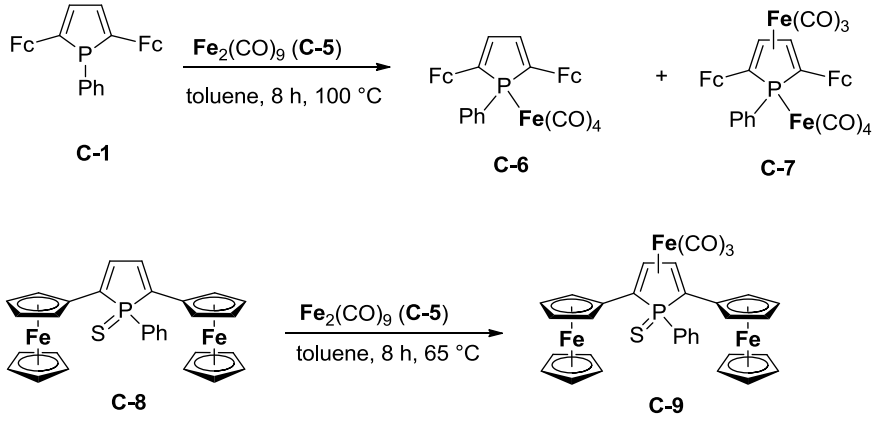

Scheme C2. Synthesis of iron carbonyl complexes **C-6**, **C-7** and **C-9**.

Compounds **C-3a–c**, **C-4a–c**, **C-6**, **C-7** and **C-9** were characterized by elemental analysis, IR and NMR (^{1}H, ^{13}C{^{1}H}, ^{31}P{^{1}H}) spectroscopy and ESI-TOF mass spectrometry. The electrochemical and spectroelectrochemical behavior was investigated by cyclic voltammetry (CV) and square wave voltammetry (SWV) as well as *in situ* UV/Vis-NIR and IR spectroelectrochemistry. The structures of **C-3b**,**c**, **C-4c**, **C-7** and **C-9** are reported.

In the ^{1}H NMR spectra of **C-3a**–**c**, **C-4a**–**c**, **C-6**, **C-7** and **C-9** one singlet for the C_5H_5 protons and four multiplets for the C_5H_4 protons are found (Experimental Section). In **C-3a**–**c** the signal for the $^{c}C_4H_2P$ protons appear as doublet at ca. 6.97 ppm with characteristic $^{3}J_{PH}$ coupling constants of 24 Hz. In **C-4a**–**c** the respective resonance signal is shifted to higher field. After complexation of the phosphorus atom to a $M(CO)_5$ unit an increase of the $^{3}J_{PH}$ coupling constant was observed when compared with **C-1**.[C33] Additional complexation of the dienic system to $Fe(CO)_3$ (**C-7**, **C-9**), leads to a shift of the $^{c}C_4H_2P$ protons to higher field and to a decrease of the $^{3}J_{PH}$ coupling constants, which is attributed to a decrease of the π-electron density and hence, a decreased ring current.

The $^{13}C\{^{1}H\}$ NMR spectra of **C-3a**–**c** show one singlet for the C_5H_5 carbons and five signals for the C_5H_4 units of which the *ipso*-carbon atom appears as doublet with $^{2}J_{CP}$ = 20 Hz. Compared with phosphole **C-1** no significant changes were found. Complexation of the phosphorus atom to $M(CO)_5$ (**C-3a**–**c**) resulted in a significant increase of $^{2}J_{CP}$ of the CH/$^{c}C_4H_2P$ moiety and $^{1}J_{CP}$ of $C^{i}/^{c}C_4H_2P$. The carbonyl carbons appear as two doublets for the *cis*- and *trans*-COs between 196–216 ppm (Experimental Section). A decrease of the size of the metal atom and therefore a better orbital overlap as well as a better M-C back-bonding resulted in a shift of the CO carbons to higher field.[C50] In the chromium complex **C-3a** the J_{CP} coupling constant for the *cis*-CO is larger than for the *trans*-COs. However, for **C-3b**,**c** the $^{2}J_{CP}$ coupling constants for the *trans*-COs have larger values. This behavior is also found for other pentacarbonyl metal compounds.[C28,C51] In the $^{13}C\{^{1}H\}$ NMR spectra of **C-4a**–**c** the signals of the phenyl groups and the dienic CH carbon atom appear as pseudotriplets as previously described by Metzinger and Harris for symmetric compounds containing two phosphine units.[C52,C53] In the tetracarbonyl iron complex **C-6** a similar signal pattern of the ferrocenyl carbon atoms as compared to **C-3a**–**c** is found (Experimental Section). A further complexation of the dienic system to $Fe(CO)_3$ as in **C-7** resulted in a strong shift of the $^{c}C_4H_2P$ carbons to higher field (72–87 ppm) and the $^{2}J_{CP}$ decreases from 16.0 Hz to 3.9 Hz. This significant shift correlates with an adjustment of the bond lengths of the C1–C2, C2–C3 and C3–C4 bonds (X-ray diffraction analysis).

The $^{31}P\{^{1}H\}$ NMR spectra of all compounds are characterized by one singlet, whereby complexation of the phosphorus atom to $M(CO)_n$ (n = 5, M = Cr, Mo, W; n = 4, M = Fe) induces a shift to lower field, when compared with **C-1**. With an increase of the metal size and an increased shielding of the phosphorus atom, the ^{31}P signal is shifted to higher field following the trend described in literature C27. Additional complexation of the dienic system

to a $Fe(CO)_3$ moiety resulted in a shift to higher field. For tungsten complexes **C-3a** and **C-4a**, the characteristic tungsten satellites with $^1J_{31P\text{-}183W}$ coupling constants of 224 Hz (**C-3a**) and 220 Hz (**C-4a**), respectively, were observed.

The IR spectra of all compounds exhibit the characteristic carbonyl stretching vibrations between 2071–1872 cm^{-1} (Experimental Section). For the pentacarbonyl metal complexes **C-3a–c** four CO vibrations with similar frequencies throughout the series at approximately 2070 cm^{-1}, 1990 cm^{-1}, 1940 cm^{-1} and 1920 cm^{-1} were found, which is in accordance for such fragments.[C24,C28,C54,C55] For the tetracarbonyl metal complexes **C-4a–c** four carbonyl vibrations at lower energies at approximately 2010 cm^{-1}, 1910 cm^{-1}, 1900 cm^{-1} and 1880 cm^{-1} were observed, indicating a *cis*-configuration of the two phosphole moieties.

Due to the weaker π-acceptor ability of the phosphole motif, the electron density of the metal atom is increased and the M–C_{CO} back bonding to the carbonyl ligands is stronger. Therefore, the C–O bonds are weaker and the carbonyl stretching frequencies were observed at lower energies. For the iron carbonyl complex **C-6** also four carbonyl vibrations at 2046 cm^{-1}, 1967 cm^{-1}, 1941 cm^{-1} and 1931 cm^{-1} as characteristic for the $Fe(CO)_4$ fragment could be assigned.[C14,C56] Coordination of the dienic unit to a $Fe(CO)_3$ building block in **C-7** led to the appearance of three additional vibrations in all at 2062 cm^{-1}, 2047 cm^{-1}, 1998 cm^{-1}, 1983 cm^{-1}, 1975 cm^{-1}, 1960 cm^{-1} and 1937 cm^{-1}. A similar ν_{CO} motif was observed for **C-9** (2041 cm^{-1}, 1995 cm^{-1}, 1963 cm^{-1}).

The molecular structures of **C-3b**,**c**, **C-4c**, **C-7** and **C-9** in the solid state have been determined by single-crystal X-ray diffraction analysis. The ORTEP diagrams with selected bond lengths (Å), bond angles (°) and torsion angles (°) are shown in the captions of Figures C1 (**C-3b,c**), C2 (**C-4c**), C3 (**C-7**, **C-9**) and in Table SI1 (Supporting Information).
The title compounds crystallize in the triclinic space group $P\bar{1}$ (**C-3b**), in the monoclinic space group *Pc* (**C-3c**) and $P2_1/c$ (**C-7**) and in the orthorhombic space group *Pbcn* (**C-4c**) and $Pca2_1$ (**C-9**) with one (**C-3b**, **C-4c**, **C-7** and **C-9**) or two (**C-3c**) crystallographically independent molecules in the asymmetric unit. In addition, inter- and intramolecular π-π interactions in all crystallized compounds between the C_6H_5, C_5H_5 and C_4H_2P ring are characteristic (Figures SI1 (**C-3b**), SI2 (**C-3c**), SI3 (**C-4c**), SI4 (**C-7**), SI5 (**C-9**) and SI6 (**C-9**).

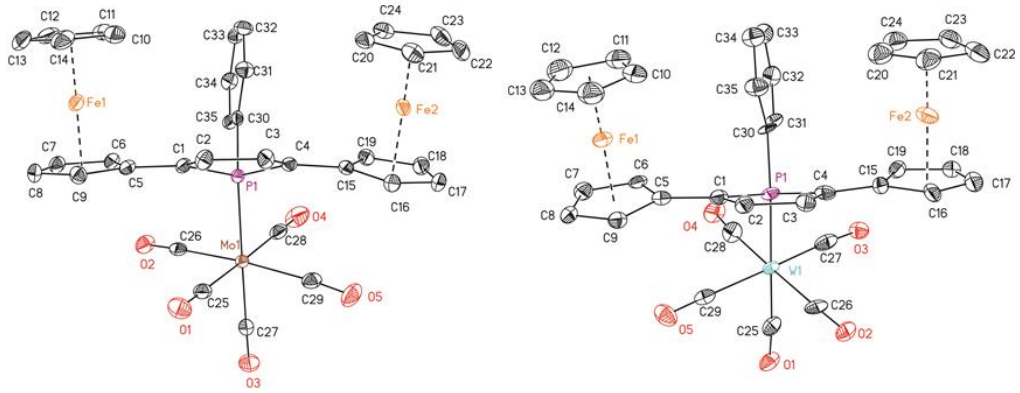

Figure C1. ORTEP diagrams (50 % (**C-3b**) and 30 % (**C-3c**) probability level) of the molecular structures of **C-3b** (left) and **C-3c** (right) with the atom-numbering scheme. All hydrogen atoms, and the other molecule of the asymmetric unit of **C-3c** have been omitted for clarity. Selected bond distances (Å), angles (°), and torsion angles (°):**C-3b**, P1–C1 = 1.821(2), C1–C2 = 1.355(3), C2–C3 = 1.457(3), C3–C4 = 1.345(3), C4–P1 = 1.818(2), P1–C30 = 1.832(2), P1–Mo1 = 2.5041(6), Mo1–C25 = 2.056(2), Mo1–C27 = 2.012(2), C25–O1 = 1.139(3), C1−P1−C4 = 91.74(10), P1–Mo1–C25 = 85.29(6), P1–Mo1–C27 = 177.80(7), Mo1–P1–C30 = 122.10(7), Mo1–P1–C1 = 116.02(7), O1–C25–Mo1 = 177.9(2), C1−P1−C30 = 103.82(9), C30−P1−C4 = 104.46(9). **C-3c**, P1–C1 = 1.82(2), C1–C2 = 1.36(3), C2–C3 = 1.45(3), C3–C4 = 1.31(3), C4–P1 = 1.84(2), P1–C30 = 1.832(19), P1–W1 = 2.524(6), W1–C25 = 2.00(3), C25–O1 = 1.18(3), C1−P1−C4 = 91.2(10), P1–W1–C25 = 174.5(8), P1–W1–C26 = 86.8(6), W1–C25–O1 = 173(2), W1–P1–C30 = 120.5(7), W1–P1–C1 = 113.9(7), W1–P1–C4 = 115.3(7), C1−P1−C30 = 106.0(9), C30−P1−C4 = 105.8(10), C2−C3−C4−P1 = -7(2), P1−C1−C2−C3 = 5(2).

The molybdenum and tungsten complexes **C-3b** and **C-3c** (Figure C1) show somewhat distorted octahedral geometries. The C–C and P–C bond lengths are similar for both complexes (Figure C1). The Mo–C_{CO} bonds for *cis*-CO in **C-3b** range between 2.042(2)–2.059(2) Å, while the shortest one for *trans*-CO (2.012(2) Å) is observed, which is in accordance with the stronger M–C_{CO} back-bonding for the *trans*-CO.[C57,C58] The C–O bond lengths range between 1.135(3)–1.140(3) Å with no significant differences for *cis*- or *trans*-CO. The bond angles around the metal atom M (*trans*-C–M–C: 174.12(8)–177.80(7) ° and *cis*-C–M–C: 85.72(9)–93.13(9) °) show only small deviations from an ideal octahedral geometry. The M–C–O unit is with 175.0(2)–179.1(2) ° almost linear and resemble those found in literature for $M(CO)_5$-phosphole complexes.[C17] The tetracarbonyl tungsten complex **C-4c** (Figure C2) shows a distorted octahedral environment around the tungsten atom with *cis* oriented phosphole units. As already discussed for **C-3b**,**c**, the W–C_{CO} bond for *trans*-CO (1.990(3) Å) is shorter than for the *cis*-COs (2.040(3) Å), indicating that the phosphole is a weaker π-acceptor ligand than the carbonyl groups. In the diiron heptacarbonyl complex **C-7** one $Fe(CO)_4$ fragment is coordinated by the phosphorus atom and one $Fe(CO)_3$ unit by the dienic system of the $^{c}C_4H_2P$ motif. This coordination leads to a distortion of the phosphole

ring with the phosphorus atom 33.066(4) ° out of the C_4 plane (α). The same effect is observed for **C-9** with α = 29.758(3) °. In all other phospholes α is smaller than 10 ° (**C-3b**, 6.808(14) °; **C-3c**, 8.41(2) °; **C-4c**, 4.875(3) °).

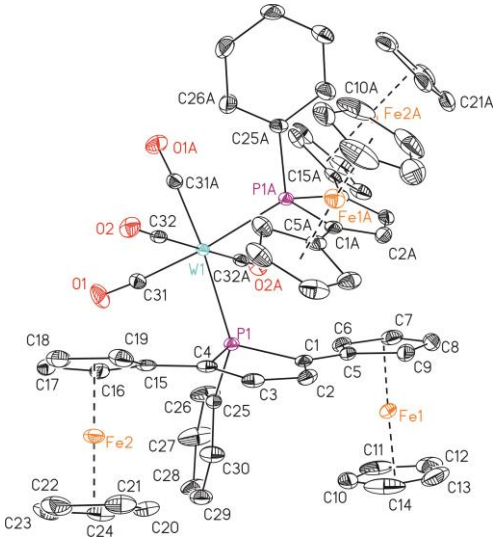

Figure C2. ORTEP diagram (50 % probability level) of the molecular structure of **C-4c** with the atom-numbering scheme. All hydrogen atoms and two molecules of dichloromethane have been omitted for clarity. Selected bond distances (Å), angles (°), and torsion angles (°): P1–C1 = 1.832(3), C1–C2 = 1.344(5), C2–C3 = 1.450(5), C3–C4 = 1.342(5), C4–P1 = 1.824(3), P1–C25 = 1.836(3), P1–W1 = 2.5356(8), W1–C31 = 1.990(3), W1–C32 = 2.040(3), C31–O1 = 1.152(4), C32–O2 = 1.144(4), C1−P1−C4 = 91.46(15), C31–W1–C31A = 84.74(19), C32A–W1–C32 = 177.44(18), C31–W1–P1A = 174.39(9), C31–W1–P1 = 89.66(9), C32A–W1–P1 = 91.68(9), C32–W1–P1 = 90.04(9), P1A–W1–P1 = 95.95(4), W1–C31–O1 = 176.0(3), W1–C32–O2 = 175.8(3), W1–P1–C25 = 119.17(11), W1–P1–C1 = 122.11(10), W1–P1–C4 = 115.06(10), C1−P1−C25 = 101.07(14), C25−P1−C4 = 103.21(14), C2−C3−C4−P1 = -4.1(3), P1−C1−C2−C3 = 3.1(3). (Symmetry generated atoms are indicated by the suffix A; symmetry code: -x+3,y,-z-1/2.)

A similar deflection is observed for related compounds, *e. g.* the coordination of 1-phenyl-3,4-dimethylphosphole to $Fe(CO)_3$ (30 °).[C16] Furthermore, in $Fe(CO)_3$ complexes **C-7** and **C-9** the complexation of the dienic system to the transition metal fragment led to a shortening of the C-C single bonds and an elongation of the C=C double bonds (C1–C2: **C-7**, 1.426(4) Å; **C-9**, 1.432(7) Å, C2–C3: **C-7**, 1.407(4) Å; **C-9**, 1.408(7) Å, C3–C4: **C-7**, 1.445(4) Å; **C-9**, 1.414(8) Å).

The iron atom of the $Fe(CO)_4$ fragment in **C-7** (Figure C3) possesses a distorted trigonal-bipyramidal geometry with two carbonyl ligands in the axial positions (C34–Fe4–C36 = 176.96(14) °), whereas the phosphole unit is in the equatorial one located (*e. g.* C37–Fe4–P1 = 121.32(10)). The iron atom Fe3 in **C-7** and **C-9** shows a distorted tetrahedral geometry.

In contrast to **C-8**[C33], in **C-3b**,**c**, **C-4c** and **C-9** the ferrocenyls are parallel oriented and almost coplanar to the heterocyclic core (torsion of the C_5H_4 plane to the phosphole core: 7(4) ° (**C-3c**) to 24.4(5) ° (**C-4c**)). In contrast, in **C-7** one ferrocenyl moiety is almost coplanar (torsion angle of the C_5H_4 plane to the phosphole plane: 24.1(4) °), while the other one is twisted (80.9(4) °).

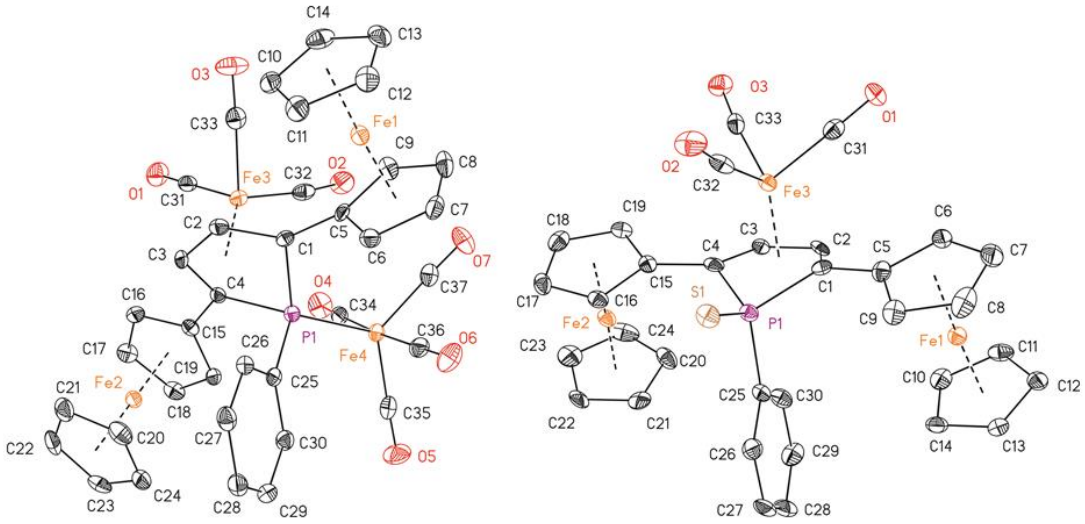

Figure C3. ORTEP diagrams (50 % probability level) of the molecular structures of **C-7** (left) and **C-9** (right) with the atom-numbering scheme. All hydrogen atoms have been omitted for clarity. Selected bond distances (Å), angles (°), and torsion angles (°):**C-7**, P1–C1 = 1.827(3), C1–C2 = 1.426(4), C2–C3 = 1.407(4), C3–C4 = 1.445(4), C4–P1 = 1.827(3), P1–C25 = 1.862(3), P1–Fe4 = 2.2360(8), C31–O1 = 1.141(3), C34–O4 = 1.136(3), Fe4–C34 = 1.800(4), Fe3–C31 = 1.796(3), C1−P1−C4 = 85.90(13), C4−P1−C25 = 104.12(12), C1–P1–C25 = 104.87(12), C4–P1–Fe4 = 126.17(9), C1–P1–Fe4 = 118.81(9), C25–P1–Fe4 = 112.69(9), Fe3–C31–O1 = 179.0(3), Fe4–C34–O4 = 176.6(3), C31–Fe3–C32 = 95.46(13), C34–Fe4–C35 = 91.11(13), C37–Fe4–C35 = 121.47(13), C34–Fe4–C36 = 176.96(14), C37–Fe4–P1 = 121.32(10). **C-9**, P1–C1 = 1.808(5), C1–C2 = 1.432(7), C2–C3 = 1.408(7), C3–C4 = 1.414(8), C4–P1 = 1.810(6), C1–C5 = 1.453(7), C4–C15 = 1.473(7), P1–C25 = 1.828(6), P1–S1 = 1.955(2), C31–O1 = 1.132(6), Fe3–C31 = 1.800(6), C1−P1−C4 = 87.4(2), C1−P1−C25 = 108.5(2), C4−P1−C25 = 110.4(2), C1–P1–S1 = 118.8(2), C4–P1–S1 = 119.3(2), C25–P1–S1 = 110.3(2), Fe3–C31–O1 = 178.7(5), C31–Fe3–C32 = 96.4(3).

Electrochemistry and Spectroelectrochemistry

The redox properties of the metal carbonyl complexes **C-3a–c**, **C-4a–c**, **C-6**, **C-7** and **C-9** were investigated by cyclic voltammetry (= CV), square wave voltammetry (= SWV) and spectroelectrochemistry (*in situ* UV/Vis-NIR and IR spectroscopy). As supporting electrolyte an anhydrous dichloromethane solution containing 0.1 mol·L^{-1} of $[N^nBu_4][B(C_6F_5)_4]$ was used.[C59] The voltammetry measurements were performed at 25 °C and a scan rate of 100 mV·s^{-1}. All potentials are referenced to the FcH/FcH^+ redox couple.[C60] The CV data are summarized in Table C1.

The ferrocenyl groups of phospholes **C-3a**–**c** (Figure C4) and **C-4a**–**c** (Figure C5) can be oxidized separately showing two (**C-3a**–**c**) or four (**C-4a**–**c**) reversible redox processes. The coordination of the phosphorus atom to $M(CO)_5$ in **C-3a**–**c** leads to a somewhat decreased redox separation, when compared to **C-1**. The respective metal atoms Cr, Mo and W show an irreversible redox event at 1240 mV (**C-3a**), 1335 mV (**C-3b**) and 1400 mV (**C-3c**) (Table C1). Nevertheless, the redox potential for the oxidation process of M is in the range of other metal carbonyl complexes, for example, 1-phenyldibenzophosphole metal pentacarbonyls.[C61] Compounds **C-3b** and **C-3c** show irreversible redox events between -600 mV and 1500 mV *vs* FcH/FcH^+, indicating a decomposition of the complex upon oxidation of the phosphorus-bonded metal center (Figure SI7).

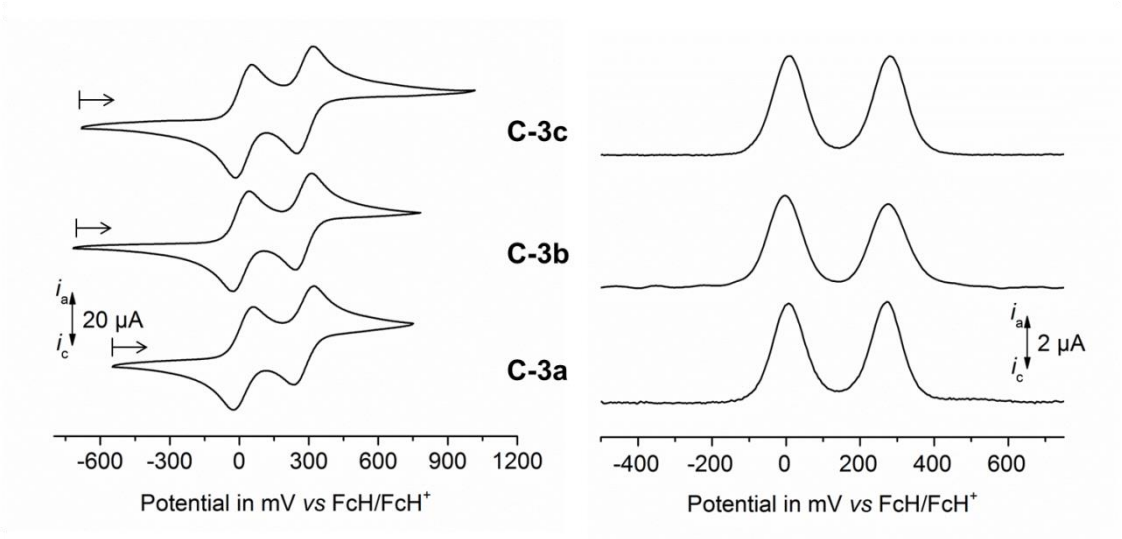

Figure C4. Left: Cyclic voltammograms (potential area: -600–1200 mV) of **C-3a**–**c**; scan rate: 100 $mV \cdot s^{-1}$. Right: Square wave voltammograms (-400–700 mV) of **C-3a**–**c** in dichloromethane solutions (1.0 $mmol \cdot L^{-1}$) at 25 °C, supporting electrolyte 0.1 $mol \cdot L^{-1}$ $[N^nBu_4][B(C_6F_5)_4]$, working electrode: glassy carbon electrode.

In disubstituted phosphole complexes **C-4a**–**c**, the redox potential of the first redox event is shifted to a lower potential, which indicates a higher electron density of the ferrocenyl units if compared to **C-3a**–**c** (Figure C5, Table C1). As observed for **C-3b**,**c**, irreversible redox events were found for **C-4a**–**c** between -600 mV and 1600 mV *vs* FcH/FcH^+ (Figure SI8).

Table C1. Cyclic voltammetry data of C-3a–c, C-4a–c and C-9.[a]

Compd.	$E_1^{\circ\prime}$ in mV[b] (ΔE_p in mV)[c]	$E_2^{\circ\prime}$ in mV[b] (ΔE_p in mV)[c]	$E_3^{\circ\prime}$ in mV[b] (ΔE_p in mV)[c]	$E_4^{\circ\prime}$ in mV[b] (ΔE_p in mV)[c]	E_{pa} in mV[d]	$\Delta E^{\circ\prime}$ in mV[e]
C-3a	15 (86)	280 (85)	-	-	1240	265
C-3b	10 (78)	280 (61)	-	-	1335	270
C-3c	20 (70)	285 (67)	-	-	1400	265
C-4a	-95 (65)	10 (86)	260 (82)	410 (64)	1220	105/250/150
C-4b	-115 (68)	15 (74)	270 (67)	415 (65)	1325	130/255/145
C-4c	-100 (67)	20 (81)	270 (77)	420 (66)	1365	120/250/150
C-9	5 (82)	195 (82)	-	-	-	190

[a]Potentials *vs* FcH/FcH^+, scan rate 100 $mV \cdot s^{-1}$ at a glassy carbon electrode of **C-3a–c**, **C-4a–c** and **C-9** (1.0 $mmol \cdot L^{-1}$ using 0.1 $mol \cdot L^{-1}$ $[N^nBu_4][B(C_6F_5)_4]$ as supporting electrolyte) in anhydrous dichloromethane at 25 °C. [b]$E^{\circ\prime}$ = Formal potential. [c]ΔE_p = Difference between the oxidation and the reduction potential. [d]E_{pa} = Anodic peak potential. [e]$\Delta E^{\circ\prime}$ = Potential difference between the two ferrocenyl-related redox processes.

Due to substitution of the strong σ-donating and π-accepting carbonyl ligand with the strong σ-donating but weak π-accepting phosphole ligand, the electron density at the metal atoms increases, which also increases the electron density of the ferrocenyl units. While changing the metal from Cr over Mo to W no significant changes occur concerning the redox potential and the redox separation of the ferrocenyls, indicating a similar electronic interaction of the Fc/Fc^+ termini in these three complexes. However, the potential for the oxidation of the metal atom M (Figure SI8) increases from Cr (1220 mV) to Mo (1325 mV) to W (1365 mV) (Figure SI8).

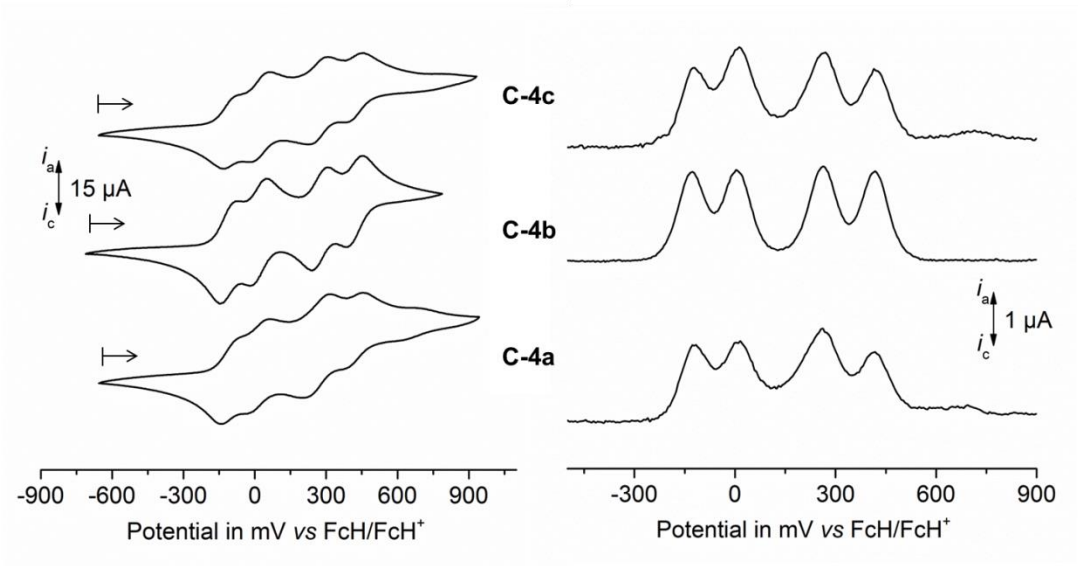

Figure C5. Left: Cyclic voltammograms (potential area: -600–900 mV) of **C-4a–c**; scan rate: 100 $mV \cdot s^{-1}$. Right: Square wave voltammograms (-500–900 mV) of **C-4a–c** in dichloromethane solutions (1.0 $mmol \cdot L^{-1}$) at 25 °C, supporting electrolyte 0.1 $mol \cdot L^{-1}$ $[N^nBu_4][B(C_6F_5)_4]$, working electrode: glassy carbon electrode.

In **C-4a**–**c** two phosphole units with four chemically equal ferrocenyl units are present. The first oxidation affords mono-cationic [**C-4a**]$^+$–[**C-4c**]$^+$. Due to the lower electrostatic repulsion ($\Delta E^{\circ\prime}_1 \approx 120$ mV) the second oxidation occurs at the ferrocenyl of the second phosphole unit. The close distance of the Fc/Fc$^+$ units resulted in a higher value for $\Delta E^{\circ\prime}_2$ between the second and third oxidation ($\Delta E^{\circ\prime}_2 \approx 250$ mV), which is comparable with the redox separations in **C-3a**–**c**. The third oxidation represents a smaller electrostatic repulsion ($\Delta E^{\circ\prime}_3 \approx 150$ mV) as it takes place at the Fc/Fc$^+$ units of different phosphole groups connected *via* the M(CO)$_4$ bridge.

The cyclic voltammograms of **C-6** and **C-7** in which the phosphorus atom is coordinated to a Fe(CO)$_4$ building block show several irreversible redox events between $E_{pa,1}$ = 110–115 mV and $E_{pa,2}$ = 305 mV (Table C2, Figure SI9), indicating that iron oxidation lead to a decomposition of the compounds during electrochemical measurements. Therefore, **C-6** and **C-7** are unsuited for further spectroelectrochemical investigations.

Table C2. Cyclic voltammetry data of complexes C-6 and C-7.[a]

Compd.	$E_{pa,1}$ in mV[b]	$E_{pa,2}$ in mV[b]
C-6	115	305
C-7	110	305

[a]Potentials *vs* FcH/FcH$^+$, scan rate 100 mV·s^{-1} at glassy carbon electrode of **C-6** and **C-7** (1.0 mmol·L^{-1} using 0.1 mol·L^{-1} [N^{n}Bu$_4$][B(C$_6$F$_5$)$_4$] as supporting electrolyte) in anhydrous dichloromethane at 25 °C. [b]E_{pa} = anodic peak potential.

The coordination of the FcC=C-C=CFc dienic system to Fe(CO)$_3$ as present in **C-9** led to a significant decrease of the $\Delta E^{\circ\prime}$ value (Figure SI10) (**C-8**, $\Delta E^{\circ\prime}$ = 240 mV; **C-9**, $\Delta E^{\circ\prime}$ = 190 mV). As result thereof, the electron density of the phosphole unit decreases and hence the potential of the first redox event is shifted to higher potentials ($E^{\circ\prime}$ = 5 mV *vs* FcH/FcH$^+$). A decrease of the redox separation might be an indication for a decreased electronic communication of the ferrocenyl termini in 2,5-position *via* the phoshole motif.

Compared to other 2,5-substituted 5-membered heterocycles, the observed redox separations are between those of 2,5-Fc$_2$-^{c}C$_4$H$_2$O ($\Delta E^{\circ\prime}$ = 290 mV)[C31] and 2,5-Fc$_2$-3,4-Ph$_2$-^{c}C$_4$SiPh$_2$ ($\Delta E^{\circ\prime}$ = 280 mV)[C35], respectively. The redox separations are significant lower when compared to 2,5-diferrocenyl-1-methyl-1*H*-pyrrole ($\Delta E^{\circ\prime}$ = 410 mV) and 2,5-diferrocenyl-1-phenyl-1*H*-pyrrole ($\Delta E^{\circ\prime}$ = 450 mV).[C31]

The redox separations of **C-3a**–**c**, **C-4a**–**c** and **C-9** indicate moderately coupled class II systems according to Robin and Day[C62], whereas the use of $\Delta E^{\circ\prime}$ is often an unsuited

measure for the determination of the electron transfer interaction.[C63] In order to classify the electron transfer between the Fc/Fc^+ termini in **C-3a–c**, **C-4a–c** and **C-9**, spectroelectrochemical (*in situ* UV/Vis-NIR and IR) measurements were performed.

The UV/Vis-NIR spectroelectrochemical studies were carried out in dichloromethane solutions containing **C-3a–c**, **C-4a–c** or **C-9** (2.0 $mmol \cdot L^{-1}$) and $[N^nBu_4][B(C_6F_5)_4]$ (0.1 $mol \cdot L^{-1}$) as supporting electrolyte in an OTTLE (= Optically Transparent Thin-Layer Electrochemical) cell.[C64] A stepwise increase of the potentials (step width: 25 mV, 50 mV or 100 mV) resulted in a subsequent oxidation of **C-3a–c**, **C-4a–c** and **C-9**. During the measurements, oxidation of the neutral compounds to mixed-valent $[\mathbf{C\text{-}3a}]^+$–$[\mathbf{C\text{-}3c}]^+$, $[\mathbf{C\text{-}4a}]^{2+}$–$[\mathbf{C\text{-}4c}]^{2+}$, $[\mathbf{C\text{-}9}]^+$ and finally to the fully oxidized species $[\mathbf{C\text{-}3a}]^{2+}$–$[\mathbf{C\text{-}3c}]^{2+}$, $[\mathbf{C\text{-}4a}]^{4+}$–$[\mathbf{C\text{-}4c}]^{4+}$, $[\mathbf{C\text{-}9}]^{2+}$ was observed. After complete oxidation, each compound was reduced at -200 mV to prove the reversibility of the process; the resulting UV/Vis-NIR spectra were identical to those of the neutral compounds.

For neutral **C-3a–c** no absorptions between 1000 and 3000 nm were observed. During the oxidation of **C-3a–c** (E ≈ 500 mV *vs* Ag/AgCl) to the mono-cationic species $[\mathbf{C\text{-}3a}]^+$–$[\mathbf{C\text{-}3c}]^+$ a broad band within this area appeared. A further increase of the potential resulted in a decrease of this absorption, a behavior typical for intervalence-charge transfer excitations (Figure C6 (**C-3b**), SI11 (**C-3a**), SI12(**C-3c**)).

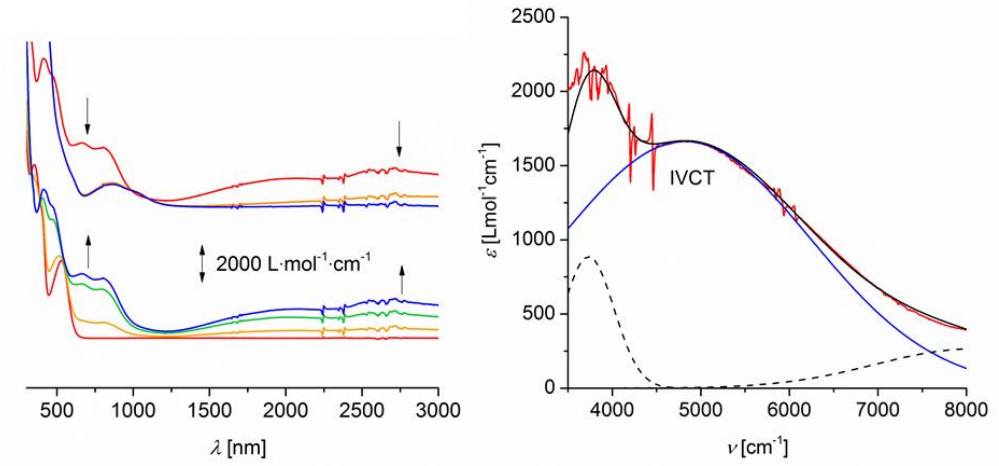

Figure C6. Left: UV/Vis-NIR spectra of **C-3b** at 25 °C in dichloromethane (2.0 $mmol \cdot L^{-1}$) at rising potentials (bottom: -200 to 520 mV; top: 520 to 800 mV *vs* Ag/AgCl); supporting electrolyte $[N^nBu_4][B(C_6F_5)_4]$; arrows indicate increasing and decreasing absorptions. Right: Deconvolution of the NIR absorptions of $[\mathbf{C\text{-}3b}]^+$ using three Gaussian shaped bands determined by spectroelectrochemistry in an OTTLE cell.

The observed spectra were deconvoluted into three Gaussian shaped bands, which represent a LF (= ligand field)[C36] transition, a further absorption which represents the edge to higher energy absorptions and the IVCT band. Therefore, the intensity ε_{max}, the full-width-at-halfheight $\Delta\nu_{1/2}$, and the ν_{max} values from the IVCT component could be determined. The sum of these three Gaussian shaped absorptions fits almost exactly with the experimental curve. The NIR data of the IVCT absorptions are summarized in Table C3.

Table C3. NIR data of the IVCT absorptions of phospholes [C-3a]$^+$–[C-3c]$^+$, [C-4a]$^{2+}$–[C-4c]$^{2+}$ and [C-9]$^+$.[a]

Compd.	ν_{max} (cm^{-1}) (ε_{max} ($L\cdot mol^{-1}\cdot cm^{-1}$))	$\Delta\nu_{1/2}$ (cm^{-1})	$(\Delta\nu_{1/2})_{theo}$[b] (cm^{-1})
[**C-3a**]$^+$	4850 (1450)	3300	3344
[**C-3b**]$^+$	4825 (1650)	3300	3337
[**C-3c**]$^+$	4850 (1450)	3250	3342
[**C-4a**]$^{2+}$[c]	4850 (1950)	3150	3345
[**C-4b**]$^{2+}$[c]	4800 (2000)	3150	3330
[**C-4c**]$^{2+}$[c]	4850 (1800)	3250	3336
[**C-9**]$^+$	5050 (400)	4700	3419

[a]In anhydrous dichloromethane containing 0.1 $mol\cdot L^{-1}$ of $[N^nBu_4][B(C_6F_5)_4]$ as supporting electrolyte at 25 °C. [b]Values calculated as $(\Delta\nu_{1/2})_{theo} = (2310\cdot\nu_{max})^{1/2}$ according to the Hush relationship for weakly coupled systems[C65]. [c]Due to the small potential difference, exclusive mono-oxidation was not achieved.

In the pentacarbonyl complexes **C-3a**–**c** the ferrocenyl metal-metal interaction is not affected by the nature of the metal atom M (Cr, Mo or W) as the IVCT absorptions have similar characteristics ($\nu_{max} \approx 4850$ cm^{-1}, $\varepsilon_{max} \approx 1500$ $L\cdot mol^{-1}\cdot cm^{-1}$, $\Delta\nu_{1/2} \approx 3300$ cm^{-1}). Compared to phosphole **C-1**, no significant changes of the IVCT absorption occurred after complexation of the phosphorus atom to $M(CO)_5$. The Fc/Fc^+ metal-metal interactions in **C-3a**–**c** are in the range of other moderately coupled diferrocenyl substituted heterocycles, *i*. *e*. 2,5-diferrocenyl furan ($\varepsilon_{max} = 1496$ $L\cdot mol^{-1}\cdot cm^{-1}$)[C31], and can be classified as moderately coupled class II systems according to Robin and Day.[C62]

A substitution of a further carbonyl group with a second phosphole unit as given in **C-4a**–**c** should result in a doubling of the intensity of the IVCT absorption as the electron transfer could occur twice. However, just a slightly increased ε_{max} value (≈ 1900 $L\cdot mol^{-1}\cdot cm^{-1}$) was observed. The full-width-at-halfheight (≈ 3150 cm^{-1}) and the ν_{max} values (≈ 4850 cm^{-1}) are similar to the pentacarbonyl complexes **C-3a**–**c** (Figure SI13 (**C-4a**), SI14 (**C-4b**) and SI15 (**C-4c**)). Recently, we have shown that the geometry at the phosphorus atom in phospholes influences the electronic interaction of the ferrocenyl termini. Thus, the deflection angle β of

the carbon atom of the substituent at phosphorus from the C1–P–C4 plane (Figure C3) shows a significant influence, for lower β values an increased Fc/Fc$^+$ metal-metal interaction was observed.[C66] In **C-3c** (β = 66.981(9) °) a lower value than in **C-4c** (β = 72.474(1) °) was determined, which could explain the lower intensity of the IVCT absorption.

Earlier studies of the electronic interactions in 2,5-diferrocenyl-1-phenyl-1*H*-phospholes showed that the oxidation of the phosphorus atom from P^{III} to P^{V} as represented in sulfide **C-8** (ε_{max} ≈ 1300 L·mol^{-1}·cm^{-1}, $\Delta\nu_{1/2}$ ≈ 4200 cm^{-1}) resulted in a slightly reduced electronic interaction of the Fc/Fc$^+$ termini, confirming that the electronic interaction takes place through the dienic system.[C33]

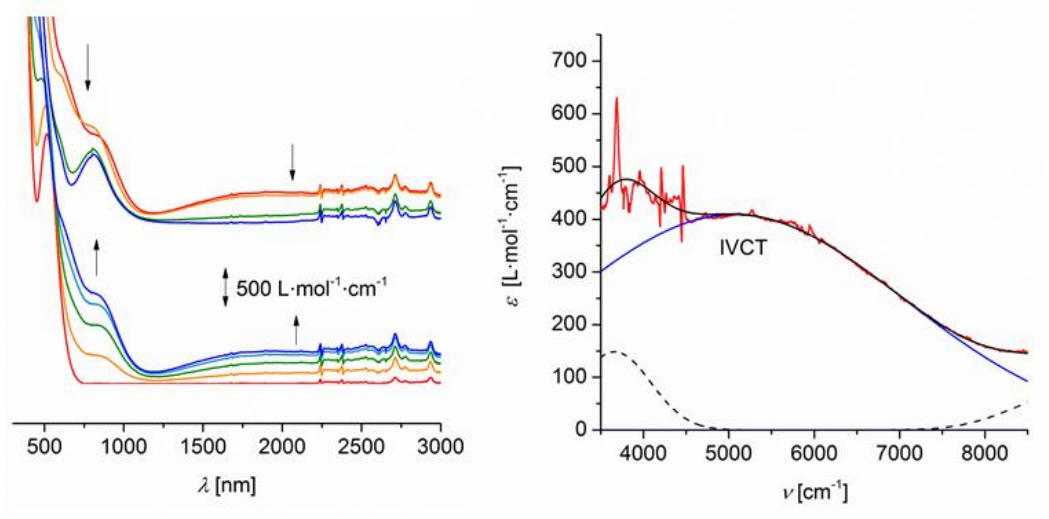

Figure C7. Left: UV/Vis-NIR spectra of **C-9** at 25 °C in dichloromethane (2.0 mmol·L^{-1}) at rising potentials (bottom: -200 to 500 mV; top: 500 to 800 mV *vs* Ag/AgCl); supporting electrolyte [N^{n}Bu$_4$][B(C$_6$F$_5$)$_4$]; arrows indicate increasing and decreasing absorptions. Right: Deconvolution of the NIR absorptions of [**C-9**]$^+$ using three Gaussian shaped bands determined by spectroelectrochemistry in an OTTLE cell.

When the dienic unit in **C-9** is η^4 coordinated to a Fe(CO)$_3$ building block, the intensity of the IVCT band (ε_{max} ≈ 400 L·mol^{-1}·cm^{-1}) decreases significantly and the full-width-at-halfheight ($\Delta\nu_{1/2}$ ≈ 4700 cm^{-1}) increases (Figure C7). Both, electronic and steric reasons may be held accountable for this decreased coupling: (i) the lower electron density in **C-9** should cause a decreased electronic interaction, and (ii) the deflection of the phosphole ring (the phosphorus atom is out of the C$_4$ plane by ca. 30 ° oriented, see X-ray discussion for more detail) also may be responsible for the lower metal-metal interaction between the Fc/Fc$^+$ units. The decreased metal-metal interaction after η^4 complexation of FcC=C-C=CFc to Fe(CO)$_3$ additionally confirms that the electron transfer takes place through the dienic unit.

In situ IR spectroelectrochemical measurements were performed in an OTTLE cell with CaF_2 windows of 5 mmol·L^{-1} (**C-9**) or 10 mmol·L^{-1} (**C-3a–c**) dichloromethane solutions using 0.1 mol·L^{-1} solutions of $[N^nBu_4][B(C_6F_5)_4]$ as supporting electrolyte. The IR spectra are depicted in Figures C8 (**C-9**), SI16 (**C-3a**), SI17 (**C-3b**) and SI18 (**C-3c**) (Supporting Information). The respective IR data are summarized in Table C4.

For neutral **C-3a–c** three bands for the CO stretchings were observed (**C-3a**, 1942 cm^{-1}, 1988 cm^{-1}, 2065 cm^{-1}; **C-3b**, 1948 cm^{-1}, 1994 cm^{-1}, 2073 cm^{-1}; **C-3c**, 1940 cm^{-1}, 1984 cm^{-1}, 2073 cm^{-1}). Oxidation of **C-3a–c** to [**C-3a**]$^+$–[**C-3c**]$^+$ and further to [**C-3a**]$^{2+}$–[**C-3c**]$^{2+}$ led to a small shift of the CO vibrations to higher frequencies. During oxidation of the ferrocenyl moieties of the phosphole unit in **C-3a–c** to [**C-3a**]$^+$–[**C-3c**]$^+$ and finally to [**C-3a**]$^{2+}$–[**C-3c**]$^{2+}$ the σ-donor ability of the phosphole ligand decreases. The decreased σ-donor ability results in a lower electron density at the metal atom resulting in a weaker π back-bonding towards the carbonyl ligands and hence the respective π^* CO orbitals are less populated. This in turn leads to weaker M–C_{CO} and stronger C–O bonds and a shift of the CO stretching vibrations to higher energies. Computational studies reveal that in addition electrostatic effects correlate with the internal harmonic carbonyl force constant (F_{CO}) and an increase of the positive charge next to the carbon atom results in a shift to higher energies.[C67]

Table C4. IR absorption data of [C-3a]$^{n+}$, [C-3b]$^{n+}$, [C-3c]$^{n+}$ and [C-9]$^{n+}$.[a]

Compd.	n = 0 [cm^{-1}]	n = 1 [cm^{-1}]	n = 2 [cm^{-1}]
[**C-3a**]$^{n+}$	1942	1947	1950
	1988	1994	-
	2065	2067	2071
[**C-3b**]$^{n+}$	1948	1952	1957
	1994	1996	-
	2073	2076	2081
[**C-3c**]$^{n+}$	1940	1944	1950
	1984	1990	-
	2073	2075	2079
[**C-9**]$^{n+}$	1988	2007	2030
	2002	2023	2044
	2054	2071	2087

[a]In anhydrous dichloromethane containing 0.1 mol·L^{-1} of $[N^nBu_4][B(C_6F_5)_4]$ as supporting electrolyte at 25 °C.

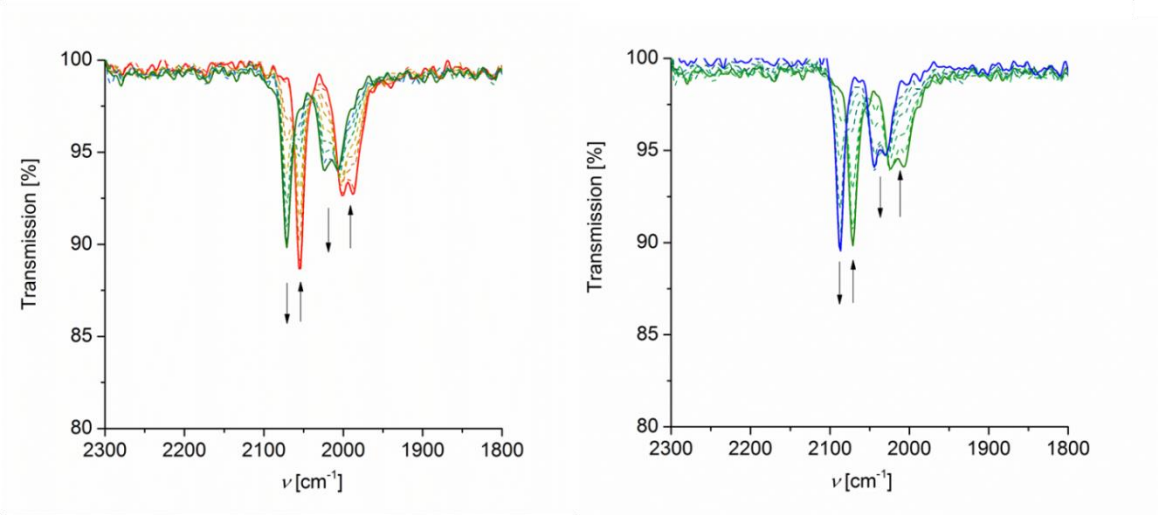

Figure C8. IR spectra (1800 – 2300 cm^{-1}) of **C-9** at 25 °C in dichloromethane (5 mmol L^{-1}) at rising potentials: (left) -200 to 590 mV; (right) 590 to 1200 mV, red: [**C-9**], green: [**C-9**]$^{+}$; blue: [**C-9**]$^{2+}$. All potentials *vs* Ag/AgCl; supporting electrolyte [$N^{n}Bu_4$][$B(C_6F_5)_4$]; arrows indicate increasing and decreasing absorptions.

In neutral **C-9**, three ν(CO) bands at 1988 cm^{-1}, 2002 cm^{-1} and 2054 cm^{-1} for the $Fe(CO)_3$ building block are characteristic (Experimental Section). During the oxidation to mono-cationic [**C-9**]$^{+}$ these bands are significantly shifted to 2007 cm^{-1}, 2023 cm^{-1} and 2071 cm^{-1}. The shift to higher energies can be explained similarly as described for **C-3a–c**. The increasing net charge on iron led to weaker Fe–C_{CO} back-bondings and hence in a stronger C≡O bond. Further oxidation to [**C-9**]$^{2+}$ resulted, as expected, in a shift to even higher energies (2030 cm^{-1}, 2044 cm^{-1}, 2087 cm^{-1}).

The spectroelectrochemical IR measurements show that the shift of the respective CO stretching vibrations upon oxidation is more pronounced when the metal carbonyl fragment is bonded to the dienic system opposed to the phosphorus atom. This demonstrates that the electronic interaction takes place *via* the dienic system as the carbonyl vibration frequencies are more affected, when the metal carbonyl fragment is bonded to the dienic system.

C3 Conclusions

The pentacarbonyl-(2,5-diferrocenyl-1-phenyl-1*H*-phosphole) metal complexes **C-3a–c** (**C-3a**, M = Cr; **C-3b**, M = Mo; **C-3c**, M = W) have been successfully prepared by the reaction of $M(CO)_5$(thf) (**C-2a**, M = Cr; **C-2b**, M = Mo; **C-2c**, M = W) with 2,5-diferrocenyl-1-phenyl-1*H*-phosphole (**C-1**) in the ratio of 1:1.

The synthesis of tetracarbonyl-*bis*(2,5-diferrocenyl-1-phenyl-1*H*-phosphole) metal complexes **C-4a–c** (**C-4a**, M = Cr; **C-4b**, M = Mo; **C-4c**, M = W) was achieved by irradiation

C-3a–c with 1 equiv. of phosphole **C-1** in tetrahydrofuran. The reaction of **C-1** with $Fe_2(CO)_9$ gave tetracarbonyl-(2,5-diferrocenyl-1-phenyl-1*H*-phosphole) iron (**C-6**) and heptacarbonyl-[μ-(2,3,4,5-η)-1-(2,5-diferrocenyl-1-phenyl-1*H*-phosphole) diiron (**C-7**). In a similar manner, 2,5-diferrocenyl-1-phenyl-1*H*-phosphole sulfide (**C-8**) was reacted with $Fe_2(CO)_9$ to afford tricarbonyl-[(2,3,4,5,-η)-(2,5-diferrocenyl-1-phenyl-1*H*-phosphole 1-sulfide) iron (**C-9**).

Molecules **C-3b**,**c**, **C-4c**, **C-7** and **C-9** have been structurally characterized by single-crystal X-ray diffraction. Complexes **C-3b**,**c** and **C-4c** possess a somewhat distorted octahedral geometry around the metal centers with a *cis* orientation of the phosphole units in **C-4c**. A comparison of the M–C_{CO} bond lengths in **C-3b** show that the shortest bond distance is observed for the *trans*-CO (2.012 Å), due to the stronger M–C_{CO} back-bonding. Coordination of the FcC=C-C=CFc unit to $Fe(CO)_3$ in **C-7** and **C-9** leads to a distortion of the phosphorus atom out of the C_4 plane by ca. 30 °. Electrochemical investigations of **C-3a–c**, **C-4a–c** and **C-9** show two (**C-3a–c**, **C-9**) or four (**C-4a–c**) separated redox events for the ferrocenyl units in 2,5-position of the phosphole ring. A coordination of the phosphorus atom to $M(CO)_5$ or $M(CO)_4$ in **C-3a–c** and **C-4a–c** has no significant influence on the redox separations $\Delta E°'$, when compared to **C-1**. Due to the decreased electron density and a deflection of the phosphole ring in **C-9** (after complexation of the dienic system to $Fe(CO)_3$), a decreased redox splitting (**C-8**, $\Delta E°'$ = 240 mV; **C-9**, $\Delta E°'$ = 190 mV) was observed. *In situ* UV/Vis-NIR measurements reveal that mixed-valent [**C-3a**]$^+$–[**C-3c**]$^+$, [**C-4a**]$^{2+}$–[**C-4c**]$^{2+}$ and [**C-9**]$^+$ exhibit IVCT absorptions of weak to moderate strength. A comparison of the IVCT bands of **C-3a–c** with that of **C-1** shows that a coordination of the phosphorus atom to metal carbonyl moieties and the nature of the metal center in these compounds have no significant influence on the electronic interactions between the Fc/Fc$^+$ termini. In contrast, the coordination of the $^cC_4H_2P$ motif to $Fe(CO)_3$ resulted in significant decreased Fc/Fc$^+$ metal-metal interaction as the intensity of the IVCT band decreased (**C-8**, $\varepsilon_{max} \approx 1300$ L·mol^{-1}·cm^{-1},[C33] **C-9**, $\varepsilon_{max} \approx 400$ L·mol^{-1}·cm^{-1}) and the full-width-at-halfheight of the IVCT band increases (**C-8**, $\Delta\nu_{1/2} \approx 4200$ cm^{-1};[D33] **C-9**, $\Delta\nu_{1/2} \approx 4700$ cm^{-1}). IR spectroelectrochemical measurements confirmed the influence of the FcC=C-C=CFc dienic system on the electronic interaction. Oxidation of **C-3a–c** to [**C-3a**]$^+$–[**C-3c**]$^+$ and finally to [**C-3a**]$^{2+}$–[**C-3c**]$^{2+}$ led to small changes of the carbonyl stretching frequencies, whereas in **C-9** the frequencies are shifted significantly to higher energy caused by the decreased σ-donor ability of the phosphole ligand influencing the π back-bonding of the metal atom to the carbonyl ligands.

C4 Experimental Section

General data

All reactions were carried out under an atmosphere of argon (5.0) using standard Schlenk techniques. Tetrahydrofuran was purified by distillation from sodium/benzophenone ketyl; toluene and dichloromethane were obtained from a solvent drying and purification system (double column solvent filtration, working pressure 0.5 bar). For electrochemistry HPLC grade dichloromethane was purified by distillation from calcium hydride. For column chromatography silica with a particle size of 40 – 60 μm (230 – 400 mesh (ASTM)) was used.

Instruments

FTIR spectra were recorded with a Nicolet IR 200 spectrometer (Thermo Comp.). NMR spectra were recorded at 298 K in the Fourier transform mode (500.3 MHz for ^{1}H, 125.7 MHz for $^{13}C\{^{1}H\}$ and 202.5 MHz for $^{31}P\{^{1}H\}$ spectra). Chemical shifts are reported in δ (parts per million) downfield from tetramethylsilane with the solvent as reference signal (^{1}H NMR: $CDCl_3$, $\delta = 7.26$; $^{13}C\{^{1}H\}$ NMR: $CDCl_3$, $\delta = 77.16$; $^{31}P\{^{1}H\}$ NMR: standard external rel. 85% H_3PO_4, $\delta = 0.0$; $P(OMe)_3$, $\delta = 139.0$, respectively).

Electrochemistry

Electrochemical measurements of **C-3a–c**, **C-4a–c**, **C-6**, **C-7** and **C-9** (1.0 mmol·L^{-1} $[N^nBu_4][B(C_6F_5)_4]$ as supporting electrolyte) in dichloromethane were performed in a dried, argon purged cell at 25 °C. For the measurements a three electrode cell containing a Pt auxiliary electrode, a glassy carbon working electrode (3.0 mm dia.) and an Ag/Ag^+ (0.01 mmol·L^{-1} $[AgNO_3]$) reference electrode fixed on a Luggin capillary was used. The working electrode was pretreated by polishing on a MicroFloc first with 1 micron and then with a ¼ micron diamond paste. The reference electrode was constructed from a silver wire inserted in a 0.01 mmol·L^{-1} $[AgNO_3]$ and a 0.1 mol·L^{-1} $[N^nBu_4][B(C_6F_5)_4]$ acetonitrile solution in a Luggin capillary with a vycor tip. This Luggin capillary was inserted in a second Luggin capillary containing a 0.1 mol·L^{-1} $[N^nBu_4][B(C_6F_5)_4]$ dichloromethane solution and a vycor tip. Experiments under the same conditions showed that all reduction and oxidation potentials were reproducible within 5 mV. Experimental potentials were referenced against an Ag/Ag^+ reference electrode but the presented results are referenced against ferrocene as an internal standard as required by IUPAC.[C60] To achieve this, each experiment was repeated in the presence of 1 mmol·L^{-1} decamethylferrocene (Fc*). Data were processed on a Microsoft Excel worksheet to set the formal reduction potentials of the FcH/FcH^+ couple to 0.0 V.

Under our conditions the Fc*/Fc*$^+$ couple appeared at -619 mV *vs* FcH/FcH$^+$, ΔE_p = 60 mV, while the FcH/FcH$^+$ couple itself was at 220 mV *vs* Ag/Ag$^+$, ΔE_p = 61 mV.[C68]

Spectroelectrochemistry

Spectroelectrochemical UV/Vis-NIR measurements of 2.0 mmol·L^{-1} solutions of **C-3a–c**, **C-4a–c**, and **C-9** in anhydrous dichloromethane containing 0.1 mol·L^{-1} of [N^{n}Bu$_4$][B(C$_6$F$_5$)$_4$] as the supporting electrolyte were performed in an OTTLE (OTTLE = Optically Transparent Thin-Layer Electrochemical)[C64] cell at 25 °C. The values obtained by deconvolution could be reproduced within ε_{max} 100 L·mol^{-1}·cm^{-1}; ν_{max} 50 cm^{-1}; $\Delta\nu_{1/2}$ 50 cm^{-1}. Spectroelectrochemical IR measurements of solutions of **C-3a–c** (10 mmol·L^{-1}) and **C-9** (5 mmol·L^{-1}) in anhydrous dichloromethane containing [N^{n}Bu$_4$][B(C$_6$F$_5$)$_4$] (0.1 mol·L^{-1}) as supporting electrolyte were performed in an OTTLE cell with CaF_2 windows.

Single Crystal X-ray Diffraction Analysis

Suitable single crystals of **C-3b**,**c**, **C-4c**, **C-9** for X-ray diffraction analysis were obtained by diffusion of *n*-hexane into a dichloromethane solution containing **C-3b**,**c**, **C-4c** or **C-9** at ambient temperature, suitable crystals of **C-7** were obtained by slow evaporation of the solvent of a *n*-hexane/diethyl ether mixture (10:1, *v*/*v*) containing **C-7**. Data were collected at ≈110 K with Mo K_α radiation (λ = 0.71073 Å). The structures were solved by direct methods and refined by full-matrix least-squares procedures on F^2.[C69,C70] All non-hydrogen atoms were refined anisotropically, and a riding model was employed in the treatment of the hydrogen atom positions.

Reagents

All starting materials were obtained from commercial suppliers and were used without further purification. 2,5-Diferrocenyl-1-phenyl-1*H*-phosphole (**C-1**) and 2,5-diferrocenyl-1-phenyl-1*H*-phosphole sulfide (**C-8**) were prepared according to published procedures.[C33]

General procedure for the synthesis of pentacarbonyl-(2,5-diferrocenyl-1-phenyl-1*H*-phosphole) compounds C-3a–c

The metal hexacarbonyls M(CO)$_6$ (**C-2a**, M = Cr; **C-2b**, M = Mo; **C-2c**, M = W) were dissolved in 150 mL of tetrahydrofuran in a photolysis equipment (mercury medium pressure lamp TQ 150) and were irradiated for 5 h at ambient temperature. The obtained M(CO)$_5$(thf) solutions were added drop-wise to 2,5-diferrocenyl-1-phenyl-1*H*-phosphole (**C-1**) dissolved in 50 mL of tetrahydrofuran. The resulting deep red mixtures were stirred overnight in the dark. All volatiles were removed in vacuo and the remaining solids were purified by column

chromatography (column size 3 × 15 cm) on silica using a 5/1 (*v*/*v*) *n*-hexane/dichloromethane mixture. Compounds **C-3a**–**c** were obtained as purple solids.

Synthesis of pentacarbonyl-(2,5-diferrocenyl-1-phenyl-1*H*-phosphole) chromium (C-3a)

Using the general synthesis procedure described above, 0.30 g (0.57 mmol) of **C-1** were reacted with 0.12 g (0.54 mmol) of **C-2a** to afford **C-3a**. Yield: 0.25 g (0.35 mmol, 62 % based on **C-1**). Anal. Calcd. for $C_{35}H_{25}CrFe_2O_5P$ (719.95 g/mol): C, 58.37; H, 3.50. Found: C, 58.67; H, 3.66. Mp.: 206 °C (decomp.). IR data (KBr, ν/cm^{-1}): 3097 w, 3048 w, 2963 s, 2924 s, 2853 m, 2063 m, 1987 m, 1942 s, 1918 m, 1627 w, 1458 w, 1412 w. ^{1}H NMR ($CDCl_3$, δ): 3.80 (m, 2 H, H$^{\alpha}$/C_5H_4), 3.89 (s, 10 H, C_5H_5), 4.19 (m, 2 H, H$^{\beta}$/C_5H_4), 4.30 (m, 2 H, H$^{\beta}$/C_5H_4), 4.60 (m, 2 H, H$^{\alpha}$/C_5H_4), 6.98 (d, $^3J_{HP}$ = 23.8 Hz, 2 H, C_4H_2P), 7.67−7.68 (m, 3 H, H^{m,p}/C_6H_5), 7.95−7.99 (m, 2 H, H^{o}/C_6H_5). ^{13}C{^{1}H} NMR ($CDCl_3$, δ): 67.5 (d, $^3J_{CP}$ = 6.7 Hz, C$^{\alpha}$/C_5H_4), 68.1 (d, $^3J_{CP}$ = 3.1 Hz, C$^{\alpha}$/C_5H_4), 69.1 (s, C$^{\beta}$/C_5H_4), 69.2 (s, C$^{\beta}$/C_5H_4), 70.0 (s, C_5H_5), 79.8 (d, $^2J_{CP}$ = 20.1 Hz, *C*^{i}/C_5H_4), 128.8 (d, $^1J_{CP}$ = 30.9 Hz, C^{i}/C_6H_5), 129.2 (d, J_{CP} = 9.9 Hz, CH/C_6H_5), 129.9 (d, $^2J_{CP}$ = 13.9 Hz, CH/C_4H_2P), 131.7 (d, J_{CP} = 2.3 Hz, CH/C_6H_5), 133.1 (d, J_{CP} = 12.2 Hz, CH/C_6H_5), 150.3 (d, $^1J_{CP}$ = 36.2 Hz, C^{i}/C_4H_2P), 216.2 (d, $^2J_{CP}$ = 12.2 Hz, *cis*-CO), 220.8 (d, $^2J_{CP}$ = 6.4 Hz, *trans*-CO). ^{31}P{^{1}H} NMR ($CDCl_3$, δ): 63.6 (s). HRMS (ESI-TOF, *m/z*): calcd for $C_{35}H_{25}CrFe_2O_5P$: 719.9540, found: 719.9512 $[M]^+$; calcd for $C_{33}H_{25}CrFe_2O_3P$: 663.9642, found: 663.9614 $[M]^+$; calcd for $C_{30}H_{25}Fe_2P$: 528.0388, found: 528.0375 $[M]^+$.

Synthesis of pentacarbonyl-(2,5-diferrocenyl-1-phenyl-1*H*-phosphole) molybdenum (C-3b)

According to the general synthesis method described earlier, 0.19 g (0.36 mmol) of **C-1** were reacted with 0.09 g (0.34 mmol) of **C-2b** to afford **C-3b**. Yield: 0.15 g (0.19 mmol, 53 % based on **C-1**). Anal. Calcd. for $C_{35}H_{25}Fe_2MoO_5P$ (765.92 g/mol): C, 55.01; H, 3.30. Found: C, 55.03; H, 3.51. Mp.: 185 °C. IR data (KBr, ν/cm^{-1}): 3087 w, 3037 w, 2955 w, 2917 w, 2854 w, 2071 s, 1991 s, 1944 s, 1923 s, 1573 w, 1434 w. ^{1}H NMR ($CDCl_3$, δ): 3.82 (m, 2 H, H$^{\alpha}$/C_5H_4), 3.87 (s, 10 H, C_5H_5), 4.18 (m, 2 H, H$^{\beta}$/C_5H_4), 4.29 (m, 2 H, H$^{\beta}$/C_5H_4), 4.59 (m, 2 H, H$^{\alpha}$/C_5H_4), 6.97 (d, $^3J_{HP}$ = 23.0 Hz, 2 H, C_4H_2P), 7.66−7.69 (m, 3 H, H^{m,p}/C_6H_5), 7.95−7.99 (m, 2 H, H^{o}/C_6H_5). ^{13}C{^{1}H} NMR ($CDCl_3$, δ): 67.0 (d, $^3J_{CP}$ = 6.6 Hz, C$^{\alpha}$/C_5H_4), 68.3 (d, $^3J_{CP}$ = 4.0 Hz, C$^{\alpha}$/C_5H_4), 69.0 (s, C$^{\beta}$/C_5H_4), 69.2 (s, C$^{\beta}$/C_5H_4), 70.0 (s, C_5H_5), 79.8 (d, $^2J_{CP}$ = 20.8 Hz, C^{i}/C_5H_4), 129.1 (d, $^1J_{CP}$ = 30.9 Hz, C^{i}/C_6H_5), 129.1 (d, J_{CP} = 10.2 Hz, CH/C_6H_5), 130.0 (d, $^2J_{CP}$ = 13.7 Hz, CH/C_4H_2P), 131.7 (d, J_{CP} = 2.2 Hz, CH/C_6H_5), 133.5 (d, J_{CP} = 13.8 Hz, CH/C_6H_5), 149.4 (d, $^1J_{CP}$ = 35.6 Hz, C^{i}/C_4H_2P), 205.1 (d, $^2J_{CP}$ = 8.3 Hz, *cis*-CO), 209.2 (d,

$^2J_{CP}$ = 21.3 Hz, *trans*-CO). $^{31}P\{^1H\}$ NMR ($CDCl_3$, δ): 44.3 (s). HRMS (ESI-TOF, *m/z*): calcd for $C_{35}H_{25}Fe_2MoO_5P$: 765.9199, found: 765.9186 $[M]^+$; $C_{33}H_{25}Fe_2MoO_3P$: 709.9300, found: 709.9283 $[M]^+$; calcd for $C_{30}H_{25}Fe_2P$: 528.0388, found: 528.0439 $[M]^+$.

Crystal Data for C-3b: $C_{35}H_{25}Fe_2MoO_5P$, M = 764.16 g·mol^{-1}, triclinic, $P\bar{1}$, λ = 0.71073 Å, *a* = 10.1774(4) Å, *b* = 13.0331(5) Å, *c* = 13.5081(5) Å, α = 80.467(3) °, β = 69.450(4) °, γ = 67.659(4), *V* = 1550.73(12) Å^3, Z = 2, ρ_{calcd} = 1.637 Mg·m^{-3}, μ = 1.415 mm^{-1}, *T* = 109.9(3) K, Θ range = 3.181-25.999°, reflections collected: 20638, independent: 6076 (R_{int} = 0.0329), R_1 = 0.0262, wR_2 = 0.0576 [I > 2σ(I)].

Synthesis of pentacarbonyl-(2,5-diferrocenyl-1-phenyl-1*H*-phosphole) tungsten (C-3c)

Using the general synthesis procedure described above, 0.11 g (0.20 mmol) of **C-1** were reacted with 0.07 g (0.20 mmol) of **C-2c** to afford **C-3c**. Yield: 0.11 g (0.13 mmol, 67 % based on **C-1**). Mp.: 174 °C. IR data (KBr, *v*/cm^{-1}): 3094 w, 3042 w, 2954 w, 2922 m, 2850 w, 2071 s, 1986 s, 1933 s, 1915 s, 1575 w, 1435 w. ^1H NMR ($CDCl_3$, δ): 3.84 (m, 2 H, H^{α}/C_5H_4), 3.88 (s, 10 H, C_5H_5), 4.19 (m, 2 H, H^{β}/C_5H_4), 4.30 (m, 2 H, H^{β}/C_5H_4), 4.60 (m, 2 H, H^{α}/C_5H_4), 6.96 (d, $^3J_{HP}$ = 24.2 Hz, 2 H, C_4H_2P), 7.66−7.71 (m, 3 H, $H^{m,p}/C_6H_5$), 7.95−8.00 (m, 2 H, H^{o}/C_6H_5). $^{13}C\{^1H\}$ NMR ($CDCl_3$, δ): 67.1 (d, $^3J_{CP}$ = 6.8 Hz, C^{α}/C_5H_4), 68.3 (d, $^3J_{CP}$ = 3.9 Hz, C^{α}/C_5H_4), 69.1 (s, C^{β}/C_5H_4), 69.3 (s, C^{β}/C_5H_4), 70.0 (s, C_5H_5), 79.6 (d, $^2J_{CP}$ = 20.2 Hz, C^{i}/C_5H_4), 128.8 (d, $^1J_{CP}$ = 35.9 Hz, C^{i}/C_6H_5), 129.2 (d, J_{CP} = 10.4 Hz, CH/C_6H_5), 130.0 (d, $^2J_{CP}$ = 14.4 Hz, CH/C_4H_2P), 131.8 (d, J_{CP} = 2.3 Hz, CH/C_6H_5), 133.5 (d, J_{CP} = 13.3 Hz, CH/C_6H_5), 149.4 (d, $^1J_{CP}$ = 40.5 Hz, C^{i}/C_4H_2P), 196.2 (d, $^2J_{CP}$ = 6.4 Hz, *cis*-CO), 198.0 (d, $^2J_{CP}$ = 20.5 Hz, *trans*-CO). $^{31}P\{^1H\}$ NMR ($CDCl_3$, δ): 26.5 ($^1J_{31P183W}$ = 224 Hz). HRMS (ESI-TOF, *m/z*): calcd for $C_{35}H_{25}Fe_2O_5PW$: 851.9655, found: 851.9573 $[M]^+$; $C_{33}H_{25}Fe_2O_3PW$: 795.9756, found: 795.9693 $[M]^+$; calcd for $C_{30}H_{25}Fe_2P$: 528.0388, found: 528.0344 $[M]^+$.

Crystal Data for C-3c: $C_{35}H_{25}Fe_2O_5PW$, M = 852.07 g·mol^{-1}, monoclinic, *Pc*, λ = 0.71073 Å, *a* = 13.5986(8) Å, *b* = 13.4025(7) Å, *c* = 18.1802(17) Å, β = 109.437(8) °, *V* = 3124.6(4) Å^3, Z = 4, ρ_{calcd} = 1.811 Mg·m^{-3}, μ = 4.682 mm^{-1}, *T* = 111(2) K, Θ range = 3.040-24.997°, reflections collected: 13942, independent: 7192 (R_{int} = 0.0822), R_1 = 0.0562, wR_2 = 0.1082 [I > 2σ(I)].

General procedure for the synthesis of tetracarbonyl-bis(2,5-diferrocenyl-1-phenyl-1*H*-phosphole) compounds C-4a–c

The pentacarbonyl-(2,5-diferrocenyl-1-phenyl-1*H*-phosphole) complexes **C-3a**–**c** and one equiv. of **C-1** were dissolved in 200 mL of tetrahydrofuran and were irradiated in a photolysis equipment for 2 h. The resulting red mixtures were reduced to dryness in vacuo and the

remaining solids were purified by column chromatography (silica, column size 3 × 15 cm) using a 10/1 (*v*/*v*) *n*-hexane/diethyl ether mixture. Compounds **C-4a**–**c** were obtained as red solids.

Synthesis of tetracarbonyl-bis(2,5-diferrocenyl-1-phenyl-1*H*-phosphole) chromium (C-4a)

Using the general synthesis procedure described above, 0.09 g (0.13 mmol) of **C-3a** were reacted with 0.07 g (0.13 mmol) of **C-1** to afford **C-4a**. Yield: 0.05 g (0.04 mmol, 32 % based on **C-3a**). Anal. Calcd. for $C_{64}H_{50}CrFe_4O_4P_2 \cdot 2/3CH_2Cl_2$ (1220.00 g/mol): C, 60.82; H, 4.05. Found: C, 60.56; H, 4.40. Mp.: 176 °C (decomp.). IR data (KBr, ν/cm^{-1}): 3084 w, 2923 w, 2852 w, 2007 s, 1907 s, 1902 s, 1872 s, 1652 m, 1431 m. ^{1}H NMR ($CDCl_3$, δ): 3.73 (s, 20 H, C_5H_5), 3.86 (m, 4 H, C_5H_4), 4.19 (m, 4 H, C_5H_4), 4.25 (m, 4 H, C_5H_4), 4.39 (m, 4 H, C_5H_4), 5.30 (s, CH_2Cl_2), 6.26 (d, $^3J_{HP}$ = 21.4 Hz, 4 H, C_4H_2P), 7.48−7.50 (m, 6 H, $H^{m,p}/C_6H_5$), 7.88−7.92 (m, 4 H, H^o/C_6H_5). ^{13}C{^{1}H} NMR ($CDCl_3$, δ): 66.4 (bs, C_5H_4), 68.0 (s, C_5H_4), 68.7 (s, C_5H_4), 69.0 (s, C_5H_4), 69.8 (s, C_5H_5), 81.5 (pt, J_{CP} = 10.1 Hz, C^i/C_5H_4), 128.4 (C^i/C_6H_5),128.5 (pt, J_{CP} = 4.9 Hz, CH/C_6H_5), 130.6 (s, CH/C_6H_5), 131.7 (pt, $^2J_{CP}$ = 6.1 Hz, CH/C_4H_2P), 133.0 (pt, J_{CP} = 5.0 Hz, CH/C_6H_5), 146.3 (C^i/C_4H_2P). Due to the low solubility the signal for the CO carbon atoms is missing. ^{31}P{^{1}H} NMR ($CDCl_3$, δ): 61.5 (s). HRMS (ESI-TOF, *m/z*): calcd for $C_{64}H_{50}CrFe_4O_4P_2$: 1219.9992, found: 1219.9895 $[M]^+$; calcd for $C_{33}H_{25}CrFe_2O_3P$: 663.9642, found: 663.9586 $[M]^+$; calcd for $C_{30}H_{25}Fe_2P$: 528.0388, found: 528.0348 $[M]^+$.

Synthesis of tetracarbonyl-bis(2,5-diferrocenyl-1-phenyl-1*H*-phosphole) molybdenum (C-4b)

According to the general synthesis procedure described above, 0.2 g (0.23 mmol) of **C-3b** were reacted with 0.12 g (0.23 mmol) of **C-1** to afford **C-4b**. Yield: 0.14 g (0.11 mmol, 48 % based on **C-3b**). Anal. Calcd. for $C_{64}H_{50}Fe_4MoO_4P_2$ (1265.96 g/mol): C, 60.80; H, 3.99. Found: C, 60.35; H, 4.18.[C71] Mp.: 205 °C (decomp.). IR data (KBr, ν/cm^{-1}): 3090 w, 3043 w, 2958 w, 2923 w, 2851 w, 2021 s, 1917 s, 1907 s, 1878 s, 1555 w, 1432 m. ^{1}H NMR ($CDCl_3$, δ): 3.73 (s, 20 H, C_5H_5), 3.81 (m, 4 H, C_5H_4), 4.17 (m, 4 H, C_5H_4), 4.25 (m, 4 H, C_5H_4), 4.39 (m, 4 H, C_5H_4), 6.24 (d, $^3J_{HP}$ = 21.0 Hz, 4 H, C_4H_2P), 7.48−7.52 (m, 6 H, $H^{m,p}/C_6H_5$), 7.86−7.89 (m, 4 H, H^o/C_6H_5). ^{13}C{^{1}H} NMR ($CDCl_3$, δ): 66.0 (pt, J_{CP} = 2.9 Hz, C_5H_4), 68.0 (s, C_5H_4), 68.8 (s, C_5H_4), 69.00 (s, C_5H_4), 69.7 (s, C_5H_5), 81.2 (pt, J_{CP} = 10.7 Hz, C^i/C_5H_4), 128.1 (C^i/C_6H_5), 128.5 (pt, J_{CP} = 4.7 Hz, CH/C_6H_5), 130.7 (s, CH/C_6H_5), 131.5 (d, $^2J_{CP}$ = 6.6 Hz, CH/C_4H_2P), 133.5 (pt, J_{CP} = 6.3 Hz, CH/C_6H_5), 145.4 (C^i/C_4H_2P). Due to the low

solubility the signal for the CO carbon atoms is missing. $^{31}P\{^{1}H\}$ NMR ($CDCl_3$, δ): 42.98 (s). HRMS (ESI-TOF, *m/z*): calcd for $C_{64}H_{50}Fe_4MoO_4P_2$: 1265.9656, found: 1265.9678 $[M]^+$; calcd for $C_{30}H_{25}Fe_2P$: 528.0388, found: 528.0417 $[M]^+$.

Synthesis of tetracarbonyl-bis(2,5-diferrocenyl-1-phenyl-1*H*-phosphole) tungsten (C-4c)

Using the general synthesis procedure described earlier, 0.15 g (0.18 mmol) of **C-3c** were reacted with 0.1 g (0.18 mmol) of **C-1** to afford **C-4c**. Yield: 0.08 g (0.06 mmol, 33 % based on **C-3c**). Anal. Calcd. for $C_{64}H_{50}Fe_4O_4P_2W$ (1352.01 g/mol): C, 56.85; H, 3.73. Found: C, 56.95; H, 4.36.[C71] Mp.: 175 °C. IR data (KBr, ν/cm^{-1}): 3084 w, 3045 w, 2957 m, 2924 m, 2852 m, 2016 s, 1938 s, 1898 s, 1872 s, 1710 w, 1435 m. ^{1}H NMR ($CDCl_3$, δ): 3.73 (s, 20 H, C_5H_5), 3.84 (m, 4 H, C_5H_4), 4.18 (m, 4 H, C_5H_4), 4.25 (m, 4 H, C_5H_4), 4.40 (m, 4 H, C_5H_4), 6.23 (d, $^{3}J_{HP}$ = 22.2 Hz, 4 H, C_4H_2P), 7.48−7.53 (m, 6 H, $H^{m,p}/C_6H_5$), 7.87−7.90 (m, 4 H, H^{o}/C_6H_5). $^{13}C\{^{1}H\}$ NMR ($CDCl_3$, δ): 66.0 (pt, J_{CP} = 3.2 Hz, C_5H_4), 68.1 (s, C_5H_4), 68.8 (s, C_5H_4), 69.1 (s, C_5H_4), 69.7 (s, C_5H_5), 81.0 (pt, J_{CP} = 10.4 Hz, C^{i}/C_5H_4), 128.4 (C^{i}/C_6H_5), 128.6 (pt, J_{CP} = 5.1 Hz, CH/C_6H_5), 130.8 (s, CH/C_6H_5), 131.6 (pt, $^{2}J_{CP}$ = 5.1 Hz, CH/C_4H_2P), 133.5 (pt, J_{CP} = 6.0 Hz, CH/C_6H_5), 145.4 (C^{i}/C_4H_2P). Due to the low solubility the signal for the CO carbon atoms is missing. $^{31}P\{^{1}H\}$ NMR ($CDCl_3$, δ): 25.9 ($^{1}J_{31P183W}$ = 220 Hz). HRMS (ESI-TOF, *m/z*): calcd for $C_{64}H_{50}Fe_4O_4P_2W$: 1352.0110, found: 1352.0055 $[M]^+$.

Crystal Data for *cis*-C-4c: $C_{64}H_{50}Fe_4O_4P_2W \cdot 2\ CH_2Cl_2$, M = 1522.08 g·mol^{-1}, orthorhombic, *Pbcn*, λ = 0.71073 Å, *a* = 12.0616(2) Å, *b* = 17.2266(3) Å, *c* = 27.9283(5) Å, *V* = 5802.95(17) Å^3, Z = 4, ρ_{calcd} = 1.742 Mg·m^{-3}, μ = 3.241 mm^{-1}, *T* = 110.00(10) K, Θ range = 2.996-25.998°, reflections collected: 36960, independent: 5672 (R_{int} = 0.0332), R_1 = 0.0286, wR_2 = 0.0577 [I > 2σ(I)].

Synthesis of tetracarbonyl-(2,5-diferrocenyl-1-phenyl-1*H*-phosphole) iron (C-6) and heptacarbonyl-[μ-(2,3,4,5-η)-1-(2,5-diferrocenyl-1-phenyl-1*H*-phosphole) diiron (C-7)

To 0.23 g (0.43 mmol) of **C-1** dissolved in 100 mL of toluene, 0.39 g (1.07 mmol) of $Fe_2(CO)_9$ (**C-5**) were added in a single portion. The resulting reaction mixture was stirred for 8 h at 100 °C. After cooling the reaction mixture to ambient temperature, all volatiles were removed in vacuo and the remaining residue was purified by column chromatography (silica, column size 3 × 15 cm) using a 10/1 (*v*/*v*) *n*-hexane/diethyl ether mixture. Compounds **C-6** (first fraction) and **C-7** (second fraction) were obtained as red solids.

C-6, Yield: 0.09 g (0.13 mmol, 31 % based on **C-1**). Anal. Calcd. for $C_{34}H_{25}Fe_3O_4P$ (695.95 g/mol): C, 58.67; H, 3.62. Found: C, 58.88; H, 4.19.[C71] Mp.: 94 °C. IR data (KBr, ν/cm^{-1}): 3091 w, 3048 w, 2961 m, 2922 m, 2850 m, 2046 s, 1967 s, 1941 s, 1931 s, 1435 m. ^{1}H NMR

($CDCl_3$, δ): 3.89 (m, 2 H, C_5H_4), 3.95 (s, 10 H, C_5H_5), 4.15 (m, 2 H, C_5H_4), 4.28 (m, 2 H, C_5H_4), 4.45 (m, 2 H, C_5H_4), 6.97 (d, $^3J_{HP}$ = 27.2 Hz, 2 H, C_4H_2P), 7.62−7.65 (m, 3 H, $H^{m,p}/C_6H_5$), 7.91−7.95 (m, 2 H, H^o/C_6H_5). $^{13}C\{^1H\}$ NMR ($CDCl_3$, δ): 68.2 (d, $^3J_{CP}$ = 2.2 Hz, C^{α}/C_5H_4), 68.7 (d, $^3J_{CP}$ = 5.6 Hz, C^{α}/C_5H_4), 68.9 (s, C^{β}/C_5H_4), 69.0 (s, C^{β}/C_5H_4), 70.1 (s, C_5H_5), 79.2 (d, $^2J_{CP}$ = 19.6 Hz, C^i/C_5H_4), 127.9 (d, $^1J_{CP}$ = 39.2 Hz, C^i/C_6H_5), 129.2 (d, J_{CP} = 10.7 Hz, CH/C_6H_5), 130.8 (d, $^2J_{CP}$ = 16.0Hz, CH/C_4H_2P), 132.0 (d, J_{CP} = 1.2 Hz, CH/C_6H_5), 133.1 (d, J_{CP} = 11.7 Hz, CH/C_6H_5), 148.8 (d, $^1J_{CP}$ = 45.2 Hz, C^i/C_4H_2P), 214.0 (d, $^2J_{CP}$ = 16.8 Hz, CO). $^{31}P\{^1H\}$ NMR ($CDCl_3$, δ): 75.5 (s). HRMS (ESI-TOF, *m/z*): calcd for $C_{30}H_{25}Fe_2P$: 528.0388, found: 528.0373 $[M]^+$.

C-7, Yield: 0.08 g (0.10 mmol, 22 % based on **C-1**). Anal. Calcd. for $C_{37}H_{25}Fe_4O_7P$ (835.87 g/mol): C, 53.16; H, 3.01. Found: C, 52.75; H, 3.22. Mp.: 221 °C. IR data (KBr, ν/cm^{-1}): 3110 w, 3071 w, 2957 w, 2932 w, 2062 s, 2047 s, 1998 s, 1983 s, 1975 s, 1960 s, 1937 s, 1435 m, 1409 m. ^1H NMR ($CDCl_3$, δ): 3.86 (s, 10 H, C_5H_5), 4.13 (m, 2 H, C_5H_4), 4.21 (m, 4 H, C_5H_4), 4.47 (m, 2 H, C_5H_4), 6.14 (d, $^3J_{HP}$ = 8.0 Hz, 2 H, C_4H_2P), 7.44–7.47 (m, 1 H, H^p/C_6H_5), 7.54−7.57 (m, 2 H, C_6H_5), 8.00−8.03 (m, 2 H, C_6H_5). $^{13}C\{^1H\}$ NMR ($CDCl_3$, δ): 68.5 (d, $^3J_{CP}$ = 7.4 Hz, C^{α}/C_5H_4), 68.6 (s, C^{β}/C_5H_4), 68.7 (s, C^{β}/C_5H_4), 69.0 (d, $^3J_{CP}$ = 5.0 Hz, C^{α}/C_5H_4), 69.6 (s, C_5H_5), 72.2 (d, $^1J_{CP}$ = 32.2 Hz, C^i/C_4H_2P), 83.8 (d, $^2J_{CP}$ = 13.5 Hz, C^i/C_5H_4), 87.4 (d, $^2J_{CP}$ = 3.9 Hz, CH/C_4H_2P), 128.4 (d, J_{CP} = 7.5 Hz, CH/C_6H_5), 130.9 (d, $^4J_{CP}$ = 1.5 Hz, C^p/C_6H_5), 131.7 (d, J_{CP} = 11.4 Hz, CH/C_6H_5), 144.8 (d, $^1J_{CP}$ = 4.8 Hz, C^i/C_6H_5), 210.0 (d, J_{CP} = 7.3 Hz, CO), 217.9 (d, J_{CP} = 9.6 Hz, CO). $^1P\{^1H\}$ NMR ($CDCl_3$, δ): 97.1 (s). HRMS (ESI-TOF, *m/z*): calcd for $C_{37}H_{26}Fe_4O_7P$: 836.8812, found: 836.8798 $[M + H]^+$.

Crystal Data for C-7: $C_{37}H_{25}Fe_4O_7P$, M = 835.94 g·mol^{-1}, monoclinic, $P2_1c$, λ = 0.71073 Å, a = 11.0117(3) Å, b = 17.3794(4) Å, c = 17.7478(4) Å, β = 106.792(3), V = 3251.69(15) Å^3, Z = 4, ρ_{calcd} = 1.708 Mg·m^{-3}, μ = 1.850 mm^{-1}, T = 110(2) K, Θ range = 3.354- 24.999°, reflections collected: 17512, independent: 5723 (R_{int} = 0.0417), R_1 = 0.0332, wR_2 = 0.0625 [I > 2σ(I)].

Synthesis of tricarbonyl-[(2,3,4,5,-η)-(2,5-diferrocenyl-1-phenyl-1*H*-phosphole 1-sulfide) iron (C-9)

To 0.25 g (0.45 mmol) of **C-8** dissolved in 100 mL of toluene, 0.40 g (1.10 mmol) of **C-5** were added in a single portion. The reaction mixture was then stirred for 8 h at 65 °C. After cooling it to ambient temperature, all volatiles were removed in vacuo. The remaining solid was purified by column chromatography (silica, column size 3 × 10 cm) using a 10/1 (*v*/*v*) *n*-hexane/diethyl ether mixture to afford **C-9** as purple solid. Yield: 0.07 g (0.10 mmol, 22 %

based on **C-8**). Mp.: 160 °C (decomp.). IR data (KBr, ν/cm^{-1}): 3100 w, 3084 w, 3048 w, 2964 w, 2925 w, 2854 w, 2041 s, 1995 s, 1963 s, 1740 w, 1578 m, 1429 m, 1386 m. ^{1}H NMR ($CDCl_3$, δ): 3.67 (s, 10 H, C_5H_5), 4.07 (m, 2 H, C_5H_4), 4.15 (m, 2 H, C_5H_4), 4.19 (m, 2 H, C_5H_4), 5.06 (m, 2 H, C_5H_4), 5.93 (d, $^3J_{HP}$ = 15.9 Hz, 2 H, C_4H_2P), 7.50–7.54 (m, 1 H, H^p/C_6H_5), 7.58−7.61 (m, 2 H, H^m/C_6H_5), 8.32−8.36 (m, 2 H, H^o/C_6H_5). $^{13}C\{^1H\}$ NMR ($CDCl_3$, δ): 67.7 (s, CH/C_5H_4), 68.0 (bs, CH/C_5H_4), 68.9 (C^i/C_4H_2P), 69.3 (s, CH/C_5H_4), 69.5 (s, C_5H_5), 80.0 (d, $^2J_{CP}$ = 20.0 Hz, C^i/C_5H_4). 83.1 (CH/C_4H_2P). Due to the low solubility of **9**, the signals for the phenyl group and CO carbon atoms could not unequivocally be detected. $^{31}P\{^1H\}$ NMR ($CDCl_3$, δ): 66.1 (s). HRMS (ESI-TOF, *m/z*): calcd for $C_{31}H_{25}Fe_3OPS$: 643.9408, found: 643.9380 $[M]^+$, $C_{30}H_{25}Fe_2PS$: 560.0109, found: 560.0087 $[M]^+$.

Crystal Data for C-9: $C_{33}H_{25}Fe_3O_3PS$, M = 700.11 g·mol^{-1}, orthorhombic, Pca_{21}, λ = 0.71073 Å, a = 20.8201(7) Å, b = 7.3072(2) Å, c = 18.1931(6) Å, V = 2767.84(15) Å^3, Z = 4, ρ_{calcd} = 1.680 Mg·m^{-3}, μ = 1.720 mm^{-1}, T = 106(2) K, Θ range = 2.954-26.000°, reflections collected: 9439, independent: 4765 (R_{int} = 0.0392), R_1 = 0.0348, wR_2 = 0.0650 [I > 2σ(I)].

C5 Acknowledgement

We are grateful to the Fonds der Chemischen Industrie (FCI) for generous financial support. MK and DS thank the FCI for a Ph.D. fellowship.

C6 Supporting Information Available

Figures giving further cyclic voltammograms and squre wave voltammograms, (spectro)electrochemical spectra, and CIF files giving crystallographic data for **C-3b**,**c**, **C-4c**, **C-7** and **C-9**. This material is available free of charge via the Internet at http://pubs.acs.org. Crystallographic data of **C-3b**,**c**, **C-4c**, **C-7** and **C-9** are also available from the Cambridge Crystallographic Database as file numbers CCDC 1406634 (**C-3b**), 1406635 (**C-3c**), 1406636 (**C-4c**), 1406637 (**C-7**) and 1406638 (**C-9**).

C7 Appendix

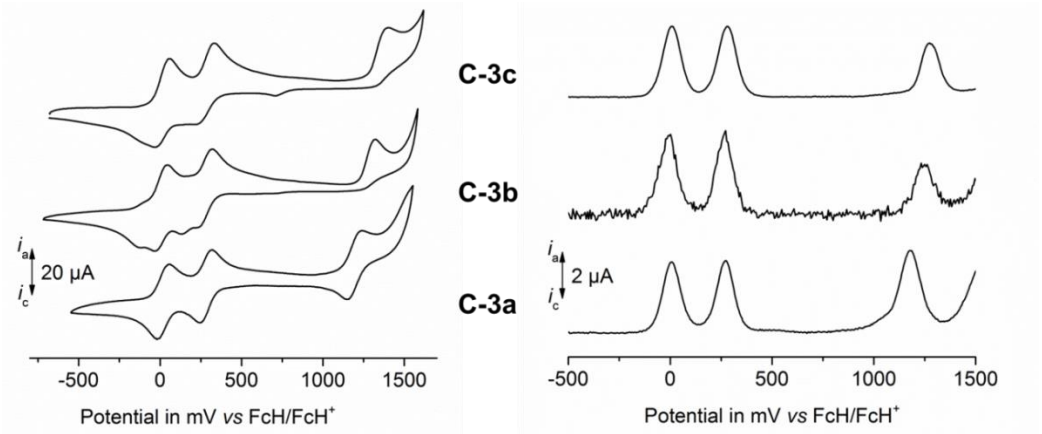

Figure SI7. Left: Cyclic voltammograms of **C-3a–c**; scan rate: 100 $mV \cdot s^{-1}$. Right: square wave voltammograms of **C-3a**–**c** in dichloromethane solutions (1.0 $mmol \cdot L^{-1}$) at 25 °C (potential area: -600 mV – 1500 mV), supporting electrolyte 0.1 $mol \cdot L^{-1}$ $[N^nBu_4][B(C_6F_5)_4]$, working electrode: glassy carbon electrode.

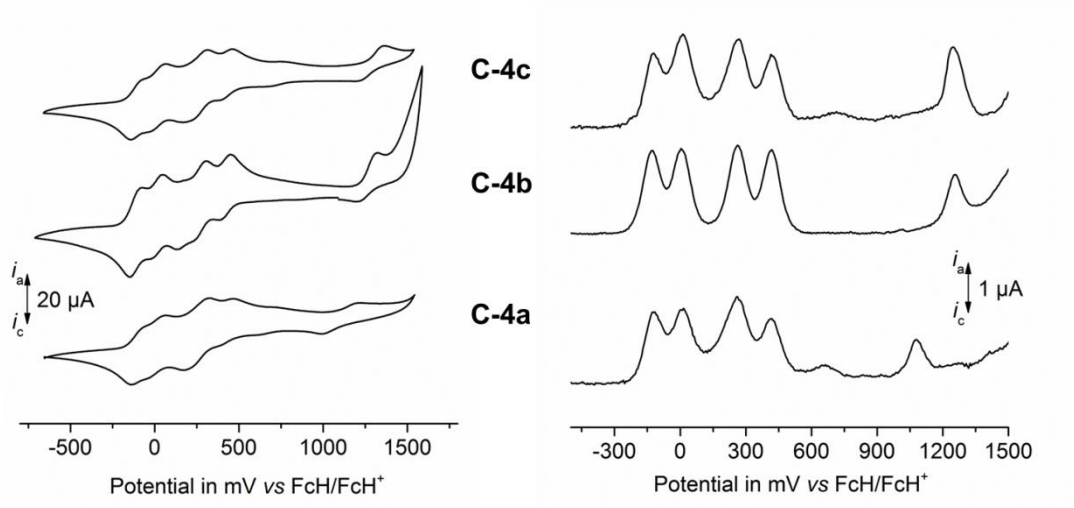

Figure SI8. Left: Cyclic voltammograms (potential area: -600 mV–1600 mV) of **C-4a–c**; scan rate: 100 $mV \cdot s^{-1}$. Right: Square wave voltammograms (potential area: -400 mV – 1500 mV) of **C-4a–c** in dichloromethane solutions (1.0 $mmol \cdot L^{-1}$) at 25 °C, supporting electrolyte 0.1 $mol \cdot L^{-1}$ $[N^nBu_4][B(C_6F_5)_4]$, working electrode: glassy carbon electrode.

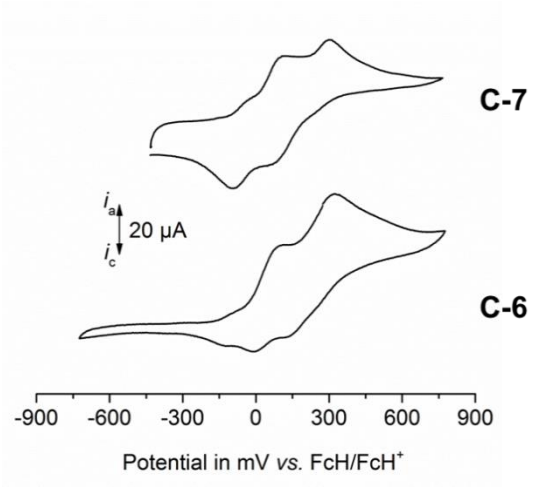

Figure SI9. Cyclic voltammograms of **C-6** and **C-7**; scan rate: 100 mV·s^{-1}; in dichloromethane solutions (1.0 mmol·L^{-1}) at 25 °C, supporting electrolyte 0.1 mol·L^{-1} [N^{n}Bu$_4$][B(C$_6$F$_5$)$_4$], working electrode: glassy carbon electrode.

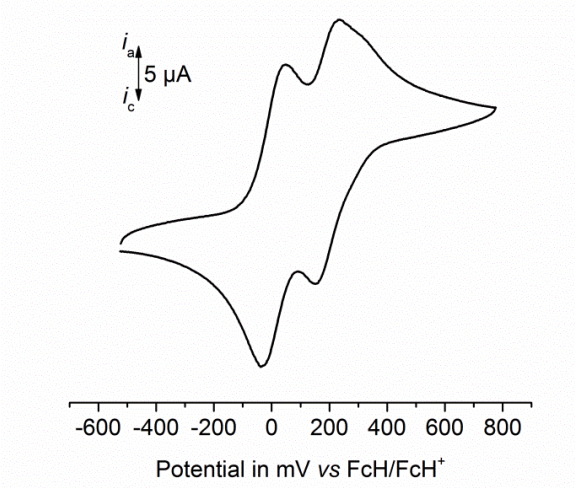

Figure SI10. Cyclic voltammograms of **C-9**; scan rate: 100 mV·s^{-1}; in dichloromethane solutions (1.0 mmol·L^{-1}) at 25 °C, supporting electrolyte 0.1 mol·L^{-1} [N^{n}Bu$_4$][B(C$_6$F$_5$)$_4$], working electrode: glassy carbon electrode.

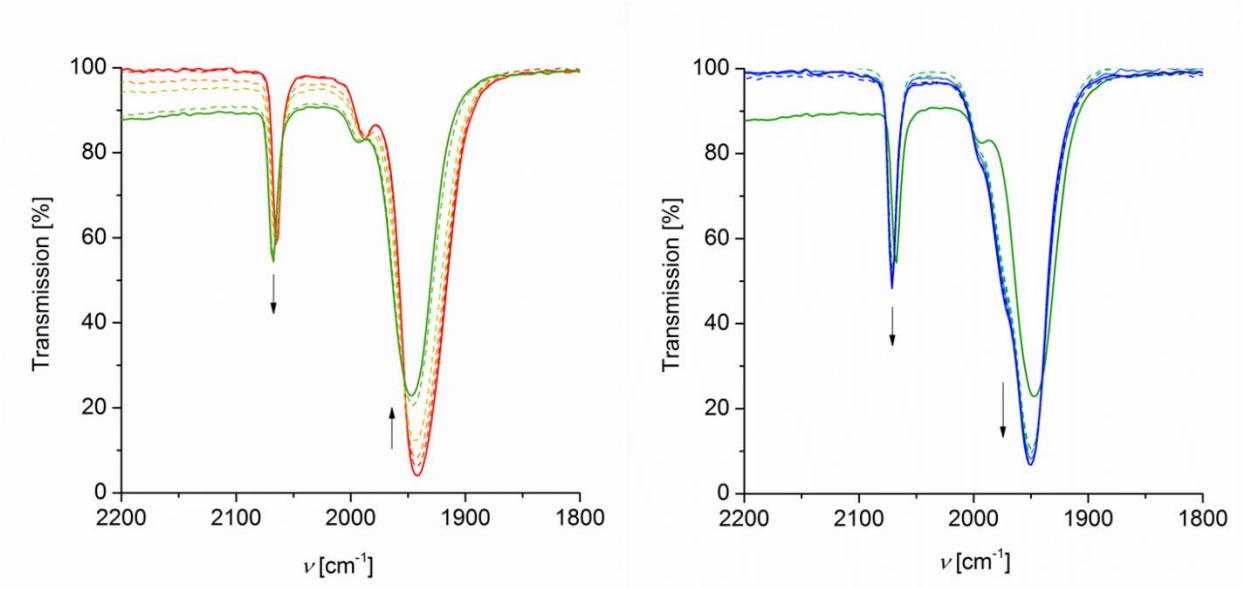

Figure SI16. IR spectra (1800–2200 cm^{-1}) of **C-3a** at 25 °C in dichloromethane (10 mmol L^{-1}) at rising potentials: (left) -200 to 475 mV; (right) 475 to 1200 mV, red: [**C-3a**], green: [**C-3a**]$^{+}$; blue: [**C-3a**]$^{2+}$. All potentials *vs* Ag/AgCl; supporting electrolyte [N^{n}Bu$_4$][B(C$_6$F$_5$)$_4$]; arrows indicate increasing and decreasing absorptions.

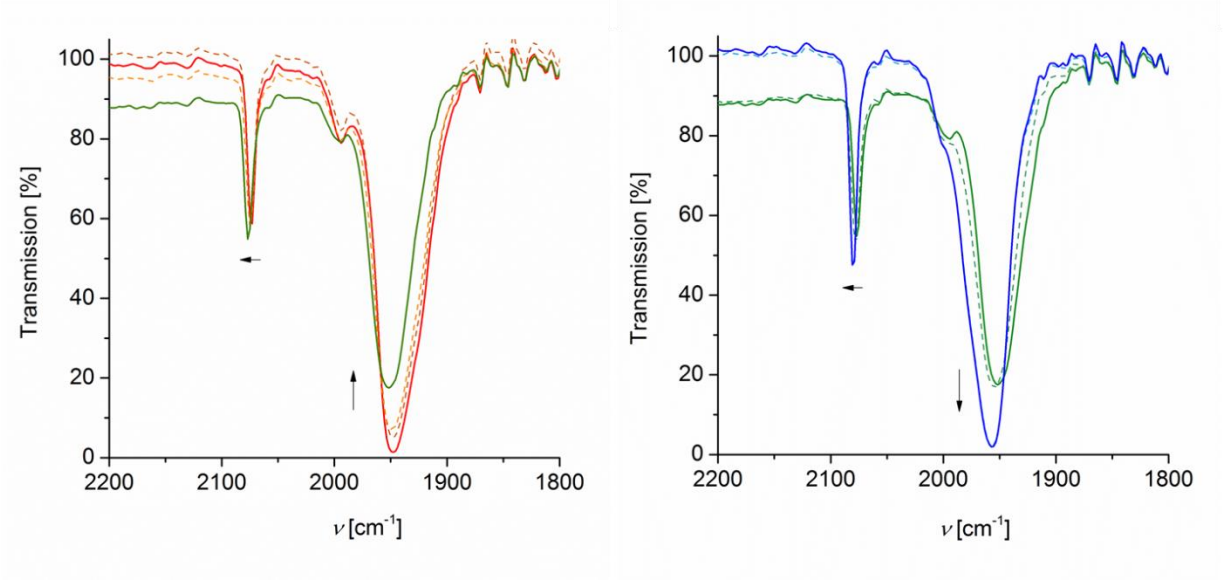

Figure SI17. IR spectra (1800–2200 cm^{-1}) of **C-3b** at 25 °C in dichloromethane (10 mmol L^{-1}) at rising potentials: (left) -200 to 400 mV; (right) 400 to 1200 mV, red: [**C-3b**], green: [**C-3b**]$^{+}$; blue: [**C-3b**]$^{2+}$. All potentials *vs* Ag/AgCl; supporting electrolyte [N^{n}Bu$_4$][B(C$_6$F$_5$)$_4$]; arrows indicate increasing and decreasing absorptions.

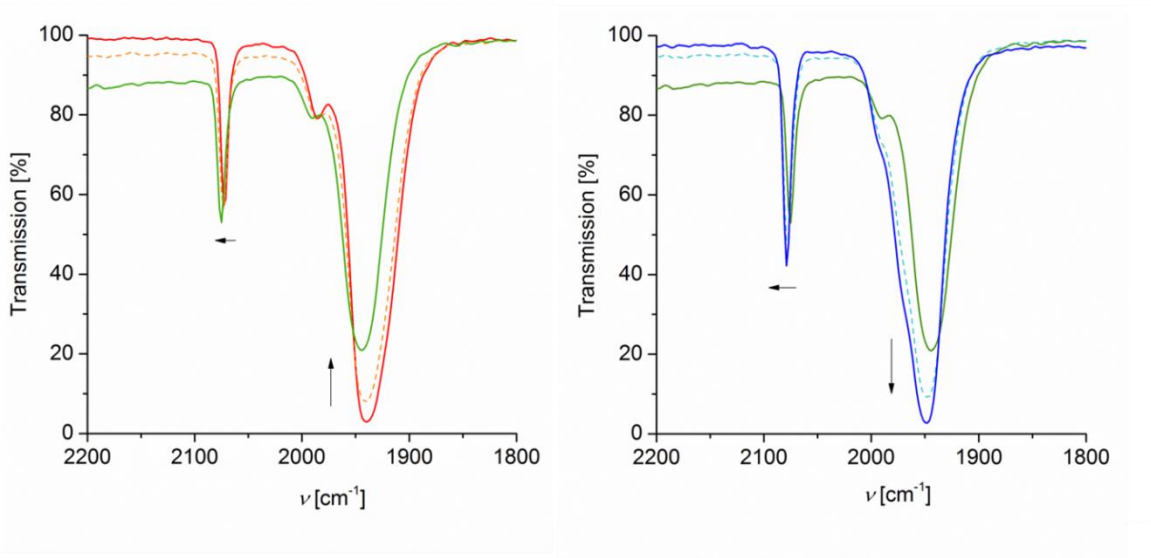

Figure SI18. IR spectra (1800–2200 cm^{-1}) of **C-3c** at 25 °C in dichloromethane (10 mmol L^{-1}) at rising potentials: (left) -200 to 400 mV; (right) 400 to 1200 mV, red: [**C-3c**], green: [**C-3c**]$^{+}$; blue: [**C-3b**]$^{2+}$. All potentials *vs* Ag/AgCl; supporting electrolyte [N^{n}Bu$_4$][B(C$_6$F$_5$)$_4$]; arrows indicate increasing and decreasing absorptions.

C8 References

[C1] F. Mathey, *Mod. Heterocycl. Chem.*; J. Alvarez-Builla, J. J. Vaquero, J. Barluenga, Eds.; Wiley-VCH Verlag GmbH & Co. KGaA: Weinheim, Germany, **2011**, 2071–2116.

[C2] L. D. Quin, *Curr. Org. Chem.* **2006**, *10*, 43–78.

[C3] L. Nyulászi, *J. Phys. Chem.* **1996**, *100*, 6194–6198.

[C4] L. Nyulászi, L. Soós, G. Keglevich, *J. Organomet. Chem.* **1998**, *566*, 29–35.

[C5] G. Keglevich, Z. Böcskei, G. M. Keserü, K. Újszászy, L. D. Quin, *J. Am. Chem. Soc.* **1997**, *119*, 5095–5099.

[C6] L. Nyulászi, *Chem. Rev.* **2001**, *101*, 1229–1246.

[C7] G. Keglevich, *Phosphorus Heterocycles II*; R. K. Bansal, Ed.; Topics in Heterocyclic Chemistry; Springer, Berlin, Heidelberg, **2010**; Vol. 21.

[C8] F. Mathey, *J. Organomet. Chem.* **1975**, *93*, 377–388.

[C9] F. Mathey, *Chem. Rev.* **1988**, *88*, 429–453.

[C10] F. Mathey, F. Mercier, C. Charrier, J. Fischer, A. Mitschler, *J. Am. Chem. Soc.* **1981**, *103*, 4595–4597.

[C11] P. Le Goff, F. Mathey, L. Ricard, *J. Org. Chem*. **1989**, *54*, 4754–4758.

[C12] G. Keglevich, R. Farkas, T. Imre, K. Ludányi, A. Szöllösy, L. Töke, *Heteroat. Chem.* **2003**, *14*, 316–319.

[C13] E. W. Abel, C. Towers, *J. Chem. Soc. Dalton Trans.* **1979**, 814–819.

[C14] F. Mathey, G. Muller, *J. Organomet. Chem.* **1977**, *136*, 241–249.

[C15] C. C. Santini, J. Fischer, F. Mathey, A. Mitschler, *Inorg. Chem.* **1981**, *20*, 2848–2852.

[C16] C. C. Santini, F. Mathey, *J. Organomet. Chem.* **1984**, *266*, 285–293.

[C17] Y. Dienes, M. Eggenstein, T. Neumann, U. Englert, T. Baumgartner, *Dalton Trans.* **2006**, 1424–1433.

[C18] Y. Dienes, M. Eggenstein, T. Kárpáti, T. C. Sutherland, L. Nyulászi, T. Baumgartner, *Chem. Eur. J.* **2008**, *14*, 9878–9889.

[C19] S. Durben, T. Baumgartner, *Inorg. Chem.* **2011**, *50*, 6823–6836.

[C20] Y. Dienes, U. Englert, T. Baumgartner, *Z. Anorg. Allg. Chem.* **2009**, *635*, 238–244.

[C21] H. Chen, W. Delaunay, J. Li, Z. Wang, P. A. Bouit, D. Tondelier, B. Geffroy, F. Mathey, Z. Duan, R. Réau, M. Hissler, M. *Org. Lett.* **2013**, *15*, 330–333.

[C22] Y. Ren, T. Baumgartner, *J. Am. Chem. Soc.* **2011**, *133*, 1328–1340.

[C23] E. H. Braye, W. Hübel, I. Caplier, *J. Am. Chem. Soc.* **1961**, *83*, 4406–4413.

[C24] R. C. Cookson, G. W. A. Fowles, D. K. Jenkins, *J. Chem. Soc.* **1965**, 6406–6409.

[C25] K. W. Muir, F. Y. Pétillon, R. Rumin, P. Schollhammer, J. Talarmin, *J. Organomet. Chem.* **2001**, *622*, 297–301.

[C26] F. Mathey, D. Thavard, *Can. J. Chem.* **1978**, *56*, 1952–1955.

[C27] K. Eichele, R. E. Wasylishen, J. M. Kessler, L. Solujic, J. H. Nelson, *Inorg. Chem.* **1996**, *35*, 3904–3912.

[C28] S. Affandi, J. H. Nelson, N. W. Alcock, O. W. Howarth, E. C. Alyea, G. M. Sheldrick, *Organometallics* **1988**, *7*, 1724–1734.

[C29] A. Hildebrandt, H. Lang, *Organometallics* **2013**, *32*, 5640–5653.

[C30] A. Hildebrandt, D. Schaarschmidt, H. Lang, *Organometallics* **2011**, *30*, 556–563.

[C31] A. Hildebrandt, D. Schaarschmidt, R. Claus, H. Lang, *Inorg. Chem.* **2011**, *50*, 10623–10632.

[C32] A. Hildebrandt, H. Lang, *Dalton Trans.* **2011**, *40*, 11831–11837.

[C33] D. Miesel, A. Hildebrandt, M. Korb, P. J. Low, H. Lang, *Organometallics* **2013**, *32*, 2993–3002.

[C34] U. Pfaff, A. Hildebrandt, D. Schaarschmidt, T. Rüffer, P. J. Low, H. Lang, *Organometallics* **2013**, *32*, 6106–6117.

[C35] S. W. Lehrich, A. Hildebrandt, T. Rüffer, M. Korb, P. J. Low, H. Lang, *Organometallics* **2014**, *33*, 4836–4845.

[C36] J. M. Speck, R. Claus, A. Hildebrandt, T. Rüffer, E. Erasmus, L. van As, J. C. Swarts, H. Lang, *Organometallics* **2012**, *31*, 6373–6380.

[C37] K. Kaleta, F. Strehler, A. Hildebrandt, T. Beweries, P. Arndt, T. Rüffer, A. Spannenberg, H. Lang, U. Rosenthal, *Chem. Eur. J.* **2012**, *18*, 12672–12680.

[C38] K. Kaleta, A. Hildebrandt, F. Strehler, P. Arndt, H. Jiao, A. Spannenberg, H. Lang, U. Rosenthal, *Angew. Chem.* **2011**, *123*, 11444–11448. *Angew. Chem. Int. Ed.* **2011**, *50*, 11248-11252.

[C39] U. Pfaff, A. Hildebrandt, D. Schaarschmidt, T. Hahn, S. Liebing, J. Kortus, H. Lang, *Organometallics* **2012**, *31*, 6761–6771.

[C40] U. Pfaff, A. Hildebrandt, M. Korb, H. Lang, *Polyhedron* **2015**, *86*, 2–9.

[C41] A. Hildebrandt, U. Pfaff, H. Lang, *Rev. Inorg. Chem.* **2011**, *31*, 111–141.

[C42] A. Hildebrandt, T. Rüffer, E. Erasmus, J. C. Swarts, H. Lang, *Organometallics* **2010**, *29*, 4900–4905.

[C43] S. W. Lehrich, A. Hildebrandt, M. Korb, H. Lang, *J. Organomet. Chem.* **2015**, *792*, 37–45.

[C44] U. Pfaff, G. Filipczyk, A. Hildebrandt, M. Korb, H. Lang, *Dalton Trans.* **2014**, *43*, 16310–16321.

[C45] H. Lang, G. Mohr, O. Scheidsteger, G. Huttner, *Chem. Ber.* **1985**, *118*, 574–596.

[C46] W. Strohmeier, F. Müller, *Chem. Ber.* **1967**, *100*, 2812–2821.

[C47] W. Strohmeier, K. Gerlach, *Chem. Ber.* **1961**, *94*, 398–406.

[C48] R. B. King, N. D. Sadanani, *Inorg. Chem.* **1985**, *24*, 3136–3139.

[C49] J. Lach, C.-Y. Guo, M. K. Kindermann, P. G. Jones, J. Heinicke, *Eur. J. Org. Chem.* **2010**, 1176–1186.

[C50] Z. Özer, S. Özkar, *Phosphorus, Sulfur, and Silicon* **1992**, *70*, 339–349.

[C51] G. M. Bodner, M. P. May, L. E. McKinney, *Inorg. Chem.* **1980**, *19*, 1951–1958.

[C52] R. K. Harris, *Can. J. Chem.* **1964**, *42*, 2275–2281.

[C53] H. G. Metzinger, *Org. Magn. Reson.* **1971**, *3*, 485–494.

[C54] R. Mathieu, M. Lenzi, R. Poilblanc, *Inorg. Chem.* **1970**, *9*, 2030–2034.

[C55] M. S. Davies, G. W. Allen, M. J. Aroney, T. W. Hambley, R. K. Pierens, *J. Mol. Struct.* **1994**, *326*, 81–91.

[C56] H. Schumann, O. Stelzer, U. Niederreuther, *J. Organomet. Chem.* **1969**, *16*, P64–P66.

[C57] G. Frenking, K. Wichmann, N. Fröhlich, J. Grobe, W. Golla, D. Le Van, B. Krebs, M. Läge, *Organometallics* **2002**, *21*, 2921–2930.

[C58] M. M. Hossain, H.-M. Lin, S.-G. Shyu, *Eur. J. Inorg. Chem.* **2001**, 2655–2659.

[C59] W. E. Geiger, F. Barrière, *Acc. Chem.Res.* **2010**, *43*, 1030–1039.

[C60] G. Gritzner, J. Kuta, *Pure Appl. Chem.* **1984**, *56*, 461–466.

[C61] E. B. Milosavljevic, L. Solujic, S. Affandi, J. H. Nelson, *Organometallics* **1988**, *7*, 1735–1740.

[C62] M. B. Robin, P. Day, *Adv. Inorg. Chem. Radiochem.* **1967**, *10*, 247–422.

[C63] R. F. Winter, *Organometallics* **2014**, *33*, 4517–4536.

[C64] M. Krejčik, M. Daněk, F. Hartl, *Electroanal. Chem.* **1991**, *317*, 179–187.

[C65] N. S. Hush, *Electrochim. Acta* **1968**, *13*, 1005–1023.

[C66] D. Miesel, A. Hildebrandt, M. Korb, D. A. Wild, P. J. Low, H. Lang, *Chem. Eur. J.* **2015,** *21*, 11545–11559.

[C67] A. S. Goldman, K. Krogh-Jespersen, *J. Am. Chem. Soc.* **1996**, *118*, 12159–12166.

[C68] A. Nafady, W. E. Geiger, *Organometallics* **2008**, *27*, 5624–5631.

[C69] G. M. Sheldrick, *Acta Crystallogr., Sect. A* **1990**, *46*, 467–473.

[C70] G. M. Sheldrick, SHELXL-97. *Progr. Cryst. Struct. Refinement* **1997**, University of Göttingen.

[C71] Although these results are outside the range viewed as establishing analytical purity, they are provided to illustrate the best values obtained to date.

D Electronic Interactions in Gold(I) Complexes of 2,5-Diferrocenyl-1-phenyl-1*H*-phosphole

Dominique Miesel, Alexander Hildebrandt, Marcus Korb and Heinrich Lang*

Veröffentlicht in *Journal of Organometallic Chemistry*, **2015**, *803*, 104–110.

Anders als zu den in Kapitel C verwendeten Metall(0)-Komplexfragmenten zur Koordination des freien Elektronenpaares des Phosphoratoms sollte eine Koordination des freien Elektronenpaars vom P-Atom an Metall(I)-Komplexe einen deutlich größeren Einfluss auf die Elektronendichte des Phospholringes haben. Dazu erfolgte die Synthese einer Reihe von Gold(I)-Komplexen des 2,5-Diferrocenyl-1-phenyl-1*H*-phosphols und deren (spektro)-elektrochemische Charakterisierung.

Die in Kapitel D präsentierten Ergebnisse wurden selbstständig unter Anleitung von Prof. Dr. Heinrich Lang und Dr. Alexander Hildebrandt erstellt. Die kristallografischen Messungen erfolgten von Marcus Korb.

D1 Introduction

In recent years, molecules bearing two or more redox-active metal fragments connected *via* a π-conjugated bridging unit were intensively studied as they can be applied in electron transfer studies and therefore, can be regarded as models for molecular wires.[D1–D6] Ferrocenyl units are well suited as redox-active termini due to the stability of the Fc/Fc^+ redox couple and their straightforward modification possibilities.[D2] Recently, we have shown that π-conjugated connecting units are well suited to facilitate electron transfer between mixed-valent redox-active termini, while also granting the possibility to modify their electronic properties.[D4,D7–D18] In this respect, modifications of the heteroatom, the backbone of the heterocycle, or the ferrocenyl unit can influence the metal-metal interactions of the ferrocenyl moieties bonded to the heterocycle.[D14,D19]

In contrast to analogous heterocycles, the chemistry of phospholes has for long not been in the focus of research. However, in recent years phospholes have attracted more interest especially due to the straightforward modification possibilities at the phosphorus lone pair,

and it could be shown that the electronic nature of the π-system could easily be modified.[D20–D34] Chemical functionalization of the phosphorus atom, such as oxidation from P^{III} to P^{V} or complexations, make these molecules suitable for fine-tuning of electronic properties in the design of new materials.[D29,D33,D35–D39] Gold phosphole complexes, for example, have shown to exhibit interesting photophysical properties.[D40–D45]

In earlier studies we have shown that the strength of the electronic interaction of the Fc/Fc^{+} termini *via* the heterocyclic core in 2,5-diferrocenyl-1-phenyl-1*H*-phosphole is decreased when compared to the pyrrole analogues.[D46] An increase of the steric demand of the substituent bonded to phosphorus led to an increased metal-metal interaction *via* the phosphole motif.[D47]

In addition, the complexation of the phosphorus atom to a M(0) fragment in 2,5-diferrocenyl-1-phenyl-1*H*-phosphole metal carbonyl complexes barely influences the metal-metal interactions.[D48] In contrast, cationic metal fragments such as Au(I) are expected to have a greater influence on the electronics of the phosphole unit as a result of their greater net-electronegativity.

Herein, we report on the synthesis of gold(I) complexes of 2,5-diferrocenyl-1-phenyl-1*H*-phosphole. UV/Vis-NIR spectroelectrochemistry was carried out to examine the influence of the metal(I) center on the electronic interaction of the Fc/Fc^{+} groups.

D2 Results and Discussion

Synthesis and characterization

Chloro(2,5-diferrocenyl-1-phenyl-1*H*-phosphole) gold (**D-3**) was synthesized by the reaction of 2,5-diferrocenyl-1-phenyl-1*H*-phosphole (**D-1**)[D46] with chloro(thiobis[methane]) gold (**D-2**). The reaction of **D-2** with ethynylferrocene or phenylacetylene using catalytical amounts of [CuI] and one equiv. of **D-1** in a mixture of tetrahydrofuran/diisopropylamine (ratio 1:1, *v*/*v*) resulted in the formation of arylethynyl-(2,5-diferrocenyl-1-phenyl-1*H*-phosphole) gold **D-4a**,**b** (aryl: **a** = ferrocenyl; **b** = phenyl) (Scheme D1). Using the same reaction procedure but applying 0.5 equiv. of 1,4-diethynylbenzene produced [μ-(1,4-phenylenedi-2,1-ethynediyl)]bis(2,5-diferrocenyl-1-phenyl-1*H*-phosphole) digold (**D-5**).

Compounds **D-3**, **D-4a**,**b** and **D-5** are stable towards air and moisture in the solid state and in solution. They were characterized by elemental analysis, IR and NMR (^{1}H, $^{13}C\{^{1}H\}$, $^{31}P\{^{1}H\}$) spectroscopy, and ESI-TOF mass spectrometry. The redox behavior was investigated by cyclic (CV) and square wave voltammetry (SWV) and the

spectroelectrochemical behavior was studied by *in situ* UV/Vis-NIR measurements. In addition, the structure of **D-4a** in the solid state was determined by single-crystal X-ray diffraction analysis.

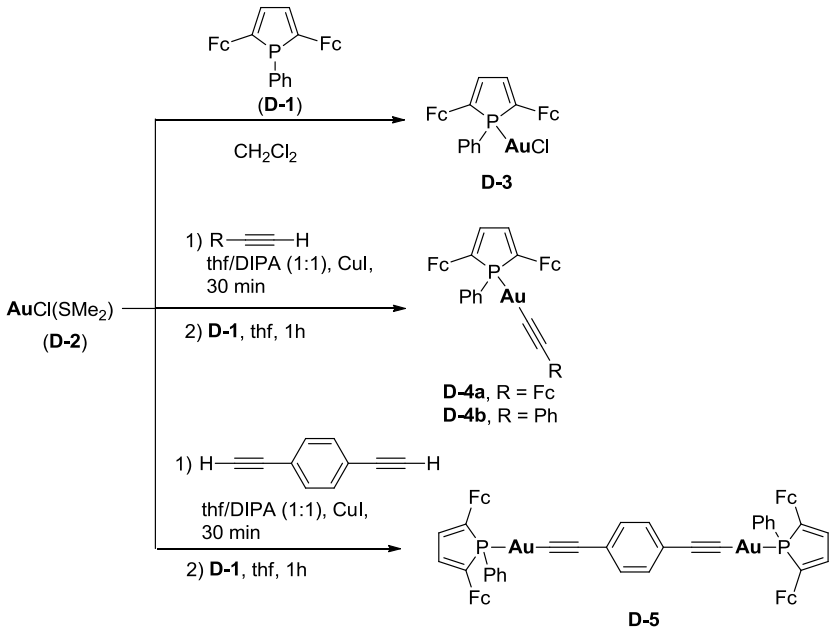

Scheme D1. Synthesis of gold complexes **D-3**, **D-4a**,**b** and **D-5**. Fc = Fe(η^5-C_5H_5)(η^5-C_5H_4); thf = tetrahydrofuran, DIPA = diisopropylamine.

In the ^{1}H NMR spectra of **D-3**, **D-4a**, **D-4b** and **D-5** one singlet for the C_5H_5 protons and four multiplets between 4.1 ppm and 4.6 ppm for the C_5H_4 protons were observed of the ferrocenyl units. In **D-4a**, one additional singlet and two multiplets were found for the Fc/FcC≡C group (Experimental Section). The signals for the ferrocenyl moieties in **D-3**, **D-4a**, **D-4b** and **D-5** are slightly shifted to lower field when compared to **D-1**.[D46] For the phosphole protons a doublet at approximately 6.9 ppm with a $^3J_{PH}$ coupling constant of 27 Hz is characteristic. The complexation of the phosphorus atom to the gold fragment leads to an increase of the coupling constant (*i. e.*; **D-1**, $^3J_{PH}$ = 11.4 Hz[D46]; **D-3**, $^3J_{PH}$ = 29.5 Hz). The signals for the C_6H_5 groups appear, as multiplets between 7.4 ppm and 7.9 ppm and the C_6H_4 protons in **D-5** as singlet at 7.4 ppm.

The C≡C carbon atoms are found between 101.8 and 103.4 ppm in the $^{13}C\{^1H\}$ NMR spectra.[D49–D51] Due to the low solubility of **D-5** no $^{13}C\{^1H\}$ NMR spectrum could be obtained. The coordination of the phosphorus atom in **D-3**, **D-4a** and **D-4b** to the gold moiety leads to a shift of the $^cC_4H_2P$ *ipso*-carbon atom to higher field (≈ 140 ppm), which is accompanied by a significant increase $^1J_{CP}$ (≈ 50 Hz) (Experimental Section).

Phosphorus coordination to Au(I) results in a shift of the phosphorus signal from 5.1 ppm[D46] in **D-1** to lower field (**D-3**, 30.4 ppm; **D-4a**, 43.2 ppm; **D-4b**, 43.1 ppm; **D-5**, 43.1 ppm) in the $^{31}P\{^{1}H\}$ spectra.

The IR spectra of **D-4a**,**b** and **D-5** are characterized by $\nu_{C\equiv C}$ absorptions at 2107 cm^{-1} (**D-4a**,**b**) and 2117 cm^{-1} (**D-5**), respectively.

The molecular structure of **D-4a** in the solid state was determined by single-crystal X-ray diffraction analysis. The ORTEP diagram of this compound with selected bond lengths (Å), bond angles (°) and torsion angles (°) is shown in Figure D1.

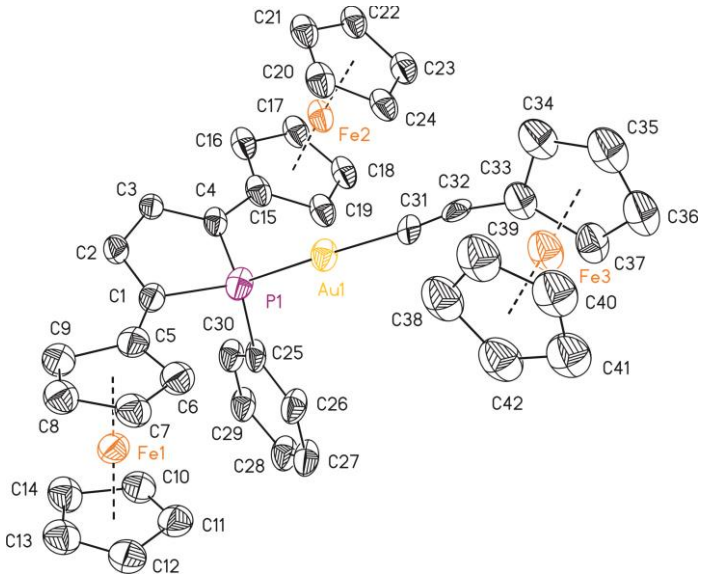

Figure D1. ORTEP diagram (30 % probability level) of the molecular structure of **D-4a** with the atom numbering scheme. All hydrogen atoms have been omitted for clarity. Selected bond distances (Å), angles (°), and torsion angles (°): P1–C1 = 1.86(2), C1–C2 = 1.36(3), C2–C3 = 1.47(3), C3–C4 = 1.35(3), C4–P1 = 1.76(2), P1–C25 = 1.84(2), P1–Au1 = 2.262(6), Au1–C31 = 2.091(18), C31–C32 = 1.112(16), D1–Fe1 = 1.636(4), D2–Fe1 = 1.645(4), D3–Fe2 = 1.635(4), D4–Fe2 = 1.642(4), D5–Fe3 = 1.653(4), D6–Fe3 = 1.620(4), D1–Fe1–D2 = 177.8(3), D3–Fe2–D4 = 176.9(3), D5–Fe3–D6 = 179.0(3), C1−P1−C4 = 94.7(10), P1–Au1–C31 = 178.4(5), Au1–C31–C32 = 175(2), Au1–P1–C1 = 117.4(7), Au1–P1–C4 = 115.7(8), C1−P1−C25 = 105.1(10), C4−P1−C25 = 105.5(11), C5–D1–D2–C10 = 5.6(17), C15–D3–D4–C20 = 1.1(17), C33–D5–D6–C38 = -22.1(19). D1 = centroid of C5–C9; D2 = centroid of C10–C14, D3 = centroid of C15–C19; D4 = centroid of C20–C24, D5 = centroid of C33–C37, D6 = centroid of C38–C42.

Compound **D-4a** crystallizes in the monoclinic space group $P2_1/c$ with one crystallographically independent molecule in the asymmetric unit. As expected, the gold atom adopts a linear geometry (P1–Au1–C31 = 178.4(5) °, Au1–C31–C32 = 175(2) °). The bond angles and distances of the gold(I) alkynyl fragment resembles those found for similar complexes.[D51,D52] The phosphorus atom exhibits a typical tetrahedral environment with bond angles between 105 ° and 117 °, the phosphole ring is not planar (rms deviation 0.0120, with

phosphorus out of the C_4H_2 plane by -0.11(3) Å). The ferrocenyl units are oriented antiparallelly and almost co-planar to the heterocyclic core (24(4) ° for Fe1, -1(4) ° for Fe2). The crystal packing of **D-4a** is stabilized by strong intra- (Figure SI1, green) and intermolecular (Figure SI1 blue) *T*-shaped π-π interactions.[D53] The intramolecular stabilization occurs between the C_5H_5 cyclopentadienyl ligands (of Fe1) and the phenyl ring. Dimeric structures are formed between the Fe2 and the Fe3 C_5H_4 cycles. These dimers are connected over the C_5H_4 cycle of Fe1 and the unsubstituted cyclopentadienyl of the ethynyl ferrocenyl substituent (Figure SI1), resulting in a two-dimensional network plane spreading along the *b*-axis [010] (Figure SI2, top) and along [201] (Figure SI2, bottom).

Electrochemistry and Spectroelectrochemistry

The electrochemical properties of complexes **D-3**, **D-4a**,**b** and **D-5** were investigated by cyclic voltammetry, square wave voltammetry and spectroelectrochemistry (UV/Vis-NIR). An anhydrous dichloromethane solution containing 0.1 mol·L^{-1} [N^{n}Bu$_4$][B(C$_6$F$_5$)$_4$] was used as supporting electrolyte.[D54] The voltammetry measurements were performed at 25 °C. All potentials are referenced to the FcH/FcH$^+$ redox couple.[D55] The data of the cyclic voltammetric experiments at a scan rate of 100 mV·s^{-1} are summarized in Table D1 and the cyclic voltammograms of **D-3**, **D-4a**,**b** and **D-5** are depicted in Figure D2.

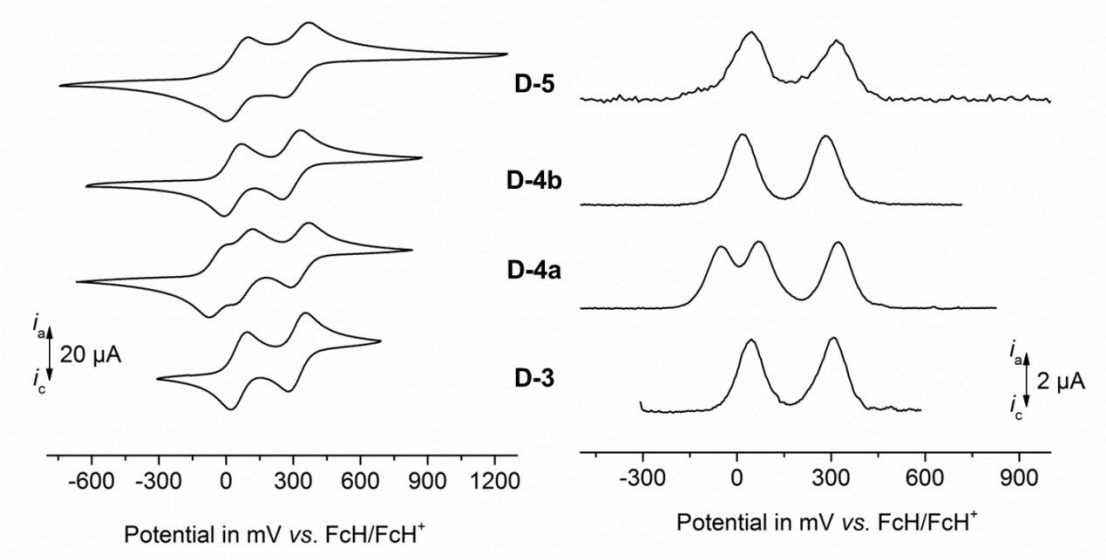

Figure D2. Left: Cyclic voltammograms of **D-3**, **D-4a**,**b** and **D-5**; scan rate: 100 mV·s^{-1}; right: square wave voltammograms of **D-3**, **D-4a**,**b** and **D-5**; in dichloromethane solutions (1.0 mmol·L^{-1}) at 25 °C, supporting electrolyte 0.1 mol·L^{-1} [N^{n}Bu$_4$][B(C$_6$F$_5$)$_4$], working electrode: glassy carbon electrode (surface area 0.031 cm²).

In the cyclic voltammograms of **D-3** and **D-4b** two separated redox events for the ferrocenyl units in 2 and 5 position were observed with a redox separation of $\Delta E^{\circ\prime}$= 260 mV. The coordination of the phosphorus atom to gold resulted in a slight decrease of the redox splitting when compared to **D-1** ($\Delta E^{\circ\prime}$ = 280 mV[D46]). The additional ferrocenyl group of the ethynylferrocenyl unit in **D-4a** leads to a third redox event in the cyclic voltammogram (Figure D2). A comparison with **D-3** allows the assignment of the first event to the ethynylferrocenyl unit ($E_1^{\circ\prime}$ = -35 mV) followed by oxidation of the ferrocenyl groups in 2 and 5 position of the phosphole species with $\Delta E^{\circ\prime}$ = 250 mV.

In the cyclic voltammogram of **D-5** two redox processes with $\Delta E^{\circ\prime}$ values of 265 mV for the four ferrocenyl units were found. Thereby, high ΔE_p values of 92 mV and 112 mV were observed indicating that two redox processes take place in a close potential area. Therefore, the $\Delta E^{\circ\prime}$ values for the separation between the 1st and 2nd process and the 3rd and 4th process were determined according to Richardson and Taube[D56] giving redox separations for both processes of approximately 65 mV.

Table D1. Cyclic voltammetry data of compounds D-3, D-4a,b and D-5.[a]

Compd.	$E_1^{\circ\prime}$ in mV[b] (ΔE_p in mV)[c]	$E_2^{\circ\prime}$ in mV[b] (ΔE_p in mV)[c]	$E_3^{\circ\prime}$ in mV[b] (ΔE_p in mV)[c]	$\Delta E^{\circ\prime}$ in mV[d]
D-3	55 (74)	315 (74)	-	260
D-4a	-35 (83)	75 (79)	325 (77)	130/250
D-4b	30 (72)	290 (80)	-	260
D-5	50 (92)	315 (112)	-	265

[a]Potentials *vs* FcH/FcH^+, scan rate 100 $mV \cdot s^{-1}$ at a glassy carbon electrode of **D-3**, **D-4a**,**b** and **D-5**, dichloromethane, 25 °C. [b]$E^{\circ\prime}$ = Formal potential. [c]ΔE_p = Difference between the oxidation and the reduction potential. [d]$\Delta E^{\circ\prime}$ = Potential difference between the two ferrocenyl-related redox processes.

The redox separations in **D-3**, **D-4a**,**b** and **D-5** resemble those for similar ferrocenyl substituted heterocycles such as 2,5-diferrocenyl thiophene ($\Delta E^{\circ\prime}$ = 260 mV) and 2,5-diferrocenyl furan ($\Delta E^{\circ\prime}$ = 290 mV).[D14] The redox separations of the ferrocenyls can be an indication for a moderate electron transfer between the Fc/Fc^+ units, however, other factors may also influence $\Delta E^{\circ\prime}$.[D57] Thus, spectroelectrochemical measurements were performed to quantify the strength of the electronic interactions.

The UV/Vis-NIR spectroelectrochemical studies of **D-3**, **D-4a**,**b** and **D-5** (2.0 $mmol \cdot L^{-1}$ dichloromethane solutions, 0.1 $mol \cdot L^{-1}$ of $[N^nBu_4][B(C_6F_5)_4]$ as supporting electrolyte) were performed in an OTTLE (= Optically Transparent Thin-Layer Electrochemical) cell.[D58]

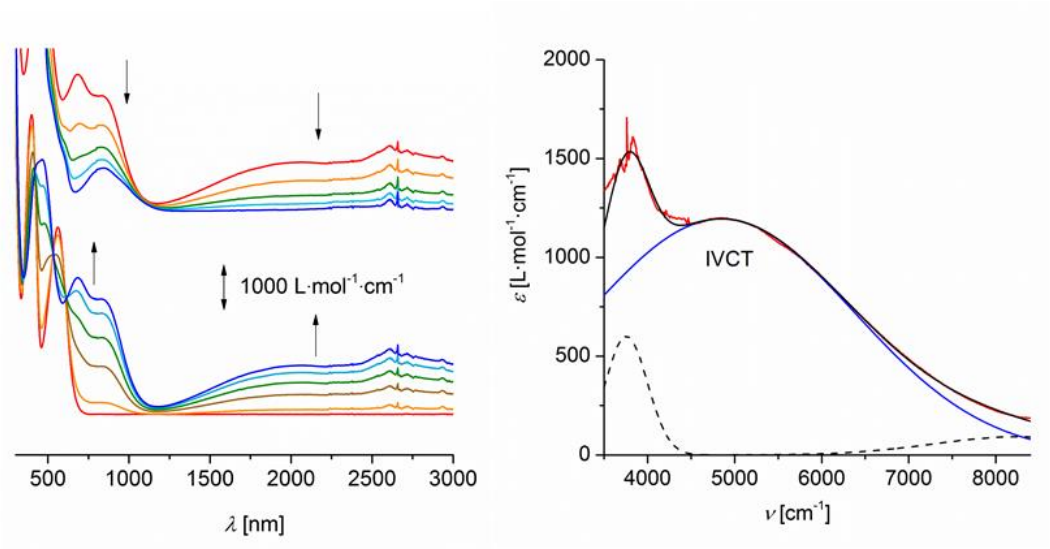

Figure D3. Left: UV/Vis-NIR spectra of **D-4b** at 25 °C in dichloromethane (2.0 mmol·L^{-1}) at rising potentials (bottom: -200 to 500 mV; top: 500 to 800 mV *vs* Ag/AgCl); supporting electrolyte [N^{n}Bu$_4$][B(C$_6$F$_5$)$_4$]; arrows indicate increasing and decreasing absorptions. Right: Deconvolution of the NIR absorptions of [**D-4b**]$^+$ using three Gaussian shaped bands determined by spectroelectrochemistry in an OTTLE cell.

Compounds **D-3**, **D-4a**,**b** and **D-5** were oxidized by a stepwise increase of the potentials (step width: 25, 50, 100 mV). During the measurements, oxidation of neutral **D-3**, **D-4a**, **D-4b** and **D-5** to the mixed-valent species [**D-3**]$^+$, [**D-4a**]$^{2+}$, [**D-4b**]$^+$ and [**D-5**]$^{2+}$, and finally to the fully oxidized compounds [**D-3**]$^{2+}$, [**D-4a**]$^{3+}$, [**D-4b**]$^{2+}$ and [**D-5**]$^{4+}$ was performed. To prove the reversibility, each compound was reduced at -200 mV after full oxidation and the observed UV/Vis-NIR spectra were identical to those of the starting compounds. The UV/Vis-NIR spectra of **D-3**, **D-4a**,**b** and **D-5** are depicted in Figures SI3 (**D-3**), SI4 (**D-4a**), D3 (**D-4b**) and SI5 (**D-5**).

While oxidizing the neutral compounds to the mixed-valent species, a broad band between 1000 and 3000 nm developed. This absorption decreases with the formation of the fully oxidized species (above 500 mV *vs* Ag/AgCl). This behavior is typical for intervalence charge transfer (IVCT) processes.[D6,D59] The experimental spectra were deconvoluted into three Gaussian-shaped bands to obtain the characteristics for the IVCT component. These three absorptions represent a LF (ligand field)[D7] transition, a band simulating the edge to the further progress of the higher energy absorptions and the IVCT band. The sum of the three bands fits almost exactly with the experimental curve. Therefore, the full-width-at-halfheight

$\Delta\nu_{1/2}$, the intensitiy ε_{max} and the center ν_{max} of the IVCT component could be determined. The data for the IVCT bands of **D-3**, **D-4a**,**b** and **D-5** are summarized in Table D2.

Table D2. NIR data of the IVCT absorptions of $[\mathbf{D\text{-}3}]^+$, $[\mathbf{D\text{-}4a}]^{2+}$, $[\mathbf{D\text{-}4b}]^+$ and $[\mathbf{D\text{-}5}]^{2+}$.[a]

Compd.	ν_{max} (cm^{-1}) (ε_{max} ($L\cdot mol^{-1}\cdot cm^{-1}$))	$\Delta\nu_{1/2}$ (cm^{-1})	$(\Delta\nu_{1/2})_{theo}$[b] (cm^{-1})
$[\mathbf{D\text{-}3}]^+$	4800 (1300)	3750	3331
$[\mathbf{D\text{-}4a}]^{2+}$	4800 (1100)	3650	3327
$[\mathbf{D\text{-}4b}]^+$	4850 (1200)	3600	3346
$[\mathbf{D\text{-}5}]^{2+}$	4900 (2700)	3200	3368

[a] In anhydrous dichloromethane containing 0.1 $mol\cdot L^{-1}$ of $[N^nBu_4][B(C_6F_5)_4]$ as supporting electrolyte at 25 °C. [b] Values calculated as $(\Delta\nu_{1/2})_{theo} = (2310\cdot\nu_{max})^{1/2}$ according to the Hush relationships for weakly coupled systems.[D60]

Gold complexes **D-3**, **D-4a** and **D-4b** exhibit IVCT absorptions of similar characteristics ($\nu_{max} \approx 4800\ cm^{-1}$, $\varepsilon_{max} \approx 1200\ L\cdot mol^{-1}\cdot cm^{-1}$, $\Delta\nu_{1/2} \approx 3650\ cm^{-1}$) indicating similar metal-metal interactions in all three compounds.

Earlier studies covering electron transfer investigations in metal(0) carbonyl complexes of 2,5-diferrocenyl-1-phenyl-1*H*-phosphole (**D-1**) reveal that the electronic communication of the ferrocenyls in 2 and 5 position is similar to those in **D-1**.[D48] Hence, the metal(0) fragment does not significantly influence the electron density of the phosphole backbone. In contrast, for **D-3**, **D-4a** and **D-4b** the intensity of the IVCT band decreases and the full-width-at-half-height increases, when compared to uncoordinated phosphole **D-1** ($\varepsilon_{max} = 1750\ L\cdot mol^{-1}\cdot cm^{-1}$, $\Delta\nu_{1/2} = 3050\ cm^{-1}$) indicating a decreased metal-metal interaction. Since the group electronegativity of cationic gold(I) is more pronounced than in neutral M(0) carbonyls, coordination of such a fragment leads to a reduced electron density within the phosphole ligand and hence the electronic interaction through this motif is hindered.

In $[\mathbf{D\text{-}5}]^{2+}$ two phosphole units are connected *via* a Au-C≡C-C_6H_4-C≡C-Au bridge, therefore two of the mixed-valent units are present per molecule, which doubles the excitation probability for the IVCT process. Thus, the intensity of the IVCT band is almost twice ($\varepsilon_{max} = 2700\ L\cdot mol^{-1}\cdot cm^{-1}$) as for monophospholes **D-3** and **D-4a**,**b**.

The strength of the electronic interaction in **D-3**, **D-4a** and **D-4b** is similar to those of the chalcogenides 2,5-diferrocenyl-1-phenyl-1*H*-phosphole sulfide and –selenide ($\varepsilon_{max} \approx 1200\ L\cdot mol^{-1}\cdot cm^{-1}$, $\Delta\nu_{1/2} = 4200\ cm^{-1}$) showing that the oxidation of P^{III} to P^V has a similar influence on the electronic interaction of the Fc/Fc^+ termini as the coordination of the

phosphorus atom to Au(I).[D46] The metal-metal interactions are decreased when compared with 2,5-disubstituted pyrroles, *i. e.* 2,5-diferrocenyl-1-methyl-1*H*-pyrrole (ε_{max} = 3145 $L \cdot mol^{-1} \cdot cm^{-1}$).[D14]

D3 Conclusion

Chloro(2,5-diferrocenyl-1-phenyl-1*H*-phosphole) gold (**D-3**) was successfully synthesized by the reaction of 2,5-diferrocenyl-1-phenyl-1*H*-phosphole (**D-1**) with $AuCl(SMe_2)$ (**D-2**). Arylethynyl-(2,5-diferrocenyl-1-phenyl-1*H*-phosphole) gold (**D-4a**, aryl = ferrocenyl; **D-4b**, aryl = phenyl) were prepared *via* a modified reaction procedure according to Vicente *et al*. by reacting **D-2** with ethynylferrocene or ethynylbenzene, [CuI] and one equiv. of **D-1**.[D61] In a similar reaction procedure, 0.5 equiv. of 1,4-diethynylbenzene as alkyne component were reacted with 1 equiv. of **D-1** and 1 equiv. of **D-2** to [μ-(1,4-phenylenedi-2,1-ethynediyl)]-bis(2,5-diferrocenyl-1-phenyl-1*H*-phosphole) digold (**D-5**). Molecule **D-4a** could be characterized structurally by single-crystal X-ray diffraction analysis showing a linear coordination of the gold atom. Cyclic voltammetry measurements of **D-3**, **D-4a** and **D-4b** showed one reversible redox process for each ferrocenyl unit with redox separations $\Delta E^{\circ\prime}$ of approximately 260 mV between the ferrocenyl groups in 2 and 5 position. In the cyclic voltammogram of **D-5** two redox events with large ΔE_p values of 92 and 112 mV for the four ferrocenyls could be observed. Spectroelectrochemical measurements indicated that **D-3**, **D-4a**,**b** and **D-5** exhibit IVCT absorptions with characteristics for electron transfers of moderate strength. The coordination of the phosphorus atom to the gold(I) fragment resulted in a decreased electronic interaction if compared to **D-1**. The IVCT band of **D-5** shows twice the intensity and a slightly decreased full-width-at-half-height value in comparison with **D-3**, **D-4a** and **D-4b**. This is in accordance with the expectation as the complex exhibits two phosphole motifs and the electron transfer excitation has twice the probability. In contrast to the coordination of 2,5-diferrocenyl phosphole to a metal(0) complex fragment such as $M(CO)_n$ (M = Cr, Mo, W, n = 5; M = Fe, n = 4)[D48], gold(I) influences the electronic interaction between the Fc/Fc^+ units. Gold complexes **D-3**, **D-4a**,**b** and **D-5** could be classified as moderately coupled class II systems according to Robin and Day.[D62]

D4 Experimental Section

General data

All reactions were carried out under an argon (5.0) atmosphere using standard Schlenk techniques. Tetrahydrofuran was purified by distillation from sodium/benzophenone ketyl, diisopropylamine was purified by distillation from calcium hydride; *n*-hexane and dichloromethane were obtained from a MBRAUN (MB-SPS 800) solvent drying and purification system (double column solvent filtration, working pressure 0.5 bar). For electrochemistry HPLC grade dichloromethane was purified by distillation from calcium hydride. For column chromatography alumina with a particle size of 90 μm (standard, Merck KGaA) was used.

Instruments

FT IR spectra were recorded with a Nicolet IR 200 spectrometer (Thermo Company). NMR spectra were recorded with a Bruker Avance III 500 spectrometer (500.3 MHz for ^{1}H, 125.7 MHz for ^{13}C{^{1}H} and 202.5 MHz for ^{31}P{^{1}H} spectra). Chemical shifts are reported in δ (parts per million) downfield from tetramethylsilane with the solvent as reference signal (^{1}H NMR: $CDCl_3$, δ = 7.26; ^{13}C{^{1}H} NMR: $CDCl_3$, δ = 77.16; ^{31}P{^{1}H} NMR: standard external rel. 85% H_3PO_4, δ = 0.0; $P(OMe)_3$, δ = 139.0). The melting points were determined using a Gallenkamp MFB 595 010 M melting point apparatus. Elemental analyses were performed with a Thermo FlashAE 1112 instrument. High-resolution mass spectra were recorded with a Bruker Daltonik micrOTOF-QII spectrometer.

Electrochemistry

Electrochemical measurements of **D-3**, **D-4a**,**b** and **D-5** (1.0 mmol·L^{-1} [N^{n}Bu$_4$][B(C$_6$F$_5$)$_4$] as supporting electrolyte) in anhydrous dichloromethane were performed in a dried, argon purged electrochemical cell at 25 °C with a Radiometer Voltalab PGZ 100 electrochemical workstation interfaced with a personal computer. For the measurements a three electrode cell containing a Pt auxiliary electrode, a glassy carbon working electrode (surface area 0.031 cm²) and an Ag/Ag^+ (0.01 mmol·L^{-1} [$AgNO_3$]) reference electrode fixed on a Luggin capillary was used. The working electrode was pretreated by polishing on a Buehler microcloth first with a 1 micron and then with a ¼ micron diamond paste. The reference electrode was constructed from a silver wire inserted in a 0.01 mmol·L^{-1} [$AgNO_3$] and a 0.1 mol·L^{-1} [N^{n}Bu$_4$][B(C$_6$F$_5$)$_4$] acetonitrile solution in a Luggin capillary with a Vycor tip. This Luggin capillary was inserted in a second Luggin capillary containing a 0.1 mol·L^{-1}

$[N^nBu_4][B(C_6F_5)_4]$ dichloromethane solution and a Vycor tip. Experiments under the same conditions showed that all reduction and oxidation potentials were reproducible within ±5 mV. Experimental potentials were referenced against an Ag/Ag^+ reference electrode but the presented results are referenced against ferrocene as an internal standard as required by IUPAC.[D55] To achieve this, each experiment was repeated in the presence of 1 $mmol \cdot L^{-1}$ decamethylferrocene (Fc*). Data were processed on a Microsoft Excel worksheet to set the formal reduction potentials of the FcH/FcH^+ couple to 0.0 V. Under our conditions the Fc^*/Fc^{*+} redox couple was at -619 mV *vs* FcH/FcH^+, ΔE_p = 60 mV, while the FcH/FcH^+ couple itself was at 220 mV *vs* Ag/Ag^+, ΔE_p = 61 mV.[D63]

Spectroelectrochemistry

Spectroelectrochemical UV/Vis-NIR measurements of 2.0 $mmol \cdot L^{-1}$ solutions of **D-3**, **D-4a**,**b** and **D-5** in anhydrous dichloromethane containing 0.1 $mol \cdot L^{-1}$ of $[N^nBu_4][B(C_6F_5)_4]$ as the supporting electrolyte were performed in an OTTLE (= Optically Transparent Thin-Layer Electrochemical)[D58] cell with a Varian Cary 5000 spectrophotometer at 25 °C. The values obtained by deconvolution could be reproduced within ε_{max} 100 $L \cdot mol^{-1} \cdot cm^{-1}$; ν_{max} 50 cm^{-1}; $\Delta\nu_{1/2}$ 50 cm^{-1}.

Single Crystal X-ray Diffraction Analysis

Suitable single crystals of **D-4a** for X-ray diffraction analysis were obtained by diffusion of *n*-hexane into a dichloromethane solution containing **D-4a** at ambient temperature. Data were collected with an Oxford Gemini S diffractometer at 110 K with Cu K_α radiation (λ = 1.54184 Å). The structures were solved by direct methods and refined by full-matrix least-squares procedures on F^2.[D64,D65] All *non*-hydrogen atoms were refined anisotropically and a riding model was employed in the treatment of the hydrogen atom positions.

Reagents

All starting materials were obtained from commercial suppliers and were used without further purification. 2,5-Diferrocenyl-1-phenyl-1*H*-phosphole[D46], chloro(thiobis-[methane]) gold[D66] and ethynylferrocene[D67] were prepared according to published procedures.

Synthesis of chloro(2,5-diferrocenyl-1-phenyl-1*H*-phosphole) gold (D-3)

To a solution of 0.17 g (0.33 mmol) of 2,5-diferrocenyl-1-phenyl-1*H*-phosphole (**D-1**) in 50 mL of dichloromethane, 0.1 g (0.33 mmol) of $AuCl(SMe_2)$ (**D-2**) were added in a single portion. The mixture was stirred for 14 h at ambient temperature and afterwards all volatiles were removed in vacuo. The resulting residue was purified by column chromatography

(column size: 15 x 3 cm) on alumina using a *n*-hexane/dichloromethane mixture (ratio 5:1, *v*/*v*). After removing of all volatiles compound **D-3** was obtained as a purple solid. Yield: 0.18 g (0.23 mmol, 70 % based on **D-1**). Anal. Calcd. for $C_{30}H_{25}AuClFe_2P$ (759.97 g/mol): C, 47.37; H, 3.31. Found: C, 47.06; H, 3.30. Mp.: 240 °C. IR data (KBr, ν/cm^{-1}): 3080 m, 3039 m, 2922 w, 2847 w, 1577 s, 1436 s. ^{1}H NMR ($CDCl_3$, δ): 4.08 (s, 10 H, C_5H_5), 4.28 (m, 2 H, C_5H_4), 4.33 (m, 2 H, C_5H_4), 4.45 (m, 2 H, C_5H_4), 4.58 (m, 2 H, C_5H_4), 6.92 (d, $^3J_{HP}$ = 29.5 Hz, 2 H, C_4H_2P), 7.44−7.52 (m, 3 H, H^m,H^p/C_6H_5), 7.77−7.81 (m, 2 H, H^o/C_6H_5). ^{13}C{^{1}H} NMR ($CDCl_3$, δ): 67.9 (s, C_5H_4), 66.9 (s, C_5H_4), 69.9 (s, C_5H_4), 70.0 (s, C_5H_4), 70.5 (s, C_5H_5), 78.0 (d, $^2J_{CP}$ = 17.0 Hz, C^i/C_5H_4), 125.9 (d, $^1J_{CP}$ = 58.2 Hz, C^i/C_6H_5), 129.7 (d, J_{CP} = 12.3 Hz, CH/C_6H_5), 132.3 (d, $^2J_{CP}$ = 17.3 Hz, CH/C_4H_2P), 132.9 (d, J_{CP} = 2.7 Hz, CH/C_6H_5), 134.4 (d, J_{CP} = 14.5 Hz, CH/C_6H_5), 140.6 (d, $^1J_{CP}$ = 58.8 Hz, C^i/C_4H_2P). ^{31}P{^{1}H} NMR ($CDCl_3$, δ): 30.4 (s). HRMS (ESI-TOF, *m/z*): calcd for $C_{30}H_{25}AuClFe_2P$: 759.9743, found: 759.9733 $[M]^+$.

Synthesis of ferrocenylethynyl-(2,5-diferrocenyl-1-phenyl-1*H*-phosphole) gold (D-4a)

To 0.06 g (0.20 mmol) of **D-2** in 50 mL of a mixture of tetrahydrofuran/diisopropylamine (ratio 1:1; *v*/*v*), 0.07 g (0.3 mmol) of ethynyl ferrocene and 1 mg of CuI were added in a single portion and the resulting turbid mixture was stirred for 30 min at ambient temperature. Afterwards, the reaction mixture was added dropwise to a solution of 0.11 g (0.21 mmol) of **D-1** in tetrahydrofuran and the mixture was stirred for 1 h at which the color changed from red to purple. All volatiles were removed in vacuo and the resulting residue was purified by column chromatography (column size: 15 x 4 cm, alumina) using a mixture of *n*-hexane/dichloromethane (ratio 1:1, *v*/*v*) as eluent. After drying in vacuo, **D-4a** was obtained as a purple solid. Yield: 0.07 g (0.07 mmol, 41 % based on **D-1**). Anal. Calcd. for $C_{42}H_{34}AuFe_3P$ (934.01 g/mol): C, 54.00; H, 3.67. Found: C, 54.29; H, 3.61. Mp.: 120 °C. IR data (KBr, ν/cm^{-1}): 3091 m, 3045 w, 2954 w, 2923 m, 2852 m, 2107 w, 1730 w, 1577 m, 1435 m. ^{1}H NMR ($CDCl_3$, δ): 4.07 (s, 10 H, C_5H_5), 4.09 (m, 2 H, C_5H_4), 4.17 (s, 5 H C_5H_5), 4.27 (m, 2 H, C_5H_4), 4.30 (m, 2 H, C_5H_4), 4.44 (m, 2 H, C_5H_4), 4.48 (m. 2 H, C_5H_4), 4.57 (m, 2 H, C_5H_4), 6.93 (d, $^3J_{HP}$ = 26.9 Hz, 2 H, C_4H_2P), 7.43−7.50 (m, 3 H, H^m,H^p/C_6H_5), 7.80−7.84 (m, 2 H, H^o/C_6H_5). ^{13}C{^{1}H} NMR ($CDCl_3$, δ): 66.9 (d, J_{CP} = 6.1 Hz, C_5H_4/Fc-^{c}C_4H_2P), 67.3 (d, J_{CP} = 7.2 Hz, C_5H_4/Fc-^{c}C_4H_2P), 67.9 (s, C_5H_4/C≡CFc), 69.7 (s, C_5H_4/Fc-^{c}C_4H_2P), 69.7 (s, C_5H_4/Fc-^{c}C_4H_2P), 70.1 (s, C_5H_5/C≡CFc), 70.3 (s, C_5H_5/Fc-^{c}C_4H_2P), 72.0 (s, C_5H_4/C≡CFc), 78.5 (d, $^2J_{CP}$ = 17.6 Hz, C^i/C_5H_4/Fc-^{c}C_4H_2P), 101.8 (C≡C), 127.3 (d, $^1J_{CP}$ = 51.5 Hz, C^i/C_6H_5), 130.0 (d, J_{CP} = 11.7 Hz, CH/C_6H_5), 132.4–132.5 (m, CH/C_4H_2P, CH/C_6H_5), 134.7 (d, J_{CP} =

9.2 Hz, CH/C_6H_5), 142.0 (d, $^1J_{CP}$ = 53.6 Hz, C^i/C_4H_2P). $^{31}P\{^1H\}$ NMR ($CDCl_3$, δ): 43.2 (s). HRMS (ESI-TOF, *m/z*): calcd for $C_{42}H_{34}AuFe_3P$: 934.0109, found: 934.0085 $[M]^+$

Crystal Data for D-4a: $C_{42}H_{34}AuFe_3P$, M = 934.18 g·mol^{-1}, monoclinic, $P2_1/c$, λ = 1.54184 Å, a = 18.1719(18) Å, b = 15.0756(10) Å, c = 12.6151(6) Å, β = 98.091(7), V = 3421.5(4) Å^3, Z = 4, ρ_{calcd} = 1.813 Mg·m^{-3}, μ = 18.539 mm^{-1}, T = 110(2) K, Θ range = 4.598–64.485°, reflections collected: 11068, independent: 5702 (R_{int} = 0.1566), R_1 = 0.0968, wR_2 = 0.1782 [$I > 2\sigma(I)$].

Synthesis of phenylethynyl-(2,5-diferrocenyl-1-phenyl-1*H*-phosphole) gold (D-4b)

Following the synthesis procedure described above, 0.07 g (0.22 mmol) of **D-2** were reacted with 0.02 g (0.2 mmol) of ethynyl benzene, 1 mg of CuI and 0.12 g (0.22 mmol) of **D-1**. After appropriate work-up, **D-4b** was obtained as a purple solid. Yield: 0.08 g (0.10 mmol, 46 % based on **D-1**). Anal. Calcd. for $C_{38}H_{30}AuFe_2P$ (826.04 g/mol): C, 55.24; H, 3.66. Found: C, 54.81; H, 4.14. Mp.: 224 °C. IR data (KBr, ν/cm^{-1}): 3074 w, 3065 w, 2954 w, 2922 s, 2850 m, 2107 w, 1724 w, 1582 s, 1483 s. ^1H NMR ($CDCl_3$, δ): 4.09 (s, 10 H, C_5H_5), 4.27 (m, 2 H, C_5H_4), 4.31 (m, 2 H, C_5H_4), 4.49 (m, 2 H, C_5H_4), 4.59 (m, 2 H, C_5H_4), 5.30 (s, CH_2Cl_2), 6.94 (d, $^3J_{HP}$ = 27.0 Hz, 2 H, C_4H_2P), 7.18–7.23 (m, 3 H, C_6H_5), 7.44−7.51 (m, 5 H, C_6H_5), 7.81−7.85 (m, 2 H, C_6H_5). $^{13}C\{^1H\}$ NMR ($CDCl_3$, δ): 53.5 (s, CH_2Cl_2), 67.0 (s, C_5H_4), 67.2 (s, C_5H_4), 69.7 (s, C_5H_4), 69.8 (s, C_5H_4), 70.3 (s, C_5H_5), 78.4 (d, $^2J_{CP}$ = 14.4 Hz, C^i/C_5H_4), 103.4 (C≡C), 125.2 (s, C^i/C_6H_5), 126.8 (s, CH/C_6H_5), 128.1 (s, CH/C_6H_5), 129.6 (d, J_{CP} = 11.8 Hz, CH/C_6H_5), 132.4–132.5 (m, CH/C_4H_2P, CH/C_6H_5), 134.7 (d, J_{CP} = 13.2 Hz, CH/C_6H_5), 141.9 (d, $^1J_{CP}$ = 51.80 Hz, C^i/C_4H_2P). $^{31}P\{^1H\}$ NMR ($CDCl_3$, δ): 43.1 (s). HRMS (ESI-TOF, *m/z*): calcd for $C_{38}H_{30}AuFe_2PNa$: 849.0343, found: 849.0325 $[M + Na]^+$. Due to overlapping, the signal for C^i/C_6H_5 of the second phenyl group can not unequivocally be detected.

Synthesis of [μ-(1,4-phenylenedi-2,1-ethynediyl)]bis(2,5-diferrocenyl-1-phenyl-1*H*-phosphole) digold (D-5)

According to the synthesis procedure described earlier, 0.16 g (0.54 mmol) of **D-2** were reacted with 0.03 g (0.26 mmol) of 1,4-diethynyl benzene, 1 mg of CuI and 0.29 g (0.54 mmol) of **D-1** to give, after appropriate work-up, **D-5** as purple solid. Yield: 0.12 g (0.07 mmol, 29 % based on 1,4-diethynyl benzene). Anal. Calcd. for $C_{70}H_{54}Au_2Fe_4P_2$ (1574.04 g/mol): C, 53.40; H, 3.46. Found: C, 53.03; H, 3.81. Mp.: 210 °C (decomp.). IR data (KBr, ν/cm^{-1}): 3081 w, 2954 m, 2923 s, 2854 m, 2117 w, 1734 w, 1578 m, 1437 m. ^1H NMR ($CDCl_3$, δ): 4.08 (s, 20 H, C_5H_5), 4.26 (m, 4 H, C_5H_4), 4.30 (m, 4 H, C_5H_4), 4.48 (m, 4 H, C_5H_4), 4.58 (m, 4 H, C_5H_4), 6.92 (d, $^3J_{HP}$ = 27.0 Hz, 4 H, C_4H_2P), 7.38 (s, 4 H, C_6H_4),

7.43−7.49 (m, 6 H, C_6H_5), 7.80−7.85 (m, 4 H, C_6H_5). $^{31}P\{^1H\}$ NMR ($CDCl_3$, δ): 43.1 (s). HRMS (ESI-TOF, *m/z*): calcd for $C_{70}H_{55}Au_2Fe_4P_2$: 1575.0511, found: 1575.0521 $[M + H]^+$.

D5 Acknowledgement

We are grateful to the Fonds der Chemischen Industrie (FCI) for generous financial support. M.K. thanks the FCI for a Chemiefonds Fellowship.

D6 Supporting Information Available

Figures giving further (spectro)electrochemical spectra and CIF file giving crystallographic data for **D-4a**. Crystallographic data of **D-4a** are also available from the Cambridge Crystallographic Database as file number CCDC 1412989.

D7 References

[D1] P. Aguirre-Etcheverry, D. O'Hare, *Chem. Rev.* **2010**, *110*, 4839–4864.

[D2] S. Barlow, D. O'Hare, *Chem. Rev.* **1997**, *97*, 637–670.

[D3] A. Ceccon, S. Santi, L. Orian, A. Bisello, *Coord. Chem. Rev.* **2004**, *248*, 683–724.

[D4] A. Hildebrandt, U. Pfaff, H. Lang, *Rev. Inorg. Chem.* **2011**, *31*, 111–141.

[D5] F. Paul, C. Lapinte, *Coord. Chem. Rev.* **1998**, *178-180*, 431–509.

[D6] D. M. D'Alessandro, F. R. Keene, *Chem. Soc. Rev.* **2006**, *35*, 424–440.

[D7] J. M. Speck, R. Claus, A. Hildebrandt, T. Rüffer, E. Erasmus, L. van As, J. C. Swarts, H. Lang, *Organometallics* **2012**, *31*, 6373–6380.

[D8] S. W. Lehrich, A. Hildebrandt, T. Rüffer, M. Korb, P. J. Low, H. Lang, *Organometallics* **2014**, *33*, 4836–4845.

[D9] U. Pfaff, A. Hildebrandt, D. Schaarschmidt, T. Rüffer, P. J. Low, H. Lang, *Organometallics* **2013**, *32*, 6106–6117.

[D10] U. Pfaff, A. Hildebrandt, D. Schaarschmidt, T. Hahn, S. Liebing, J. Kortus, H. Lang, *Organometallics* **2012**, *31*, 6761–6771.

[D11] U. Pfaff, A. Hildebrandt, M. Korb, H. Lang, *Polyhedron* **2015**, *86*, 2–9.

[D12] A. Hildebrandt, D. Schaarschmidt, H. Lang, *Organometallics* **2011**, *30*, 556–563.

[D13] A. Hildebrandt, T. Rüffer, E. Erasmus, J. C. Swarts, H. Lang, *Organometallics* **2010**, *29*, 4900–4905.

[D14] A. Hildebrandt, D. Schaarschmidt, R. Claus, H. Lang, *Inorg. Chem.* **2011**, *50*, 10623–10632.

[D15] K. Kaleta, F. Strehler, A. Hildebrandt, T. Beweries, P. Arndt, T. Rüffer, A. Spannenberg, H. Lang, U. Rosenthal, *Chem. Eur. J.* **2012**, *18*, 12672–12680.

[D16] K. Kaleta, A. Hildebrandt, F. Strehler, P. Arndt, H. Jiao, A. Spannenberg, H. Lang, U. Rosenthal, *Angew. Chem.* **2011**, *123*, 11444–11448.

[D17] A. Hildebrandt, H. Lang, *Organometallics* **2013**, *32*, 5640–5653.

[D18] A. Hildebrandt, H. Lang, *Dalton Trans.* **2011**, *40*, 11831–11837.

[D19] S. W. Lehrich, A. Hildebrandt, M. Korb, H. Lang, *J. Organomet. Chem.* **2015**, *792*, 37–45.

[D20] F. Mathey, *Chem. Rev.* **1988**, *88*, 429–453.

[D21] F. Mathey, *Mod. Heterocycl. Chem.*; J. Alvarez-Builla, J. J. Vaquero, J. Barluenga, Eds.; Wiley-VCH Verlag GmbH & Co. KGaA: Weinheim, Germany, **2011**, 2071–2116.

[D22] L. D. Quin, *Curr. Org. Chem.* **2006**, *10*, 43–78.

[D23] G. Keglevich, Z. Böcskei, G. M. Keserü, K. Újszászy, L. D. Quin, *J. Am. Chem. Soc.* **1997**, *119*, 5095–5099.

[D24] G. Keglevich, R. Farkas, K. Ludányi, V. Kudar, M. Hanusz, K. Simon, *Heteroat. Chem.* **2005**, *16*, 104–110.

[D25] G. Keglevich, *Phosphorus Heterocycles II*; R. K. Bansal, Ed.; Topics in Heterocyclic Chemistry; Springer, Berlin, Heidelberg, **2010**; Vol. 21..

[D26] L. Nyulászi, *Chem. Rev.* **2001**, *101*, 1229–1246.

[D27] L. Nyulászi, L. Soós, G. Keglevich, *J. Organomet. Chem.* **1998**, *566*, 29–35.

[D28] L. Nyulászi, *J. Phys. Chem.* **1995**, *99*, 586–591.

[D29] E. Öberg, A. Orthaber, C. Lescop, R. Réau, M. Hissler, S. Ott, *Chem. Eur. J.* **2014**, *20*, 8421–8432.

[D30] H. Chen, W. Delaunay, J. Li, Z. Wang, P. A. Bouit, D. Tondelier, B. Geffroy, F. Mathey, Z. Duan, R. Réau, M. Hissler, *Org. Lett.* **2013**, *15*, 330–333.

[D31] Y. Matano, T. Miyajima, T. Fukushima, H. Kaji, Y. Kimura, H. Imahori, *Chem. Eur. J.* **2008**, *14*, 8102–8115.

[D32] Y. Matano, M. Fujita, A. Saito, H. Imahori, *Comptes Rendus Chim.* **2010**, *13*, 1035–1047.

[D33] C. Lescop, L. Toupet, R. Réau, *Heteroat. Chem.* **2011**, *22*, 339–347.

[D34] A. Orthaber, S. Borucki, W. Shen, R. Réau, C. Lescop, R. Pietschnig, *Eur. J. Inorg. Chem.* **2014**, 1751–1759.

[D35] P. A. Bouit, A. Escande, R. Szücs, D. Szieberth, C. Lescop, L. Nyulászi, M. Hissler, R. Réau, *J. Am. Chem. Soc.* **2012**, *134*, 6524–6527.

[D36] Y. Dienes, S. Durben, T. Kárpáti, T. Neumann, U. Englert, L. Nyulászi, T. Baumgartner, *Chem. Eur. J.* **2007**, *13*, 7487–7500.

[D37] J. Wu, S. Wu, Y. Geng, G. Yang, S. Muhammad, J. Jin, Y. Liao, Z. Su, *Theor. Chem. Acc.* **2010**, *127*, 419–427.

[D38] E. Y.-H. Hong, H.-L. Wong, V. W.-W. Yam, *Chem. Commun.* **2014**, *50*, 13272–13274.

[D39] Y. Dienes, M. Eggenstein, T. Neumann, U. Englert, T. Baumgartner, *Dalton Trans.* **2006**, 1424–1433.

[D40] X. He, A. Y. Y. Woo, J. Borau-Garcia, T. Baumgartner, *Chem. Eur. J.* **2013**, *19*, 7620–7630.

[D41] C. Romero-Nieto, K. Kamada, D. T. Cramb, S. Merino, J. Rodríguez-López, T. Baumgartner, *Eur. J. Org. Chem.* **2010**, 5225–5231.

[D42] H.-C. Su, O. Fadhel, C.-J. Yang, T.-Y. Cho, C. Fave, M. Hissler, C.-C. Wu, R. Reau, *J. Am. Chem. Soc.* **2006**, *128*, 983–995.

[D43] O. Fadhel, M. Gras, N. Lemaitre, V. Deborde, M. Hissler, B. Geffroy, R. Réau, *Adv. Mater.* **2009**, *21*, 1261–1265.

[D44] Y. Dienes, U. Englert, T. Baumgartner, *Z. Anorg. Allg. Chem.* **2009**, *635*, 238–244.

[D45] X. He, J. Lin, W. H. Kan, P. Dong, S. Trudel, T. Baumgartner, *Adv. Funct. Mater.* **2014**, *24*, 897–906.

[D46] D. Miesel, A. Hildebrandt, M. Korb, P. J. Low, H. Lang, *Organometallics* **2013**, *32*, 2993–3002.

[D47] D. Miesel, A. Hildebrandt, M. Korb, D. A. Wild, P. J. Low, H. Lang, *Chem. Eur. J.* **2015**, *21*, 11545–11559.

[D48] D. Miesel, A. Hildebrandt, M. Korb, H. Lang, *Organometallics* **2015**, *34*, 4293–4304**.**

[D49] J. Vicente, M. T. Chicote, M. M. Alvarez-Falcón, M. D. Abrisqueta, F. J. Hernández, P. G. Jones, *Inorg. Chim. Acta* **2003**, *347*, 67–74.

[D50] G. Hogarth, M. M. Álvarez-Falcón, *Inorg. Chim. Acta* **2005**, *358*, 1386–1392.

[D51] R. Packheiser, A. Jakob, P. Ecorchard, B. Walfort, H. Lang, *Organometallics* **2008**, *27*, 1214–1226.

[D52] A. Jakob, P. Ecorchard, M. Linseis, R. F. Winter, H. Lang, *J. Organomet. Chem.* **2009**, *694*, 655–666.

[D53] M. O. Sinnokrot, E. F. Valeev, C. D. Sherrill, *J. Am. Chem. Soc.* **2002**, *124*, 10887–10893.

[D54] W. E. Geiger, F. Barrière, *Acc. Chem.Res.* **2010**, *43*, 1030–1039.

[D55] G. Gritzner, J. Kuta, *Pure Appl. Chem.* **1984**, *56*, 461–466.

[D56] D. E. Richardson, H. Taube, *Inorg. Chem.* **1981**, *20*, 1278–1285.

[D57] R. F. Winter, *Organometallics* **2014**, *33*, 4517–4536.

[D58] M. Krejčik, M. Daněk, F. Hartl, *J. Electroanal. Chem.* **1991**, *317*, 179–187.

[D59] W. Kaim, B. Sarkar, G. K. Lahiri, in *Spectroelectrochemistry* (Eds.: W. Kaim, A. Klein), Royal Society Of Chemistry, Cambridge, **2008**, 68–90.

[D60] N. S. Hush, *Electrochim. Acta* **1968**, *13*, 1005–1023.

[D61] J. Vicente, M.-T. Chicote, M.-D. Abrisqueta, P. G. Jones, *Organometallics* **1997**, *16*, 5628–5636.

[D62] M. B. Robin, P. Day, *Adv. Inorg. Chem. Radiochem.* **1967**, *10*, 247–422.

[D63] A. Nafady, W. E. Geiger, *Organometallics* **2008**, *27*, 5624–5631.

[D64] G. M. Sheldrick, *Acta Crystallogr., Sect. A* **1990**, *46*, 467–473.

[D65] G. M. Sheldrick, *Progr. Cryst. Struct. Refinement* **1997**, University of Göttingen.

[D66] T. N. Hooper, C. P. Butts, M. Green, M. F. Haddow, J. E. McGrady, C. A. Russell, *Chem. Eur. J.* **2009**, *15*, 12196–12200.

[D67] J. Polin, H. Schottenberger, *Org. Synth.* **1996**, *73*, 262-367.

E Influence of P-Bonded Bulky Substituents on the Electronic Interaction in Ferrocenyl Substituted Phospholes

Dominique Miesel, Alexander Hildebrandt, Marcus Korb, Duncan A. Wild, Paul J. Low, and Heinrich Lang*

Veröffentlicht in *Chemistry – A European Journal*, **2015**, *21*, 11545–11559.

Neben den Komplexierungsmöglichkeiten lassen sich die elektronischen Eigenschaften der Phosphole auch durch die Wahl der Substituenten in 1-, 2- oder 5-Position des Phospholringes gezielt ändern. So führt die Verwendung von sterisch anspruchsvollen Substituenten zu einer Planarisierung des Phosphoratoms und somit zu einer höheren Delokalisierung im Ring. Deshalb erfolgten die Synthese 2,5-diferrocenylfunktionalisierter Phosphole mit unterschiedlich räumlich anspruchsvollen Gruppen und die Untersuchung der Auswirkung auf die Metall-Metall-Wechselwirkung.

Die in Kapitel E präsentierten Ergebnisse wurden selbstständig unter Anleitung von Prof. Dr. Heinrich Lang und Dr. Alexander Hildebrandt erstellt. Von Prof. Dr. Paul J. Low und Dr. Duncan A. Wild wurden die theoretischen Berechnungen durchgeführt. Die kristallografischen Messungen erfolgten durch Marcus Korb.

E1 Introduction

The "aromaticity" of phospholes is one of the most investigated properties of these five-membered heterocycles.[E1–E15] In contrast to other analogues heterocycles, *e. g.* pyrroles, most phospholes are non- or only slightly aromatic.[E16–E18] Phospholes exhibit a pyramidal phosphorus environment and a high inversion barrier, whereas in pyrroles a planar geometry is present due to the higher aromatic stabilization energy compensating the energy required for planarization.[E19] Due to this pyramidal environment at the phosphorus atom in phospholes, the interaction of the phosphorus lone pair with the dienic π-system is hindered. As a result, the chemistry of phospholes is different to that of other 5-membered heterocycles such as furan, thiophene and pyrrole, and due to the reactive and stereochemically active

phosphorus lone pair and dienic π-system, many different transition metal complexes of phospholes are known.[E4,E20–E26]

Theoretical investigations have revealed a strong delocalization with the 5-membered ring if the phosphorus atom adopts a planar geometry.[E27–E29] The flattening of the pyramidal phosphorus could in principle be achieved using π-acceptor or bulky substituents,[E1,E10,E30] and the idea that sterically demanding substituents at the phosphorus atom increase the delocalization in phospholes has been established by others, particularly Quin and Keglevich.[E9,E11,E31–E35]

For example, X-ray diffraction studies of 1-(2,4,6-tri-*iso*-propylphenyl)-3-methylphosphole indicate an increased planarity at the phosphorus atom compared to simpler analogues.[E35] The Bird Index,[E36] a useful tool to evaluate the aromaticity based on geometric data, for this compound increases (up to 40) compared to the unhindered 1-benzylphosphole (35).[E37] A further increase up to a value of 56 was obtained for 1-(2,4,6-tri-*tert*-butylphenyl)-3-methyl-phosphole[E33] and, as is characteristic of ring systems with pronounced delocalization, the phosphole ring participates in electrophilic substitution reactions.

Recently, we investigated a number of ferrocenyl-substituted heterocycles and examined the electronic interaction between the Fc/Fc^+ units *via* the heterocyclic core in the corresponding mixed-valent species.[E38–E49] One electron oxidation of 2,5-diferrocenyl-1-phenyl-1*H*-phosphole (**E-3a**) gives mixed-valent [**E-3a**]$^+$ which exhibits an IVCT (= intervalence charge transfer) absorption band in the NIR region of moderate energy and intensity.[E50] The comparison of the spectroscopic parameters of IVCT absorption with those from analogous mixed-valent diferrocenyl substituted heterocycles places the strength of the ferrocene/ferrocenium coupling through the phosphole ring between that mediated by 2,5-diferrocenyl substituted furan and 1-methyl-1*H*-pyrrole.[E43]

In continuation of this work, herein the concept of the planarization of phosphole rings by the use of sterically demanding substituents at the phosphorus atom is applied to a series of 2,5-diferrocenyl-substituted phospholes and the effect thereof on the electron transfer properties is discussed.

E2 Results and Discussion

Synthesis and characterization

2,5-Diferrocenyl-1-Ar-1*H*-phospholes **E-3a**–**e** (Ar = phenyl (**a**),[E50] ferrocenyl (**b**), mesityl (**c**), 2,4,6-triphenylphenyl (**d**), 2,4,6-tri-*tert*-butylphenyl (**e**)) were synthesized by

cyclization of the corresponding phosphines $ArPH_2$ **E-1a**–**e** with diferrocenyl butadiyne (**E-2**) (Scheme E1) according to a reaction procedure first described by Märkl and Potthast.[E51]

Phosphines $ArPH_2$ **E-1a**–**e** (Ar = Ph (**E-1a**), Fc; (**E-1b**), 2,4,6-$Me_3C_6H_2$ (**E-1c**), 2,4,6-Ph_3-C_6H_2 (**E-1d**), 2,4,6-$^tBu_3$-C_6H_2 (**E-1e**)) were reacted with 0.7–1.0 equiv. of *n*-butyllithium and the resulting solutions were slowly added to 1,4-diferrocenyl butadiyne (**E-2**) giving the corresponding phospholes **E-3a**–**e** (Scheme E1) upon addition of the P-H units to the C,C triple bonds.

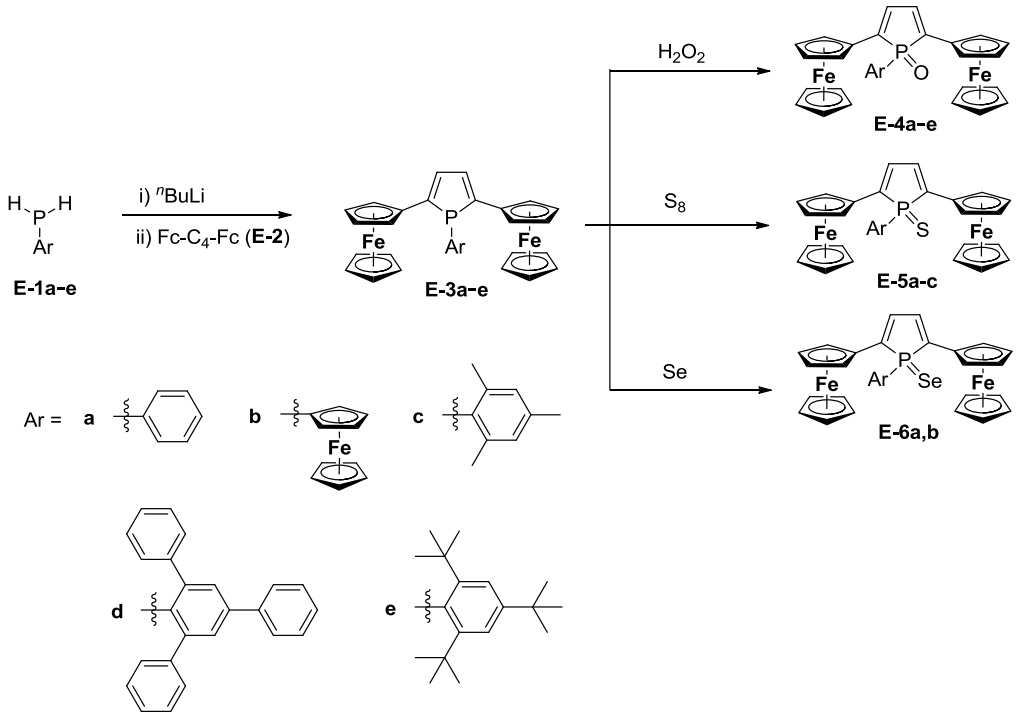

Scheme E1. Synthesis of phospholes **E-3a**–**e**, **E-4a**–**e**, **E-5a**–**c** and **E-6a**,**b**. (i) Toluene/tetrahydrofuran (1:1, v/v), 0 °C, 1 h; (ii) tetrahydrofuran, 25 °C, 12 h; Fc = Fe(η^5-C_5H_5)(η^5-C_5H_4).

Phospholes **E-3a**–**e** were treated with hydrogen peroxide, elemental sulfur or selenium to give the corresponding oxides **E-4**, sulfides **E-5** and selenides **E-6** in order to investigate the influence of the sterically demanding substituents bonded to P on the reaction behavior of the phosphorus lone pair toward chalcogenides. Each of the phospholes **E-3a**–**e** react with hydrogen peroxide giving oxides **E-4a**–**e**. Whereas the reaction of **E-3a**,**b** results in high yields after 30 min, the reaction time for **E-3c**–**e** was increased to 2 h (**E-3c**,**d**) or 5 h (**E-3e**). Phospholes **E-3a**[E50] and **E-3b** react with sulfur and selenium at room temperature within 14 h to give the corresponding phosphole sulfides **E-5a**,**b** and selenides **E-6a**,**b**. The reaction of **E-3c** with elemental sulfur results in sulfide **E-5c** in decreased yields (29 %), while phospholes **E-3d**,**e** do not react with elemental sulfur, even at temperatures up to 100 °C. The reaction of phospholes **E-3c**–**e** with elemental selenium was not successful. On the one hand,

the reaction behavior of phospholes **E-3a**–**e** toward chalcogenides could be explained by an increasing steric demand of the substituents bonded to phosphorus; on the other hand an increased contribution of the phosphorus lone pair in the π-system of the C_4H_2P motif would also result in a lower reactivity.

Compounds **E-3a**–**e**, **E-4a**–**e**, **E-5a**–**c** and **E-6a**,**b** are stable toward air and moisture both in the solid state and in solution. They have been characterized by elemental analysis, IR and NMR (^{1}H, ^{13}C{^{1}H}, ^{31}P{^{1}H}) spectroscopy and ESI-TOF mass spectrometry. The spectroscopic and electrochemical properties of **E-3a** have been described earlier.[E50] Phospholes **E-3a**–**e** show one characteristic phosphorus signal in the ^{31}P{^{1}H} NMR spectra between -6 ppm – 5 ppm which is characteristic for such type of molecules.[E4,E5] After oxidation of P^{III} to P^{V} in oxides **E-4**, sulfides **E-5** and selenides **E-6**, a shift to lower field occurred, as expected.

In the ^{13}C{^{1}H} NMR spectra the signals for the CH carbon atoms of the phosphole ring shift slightly to higher field with an increase of the steric demand within this series (Experimental Section). The stronger *C,P* coupling reflects the increasing orientation of the phosphorus lone pair toward the C3 and C4 carbon atoms and hence a more planar environment at P. This behavior is in accordance with observation in literature regarding the comparison of 1-phenyl-3-methylphosphole with 1-(2,4,6-tri-*tert*-butylphenyl)-3-methylphosphole.[E33]

For **E-3a** four multiplets for the ferrocenyl C_5H_4 protons are observed, due to the prochiral nature of the phosphorus atom, compounds **E-3b**,**e** showed two sharp signals (multiplets). For **E-3c**,**d** broad signals for the ferrocenyl C_5H_4 protons are typical. The exchange of the α and α' as well as β and β' protons is most probably caused by the inversion at the phosphorus atom, whereas the exchange might also be caused by rotation of the ferrocenyl moieties. Therefore, variable temperature (VT)-NMR experiments and line shape analysis were carried out to calculate the exchange rates and subsequently the activation parameters of this process (Table E1, Figures E1 and SI1–6). Upon heating of **E-3a**, the four multiplets coalesce and at 100 °C two sharp signals were observed (Figure SI1).

For **E-3b**–**d** a similar behavior with varying coalescence temperatures is observed and the NMR samples of these compounds showed four resolved multiplets for the α, α', β and β' C_5H_4 protons at low temperatures. However, for **E-3e** the exchange of the ferrocenyl protons could not be reduced sufficiently by cooling the sample down to -90 °C (Figure SI6). While, the activation parameters of the exchange in **E-3e** could not be determined, as the coalescence temperature is below the freezing point of the solvent, the exchange rates in **E-3a–d** could be

determined by line shape fitting of the respective spectra at the appropriate temperatures and the activation parameters were calculated using the Eyring equation (Table E1).[E52]

These results evince that an increase of the steric demand at the phosphorus atom leads to a decreasing coalescence temperature and a decreasing energy barrier for the exchange process. This trend strongly argues that the exchange process is an inversion at the phosphorus, whereas a rotation of the ferrocenyl moieties is expected to be increasingly difficult with the increase of the steric demand of the substituents. The comparison of the exchange process in **E-3a**–**d** with the rotation barrier for the free rotation around the pyrrole-ferrocenyl carbon-carbon bond in sterical demanding 2,3,4,5-tetraferrocenyl-1-phenyl-1*H*-pyrrole ($\Delta H^{\ddagger}$ = 26.8 (±1.2) kJ·mol^{-1}, $\Delta S^{\ddagger}$ = -94.1 (±4.5) J·mol^{-1}·K^{-1})[E45] shows that typically rotation processes exhibit low activation enthalpies while a prominent entropy term is present, whereas the exchange process in **E-3a**–**d** exhibit larger activation enthalpies and only a small entropy contribution. These findings further support that the observed exchange is a result of an inversion around P.

Table E1. Activation enthalpies $\Delta H^{\ddagger}$ and activation entropies $\Delta S^{\ddagger}$ for the ferrocenyl protons of E-3a–e.

Compd.	$\Delta H^{\ddagger}$ (kJ ·mol^{-1})	$\Delta S^{\ddagger}$ (J ·mol^{-1} ·K^{-1})	Coalescence temperature (°C) (solvent)
E-3a	57.9 (±3.3)	-37.8 (±10.1)	60 – 75 (toluene-d_8)
E-3b	61.3 (±2.9)	3.1 (±11.3)	-15 – 0 (methylenchloride-d_2)
E-3c	50.0 (±3.6)	-20.3 (±12.8)	-10 – 30 (tetrachlorethane-d_2)
E-3d	54.0 (±2.2)	-12.8 (±7.7)	0 – 15 (toluene-d_8)
E-3e	-	-	< -90 (toluene-d_8)

Phospholes **E-3a** and **E-3b** display similar activation enthalpies, which correlate with the comparable steric demand of the respective phosphorus atom bonded aryl moieties. An increase of the steric demand in **E-3c**,**d** results in a decrease of the activation enthalpies to $\Delta H^{\ddagger}$ = 50.0 (±3.6) kJ·mol^{-1} (**E-3c**) and $\Delta H^{\ddagger}$ = 54.0 (±2.2) kJ·mol^{-1} (**E-3d**). Phospholes **E-3a**–**d** exhibit lower activation enthalpies and similar activation entropies, when compared to 1-isopropyl-2-methyl-5-phenylphosphole ($\Delta H^{\ddagger}$ = 71.6 (±1.7) kJ·mol^{-1}; $\Delta S^{\ddagger}$ = 3.1 (±1.1) J·mol^{-1}·K^{-1}).[E15] Furthermore, **E-3c** offers the possibility to monitor the inversion process not only at the ferrocenyl moieties, but also through exchange of the methyl protons in 2,4-position of the phenyl group (Experimental Section). The determined activation barriers are

within the margin of error identical to the one determined at the ferrocenyl protons ($\Delta H^{\ddagger}$ = 54.0 (±1.2) kJ·mol^{-1}; $\Delta S^{\ddagger}$ = -8.4 (±3.7) J·mol^{-1}·K^{-1}).

It is noteworthy that despite similar activation enthalpies the coalescence temperature of **E-3b** is significantly lower than the one for **E-3a**, which is a result of the small positive activation entropy in **E-3b** (Table E1). Due to the steric demand of the *tert*-butyl ligands, **E-3e** exhibits the lowest inversion barrier within this series demonstrated by a coalescence temperature below -90 °C.

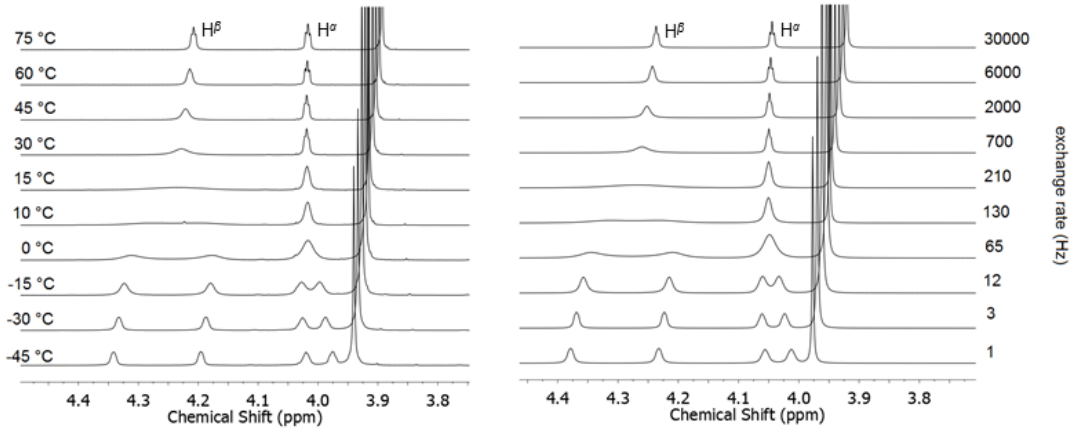

Figure E1. Left: Experimental ^{1}H NMR spectra of **E-3d** in the range of 3.8 and 4.7 ppm; toluene-d_8, various temperatures. Right: Simulated ^{1}H NMR spectra of **E-3d** in the range between 3.8 and 4.7 ppm with different exchange rates.

The molecular structures of **E-3b**–**e** in the solid state have been determined by single crystal X-ray diffraction analysis. Suitable crystals were obtained by diffusion of hexane into a dichloromethane solution containing either **E-3b**, **E-3c**, **E-3d** or **E-3e** at ambient temperature. The ORTEP diagrams with selected bond lengths (Å), bond angles (°) and torsion angles (°) are shown in Figure E2 (**E-3b**,**c**) and E3 (**E-3d**,**e**). In order to discuss the delocalization within the phosphole ring some key factors derived from the molecular geometry of the respective compounds have to be considered (Table E2, for additional X-ray discussion see Supporting Information). In phospholes **E-3c**–**e** the $^{c}C_4P$ rings show deviations from planarity), while **E-3b** possesses the most planar phosphole ring. To describe the non-planarity of the phosphole ring, the angle α describing the deflection of the phosphorus atom to the C_4 plane was calculated. For **E-3b** a smaller angle is observed than for **E-3c**, **E-3d** and **E-3e** indicating a higher planarity of the heterocyclic ring.

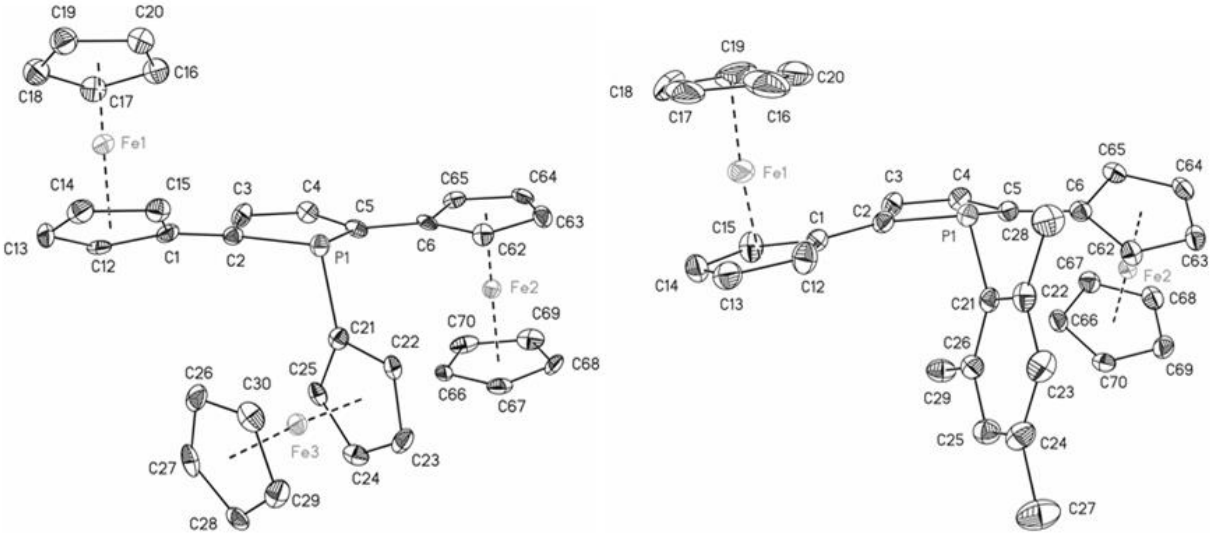

Figure E2. ORTEP diagrams (50 % probability level) of the molecular structures of **E-3b** (left) and **E-3c** (right) with the atom-numbering scheme. All hydrogen atoms and distorted atoms have been omitted for clarity. Selected bond distances (Å), angles (°), and torsion angles (°). **E-3b**, P1–C2 = 1.827(5), C2–C3 = 1.358(7), C3–C4 = 1.434(8), C4–C5 = 1.350(7), C5–P1 = 1.829(5), C1–C2 = 1.464(7), C5–C6 = 1.457(7), P1–C21 = 1.814(6), C2−P1−C5= 91.2(2), C2−P1−C21 = 109.1(2), C21−P1−C5 = 101.9(2). **E-3c**, P1–C2 = 1.797(2), C2–C3 = 1.353(3), C3–C4 = 1.440(3), C4–C5 = 1.357(3), C5–P1 = 1.803(2), C1–C2 = 1.459(3), C5–C6 = 1.462(3), P1–C21 = 1.823(2), C2−P1−C5 = 91.55(10), C2−P1−C21 = 111.58(9), C21−P1−C5 = 109.67(10).

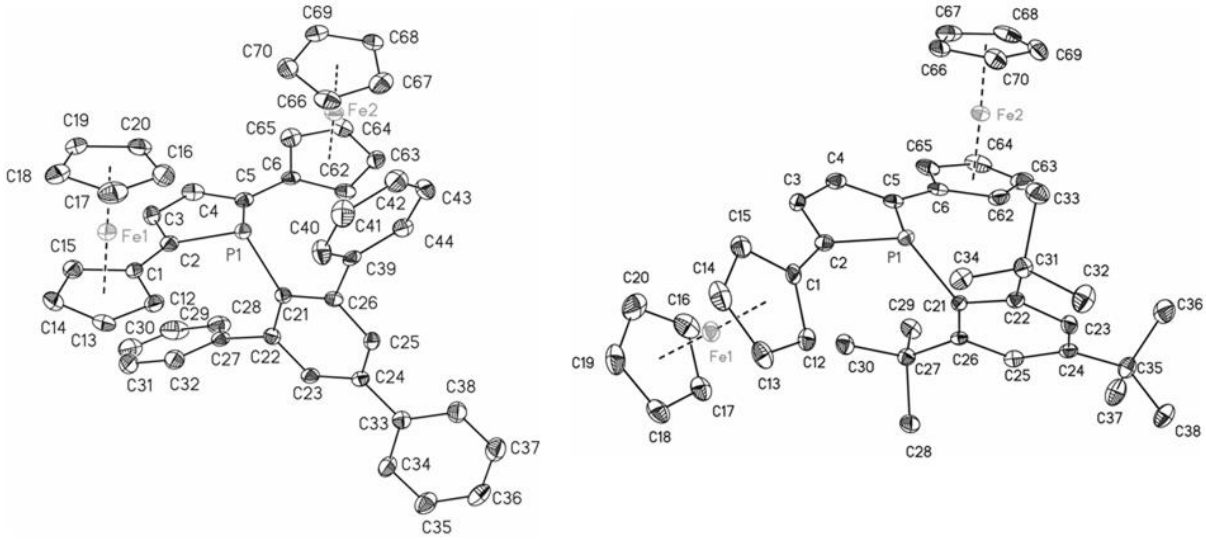

Figure E3. ORTEP diagram (50 % probability level) of the molecular structures of **E-3d** (left) and **E-3e** (right) with the atom-numbering scheme. All hydrogen atoms and the other molecule of the asymmetric unit of **E-3d** have been omitted for clarity. Selected bond distances (Å), angles (°), and torsion angles (°). **E-3d**, P1–C2 = 1.806(3), C2–C3 = 1.351(4), C3–C4 = 1.433(4), C4–C5 = 1.361(4), C5–P1 = 1.804(3), C2–C1 = 1.450(4), C5–C6 = 1.466(4), P1–C21 = 1.837(3), C2−P1−C5 = 91.82(15), C2−P1−C21 = 112.01(13), C21−P1−C5 = 106.61(14). **E-3e**, P1–C2 = 1.786(2), C2–C3 = 1.371(3), C3–C4 = 1.427(3), C4–C5 = 1.369(3), C5–P1 = 1.775(2), C2–C1 = 1.466(3), C5–C6 = 1.459(3), P1–C21 = 1.835(2), C2−P1−C5 = 93.77(10), C2−P1−C21 = 126.15(9), C21−P1−C5 = 111.36(10).

Table E2. Selected bond lengths (Å), angles (°) and the Bird Index of E-3b–e, 1-benzylphosphole[E37] (E-7) and 1-(2,4,6-tri-*tert*-butylphenyl)-3-methylphosphole[E33] (E-8).

Geometric Feature	**E-3b**	**E-3c**	**E-3d**	**E-3e**	**E-7**	**E-8**
distance P out of C_4 plane	0.137(8)	0.330(3)	0.253(5)	0.346(3)	0.208	0.294
α[a]	6.1(3)	15.22(19)	11.6(3)	16.53(12)	9.57(13)	12.88(4)
distance C_{Aryl} out of C2-P-C5 plane	1.671(6)	1.573(3)	1.613(4)	1.283(3)		
β[b]	67.563(7)	59.672(3)	61.655(5)	45.687(2)	66.94(5)	44.2(3)
sum of angles about P	302.2(6)	312.8(3)	310.4(4)	331.3(3)	302.66(9)	331.6(12)
Bird Index[c]	19.5(3)	32.25(2)	30.5(2)	46.67(8)	36.8(3)	56.6(4)

[a]α = Angle of deflection of the phosphorus atom out of the dienic carbon plane. [b]β = Angle of deflection of the carbon atom of the phosphorus substituent from the C2-P-C5 plane of the phosphole ring. [c]Calculated according to reference [E36].

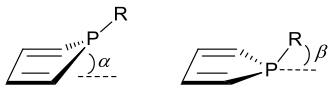

Chart E1. Illustration of angles α and β.

More important for the evaluation of the aromaticity is the angle (β) of the deflection of the substituent's carbon atom at the phosphorus from the C2-P-C5 plane of the phosphole ring, describing the possible flattening of the pyramidal phosphorus environment. This value is associated with the *p* character of the phosphorus lone pair and therefore, with its ability to interact with the phosphole π-system. Hereby, a low β angle represents a high *p* orbital contribution at the lone pair. For the sterically demanding 2,4,6-tri-*tert*-butylphenyl group in **E-3e** the highest planarity in this series was observed. This behavior demonstrates an increase of the flattening of the pyramidal phosphorus from **E-3b** < **E-3c** ≈ **E-3d** < **E-3e**. The application of crowded substituents led to a higher planarity, as compared to literature-known unhindered 1-benzylphosphole (β = 66.94(5) °).[E37] The angle β is similar to other phospholes bearing sterically demanding substituents such as 1-(2,4,6-tri-*tert*-butylphenyl)-3-methylphosphole (44.2(3) °).[E33]

Another important factor for the determination of the delocalization is the alternation of bond lengths within the heterocyclic core. An increase of delocalization should result in a

shortening of the C3-C4, P1-C2 and P1-C5 and an elongation of the C2-C3 and C4-C5 bonds. The shortest C3-C4 distance was found for **E-3e**, when compared with **E-3b**–**d**. Phosphole **E-3e** also shows the highest bond length for C2-C3 and C4-C5 and the shortest for P1-C2 and P1-C5. This behavior is an indication for an increase of delocalization in **E-3e** with the sterically demanding 2,4,6-tri-*tert*-butylphenyl substituent. For a better description, Bird developed a parameter for the effects of delocalization based on the bond distances, of which a higher delocalization results in higher values for the Bird index.[E36] A comparison of the Bird indices for **E-3b**–**e** reveal an increase in the series **E-3b** (19.5(3)) < **E-3c** (32.25(2)) ≈ **E-3d** (30.5(2)) < **E-3e** (46.67(8)).

A comparison of **E-3e** with 1-(2,4,6-tri-*tert*-butylphenyl)-3-methylphosphole (**E-8**) [E33] showed that despite identical substituents at the phosphorus atom the Bird indices are further influenced by the substitution pattern at the C_4 setup of the phosphole. The calculation of the sum of the angles about the phosphorus atom according to Schmidpeter allows the determination of the change in pyramidality of the phosphorus atom.[E53] A reduce of the pyramidality results in higher sum values. Again, **E-3e** exhibits the highest value for the sum of the phosphorus angles and therefore the lowest pyramidality. In conclusion, all these geometric criteria are an indication for an increase of planarity of the pyramidal phosphorus environment in **E-3e** and hence an increase of delocalization in the heterocyclic ring.

The trends in the changes in the pyramidal environment caused by steric demanding groups are consistent with the decreased inversion barriers by variable temperature NMR.

To shed further light on the minimum energy pathway of the aryl group inversion process, a relaxed potential energy surface scan was undertaken. The mesityl complex **E-3c** was chosen as it represents the middle of the range in terms of the steric bulk of the aryl group. Selected points along the inversion potential energy curve, defined by the C_{21}-C_2-C_3-C_4 dihedral angle, are presented in Table E3.

These data have been calculated at the B3LYP/3-21G level of theory whereby at each point the C_{21}-C_2-C_3-C_4 dihedral angle was fixed, while the remainder of the geometry was relaxed using standard optimization convergence criteria. The smaller 3-21G basis set was chosen due to computational speed, and the fact that only relative energies are required. The relaxed scan suggests as the aryl group migrates between the faces of the heterocycle, there is an initial concomitant movement of the phosphorus atom further out of the dienic carbon plane in the same direction, as highlighted by the P-C_2-C_3-C_4 dihedral angles (Table E3).

The displacement of the phosphorus continues until the C_{21}-C_2-C_3-C_4 dihedral reaches a critical angle at which point the phosphorus atom inverts. The motion of the mesityl group continues until ultimately the first and last points in Table E3 are equivalent minima. Due to uncertainty in the C_{21}-C_2-C_3-C_4 dihedral angle which defines the point at which the phosphorus atom inverts, we can only offer a conservative estimate of the inversion barrier for the mesityl **E-3c** complex of ~70 kJ/mol, which is in line with the activation barriers determined from the NMR experiments.

Table E3. Selected points along the inversion potential energy curve of E-3c.

	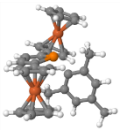	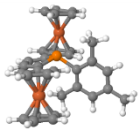	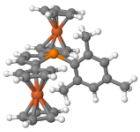	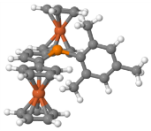	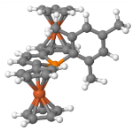	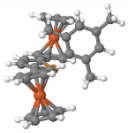
ϕ C_{21}-C_2-C_3-C_4* / °	27.6	17.2	0.0	-11.5	-14.87	-27.9
ϕ P-C_2-C_3-C_4* /°	-8.6	-14.0	-21.2	-25.2	15.55	8.6
d P-$C_{2\text{-}5}$* / Å	0.265	0.466	0.660	0.787	0.470	0.265
d C_{21}- $C_{2\text{-}5}$* / Å	1.201	0.722	0.006	0.509	0.652	1.201
α† / °	11.5	19.7	29.8	36.0	20.8	11.5
β† / °	62.3	58.3	50.4	44.6	57.6	62.3
ΔE‡ / kJ mol^{-1}	0.0	6.5	36.1	68.1	8.4	0.0

* Atom labels as defined in Figure E2.
† Angles α and β as described in Chart E1.
‡ Energy differences with respect to the minima.

In order to investigate the influence of the phosphole substitutents and associated geometric and electronic changes on the extent of electron transfer between the ferrocenyl units *via* the phosphole ring in **E-3b**–**e**, electrochemical and spectroelectrochemical measurements have been performed.

Electrochemistry and Spectroelectrochemistry

The redox properties of phospholes **E-3b–e, E-4a–e, E-5b,c and E-6b** were investigated by cyclic voltammetry, square wave voltammetry and spectroelectrochemistry (UV/Vis-NIR). As supporting electrolyte a dry dichloromethane solution containing 0.1 mol·L^{-1} of [N^{n}Bu$_4$][B(C$_6$F$_5$)$_4$] or [N^{n}Bu$_4$][PF$_6$] was used, allowing effects of ion-pairing on the stability of the oxidation products to be assessed in a qualitative fashion.[E54–E56] All potentials are referenced to the FcH/FcH$^+$ redox couple.[E57]

Table E4. Cyclic voltammetry data of compounds E-3a–e, E-4a–c, E-5a–c, E-6a,b.[a]

Compd., supporting electrolyte	$E_1^{\circ\prime}$ in mV[b] (ΔE_p in mV)[c]	$E_2^{\circ\prime}$ in mV[b] (ΔE_p in mV)[c]	$E_3^{\circ\prime}$ in mV[b] (ΔE_p in mV)[c]	$\Delta E^{\circ\prime}$ in mV[d]	K_c[e]/ 10^4
E-3a,[E50] [N^{n}Bu$_4$][PF$_6$]	-135 (76)	50 (62)		185	0.13
E-3b, [N^{n}Bu$_4$][PF$_6$]	-135 (87)	40 (72)	150 (62)	175/ 190	0.09/ 0.16
E-3c, [N^{n}Bu$_4$][PF$_6$]	-155 (77)	55 (85)		210	0.35
E-3d, [N^{n}Bu$_4$][PF$_6$]	-185 (73)	45 (81)		230	0.77
E-3e, [N^{n}Bu$_4$][PF$_6$]	-200 (76)	30 (78)		230	0.77
E-3a,[E50] [N^{n}Bu$_4$][B(C$_6$F$_5$)$_4$]	-110 (72)	170 (80)		280	5.41
E-3b, [N^{n}Bu$_4$][B(C$_6$F$_5$)$_4$]	-125 (76)	140 (72)	450 (72)	265/ 310	3.02/ 17.4
E-3c, [N^{n}Bu$_4$][B(C$_6$F$_5$)$_4$]	-140 (63)	155 (74)		295	9.70
E-3d, [N^{n}Bu$_4$][B(C$_6$F$_5$)$_4$]	-165 (75)	175 (78)		340	55.9
E-3e, [N^{n}Bu$_4$][B(C$_6$F$_5$)$_4$]	-180 (70)	135 (76)		315	21.1
E-4a, [N^{n}Bu$_4$][B(C$_6$F$_5$)$_4$]	-20 (71)	215 (71)		235	0.94
E-4b, [N^{n}Bu$_4$][B(C$_6$F$_5$)$_4$]	-35 (60)	235 (67)	580 (63)	270/ 345	3.67/ 67.9
E-4c, [N^{n}Bu$_4$][B(C$_6$F$_5$)$_4$]	-40 (64)	195 (63)		235	0.94
E-4d, [N^{n}Bu$_4$][B(C$_6$F$_5$)$_4$]	-80 (66)	185 (66)		265	3.02
E-4e, [N^{n}Bu$_4$][B(C$_6$F$_5$)$_4$]	-65 (72)	205 (76)		270	3.67
E-5a,[E50] [N^{n}Bu$_4$][B(C$_6$F$_5$)$_4$]	-15 (68)	225 (74)		240	1.14
E-5b, [N^{n}Bu$_4$][B(C$_6$F$_5$)$_4$]	-40 (80)	220 (81)	575 (84)	260/ 355	2.48/ 100
E-5c, [N^{n}Bu$_4$][B(C$_6$F$_5$)$_4$]	-45 (66)	205 (70)		250	1.68
E-6a,[E50] [N^{n}Bu$_4$][B(C$_6$F$_5$)$_4$]	-15 (71)	220 (80)		235	0.94
E-6b, [N^{n}Bu$_4$][B(C$_6$F$_5$)$_4$]	-30 (77)	220 (73)	585 (72)	250/ 365	1.68/ 147

[a]Potentials vs FcH/FcH$^+$, scan rate 100 mV·s^{-1} at a glassy carbon electrode of **E-3a**–**e**, **E-4a**–**e**, **E-5a–c** and **E-6a,b** (1.0 mmol·L^{-1} using 0.1 mol·L^{-1} [N^{n}Bu$_4$][B(C$_6$F$_5$)$_4$]; 0.3 mmol·L^{-1} (**E-3b**), 1.0 mmol·L^{-1} (**E-3a,c**–**e**) using 0.1 mol·L^{-1} [N^{n}Bu$_4$][PF$_6$] as supporting electrolyte) in dry dichloromethane at 25 °C. [b]$E^{\circ\prime}$ = Formal potential. [c]ΔE_p = difference between the oxidation and the reduction potential. [d]$\Delta E^{\circ\prime}$ = potential difference between the two ferrocenyl-related redox processes. [e]K_C = comproportionation constant.

The voltammograms of **E-3b**–**e** measured in the presence of [N^{n}Bu$_4$][B(C$_6$F$_5$)$_4$] are shown in Figure E4 and the ones measured using [N^{n}Bu$_4$][PF$_6$] as supporting electrolyte are depicted in Figure SI10. The voltammogramms of oxides **E-4a**–**e** are shown in Figure SI11 and those of sulfides **E-5b**,**c** and selenide **E-6b** in Figure SI12.

The ferrocenyl units of **E-3a**–**e**, **E-4a**–**e**, **E-5a**–**c** and **E-6a**,**b** could be oxidized individually showing two (**E-3a**, **E-3c**–**e**, **E-4a**, **E-4c**–**e**, **E-5a,c**) or three (**E-3b**, **E-4b**, **E-5b**, **E-6b**) reversible redox processes with differences between cathodic and anodic peak potentials

(ΔE_p) between 60 mV and 87 mV (Table E4). The $E^{\circ}_1{}'$ values for the first oxidation of **E-3a**–**e** are shifted to lower potentials due to an increase of the electron density within this series. A comparison with phosphole **E-3a** allows the assignment of the first two oxidations in **E-3b** to the ferrocenyl units in 2- and 5-position, followed by the oxidation of the phosphorus bonded ferrocenyl. The redox splittings ($\Delta E^{\circ\prime}$) increase in the series **E-3a** ≈ **E-3b** < **E-3c** < **E-3e** < **E-3d** indicating a larger thermodynamic stability of [**E-3d**]$^+$ associated with a greater comproportionation constant (K_c) (Table E4).

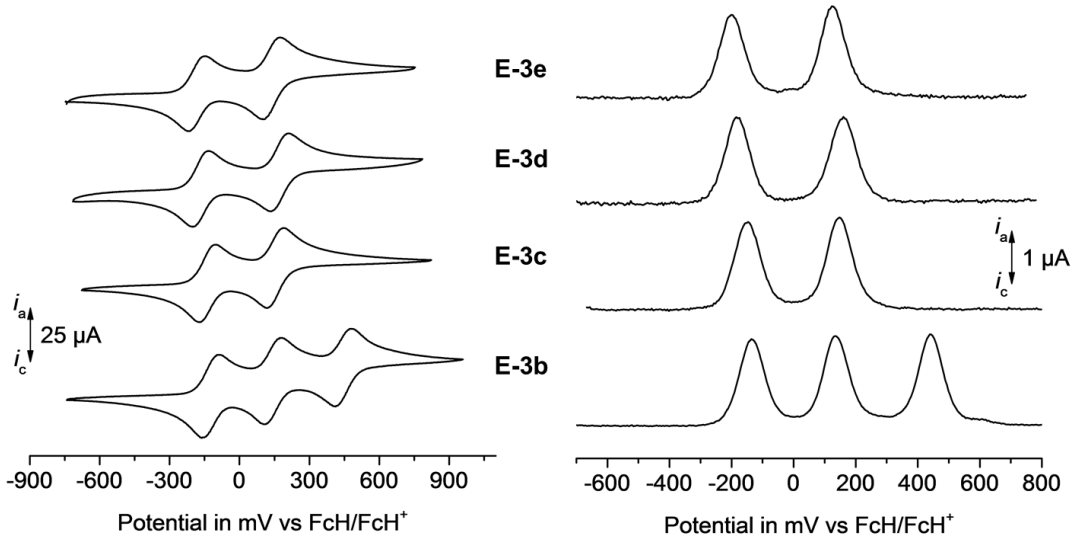

Figure E4. Left: Cyclic voltammograms of **E-3b–e**; scan rate: 100 mV·s^{-1}. Right: Square wave voltammograms of **E-3b–e** in dichloromethane solutions (1.0 mmol·L^{-1}) at 25 °C, supporting electrolyte 0.1 mol·L^{-1} [N^{n}Bu$_4$][B(C$_6$F$_5$)$_4$], working electrode: glassy carbon electrode (surface area 0.031 cm²).

Use of [N^{n}Bu$_4$][PF$_6$] as supporting electrolyte results in lower $\Delta E^{\circ\prime}$ values caused by higher ion-pairing capability (spherical diameter [PF$_6$]$^-$, 3.3 Å; [B(C$_6$F$_5$)$_4$]$^-$, 10 Å).[E58] Due to the ion pairing the small [PF$_6$]$^-$ counter-ion shields a large part of the electrostatic interactions between the ferrocenium units in [**E-3a**–**e**]$^{2+}$ and hence the electrostatic stabilization part of $\Delta E^{\circ\prime}$ is reduced. Therefore, the difference between the $\Delta E^{\circ\prime}$ ([B(C$_6$F$_5$)$_4$]$^-$) and the $\Delta E^{\circ\prime}$ ([PF$_6$]$^-$) values ($\Delta\Delta E^{\circ\prime}$) give some information on the contribution of electrostatics on the redox splitting.[E48] With exception of **E-3d** ($\Delta\Delta E^{\circ\prime}$ = 110 mV), for all species $\Delta\Delta E^{\circ\prime}$ values of ca. 90 mV were observed. The high redox splitting for **E-3d** ([N^{n}Bu$_4$][B(C$_6$F$_5$)$_4$]) may in part be caused by additional electrostatic interactions.

A comparison with other diferrocenyl-substituted heterocycles shows that the $E^{\circ}_1{}'$ and $\Delta E^{\circ\prime}$ values for **E-3a**–**E-3e** are in the range between 2,5-diferrocenylfuran (290 mV)[E43] and 2,5-diferrocenyl-1-methyl-1*H*-pyrrole (410 mV)[E43]. The increase of the redox splittings in this

series **E-3b** ≤ **E-3a** ≤ **E-3c** < **E-3e** < **E-3d** may indicate a higher electronic interaction for the ferrocenyls in phospholes with the bulky, electron-donating groups (2,4,6-triphenylphenyl and 2,4,6-tri-*tert*-butylphenyl) bonded to the P atom. While the use of $\Delta E^{\circ\prime}$ is often an unsuited measure for the determination of electron transfer interaction,[E59] the similar electrostatic contributions and likely similar energetics of solvation, reorganization and ion-pairing across the series allows the use of $\Delta E^{\circ\prime}$ to estimate the relative resonance stabilization contribution as a function of substituent. The chemical oxidation of the phosphorus atom with hydrogen peroxide, sulfur and selenium, respectively, leads to a shift to higher potentials of the first redox event of approximately 80–120 mV.

To further explore the influence of the steric properties of the P-bonded substituents on the $^{c}C_4H_2P$ core on the underlying electronic structure of the mixed-valence one-electron oxidation products, *in situ* UV/Vis-NIR measurements were carried out. The UV/Vis-NIR spectroelectrochemical measurements **E-3b**–**e** (2.0 mmol·L^{-1}) in dichloromethane containing [N^{n}Bu$_4$][B(C$_6$F$_5$)$_4$] (0.1 mol·L^{-1}) as supporting electrolyte were measured in an OTTLE (= Optically Transparent Thin-Layer Electrochemical) cell.[E60] The compounds were oxidized by stepwise increase of the potentials (step width: 25 mV, 50 mV or 100 mV). During the measurements, oxidation of the neutral compounds to mixed-valence mono-cationic [**E-3b**]$^{+}$–[**E-3e**]$^{+}$, and finally to the dicationic species [**E-3b**]$^{2+}$–[**E-3e**]$^{2+}$ occurred. After complete oxidation, each compound was reduced at -200 mV to prove the reversibility and the resulting UV/Vis-NIR spectra were identical to those of the neutral compounds.

The UV/Vis-NIR spectra of **E-3b**–**e** are depicted in Figures SI13 (**E-3b**), SI14 (**E-3c**), SI15 (**E-3d**) and E5 (**E-3e**). For neutral compounds **E-3b**–**e** no absorption in the NIR region (1000–3000 nm) could be observed. During the oxidation and the formation of mixed-valence [**E-3b**]$^{+}$–[**E-3e**]$^{+}$, a broad band between 1500 and 2500 nm arises. The further increase of the potentials resulted in the disappearance of these absorptions as well as the formation of a typical MLCT-double-band for the dicationic species at 976 and 1070 nm. The disappearance of the broad band after second oxidation is typical for intervalence charge transfer (IVCT) absorptions. The observed spectra can be deconvoluted into three Gaussian-shaped bands, which represent the IVCT excitations, a ligand field transition and a third band simulating the edge to the higher absorptions. The sum of the Gaussian-shaped absorptions fits almost exact with the experimental spectra. Thus, the intensity, ε_{max}, the full-width-at-halfheight, $\Delta\nu_{1/2}$ and the ν_{max} values for the IVCT transition could be determined.

Table E5. NIR data of the IVCT absorptions of phospholes [E-3a]$^+$–[E-3e]$^+$.[a]

Compd.	ν_{max} (cm^{-1}) (ε_{max} (L·mol^{-1}·cm^{-1}))	$\Delta\nu_{1/2}$ (cm^{-1})	$(\Delta\nu_{1/2})_{theo}$[b] (cm^{-1})
[**E-3a**]$^+$[E50]	5000 (1750)	3050	3398
[**E-3b**]$^+$	4850 (1850)	3250	3343
[**E-3c**]$^+$	4900 (2750)	2700	3365
[**E-3d**]$^+$	4650 (2650)	2800	3270
[**E-3e**]$^+$	5050 (3000)	2550	3418

[a]In dry dichloromethane containing 0.1 mol·L^{-1} of [N^{n}Bu$_4$][B(C$_6$F$_5$)$_4$] as supporting electrolyte at 25 °C. [b]Values calculated as $(\Delta\nu_{1/2})_{theo} = (2310\cdot\nu_{max})^{1/2}$ according to the Hush relationships for weakly coupled systems.[E61]

Compounds [**E-3b**]$^+$–[**E-3e**]$^+$ show IVCT absorptions of moderate strength, summarized in Table E5 and illustrated for [**E-3e**]$^+$ in Figure E5. Deconvolution of the band envelope into a sum of Gaussian-shaped bands is provided, although the assumptions of the appropriateness of Gaussian-shaped sub-bands (especially for strongly coupled complexes) and the potential for multiple solutions to the deconvolution means that such data must be treated cautiously. Nevertheless, for weakly coupled (Class II) systems, Gaussian-shaped bands are largely expected, and the use of the minimum number of sub-bands gives consistent fits, so these data are analyzed further here. A comparison of **E-3b** with phosphole **E-3a**[E50] shows that both compounds exhibit a IVCT transition of similar strength (**E-3a**, ε_{max} = 1750 L·mol^{-1}·cm^{-1}, $\Delta\nu_{1/2}$ = 3050 cm^{-1}; **E-3b**, ε_{max} = 1850 L·mol^{-1}·cm^{-1}, $\Delta\nu_{1/2}$ = 3250 cm^{-1}).

The mesityl-functionalized derivative **E-3c** possesses similar energies, but shows a significantly increase of the intensity (ε_{max} = 2750 L·mol^{-1}·cm^{-1}) and a decrease of the full-width-at-halfheight ($\Delta\nu_{1/2}$ = 2700 cm^{-1}) consistent with an increased coupling between the ferrocene and ferrocenium moieties through the phosphole bridge. Compound **E-3d** exhibits similar ε_{max} and $\Delta\nu_{1/2}$ values as **E-3c**, but a lower energy for the IVCT transition (Table E5). A further increase of the electronic interaction was achieved for **E-3e** featuring the 2,4,6-tri-*tert*-butylphenyl group, for which the intensity increases further to ε_{max} = 3000 L·mol^{-1}·cm^{-1} and the full-width-at-halfheight decreases to $\Delta\nu_{1/2}$ = 2550 cm^{-1}.

In this respect, a flattening of the P pyramidal environment (see X-ray discussion) caused by the steric strain of the P-bonded substituent is consistent with the proposed enhanced electronic coupling between the ferrocenyl units. Based on the intensity and half-height band-width of the IVCT band, phospholes **E-3b**–**e** can be classified as moderately coupled class II systems according to the scheme introduced by Robin and Day.[E62]

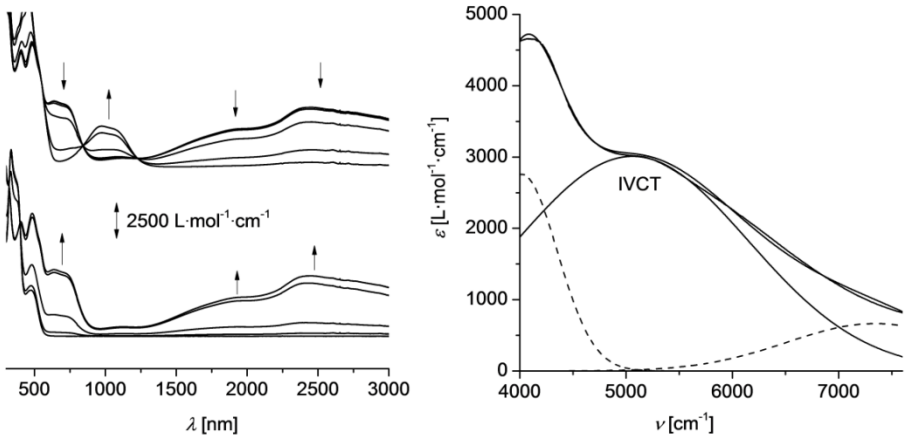

Figure E5. Left: UV/Vis-NIR spectra of **E-3e** at 25 °C in dichloromethane (2.0 mmol·L^{-1}) at rising potentials (bottom: -200 to 215 mV; top: 215 to 800 mV vs Ag/AgCl); supporting electrolyte [N^{n}Bu$_4$][B(C$_6$F$_5$)$_4$]. Right: Deconvolution of the NIR absorptions of [**E-3e**]$^+$ using three Gaussian shaped bands determined by spectroelectrochemistry in an OTTLE cell.

A comparison of the IVCT absorption of **E-3e** with other diferrocenyl-substituted heterocycles shows that it exhibits similarly strong intermetallic interactions as 2,5-diferrocenyl-1-methyl-1*H*-pyrrole (ε_{max} = 3145 L·mol^{-1}·cm^{-1}, $\Delta\nu_{1/2}$ = 2314 cm^{-1})[E43] and ferrocenyl-substituted siloles (ε_{max} = 3150 L·mol^{-1}·cm^{-1}, $\Delta\nu_{1/2}$ = 2950 cm^{-1}).[E42]

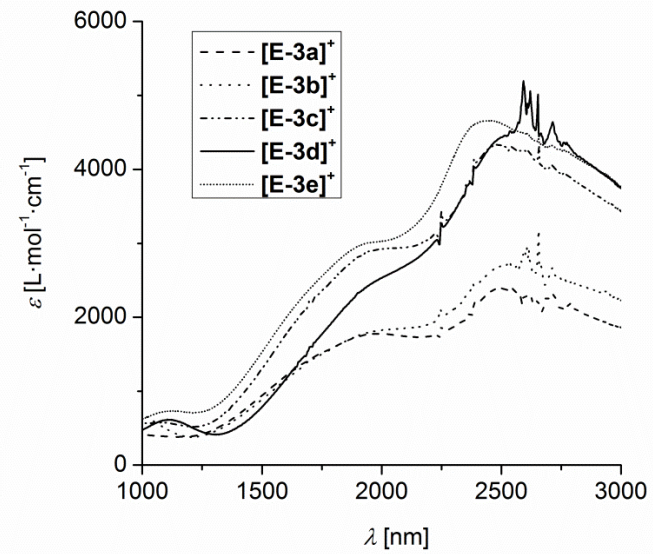

Figure E6. UV/Vis-NIR spectra of *in situ* generated [**E-3a**]$^+$–[**E-3e**]$^+$ at 25 °C in dichloromethane (2.0 mmol·L^{-1}), supporting electrolyte [N^{n}Bu$_4$][B(C$_6$F$_5$)$_4$].

E3 Computational studies

To augment the discussions and interpretations of the electrochemical and NIR data, electronic structure calculations for the representative complexes [**E-3a´**]$^{n+}$,[E50] [**E-3c´**]$^{n+}$, [**E-3d´**]$^{n+}$ and [**E-3e´**]$^{n+}$ were performed (n = 0, 1; Gaussian09, B3LYP, LANL2DZ for Fe,

6-31G** all other atoms, CPCM (dichloromethane) solvent model), the electronic structure of [**E-3a´**]$^{n+}$ having been previously discussed from calculations with a smaller basis set (3-21G* all atoms) (the prime ´ notation being used to distinguish the computational systems from the physical samples). The geometry optimizations revealed many local minima, which can be principally described in terms of the disposition of the ferrocenyl moieties relative to the phosphole substituent (*syn* vs *anti*) and, in the case of the cations, localization of the charge on either of the non-equivalent ferrocences in these chiral systems, with single point energies that differ by less than 6 kJ $\cdot$mol^{-1}.

Table E6. Calculated relative energies, selected geometric parameters and the Bird Index for syn- and anti-isomers of E-3a´, E-3c´, E-3d´ and E-3e´, with reference data from the molecular structures.

Geometric Feature	*syn-* **E-3a´**	*anti-* **E-3a´**	*anti-* **E-3c**	*syn-* **E-3c´**	*anti-* **E-3c´**	*syn-* **E-3d**	*syn-* **E-3d´**	*anti-* **E-3d´**	*anti-* **E-3e**	*syn-* **E-3e´**	*anti-* **E-3e´**
relative energy / kJ.mol^{-1}	0	+0.5		0	+3.2		0	+3.1		+2.7	0
distance P out of C_4 plane / Å	0.176	0.205	0.330(3)	0.268	0.282	0.253(5)	0.292	0.301	0.346(3)	0.317	0.303
α / °	7.85	9.19	15	12.16	12.86	11	13.34	13.82	16	14.86	14.26
distance C_{Aryl} out of C1-P-C4 plane / Å	1.726	1.704	1.573(6)	1.593	1.577	1.613(4)	1.583	1.546	1.283(3)	1.305	1.281
β / °	68.84	67.15	59	59.35	58.47	61	58.57	56.58	44	45.17	43.98
sum of angles about P / °	300.35	302.78	312	313.36	314.63	310	314.25	317.18	331	331.51	332.85
Bird Index	19.2	20.1	32	26.3	27.6	30	28.4	29.0	46	39	40.6
Mulliken charge (P)	0.376	0.369		0.398	0.388		0.406	0.402		0.389	0.379

Turning attention initially to the closed shell systems, geometry optimizations revealed trends in excellent agreement with those determined from the crystallographic structures. Tables of critical bond lengths and angles are given in the supporting information, with the greatest deviation in bond lengths (0.05 Å) being associated with the Fe-Cp(centroid) distance. Other calculated bond lengths are generally within 0.02 Å of the crystallographically determined structures and bond angles generally fall within 2 °. Of some considerable interest here is the degree to which the computational model reproduce the trends in the key angles α, the especially the important parameter β, the sum of angles at the phosphorus center, and the Bird Index (Table E6). The general features of the HOMO and LUMO orbitals vary little

across the series, and are generally well described in terms of 1,4-disubstituted butadiene-like backbone, with the HOMO composition essentially invariant as a function of the phosphole substitutents, and featuring approximately 30:40:30 (Fc:C_4H_4:Fc) character, and a negligible contribution from the phosphorus atom (Table E7). However, when looking somewhat deeper into the orbital manifold, some important trends in the electronic structure can be found that may explain the structural and electronic variations that are evinced in the key parameters α, β and the Bird Index. For the parent system **E-3a´** the first orbital with appreciable P(p) / C_4H_4 (π) character, which also closely resemble the highest lying π-orbital of the prototypical 5-membered aromatic system $[C_5H_5]^-$, are the HOMO-5, which lie 1.45 - 1.52 eV below the HOMO (Table E7). In progressing through the series *syn*/*anti*-**E-3c´**, *syn*/*anti*-**E-3d´** and *syn*/*anti*-**E-3e´** the HOMO-5 becomes the only high-lying orbital with important P(p)-C_4H_2(π) character, and the contribution from this fragment of the π system is significantly increased for the bulkier aryl groups (Table E7, Figure E7).

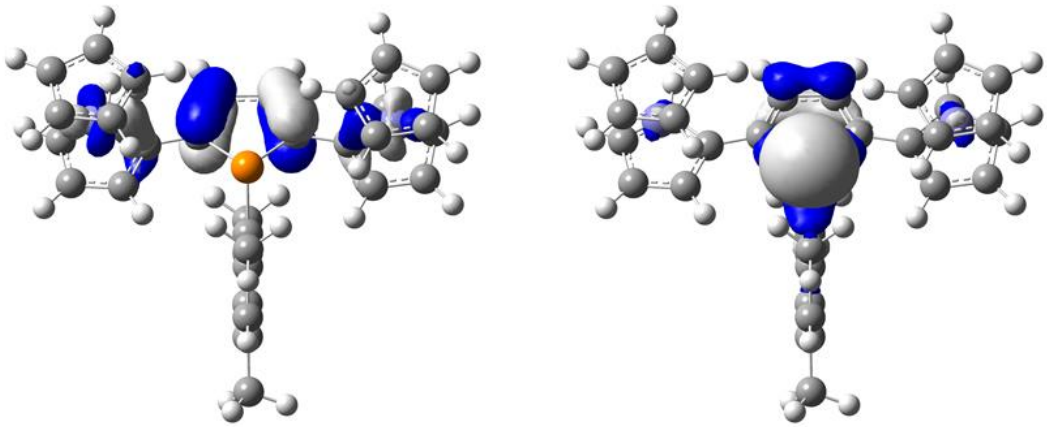

Figure E7. Plots of the HOMO (left) and HOMO-5 (right) of syn-**E-3c'** (isosurface ±0.04 (e bohr^{-3})$^{1/2}$).

The energy gap between the HOMO-5 and the HOMO also decreases along the series **E-3a´** > **E-3c´** > **E-3d´** > **E-3e´**. It is therefore very likely that the increasing aromatic character as a function of the bulk of the aryl group evinced in the structural data is due to the π character of the HOMO-5. In turning attention to the radical cations, the optimization is complicated not only by the presence of *anti*- and *syn*- isomers, which differ in energy by <6 kJ mol^{-1} (Table E7), but also by the stereochemically distinct nature of the redox-active ferrocenyl

moieties. For convenience and clarity of discussion, only one redox isomer of each of the lowest energy localized, *anti*- and *syn*- conformers are described here.

Table E7. Composition (%) and energy (eV) of selected orbitals in the frontier region of *syn*- and *anti*-isomers of E-3a´, E-3c´, E-3d´ and E-3e´.

Orbital	energy / eV	Fc(1)	C_4H_4	P	Ar	Fc(2)
anti-**E-3a´**						
LUMO	–1.60	15	56	8	5	15
HOMO	–5.05	32	38	0	1	29
HOMO-5	–6.50	20	7	27	6	39
HOMO-7	–6.55	3	7	17	4	69
syn-**E-3a´**						
LUMO	–1.58	16	56	8	5	16
HOMO	–5.05	30	39	0	1	30
HOMO-5	–6.51	42	3	12	1	42
HOMO-7	–6.57	20	15	41	5	20
anti-**E-3c´**						
LUMO	–1.49	16	53	9	5	16
HOMO	–5.05	31	39	0	1	29
HOMO-5	–6.28	2	22	56	14	7
syn-**E-3c´**						
LUMO	–1.47	17	54	8	5	16
HOMO	–5.03	30	40	0	1	29
HOMO-5	–6.27	6	21	58	8	7
anti-**E-3d´**						
LUMO	–1.37	5	33	7	45	10
HOMO	–5.10	19	38	1	1	41
HOMO-5	–6.05	1	19	41	36	2
syn-**E-3d´**						
LUMO	–1.46	15	51	9	9	16
HOMO	–4.98	28	42	0	1	29
HOMO-5	–6.06	4	17	41	36	2
anti-**E-3e´**						
LUMO	–1.27	14	48	11	9	17
HOMO	–5.04	23	39	1	1	36
HOMO-5	–5.84	2	28	54	13	3
syn-**E-3e´**						
LUMO	–1.35	17	48	10	8	17
HOMO	–4.96	28	41	0	1	30
HOMO-5	–5.89	4	25	55	12	4

As with the neutral (closed shell) analogues, the parent system *anti*- and *syn*-[**E-3a´**]$^+$ provide convenient benchmarks against which to make comparison with other members of the series. The *syn* and *anti* forms of [**E-3a´**]$^+$ are well described in terms of a classical 'mixed-valence' species, with clear structural evidence for the oxidation of one, but not both,

ferrocenyl moieties and a change in the bond length alternation along the butadiene backbone (Table E9). Thus, the Fe(1)-Cp(01) distance in **E-3a´** elongates in [**E-3a´**]$^+$ whilst the Fe(2)-Cp(06) distances are almost unchanged.

Table E8. Composition (%) and energy (eV) of *β*-HOMO and *β*-LUMO orbitals of *syn*- and *anti*-isomers of [E-3a´]$^+$, [E-3c´]$^+$, [E-3d´]$^+$ and [E-3e´]$^+$.

Orbital	energy / eV	Fc(1)	C_4H_4	P	Ar	Fc(2)
anti-[**E-3a´**]$^+$						
β-LUMO	–3.61	85	11	1	0	3
β-HOMO	–5.75	8	19	0	0	72
syn-[**E-3a´**]$^+$						
β-LUMO	–3.63	85	11	1	0	3
β-HOMO	–5.74	8	20	1	1	70
anti-[**E-3c´**]$^+$						
β-LUMO	–3.57	85	11	1	0	3
β-HOMO	–5.73	8	19	1	0	71
syn-[**E-3c´**]$^+$						
β-LUMO	–3.59	85	10	1	0	3
β-HOMO	–5.73	9	21	1	1	69
anti-[**E-3d´**]$^+$						
β-LUMO	–3.53	86	9	1	1	3
β-HOMO	–5.70	8	20	1	1	71
syn-[**E-3d´**]$^+$						
β-LUMO	–3.58	85	10	1	0	3
β-HOMO	–5.68	9	22	1	1	67
anti-[**E-3e´**]$^+$						
β-LUMO	–4.20	51	21	0	0	28
β-HOMO	–5.20	36	4	3	1	56
syn-[**E-3e´**]$^+$						
β-LUMO	–3.55	86	9	2	0	3
β-HOMO	–5.66	8	19	2	1	71

Similarly, the pattern of short / long / short bonds along the butadiene backbone that characterize neutral complexes **E-3a´** becomes less pronounced in [**E-3a´**]$^+$. The intra-ring P-C distances are largely unaffected by the oxidation process, consistent with the notion of limited P(p)-C_4H_2(π) character in these parent complexes. Consistent with these geometric observations, the *β*-HOMO and *β*-LUMO localized on different ferrocenyl moieties, and the butadiene-like fragment (Table E8). There is little involvement of the phosphorus center in these orbitals.

As the steric bulk of the phosphole substitutent increases, there is little change in the composition of the *β*-HOMO and *β*-LUMO which all indicate rather localized electronic structures, except in the case of the most sterically congested example *anti*-[**E-3e´**]$^+$.

Table E9. Selected bond lengths (Å) associated with the phosphole ring in *syn*- and *anti*-isomers of [E-3a´]$^+$, [E-3c´]$^+$, [E-3d´]$^+$ and [E-3e´]$^+$.

	anti-[**E-3a**]$^+$	*syn*-[**E-3a**]$^+$	*anti*-[**E-3c**]$^+$	*syn*-[**E-3c**]$^+$	*syn*-[**E-3d**]$^+$	*anti*-[**E-3d**]$^+$	*syn*-[**E-3e**]$^+$	*anti*-[**E-3e**]$^+$
relative energy	0 kJ/mol	+2.1 kJ/mol	0 kJ/mol	+2.5 kJ/mol	0 kJ/mol	+3.5 kJ/mol	0 kJ/mol	+2.6 kJ/mol
C2-C3	1.3783	1.3781	1.3854	1.3846	1.3848	1.3849	1.3944	1.3942
C3-C4	1.4314	1.4308	1.4237	1.4236	1.4214	1.4228	1.4125	1.4137
C4-C5	1.3761	1.3766	1.3825	1.3832	1.3835	1.3817	1.3928	1.3942
P-C2	1.8341	1.8317	1.8230	1.8208	1.8159	1.8238	1.8067	1.7997
P-C5	1.8307	1.8328	1.8163	1.8162	1.8163	1.8144	1.7875	1.7832
$\alpha^{[a]}$	8.89	8.70	12.42	12.67	13.85	12.26	13.93	13.51
$\beta^{[b]}$	67.39	67.60	58.49	58.44	57.09	58.45	43.05	40.61
Bird Index	24.2	24.3	32.5	33.0	34.1	32.5	45.4	48.5

[a]α = Angle of deflection of phosphorus atom out of dienic carbon plane. [b]β = Angle of deflection of the carbon atom of the phosphorus substituent from the C2-P-C5 plane of the phosphole ring.

Here, there is a rather more even distribution of the β–LUMO (51:28%) and β–HOMO (36:56%) over both ferrocene moieties (Table E8). Perhaps more informative than the trends in a subset of the molecular orbitals, are the geometric trends within the phosphole moiety, which reflect the sum of bonding interactions through the molecular framework (Table E9). The most obvious trend is the increasing loss of buta-1,3-diene character in the C_4H_2 fragment as the aryl group increases in steric bulk, consistent with the progressive increase in delocalized electronic character in the bridge. This is compounded by a progressive decrease in the P-C bond lengths, which indicates increasing multiple bond character, also consistent with the concept of a more delocalized structure to the phosphole bridge in these mixed-valence complexes. This increasingly pronounced delocalization within the heterocyclic ring is best reflected by the change of the Bird Index within mixed-valent [**E-3a´**]$^+$, [**E-3c´**]$^+$, [**E-3d´**]$^+$ and [**E-3e´**]$^+$ (Table E9). While for both conformers of [**E-3a´**]$^+$ values of ca. 24 are obtained, the increase in the steric strain within the more crowded compounds results in higher Bird indices up to a value of 48.5 for *anti*-[**E-3e´**]. The trends observed for α and β are also in accordance to the ones observed by X-ray diffraction analysis for neutral **E-3b-e**. The subtle, but important, structural rearrangement of the bridge serves to enhance the aromaticity, or at least the degree of delocalization, within the bridging ligand, despite the substantially metal localized redox chemistry. It is very likely that this increased delocalization also serves to stabilize the mixed-valence form and accounts in part for the larger K_c values for the bulkier members of the series [**E-3n**]$^+$. It is more difficult to trace the origins of the enhanced delocalization, and accompanying optical properties, to a single molecular orbital or transition

between pairs of orbitals. This is perhaps not unexpected given that the for an $n\pi$ electron ring system, all of the n/2 lowest energy π orbitals contribute to the aromaticity (or anti-aromaticity) of the system. It seems that here the combination of the aryl moiety, which provides a steric contribution to the planarity of the five-membered 2,5-ferrocenyl-$^{c}C_4H_2PAr$ ring, the ferrocenyl redox centers, which provide 18 / 17-valence electron configurations that can be used to stabilize the localized mixed valence configuration, and the potentially 6π system for which simple Hückel theory predicts aromatic character, when in a planar system is important in deriving the enhanced delocalization seen for the bulkier members of the series of complexes explored here. Such sterically and electronically flexible, but redox innocent, bridges open even further realms of complexity in the study of mixed-valence complexes.

E4 Conclusions

2,5-Diferrocenyl-1-Ar-1*H*-phospholes **E-3b**–**e** (Ar = ferrocenyl (**b**), mesityl (**c**), 2,4,6-triphenylphenyl (**d**), 2,4,6-tri-*tert*-butylphenyl (**e**)) were synthesized by the reaction of 1,4-diferrocenyl butadiyne and the corresponding arylphosphines $ArPH_2$ (**E-1b**–**e**). Variable temperature NMR experiments were carried out to determine the activation enthalpy and activation entropy of the inversion at the phosphorus atom. Thereby, a decrease of the activation enthalpy, as well as the coalescence temperature with enlargement of the substituent at the phosphorus atom is characteristic. A comparison of the activation parameters with 1-isopropyl-2-methyl-5-phenylphosphole[E15] shows that phospholes **E-3b**–**d** exhibit lower activation enthalpies and similar activation entropies.

Compounds **E-3b**–**e** have been structurally characterized by single-crystal X-ray diffraction. An increased planarity of the pyramidal phosphorus environment was found, when the bulky 2,4,6-tri-*tert*-butylphenyl substituent was applied (**E-3e**). This increased flattening is in accordance with the observations in literature as 1-(2,4,6-tri-*tert*-butylphenyl)-3-methylphosphole[E33] exhibit an enhanced delocalization when compared to unhindered analogues. Calculations of the Bird Index[E36] revealed higher delocalization for phospholes with more bulky substituents (*e.g.*, **E-3e**).

Electrochemical measurements showed that each ferrocenyl unit could be oxidized separately, indicating an electronic interaction between them. Cationic $[\mathbf{E\text{-}3b}]^+$–$[\mathbf{E\text{-}3e}]^+$ exhibit IVCT absorptions of moderate strength determined by UV/Vis-NIR measurements. Comparison with **E-3a** (Ar = phenyl) shows an increased interaction between Fc/Fc^+ for the phospholes with sterically demanding substituents on the phosphorus atom. Measurements

using different electrolytes ($[B(C_6F_5)_4]^-$ and $[PF_6]^-$) allow some insight in the electrostatic contribution on the redox splitting, demonstrating that throughout the series the electrostatic interactions are similar. The highest interaction determined by spectroelectrochemical measurements was observed for **E-3e** (ε_{max} = 3000 L·mol^{-1}·cm^{-1}, $\Delta\nu_{1/2}$ = 2550 cm^{-1}). It could be shown that a variation of the substituents of the phosphorus atom influences the electronic interaction of the ferrocenyls in 2- and 5-position.

Phospholes **E-3b**–**e** could be classified as moderate coupled class II system according to Robin and Day. Compared with other diferrocenyl substituted heterocycles, the strength of the electronic interaction in **E-3e** is in the same range as 2,5-diferrocenyl-1-methyl-1*H*-pyrrole (ε_{max} = 3145 L·mol^{-1}·cm^{-1}, $\Delta\nu_{1/2}$ = 2314 cm^{-1}).[E43] The further planarization of the ring system and increased aromatic character of the phosphole ring indicated by DFT-based calculations provides an additional, and unexpected, contribution to the stabilization of the mixed-valence state.

E5 Experimental Section

General data

All reactions were carried out under an argon (5.0) atmosphere using standard Schlenk techniques. Tetrahydrofuran was purified by distillation from sodium/benzophenone ketyl; toluene and dichloromethane were obtained from a MBRAUN (MB-SPS 800) solvent drying and purification system (double column solvent filtration, working pressure 0.5 bar). For electrochemistry HPLC grade dichloromethane was purified by distillation from calcium hydride. For column chromatography silica was used with a particle size of 40–60 µm (230–400 mesh (ASTM), Fa. Macherey-Nagel).

Instruments

FT IR spectra were recorded with a Nicolet IR 200 spectrometer (Fa. Thermo). NMR spectra were recorded with a Bruker Avance III 500 spectrometer (500.3 MHz for ^{1}H, 125.7 MHz for ^{13}C{^{1}H} and 202.5 MHz for ^{31}P{^{1}H} spectra). Chemical shifts are reported in δ (parts per million) downfield from tetramethylsilane with the solvent as reference signal (^{1}H NMR: $CDCl_3$, δ = 7.26; $C_2D_2Cl_4$, δ = 5.91; C_7D_8, δ = 2.09; ^{13}C{^{1}H} NMR: $CDCl_3$, δ = 77.16; ^{31}P{^{1}H} NMR: standard external rel. 85% H_3PO_4, δ = 0.0; $P(OMe)_3$, δ = 139.0, respectively). For temperatures in the Eyring plot the system temperature was corrected by methanol (173–298 K) or ethylene glycol standards (298–373 K). The melting points were determined using a Gallenkamp MFB 595 010 M melting point apparatus. Elemental analyses were measured

with a Thermo FlashAE 1112 instrument. High-resolution mass spectra were recorded with a Bruker Daltonik micrOTOF-QII spectrometer.

Electrochemistry

Electrochemical measurements of **E-3b**–**e**, **E-4a**–**e**, **E-5b**,**c** and **E-6b** (1.0 mmol·L^{-1} using [N^{n}Bu$_4$][B(C$_6$F$_5$)$_4$]; 0.3 mmol·L^{-1} (**E-3b**), 1.0 mmol·L^{-1} (**E-3c**–**e**) using [N^{n}Bu$_4$][PF$_6$]) in dichloromethane were performed in a dried, argon purged cell at 25 °C with a Radiometer Voltalab PGZ 100 electrochemical workstation interfaced with a personal computer. 0.1 mol·L^{-1} [N^{n}Bu$_4$][B(C$_6$F$_5$)$_4$] or [N^{n}Bu$_4$][PF$_6$] were used as supporting electrolyte. For the measurements a three electrode cell containing a Pt auxiliary electrode, a glassy carbon working electrode (surface area 0.031 cm²) and an Ag/Ag$^+$ (0.01 mmol·L^{-1} [AgNO$_3$]) reference electrode fixed on a Luggin capillary was used. The working electrode was pretreated by polishing on a Buehler microcloth first with 1 micron and then ¼ micron diamond paste. The reference electrode was constructed from a silver wire inserted into a 0.01 mmol·L^{-1} [AgNO$_3$] and 0.1 mol·L^{-1} [N^{n}Bu$_4$][B(C$_6$F$_5$)$_4$] or [N^{n}Bu$_4$][PF$_6$] acetonitrile solution in a Luggin capillary with a vycor tip. This Luggin capillary was inserted in a second Luggin capillary containing a 0.1 mol·L^{-1} [N^{n}Bu$_4$][B(C$_6$F$_5$)$_4$] or [N^{n}Bu$_4$][PF$_6$] dichloromethane solution and a vycor tip. Experiments under the same conditions showed that all reduction and oxidation potentials were reproducible within 5 mV. Experimental potentials were referenced against an Ag/Ag$^+$ reference electrode but the presented results are referenced against ferrocene as an internal standard as required by IUPAC.[E57] To achieve this, each experiment was repeated in the presence of 1 mmol·L^{-1} decamethylferrocene (Fc*). Data were processed on a Microsoft Excel worksheet to set the formal reduction potentials of the FcH/FcH$^+$ couple to 0.0 V. Under our conditions the Fc*/Fc*$^+$ couple was at -619 mV *vs* FcH/FcH$^+$, ΔE_p = 60 mV, while the FcH/FcH$^+$ couple itself was at 220 mV *vs.* Ag/Ag$^+$, ΔE_p = 61 mV.[E63]

Spectroelectrochemistry

Spectroelectrochemical UV/Vis-NIR measurements of 2.0 mmol·L^{-1} solutions of **E-3b–e** in dry dichloromethane containing 0.1 mol·L^{-1} of [N^{n}Bu$_4$][B(C$_6$F$_5$)$_4$] as the supporting electrolyte were performed in an OTTLE (OTTLE = Optically Transparent Thin-Layer Electrochemical)[E60] cell with a Varian Cary 5000 spectrophotometer at 25 °C. The values obtained by deconvolution could be reproduced within ε_{max}: 100 L·mol^{-1}·cm^{-1}; ν_{max} 50 cm^{-1}; $\Delta\nu_{1/2}$ 50 cm^{-1}.

Single Crystal X-ray Diffraction Analysis

Suitable single crystals of **E-3b**–**e** for X-ray diffraction analysis were obtained by diffusion of hexane into a dichloromethane solution containing **E-3b**–**e** at ambient temperature. Data were collected with an Oxford Gemini S diffractometer at 104 K (**E-3e**) and 110 K (**E-3b**–**d**) with Mo K_α radiation (λ = 0.71073 Å). The structures were solved by direct methods and refined by full-matrix least-squares procedures on F^2.[E64,E65] All non-hydrogen atoms were refined anisotropically, and a riding model was employed in the treatment of the hydrogen atom positions.

Reagents

All starting materials were obtained from commercial suppliers and used without further purification. Ferrocenylphosphine,[E66] 2,4,6-mesitylphosphine,[E67] 2,4,6-tri-*tert*-butylphenylphosphine,[E68] (2,4,6-tri-*tert*-phenyl)phenylphosphine,[E69] 1,4-diferrocenyl butadiyne[E70] and 2,5-diferrocenyl-1-phenyl-1*H*-phosphole[E50] were prepared according to published procedures.

General procedure for the synthesis of 2,5-diferrocenyl-1-Ar-1*H*-phosphole (E-3)

Phosphines **E-1b**–**e** were dissolved in a mixture of 40 mL tetrahydrofuran/toluene (1:1, *v*:*v*) and at 0 °C *n*-butyllithium was added drop-wise. The resulting solution was stirred for 30 min at 0 °C and was then added drop-wise to a solution of 1,4-diferrocenyl butadiyne (**E-2**) in 20 mL of tetrahydrofuran. The resulting solution was stirred overnight at ambient temperature and afterwards all volatiles were removed in vacuum. The remaining solid was purified under argon by column chromatography (column size: 4 × 20 cm) on silica using a mixture of hexane/dichloromethane of ratio 10:1 (v/v) as eluent to give **E-3b**–**e** as orange colored solids.

Synthesis of 1,2,5-triferrocenyl-1*H*-phosphole (E-3b)

Following the general procedure described above, 0.22 g (1.0 mmol) of ferrocenylphosphine (**E-1b**) were reacted with 0.4 mL (1.0 mmol) of 2.5 M *n*-butyllithium and 0.42 g (1.0 mmol) of **E-2**. After appropriate work-up, **E-3b** could be obtained as orange solid. Yield 0.17 g (0.3 mmol, 26 % based on **E-1b**). Anal. Calcd. for $C_{34}H_{29}Fe_3P$ (636.01 g/mol): C, 64.20; H, 4.60. Found: C, 64.16; H, 4.82. Mp.: 165-170 °C (decomp.). IR data (KBr, ν/cm^{-1}): 3094 m, 3050 w, 2920 m, 2851 w, 1654 m, 1410 w. ^{1}H NMR ($CDCl_3$, δ): 3.96 (s, 5 H, C_5H_5 (P-Fc)), 4.07–4.09 (m, 12 H, C_5H_5/C_5H_4 (P-Fc)), 4.16–4.17 (m, 2 H, C_5H_4 (P-Fc)), 4.28 (m, 4 H, C_5H_4), 4.57 (m, 4 H, C_5H_4), 6.95 (d, $^3J_{HP}$ = 10.9 Hz, 2 H, C_4H_2P). ^{13}C{^{1}H} NMR ($CDCl_3$, δ): 67.45 (bs, C_5H_4), 68.56 (s, C_5H_4), 69.26 (s, C_5H_5 (P)), 69.50 (d, J_{CP} = 4.5 Hz, C_5H_4 (P)),

69.97 (s, C_5H_5), 71.26 (d, J_{CP} = 13.50 Hz, C_5H_4 (P)), 75.07 (d, $^1J_{CP}$ = 13.1 Hz, C^i/C_5H_4 (P)), 83.71 (d, $^2J_{CP}$ = 21.0 Hz, C^i/C_5H_4), 131.39 (d, $^2J_{CP}$ = 8.0 Hz, CH/C_4H_2P), 147.69 (d, $^1J_{CP}$ = 1.5 Hz, C^i/C_4H_2P). $^{31}P\{^1H\}$ NMR ($CDCl_3$, δ): -1.88 (s). HRMS (ESI-TOF, *m/z*): calcd for $C_{34}H_{29}Fe_3P$: 636.0051, found: 636.0057 $[M]^+$.

Crystal Data for E-3b: $C_{34}H_{29}Fe_3P$, M = 636.09 g·mol^{-1}, triclinic, *P*–1, λ = 0.71073 Å, *a* = 5.8730(3) Å, *b* = 11.6114(7) Å, *c* = 18.7807(12) Å, α = 89.127(5) °, β = 81.288(5) °, γ = 87.524(4) °, *V* = 1264.72(13) Å^3, Z = 2, ρ_{calcd} = 1.670 Mg·m^{-3}, μ = 1.785 mm^{-1}, *T* = 110(2) K, Θ range = 3.292-24.999°, reflections collected: 6997, independent: 6997 (R_{int} = 0.0550), R_1 = 0.0476, wR_2 = 0.1078 [I > 2σ(I)].

Synthesis of 2,5-diferrocenyl-1-mesityl-1*H*-phosphole (E-3c)

Using the general synthesis procedure described earlier, 0.15 g (1.0 mmol) of mesitylphosphine (**E-1c**) were treated with 0.3 mL (0.7 mmol) of 2.5 M *n*-butyllithium and 0.41 g (1.0 mmol) of **E-2**. After appropriate work-up, **E-3c** could be obtained as orange solid. Yield 0.26 g (0.5 mmol, 47 % based on **E-1c**). Anal. Calcd. for $C_{33}H_{31}Fe_2P$ (570.09 g/mol): C, 69.50; H, 5.48. Found: C, 69.76; H, 5.63. Mp.: 209 °C. IR data (KBr, ν/cm^{-1}): 3090 m, 3035 w, 2951 w, 2917 m, 2854 w, 1645 m, 1601 m, 1450 m, 1411 m, 1374 m. ^1H NMR ($C_2D_2Cl_4$, 70 °C, δ): 2.26 (s, 3 H, *p*-CH_3), 2.39 (s, 6 H, *o*-CH_3), 3.99 (s, 10 H, C_5H_5), 4.14 (m, 4 H, C_5H_4), 4.23 (m, 4 H, C_5H_4), 6.77 (d, $^3J_{HP}$ = 10.6 Hz, 2 H, C_4H_2P), 6.88 (s, 2 H, C_6H_2). $^{13}C\{^1H\}$ NMR ($CDCl_3$, δ): 21.36 (s, CH_3), 66.25 (d, J_{CP} = 4.9 Hz, CH/C_5H_4), 68.44 (s, CH/C_5H_4), 69.98 (s, C_5H_5), 83.09 (d, $^2J_{CP}$ = 18.3 Hz, C^i/C_5H_4), 125.89 (d, J_{CP} = 10.6 Hz, C^i/C_6H_2), 128.50 (d, $^2J_{CP}$ = 15.8 Hz, CH/C_4H_2P), 129.50 (d, $^3J_{CP}$ = 4.2 Hz, CH/C_6H_2), 140.78 (d, J_{CP} = 1.9 Hz, C^i/C_6H_2), 145.17 (d, $^1J_{CP}$ = 2.4 Hz, C^i/C_4H_2P). $^{31}P\{^1H\}$ NMR ($CDCl_3$, δ): -4.60 (s). HRMS (ESI-TOF, *m/z*): calcd for $C_{33}H_{31}Fe_2P$: 570.0858, found: 570.0897 $[M]^+$.

Crystal Data for E-3c: $C_{33}H_{31}Fe_2P$, M = 570.25 g·mol^{-1}, monoclinic, $P2_1/c$, λ = 0.71073 Å, *a* = 20.1433(9) Å, *b* = 11.2701(5) Å, *c* = 11.7872(4) Å, β = 105.211(4) °, *V* = 2582.15(19) Å^3, Z = 4, ρ_{calcd} = 1.467 Mg·m^{-3}, μ = 1.207 mm^{-1}, *T* = 110.00(14) K, Θ range = 2.925-26.000 °, reflections collected: 11287, independent: 5025 (R_{int} = 0.0298), R_1 = 0.0347, wR_2 = 0.0758 [I > 2σ(I)].

Synthesis of 2,5-diferrocenyl-1-(2,4,6-triphenylphenyl)-1*H*-phosphole (E-3d)

(2,4,6-Triphenylphenyl)phosphine (**E-1d**) (0.30 g, 0.9 mmol), 0.3 mL (0.8 mmol) of 2.5 M *n*-butyllithium and 0.38 g (0.9 mmol) of **E-2** were reacted accordingly to the general procedure described earlier, affording **E-3d** as orange solid. Yield 0.18 g (0.2 mmol, 26 %

based on **E-1d**). Anal. Calcd. for $C_{48}H_{37}Fe_2P$ (696.23 g/mol): C, 76.21; H, 4.93. Found: C, 75.98; H, 5.14. Mp.: 238 °C. IR data (KBr, ν/cm^{-1}): 3091 w, 3029 w, 2923 m, 2853 m, 1639 m, 1586 m, 1491 m. ^{1}H NMR (C_7D_8, 90 °C, δ): 3.94 (s, 10 H, C_5H_5), 4.07 (m, 4 H, C_5H_4), 4.25 (m, 4 H, C_5H_4), 6.19 (d, $^3J_{HP}$ = 12.1 Hz, 2 H, C_4H_2P), 7.08–7.11 (m, 3 H, C_6H_5), 7.11–7.17 (m, 7 H, C_6H_5), 7.34–7.39 (m, 3 H, C_6H_5), 7.52 (d, $^4J_{HP}$ = 1.6 Hz, 2H, C_6H_2). ^{13}C{^{1}H} NMR ($CDCl_3$, δ): 66.40 (bs, C_5H_4), 68.32 (s, C_5H_4), 70.01 (s, C_5H_5), 83.27 (d, $^2J_{CP}$ = 17.7 Hz, C^i/C_5H_4), 127.30 (s, CH/C_6H_5), 127.37 (bs, C_{phenyl}), 127.82 (d, J_{CP} = 17.3 Hz, C_{phenyl}), 128.14 (s, CH/C_6H_5), 128.70 (d, $^2J_{CP}$ = 14.7 Hz, CH/C_4H_2P), 128.99 (s, CH/C_6H_5), 130.39 (bs, C_{phenyl}), 139.69 (s, C_{phenyl}), 142.03 (d, J_{CP} = 1.62 Hz, C_{phenyl}), 147.40 (s, C^i/C_4H_2P). ^{31}P{^{1}H} NMR ($CDCl_3$, δ): -6.38 (s). HRMS (ESI-TOF, *m/z*): calcd for $C_{48}H_{37}Fe_2P$: 756.1328, found: 756.1349 $[M]^+$.

Crystal Data for E-3d: $C_{48}H_{37}Fe_2P$, M = 756.44 g·mol^{-1}, monoclinic, $P2_1/c$, λ = 0.71073 Å, a = 13.1656(3) Å, b = 19.4986(6) Å, c = 28.1129(9) Å, β = 98.298(2) °, V = 7141.3(4) Å^3, Z = 8, ρ_{calcd} = 1.407 Mg·m^{-3}, μ = 0.892 mm^{-1}, T = 110 K, Θ range = 2.880-25.000°, reflections collected: 39538, independent: 12534 (R_{int} = 0.0663), R_1 = 0.0489, wR_2 = 0.0889 [I > 2σ(I)].

Synthesis of 2,5-diferrocenyl-1-(2,4,6-tri-*tert*-butylphenyl)-1*H*-phosphole (E-3e)

2,4,6-Tri-*tert*-butylphenylphosphine (**E-1e**) (0.25 g, 0.9 mmol), 0.4 mL (0.9 mmol) of 2.5 M *n*-butyllithium and 0.43 g (1.0 mmol) of **E-2** were reacted accordingly to the general procedure described earlier. Yield 0.23 g (0.3 mmol, 36 % based on **E-1e**). Anal. Calcd. for $C_{42}H_{49}Fe_2P$ (696.23 g/mol): C, 72.43; H, 7.09. Found: C, 72.52; H, 7.46. Mp.: 222 °C (decomp.). IR data (KBr, ν/cm^{-1}): 3094 m, 3074 m, 2964 s, 2902 m, 2861 m, 1643 w, 1594 m, 1476 m, 1464 m, 1406 m, 1362 m. ^{1}H NMR ($CDCl_3$, δ): 1.35 (s, 9 H, CH_3), 1.37 (s, 18 H, CH_3), 4.02 (s, 10 H, C_5H_5), 4.03 (m, 4 H, C_5H_4), 4.06 (m, 4 H, C_5H_4), 6.95 (d, $^3J_{HP}$ = 14.9 Hz, 2 H, C_4H_2P), 7.52 (d, $^4J_{HP}$ = 3.1 Hz, 2H, C_6H_2). ^{13}C{^{1}H} NMR ($CDCl_3$, δ): 31.32 (s, *p*-C(CH_3)$_3$, 33.53 (d, $^4J_{CP}$ = 3.9 Hz, *o*-C(CH_3)$_3$, 67.58 (d, J_{CP} = 3.4 Hz, CH/C_5H_4), 67.72 (s, CH/C_5H_4), 69.88 (s, C_5H_5), 83.35 (d, $^2J_{CP}$ = 19.2 Hz, C^i/C_5H_4), 121.15 (d, J_{CP} = 19.5 Hz, C^i/C_6H_2), 123.81 (d, $^3J_{CP}$ = 9.5 Hz, CH/C_6H_2), 124.28 (d, $^2J_{CP}$ = 25.1 Hz, CH/C_4H_2P), 142.31 (d, $^1J_{CP}$ = 8.6 Hz, C^i/C_4H_2P), 153.09 (d, J_{CP} = 2.3 Hz, C^i/C_6H_2), 159.48 (d, J_{CP} = 12.3 Hz, C^i/C_6H_2). ^{31}P{^{1}H} NMR ($CDCl_3$, δ): 0.08 (s). HRMS (ESI-TOF, *m/z*): calcd for $C_{42}H_{49}Fe_2P$: 696.2267, found: 696.2300 $[M]^+$.

Crystal Data for E-3e: $C_{42}H_{49}Fe_2P$, M = 696.48 g·mol^{-1}, monoclinic, $P2_1/c$, λ = 0.71073 Å, a = 19.7980(5) Å, b = 15.0040(4) Å, c = 12.2254(3) Å, β = 105.996(3) °, V = 3490.93(16) Å^3, Z = 4, ρ_{calcd} = 1.325 Mg·m^{-3}, μ = 0.906 mm^{-1}, T = 104(6) K, Θ range = 2.919-24.995°,

reflections collected: 14377, independent: 6113 (R_{int} = 0.0304), R_1 = 0.0333, wR_2 = 0.0672 [I > 2σ(I)].

General procedure for the synthesis of the phosphole oxides E-4a–e

For the synthesis of the phosphole oxides, 20 mL H_2O_2 (1 wt%, 6 mmol) were added to a solution of phospholes **E-3a**–**e** dissolved in 20 mL of dichloromethane, and the reaction mixture was stirred at ambient temperature. The organic layer was separated and the aqueous phase was extracted with dichloromethane (3x10 mL). The combined organic extracts were dried with magnesium sulfate and the solvent was removed in vacuo. The resulting solids were purified by column chromatography (column size: 2x10 cm, silica, n-hexane/dichloromethane (10:1, v/v).

Synthesis of 2,5-diferrocenyl-1-phenyl-1*H*-phosphole oxide (E-4a)

Using the general synthesis procedure described above, 0.10 g (0.19 mmol) of **E-3a** were reacted for 30 min with H_2O_2 to afford **E-4a** as purple solid. Yield 0.08 g (0.15 mmol, 79 % based on **E-3a**). Anal. Calcd. for $C_{30}H_{25}Fe_2OP$ (544.03 g/mol): C, 66.21; H, 4.63. Found: C, 66.22; H, 5.04. Mp.: 143 °C. IR data (KBr, ν/cm^{-1}): 3087 m, 3045 w, 2954 w, 2922 m, 2854 w, 1584 m, 1435 m, 1403 w. ^{1}H NMR ($CDCl_3$, δ): 3.99 (s, 10 H, C_5H_5), 4.27 (m, 2 H, H^{β}/C_5H_4), 4.32 (m, 2 H, H^{β}/C_5H_4), 4.34 (m, 2 H, H^{α}/C_5H_4), 4.58 (m, 2 H, H^{α}/C_5H_4), 6.80 (d, $^3J_{HP}$ = 37.7 Hz, 2 H, C_4H_2P), 7.52-7.55 (m, 3 H, C_6H_5), 7.94-7.98 (m, 2 H, C_6H_5). ^{13}C{^{1}H} NMR ($CDCl_3$, δ): 65.95 (d, $^3J_{CP}$ = 6.1 Hz, C^{α}/C_5H_4), 67.28 (d, $^3J_{CP}$ = 5.2 Hz, C^{α}/C_5H_4), 69.77 (s, C^{β}/C_5H_4), 69.99 (s, C_5H_5), 77.73 (d, $^2J_{CP}$ = 13.6 Hz, C^{i}/C_5H_4), 129.14 (d, J_{CP} = 12.0 Hz, CH/C_6H_5), 130.01 (d, J_{CP} = 27.8 Hz, CH/C_6H_5), 130.74 (d, $^2J_{CP}$ = 10.5 Hz, CH/C_4H_2P), 130.85 (d, $^1J_{CP}$ = 91.11 Hz, C^{i}/C_6H_5), 132.29 (s, CH/C_6H_5), 137.97 (d, $^1J_{CP}$ = 97.0 Hz, C^{i}/C_4H_2P). ^{31}P{^{1}H} NMR ($CDCl_3$, δ): 38.83 (s). HRMS (ESI-TOF, *m/z*): calcd for $C_{30}H_{25}Fe_2OP$: 544.0337, found: 544.0329 $[M]^+$.

Synthesis of 1,2,5-triferrocenyl-1*H*-phosphole oxide (E-4b)

According to the general synthesis method described above, 0.10 g (0.16 mmol) of **E-3b** were reacted for 30 min with H_2O_2 giving **E-4b** as purple solid. Yield 0.06 g (0.09 mmol, 56 % based on **E-3b**). Mp.: 186 °C (decomp.). IR data (KBr, ν/cm^{-1}): 3083 m, 3037 w, 2952 w, 2923 m, 2847 w, 1584 m, 1513 m, 1409 m, 1339 m. ^{1}H NMR ($CDCl_3$, δ): 4.07 (s, 5 H, C_5H_5(P)), 4.19 (s, 10 H, C_5H_5), 4.31 (m, 2 H, C_5H_4), 4.39 (m, 4 H, C_5H_4), 4.41 (m, 2 H, C_5H_4), 4.62 (m, 2 H, C_5H_4), 4.88 (m, 2 H, C_5H_4), 6.77 (d, $^3J_{HP}$ = 37.12 Hz, 2 H, C_4H_2P). ^{13}C{^{1}H} NMR ($CDCl_3$, δ): 66.84 (d, $^3J_{CP}$ = 7.0 Hz, C^{α}/C_5H_4), 68.62 (d, $^3J_{CP}$ = 2.7 Hz,

C^{α}/C_5H_4), 69.37 (s, C^{β}/C_5H_4), 69.71 (s, C^{β}/C_5H_4), 70.06 (s, C_5H_5(P)), 70.34 (s, C_5H_5), 70.89 (d, J_{CP} = 10.0 Hz, CH/C_5H_4(P)), 71.57 (d, J_{CP} = 13.1 Hz, CH/C_5H_4(P)), 72.71 (d, $^1J_{CP}$ = 106.16 Hz, C^i/C_5H_4(P)), 79.00 (d, $^2J_{CP}$ = 14.2 Hz, C^i/C_5H_4), 129.45 (d, $^2J_{CP}$ = 29.3 Hz, CH/C_4H_2P), 138.15 (d, $^1J_{CP}$ = 99.3 Hz, C^i/C_4H_2P). $^{31}P\{^1H\}$ NMR ($CDCl_3$, δ): 40.72 (s). HRMS (ESI-TOF, *m/z*): calcd for $C_{34}H_{29}Fe_3OP$: 652.0001, found: 651.9997 $[M]^+$.

Synthesis of 2,5-diferrocenyl-1-mesityl-1*H*-phosphole oxide (E-4c)

According to the general procedure described earlier, 0.09 g (0.15 mmol) of **E-3c** were reacted for 2 h with H_2O_2 to afford **E-4c** as purple solid. Yield 0.06 g (0.10 mmol, 65 % based on **E-3c**). Anal. Calcd. for $C_{33}H_{31}Fe_2OP$ (586.08 g/mol): C, 67.61; H, 5.33. Found: C, 67.17; H, 5.72. Mp.: 193 °C. IR data (KBr, ν/cm^{-1}): 3084 m, 3048 w, 2954 w, 2922 m, 2852 w, 1603 m, 1587 m, 1448 w, 1409 m. ^1H NMR ($CDCl_3$, δ): 2.27 (bs, 3 H, CH_3), 2.30 (s, 3 H, CH_3), 3.18 (bs, 3 H, CH_3), 4.13 (s, 10 H, C_5H_5), 4.17 (m, 2 H, H^{α}/C_5H_4), 4.23 (m, 2 H, H^{β}/C_5H_4), 4.31 (m, 2 H, H^{β}/C_5H_4), 4.51 (m, 2 H, H^{α}/C_5H_4), 6.75 (d, $^3J_{HP}$ = 35.9 Hz, 2 H, C_4H_2P), 6.83 (bs, 1 H, C_6H_2), 7.07 (bs, 1 H, C_6H_2). $^{13}C\{^1H\}$ NMR ($CDCl_3$, δ): 21.22 (s, CH_3), 24.16 (bs, CH_3), 65.77 (d, $^3J_{CP}$ = 6.6 Hz, C^{α}/C_5H_4), 67.11 (d, $^3J_{CP}$ = 4.7 Hz, C^{α}/C_5H_4), 69.53 (s, C^{β}/C_5H_4), 69.90 (s, C_5H_5), 78.60 (d, $^2J_{CP}$ = 13.4 Hz, C^i/C_5H_4), 122.81 (d, $^1J_{CP}$ = 87.99 Hz, C^i/C_6H_2), 130.56 (d, $^2J_{CP}$ = 26.5 Hz, CH/C_4H_2P), 130.85 (bs, CH/C_6H_2), 132.55 (bs, CH/C_6H_2), 138.94 (d, $^1J_{CP}$ = 94.7 Hz, C^i/C_4H_2P), 141.66 (d, $^3J_{CP}$ = 2.7 Hz, C^i/C_6H_2). $^{31}P\{^1H\}$ NMR ($CDCl_3$, δ): 42.49 (s). HRMS (ESI-TOF, *m/z*): calcd for $C_{33}H_{31}Fe_2OP$: 586.0807, found: 586.0748 $[M]^+$.

Synthesis of 2,5-diferrocenyl-1-(2,4,6-triphenylphenyl)-1*H*-phosphole oxide (E-4d)

According to the general procedure described earlier, 0.13 g (0.19 mmol) of **E-3d** were reacted for 2 h with H_2O_2 to afford **E-4d** as purple solid. Yield 0.09 g (0.12 mmol, 63 % based on **E-3d**). Mp.: 160 °C (decomp.). IR data (KBr, ν/cm^{-1}): 3078 w, 3055 w, 2961 w, 2922 m, 2854 w, 1584 w, 1490 m, 1438 m. ^1H NMR ($CDCl_3$, δ): 4.16 (s, 10 H, C_5H_5), 4.34 (m, 6 H, C_5H_4), 4.28 (m, 2 H, H^{α}/C_5H_4), 5.83 (d, $^3J_{HP}$ = 36.9 Hz, 2 H, C_4H_2P), 7.30-7.61 (m, 17 H, Ph). $^{13}C\{^1H\}$ NMR ($CDCl_3$, δ): 65.81 (d, $^3J_{CP}$ = 7.8 Hz, C^{α}/C_5H_4), 67.80 (d, $^3J_{CP}$ = 2.7 Hz, C^{α}/C_5H_4), 69.03 (s, C^{β}/C_5H_4), 69.24 (s, C^{β}/C_5H_4), 70.12 (s, C_5H_5), 79.13 (d, $^2J_{CP}$ = 14.2 Hz, C^i/C_5H_4), 125.04 (d, $^1J_{CP}$ = 85.4 Hz, C^i/C_6H_2), 126.43 (bs, C_{phenyl}), 127.32 (s, CH/C_6H_5), 127.63 (bs, C_{phenyl}), 128.41 (s, C_{phenyl}), 128.99 (s, C_{phenyl}), 130.05 (bs, C_{phenyl}), 131.71 (d, J_{CP} = 27.8 Hz, C_{phenyl}) 137.73 (d, J_{CP} = 27.8, C_{phenyl}), 137.67 (d, $^1J_{CP}$ = 97.9 Hz, C^i/C_4H_2P), 139.00

(s, C_{phenyl}), 142.16 (d, J_{CP} = 2.5 Hz, CH/C_6H_5). $^{31}P\{^1H\}$ NMR ($CDCl_3$, δ): 36.63 (s). HRMS (ESI-TOF, *m/z*): calcd for $C_{48}H_{37}Fe_2OP$: 772.1277, found: 772.1281 $[M]^+$.

Synthesis of 2,5-diferrocenyl-1-(2,4,6-tri-*tert*-butylphenyl)-1*H*-phosphole oxide (E-4e)

According to the general procedure described earlier, 0.10 g (0.14 mmol) of **E-3e** were reacted for 5 h with H_2O_2 to afford **E-4e** as purple solid. Yield 0.05 g (0.07 mmol, 50 % based on **E-3e**). Mp.: 195-200 °C (decomp.). IR data (KBr, ν/cm^{-1}): 3094 w, 3071 w, 2961 m, 2912 m, 2854 w, 1588 m, 1471 m, 1390 m, 1357 m. ^1H NMR ($CDCl_3$, δ): 1.26 (s, 9 H, CH_3), 1.32 (s, 9 H, CH_3), 1.49 (s, 9 H, CH_3), 4.12 (m, 2 H, C_5H_4), 4.17 (m, 12 H, C_5H_5/C_5H_4), 4.26 (m, 2 H, C_5H_4), 4.51 (m, 2 H, C_5H_4), 6.73 (d, $^3J_{HP}$ = 37.6 Hz, 2 H, C_4H_2P), 7.10 (s, 1 H, C_6H_2), 7.51 (s, 1 H, C_6H_2). $^{13}C\{^1H\}$ NMR ($CDCl_3$, δ): 31.25 (s, CH_3), 33.53 (s, CH_3), 34.05 (s, CH_3), 67.44 (bs, CH/C_5H_4), 68.51 (d, J_{CP} = 15.9 Hz, CH/C_5H_4), 70.12 (s, C_5H_5), 70.74 (bs, CH/C_5H_4), 80.26 (d, $^2J_{CP}$ = 13.8 Hz, C^i/C_5H_4), 124.02 (d, $^1J_{CP}$ = 88.4 Hz, C^i/C_6H_2), 124.12 (d, J_{CP} = 12.1 Hz, CH/C_6H_2), 125.37 (d, J_{CP} = 11.7 Hz, CH/C_6H_2), 131.11 (d, $^2J_{CP}$ = 24.7 Hz, CH/C_4H_2P), 144.04 (d, $^1J_{CP}$ = 83.8 Hz, C^i/C_4H_2P), 152.16 (d, J_{CP} = 4.0 Hz, C^i/C_6H_2), 157.95 (d, J_{CP} = 10.1 Hz, C^i/C_6H_2), 164.25 (d, J_{CP} = 4.8 Hz, C^i/C_6H_2). $^{31}P\{^1H\}$ NMR ($CDCl_3$, δ): 43.16 (s). HRMS (ESI-TOF, *m/z*): calcd for $C_{42}H_{49}Fe_2OP$: 712.2216, found: 712.2217 $[M]^+$.

General procedure for the synthesis of the seleno- and thiophosphines E-5b,c and E-6b

For the synthesis of the thio- and selenophospines, the phosphines **E-3b**,**c** and a two- to threefold excess of elemental sulfur or selenium were dissolved in 20 mL of degassed dichloromethane and the reaction mixture was stirred for 3 h at ambient temperature. To remove the excess sulfur or selenium, the appropriate reaction mixture was filtered through 5 cm of Celite, and the solution was concentrated in vacuo. The remaining residue was purified by column chromatography (column size: 2 x 10 cm, silica, *n*-hexane/dichloromethane (5/1, v/v).

Synthesis of 1,2,5-triferrocenyl-1*H*-phosphole sulfide (E-5b)

Using the general synthesis procedure described earlier, 0.10 g (0.16 mmol) of **E-3b** were treated with 0.12 g (0.47 mmol) of elemental sulfur to afford **E-5b** as purple solid. Yield 0.09 g (0.14 mmol, 88 % based on **E-3b**). Anal. Calcd. for $C_{34}H_{29}Fe_3PS$ (667.98 g/mol): C, 61.12; H, 4.37. Found: C, 61.32; H, 4.57. Mp.: 207 °C. IR data (KBr, ν/cm^{-1}): 3084 m, 2954 w, 2919m, 2854 w, 1584 m, 1529 m, 1409 m. ^1H NMR ($CDCl_3$, δ): 4.03 (s, 5 H, C_5H_5(P)), 4.15 (s, 10 H, C_5H_5), 4.31 (m, 2 H, C_5H_4(P)), 4.37-4.41 (m, 6 H, C_5H_4), 4.68 (m, 2 H, H^α/C_5H_4), 5.14 (m, 2 H, H^α/C_5H_4), 6.82 (d, $^3J_{HP}$ = 36.13 Hz, 2 H, C_4H_2P). $^{13}C\{^1H\}$ NMR

($CDCl_3$, δ): 67.25 (d, $^3J_{CP}$ = 6.9 Hz, C^{α}/C_5H_4), 68.23 (d, $^3J_{CP}$ = 3.4 Hz, C^{α}/C_5H_4), 69.13 (s, C^{β}/C_5H_4), 69.63 (s, C^{β}/C_5H_4), 70.20 (s, C_5H_5(P)), 70.63 (s, C_5H_5), 70.82 (d, J_{CP} = 10.0 Hz, CH/C_5H_4(P)), 71.15 (d, J_{CP} = 13.6 Hz, CH/C_5H_4(P)), 75.68 (d, $^1J_{CP}$ = 85.30 Hz, C^i/C_5H_4(P)), 78.88 (d, $^2J_{CP}$ = 16.2 Hz, C^i/C_5H_4), 129.76 (d, $^2J_{CP}$ = 25.2 Hz, CH/C_4H_2P), 140.82 (d, $^1J_{CP}$ = 82.2 Hz, C^i/C_4H_2P). $^{31}P\{^1H\}$ NMR ($CDCl_3$, δ): 46.59 (s). HRMS (ESI-TOF, *m/z*): calcd for $C_{34}H_{29}Fe_3PS$: 667.9772, found: 667.9723 $[M]^+$.

Synthesis of 2,5-diferrocenyl-1-mesityl-1*H*-phosphole sulfide (E-5c)

Using the general synthesis procedure described earlier, 0.10 g (0.17 mmol) of **E-3c** were treated with 0.12 g (0.47 mmol) of elemental sulfur to afford **E-5c** as purple solid. Yield 0.03 g (0.05 mmol, 29 % based on **E-3c**). Anal. Calcd. for $C_{33}H_{31}Fe_2PS$ (602.06 g/mol): C, 65.80; H, 5.19. Found: C, 65.88; H, 5.90. Mp.: 275-285 °C (decomp.). IR data (KBr, ν/cm^{-1}): 3091 w, 3071 w, 2961 w, 2924 m, 2851 w, 1602 m, 1444 m, 1410 m, 1383 w. ^1H NMR ($CDCl_3$, δ): 2.26 (s, 3 H, *p*-CH_3), 2.79 (bs, 6 H, *o*-CH_3), 4.08 (s, 10 H, C_5H_5), 4.28 (m, 2 H, H^{β}/C_5H_4), 4.30 (m, 2 H, H^{β}/C_5H_4), 4.41 (m, 2 H, H^{α}/C_5H_4), 4.55 (m, 2 H, H^{α}/C_5H_4), 6.75 (d, $^3J_{HP}$ = 36.1 Hz, 2 H, C_4H_2P), 6.90 (d, $^4J_{HP}$ = 3.9 Hz, 2 H, C_6H_2). $^{13}C\{^1H\}$ NMR ($CDCl_3$, δ): 21.06 (s, *p*-CH_3), 23.75 (bs, *o*-CH_3), 66.47 (d, $^3J_{CP}$ = 6.5 Hz, C^{α}/C_5H_4), 67.34 (d, $^3J_{CP}$ = 5.5 Hz, C^{α}/C_5H_4), 69.35 (s, C^{β}/C_5H_4), 69.41 (C^{β}/C_5H_4), 70.32 (s, C_5H_5), 78.35 (d, $^2J_{CP}$ = 15.5 Hz, C^i/C_5H_4), 120.37 (d, J_{CP} = 67.4 Hz, C^i/C_6H_2), 128.34 (d, $^2J_{CP}$ = 24.3 Hz, CH/C_4H_2P), 132.47 (d, $^3J_{CP}$ = 11.7 Hz, CH/C_6H_2), 141.53 (d, J_{CP} = 2.7 Hz, C^i/C_6H_2), 144.86 (d, $^1J_{CP}$ = 79.5 Hz, C^i/C_4H_2P). $^{31}P\{^1H\}$ NMR ($CDCl_3$, δ): 45.54 (s). HRMS (ESI-TOF, *m/z*): calcd for $C_{33}H_{31}Fe_2PS$: 602.0578, found: 602.0562 $[M]^+$.

Synthesis of 1,2,5-triferrocenyl-1*H*-phosphole selenide (E-6b)

Using the general synthesis procedure described earlier, 0.09 g (0.14 mmol) of **E-3b** were treated with 0.02 g (0.25 mmol) of elemental selenium to afford **E-6b** as purple solid. Yield 0.07 g (0.10 mmol, 71 % based on **E-3b**). Anal. Calcd. for $C_{34}H_{29}Fe_3PSe$ (715.92 g/mol): C, 57.11; H, 4.09. Found: C, 57.17; H, 4.24.Mp.: 225 °C. IR data (KBr, ν/cm^{-1}): 3087 m, 3035 w, 2951 w, 2922 m, 2854 w, 1579 m, 1419 m. ^1H NMR ($CDCl_3$, δ): 4.03 (s, 5 H, C_5H_5(P)), 4.16 (s, 10 H, C_5H_5), 4.33 (m, 2 H, C_5H_4(P)), 4.38 (m, 4 H, C_5H_4), 4.42 (m, 2 H, $H^{\beta}C_5H_4$), 4.71 (m, 2 H, H^{α}/C_5H_4), 5.25 (m, 2 H, H^{α}/C_5H_4), 6.83 (d, $^3J_{HP}$ = 35.5 Hz, 2 H, C_4H_2P). $^{13}C\{^1H\}$ NMR ($CDCl_3$, δ): 67.65 (d, $^3J_{CP}$ = 6.8 Hz, C^{α}/C_5H_4), 68.19 (d, $^3J_{CP}$ = 3.5 Hz, C^{α}/C_5H_4), 69.23 (s, C^{β}/C_5H_4), 69.69 (s, C^{β}/C_5H_4), 70.32 (s, C_5H_5(P), 70.83 (s, C_5H_5), 70.96 (d, J_{CP} = 9.9 Hz, CH/C_5H_4(P)), 71.30 (d, J_{CP} = 6.8 Hz, CH/C_5H_4(P)), 74.34 (d, $^1J_{CP}$ = 76.1 Hz,

$C^i/C_5H_4(P)$), 79.19 (d, $^2J_{CP}$ = 16.7 Hz, C^i/C_5H_4), 129.98 (d, $^2J_{CP}$ = 23.5 Hz, CH/C_4H_2P), 140.56 (d, $^1J_{CP}$ = 74.4 Hz, C^i/C_4H_2P). $^{31}P\{^1H\}$ NMR ($CDCl_3$, δ): 28.69 ($^1J_{PSe}$ = 731 Hz). HRMS (ESI-TOF, *m/z*): calcd for $C_{34}H_{29}Fe_3PSe$: 715.9221, found: 715.9198 $[M]^+$.

E6 Acknowledgement

We are grateful to the Fonds der Chemischen Industrie (FCI) for generous financial support. M. K. thanks the FCI for a Chemiefonds Fellowship.

E7 Supporting Information Available

Figures giving further VT-NMR spectra, (spectro)electrochemical spectra, computational methods, Tables summarizing bond lengths, bond and torsion angles from optimized geometries, coordinates of optimized geometries in .xyz format, and CIF files giving crystallographic data for **E-3b**–**e**. This material is available free of charge via the Internet at http://pubs.acs.org. Crystallographic data of **E-3b**–**e** are also available from the Cambridge Crystallographic Database as file numbers CCDC 1055024 (**E-3b**), 1055025 (**E-3c**), 1055026 (**E-3d**) and 1055027 (**E-3e**).

E8 Appendix

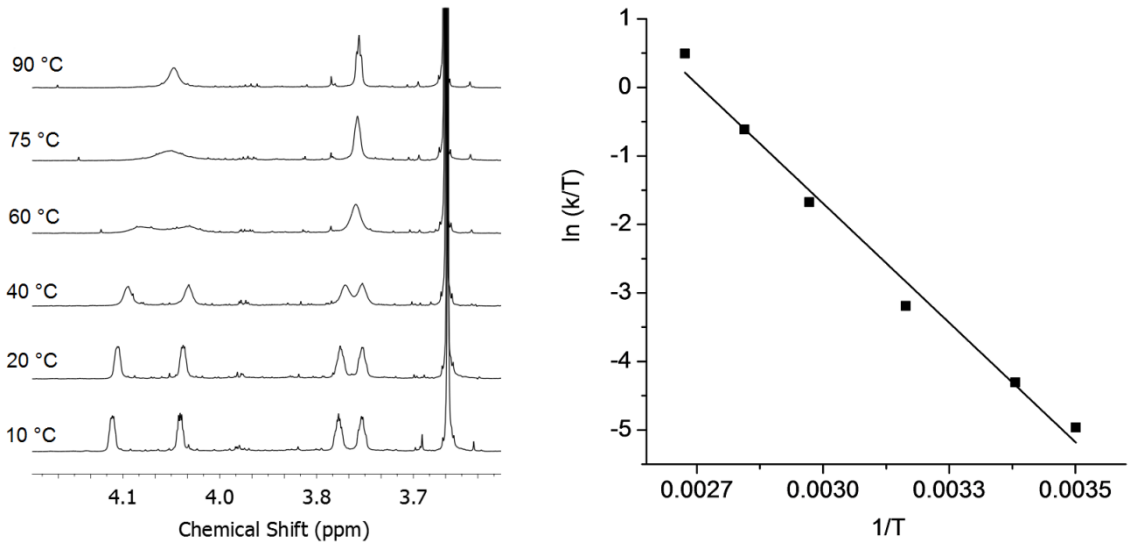

Figure SI1. Left: Experimental ^1H NMR spectra of **E-3a** in the range of 3.6 and 4.2 ppm; toluene-d_8, various temperatures. Right: Graphical analysis according to Eyring for the determination of the parameters for the ferrocenyl protons from experimental ^1H NMR studies, linear regression: R^2 = 0.9844.

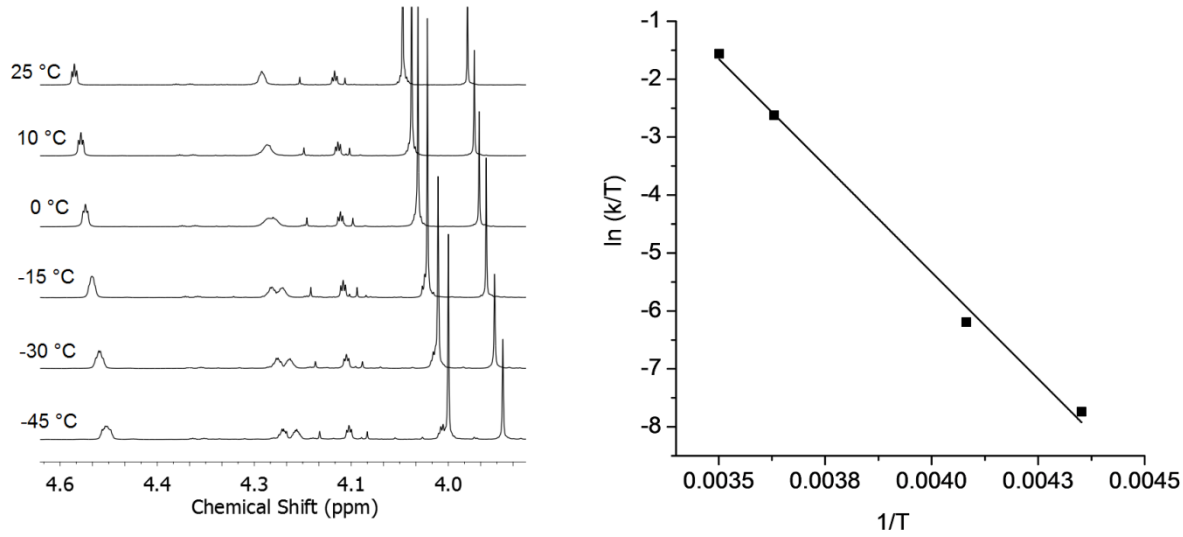

Figure SI2. Left: Experimental ^{1}H NMR spectra of **E-3b** in the range of 3.8 and 4.6 ppm; methylenchloride-d_2, various temperatures. Right: Graphical analysis according to Eyring for the determination of the parameters for the ferrocenyl protons from experimental ^{1}H NMR studies, linear regression: $R^2 = 0.99338$.

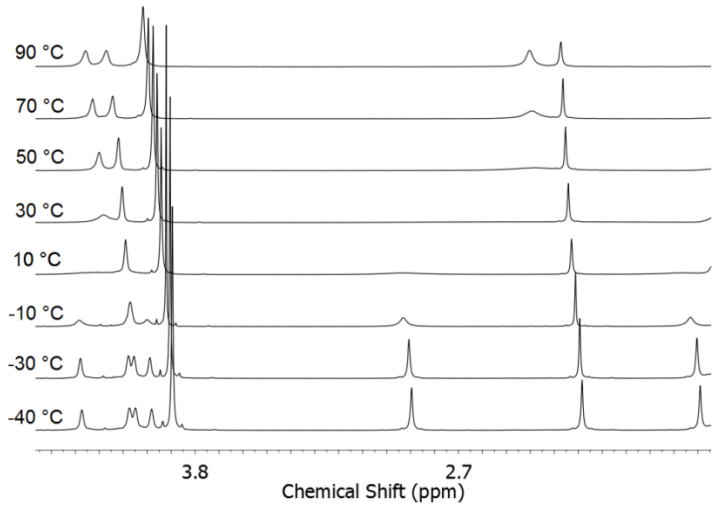

Figure SI3. Experimental ^{1}H NMR spectra of **E-3c** in the range of 1.7 and 4.7 ppm; $C_2D_2Cl_4$, various temperatures.

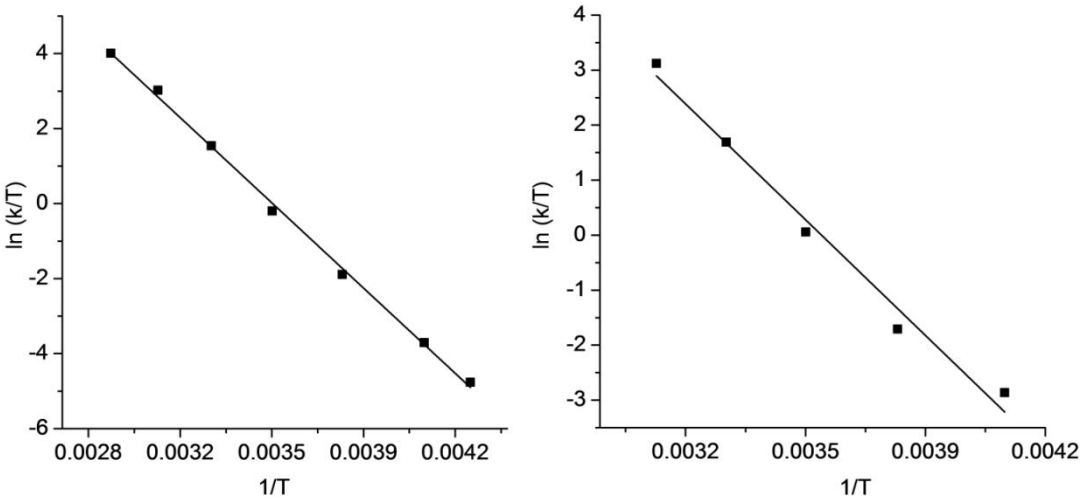

Figure SI4. Left: Graphical analyses according to Eyring for the determination of the parameters for the methyl protons from experimental ^{1}H NMR studies in **E-3c**, linear regression: $R^2 = 0.99778$. Right: Graphical analysis according to Eyring for the determination of the parameters for the ferrocenyl protons from experimental ^{1}H NMR studies in **E-3c**, linear regression: $R^2 = 0.97958$.

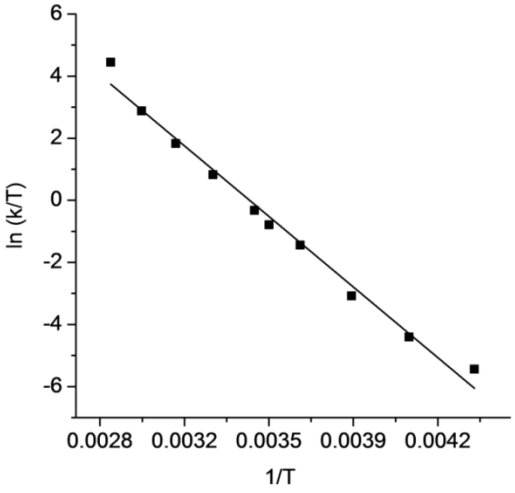

Figure SI5. Graphical analysis according to Eyring for the determination of the parameters for the ferrocenyl protons from experimental ^{1}H NMR studies in **E-3d**, linear regression: $R^2 = 0.98555$.

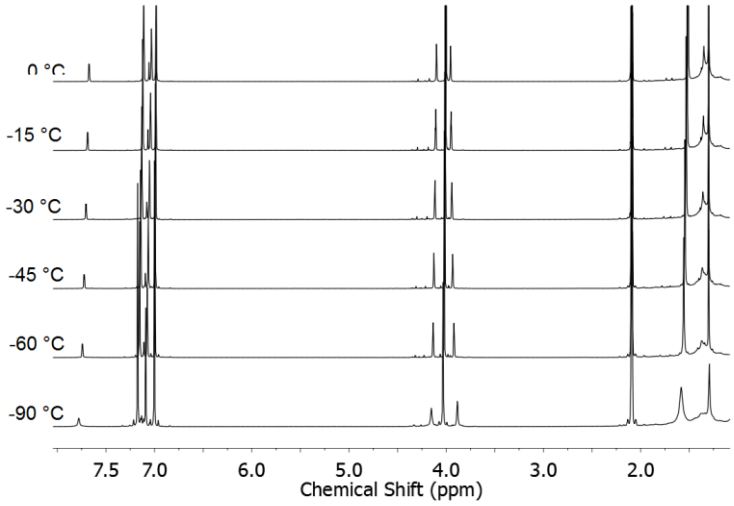

Figure SI6. Experimental ^{1}H NMR spectra of **E-3e** in the range of 1.4 and 8.0 ppm; toluene-d_8, various temperatures.

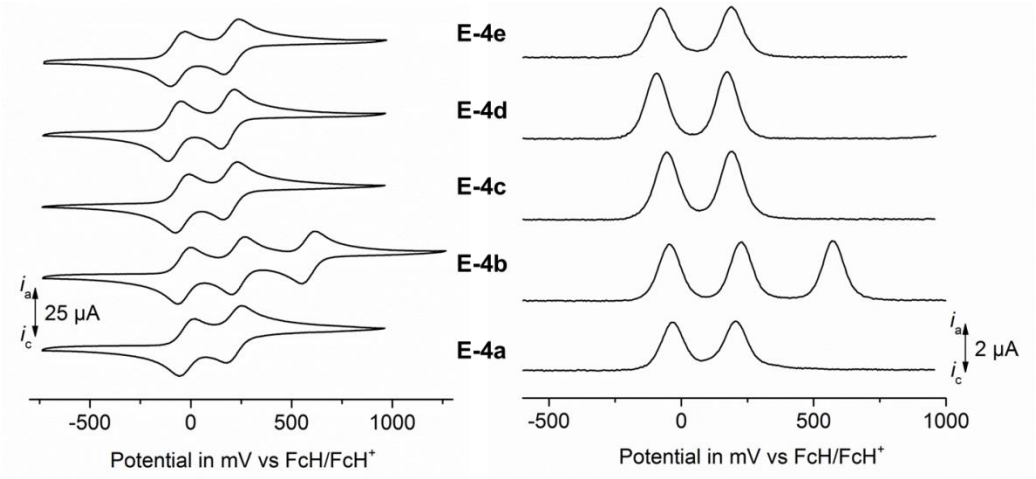

Figure SI11. Left: Cyclic voltammograms of **E-4a–e**; scan rate: 100 mV. Right: Square wave voltammograms of **E-4a–e** in dichloromethane solutions (1.0 mmol·L^{-1}) at 25 °C, supporting electrolyte 0.1 mol·L^{-1} [N^{n}Bu$_4$][B(C$_6$F$_5$)$_4$].

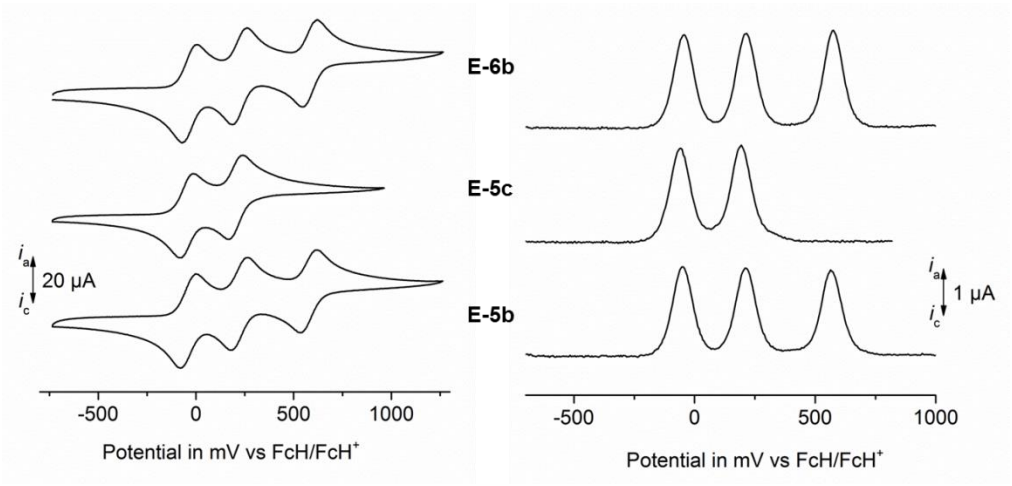

Figure SI12. Left: Cyclic voltammograms of **E-5b**,**c** and **E-6b**; scan rate: 100 mV. Right: Square wave voltammograms of **E-5b**,**c** and **E-6b** in dichloromethane solutions (1.0 mmol·L^{-1}) at 25 °C, supporting electrolyte 0.1 mol·L^{-1} [N^nBu_4][$B(C_6F_5)_4$].

E9 References

[E1] L. Nyulászi, L. Soós, G. Keglevich, *J. Organomet. Chem.* **1998**, *566*, 29–35.

[E2] M. K. Cyrański, P. von. Ragué Schleyer, T. M. Krygowski, H. Jiao, G. Hohlneicher, *Tetrahedron* **2003**, *59*, 1657–1665.

[E3] L. Nyulászi, *Chem. Rev.* **2001**, *101*, 1229–1246.

[E4] F. Mathey, *Mod. Heterocycl. Chem.*; J. Alvarez-Builla, J. J. Vaquero, J. Barluenga, Eds.; Wiley-VCH Verlag GmbH & Co. KGaA: Weinheim, Germany, **2011**, 2071–2116.

[E5] F. Mathey, *Chem. Rev.* **1988**, *88*, 429–453.

[E6] A. Peña-Gallego, J. Rodríguez-Otero, E. M. Cabaleiro-Lago, *J. Mol. Model.* **2012**, *18*, 765–770.

[E7] S. Noorizadeh, M. Dardab, *Chem. Phys. Lett.* **2010**, *493*, 376–380.

[E8] L. Nyulászi, O. Hollóczki, C. Lescop, M. Hissler, R. Réau, *Org. Biomol. Chem.* **2006**, *4*, 996–998.

[E9] G. Keglevich, R. Farkas, T. Imre, K. Ludányi, A. Szöllösy, L. Töke, *Heteroat. Chem.* **2003**, *14*, 316–319.

[E10] L. Nyulászi, *J. Phys. Chem.* **1996**, *100*, 6194–6198.

[E11] L. D. Quin, A. S. Ionkin, R. Kalgutkar, G. Keglevich, *Phosphorus. Sulfur. Silicon Relat. Elem.* **1996**, *109*, 433–436.

[E12] D. Delaere, A. Dransfeld, M. T. Nguyen, L. G. Vanquickenborne, *J. Org. Chem.* **2000**, *65*, 2631–2636.

[E13] A. T. Balaban, D. C. Oniciu, A. R. Katritzky, *Chem. Rev.* **2004**, *104*, 2777–2812.

[E14] W. Schaefer, A. Schweig, F. Mathey, *J. Am. Chem. Soc.* **1976**, *98*, 407–414.

[E15] W. Egan, R. Tang, G. Zon, K. Mislow, *J. Am. Chem. Soc.* **1970**, *92*, 1442–1444.

[E16] E. Mattmann, F. Mathey, A. Sevin, G. Frison, *J. Org. Chem.* **2002**, *67*, 1208–1213.

[E17] D. B. Chesnut, L. J. Bartolotti, *Chem. Phys.* **2000**, *253*, 1–11.

[E18] D. B. Chesnut, L. D. Quin, *Heteroat. Chem.* **2007**, *18*, 754–758.

[E19] G. Keglevich, *Phosphorus Heterocycles II*; R. K. Bansal, Ed.; Topics in Heterocyclic Chemistry; Springer, Berlin, Heidelberg, **2010**; Vol. 21..

[E20] E. Jortzik, M. Farhadi, R. Ahmadi, K. Tóth, J. Lohr, B. M. Helmke, S. Kehr, A. Unterberg, I. Ott, R. Gust, V. Deborde, E. Davioud-Charvet, R. Réau, K. Becker, C. Herold-Mende, *Biochim. Biophys. Acta* **2014**, *1844*, 1415–1426.

[E21] K. Fourmy, S. Mallet-Ladeira, O. Dechy-Cabaret, M. Gouygou, *Dalton Trans.* **2014**, *43*, 6728–6734.

[E22] K. Fourmy, S. Mallet-Ladeira, O. Dechy-Cabaret, M. Gouygou, *Organometallics* **2013**, *32*, 1571–1574.

[E23] M. P. Duffy, Y. Lin, L. Y. Ting, F. Mathey, *New J. Chem.* **2011**, *35*, 2001–2003.

[E24] M. Sebastian, M. Hissler, C. Fave, J. Rault-Berthelot, C. Odin, R. Réau, *Angew. Chem., Int. Ed.* **2006**, *45*, 6152–6155.

[E25] H.-C. Su, O. Fadhel, C.-J. Yang, T.-Y. Cho, C. Fave, M. Hissler, C.-C. Wu, R. Réau, *J. Am. Chem. Soc.* **2006**, *128*, 983–995.

[E26] F. Leca, M. Sauthier, V. Deborde, L. Toupet, R. Réau, *Chem. Eur. J.* **2003**, *9*, 3785–3795.

[E27] D. Delaere, M. T. Nguyen, L. G. Vanquickenborne, *Phys. Chem. Chem. Phys.* **2002**, *4*, 1522-1530.

[E28] L. Nyulászi, *Tetrahedron* **2000**, *56*, 79–84.

[E29] F. G. N. Cloke, P. B. Hitchcock, P. Hunnable, J. F. Nixon, L. Nyulászi, E. Niecke, V. Thelen, *Angew. Chem. Int. Ed.* **1998**, *37*, 1083–1086.

[E30] L. Nyulászi, *J. Phys. Chem.* **1995**, *99*, 586–591.

[E31] G. Keglevich, R. Farkas, K. Ludányi, V. Kudar, M. Hanusz, K. Simon, *Heteroat. Chem.* **2005**, *16*, 104–110.

[E32] L. D. Quin, G. Keglevich, A. S. Ionkin, R. Kalgutkar, G. Szalontai, *J. Org. Chem.* **1996**, *61*, 7801–7807.

[E33] G. Keglevich, Z. Böcskei, G. M. Keserü, K. Újszászy, L. D. Quin, *J. Am. Chem. Soc.* **1997**, *119*, 5095–5099.

[E34] L. Nyulászi, G. Keglevich, L. D. Quin, *J. Org. Chem.* **1996**, *61*, 7808–7812.

[E35] G. Keglevich, L. D. Quin, Z. Böcskei, G. M. Keserü, R. Kalgutkar, P. M. Lahti, *J. Organomet. Chem.* **1997**, *532*, 109–116.

[E36] C. W. Bird, *Tetrahedron* **1985**, *41*, 1409–1414.

[E37] P. Coggon, A. T. McPhail, *J. Chem. Soc., Dalton Trans.* **1973**, 1888–1891.

[E38] U. Pfaff, A. Hildebrandt, D. Schaarschmidt, T. Rüffer, P. J. Low, H. Lang, *Organometallics* **2013**, *32*, 6106–6117.

[E39] A. Hildebrandt, H. Lang, *Organometallics* **2013**, *32*, 5640–5653.

[E40] J. M. Speck, R. Claus, A. Hildebrandt, T. Rüffer, E. Erasmus, L. van As, J. C. Swarts, H. Lang, *Organometallics* **2012**, *31*, 6373–6380.

[E41] A. Hildebrandt, H. Lang, *Dalton Trans.* **2011**, *40*, 11831–11837.

[E42] S. W. Lehrich, A. Hildebrandt, T. Rüffer, M. Korb, P. J. Low, H. Lang, *Organometallics* **2014**, *33*, 4836–4845.

[E43] A. Hildebrandt, D. Schaarschmidt, R. Claus, H. Lang, *Inorg. Chem.* **2011**, *50*, 10623–10632.

[E44] A. Hildebrandt, U. Pfaff, H. Lang, *Rev. Inorg. Chem.* **2011**, *31*, 111–141.

[E45] A. Hildebrandt, D. Schaarschmidt, H. Lang, *Organometallics* **2011**, *30*, 556–563.

[E46] K. Kaleta, A. Hildebrandt, F. Strehler, P. Arndt, H. Jiao, A. Spannenberg, H. Lang, U. Rosenthal, *Angew. Chem.* **2011**, *123*, 11444–11448.

[E47] K. Kaleta, F. Strehler, A. Hildebrandt, T. Beweries, P. Arndt, T. Rüffer, A. Spannenberg, H. Lang, U. Rosenthal, *Chem. Eur. J.* **2012**, *18*, 12672–12680.

[E48] S. W. Lehrich, A. Hildebrandt, M. Korb, H. Lang, *J. Organomet. Chem.* **2015**, *792*, 37–45.

[E49] U. Pfaff, A. Hildebrandt, M. Korb, H. Lang, *Polyhedron* **2015**, *86*, 2–9.

[E50] D. Miesel, A. Hildebrandt, M. Korb, P. J. Low, H. Lang, *Organometallics* **2013**, *32*, 2993–3002.

[E51] G. Märkl, R. Potthast, *Angew. Chem. Int. Ed.* **1967**, *6*, 86.

[E52] H. Günther, *NMR Spectroscopy: Basic Principles, Concepts, And Aplications in Chemistry*, John Wiley & Sons: New York, **1996**.

[E53] G. Jochem, H. Nöth, A. Schmidpeter, *Chem. Ber.* **1996**, *129*, 1083–1086.

[E54] W. E. Geiger, F. Barrière, *Acc. Chem.Res.* **2010**, *43*, 1030–1039.

[E55] F. Barrière, W. E. Geiger, *J. Am. Chem. Soc.* **2006**, *128*, 3980–3989.

[E56] F. Barrière, N. Camire, W. E. Geiger, U. T. Mueller-Westerhoff, R. Sanders, *J. Am. Chem. Soc.* **2002**, *124*, 7262–7263.

[E57] G. Gritzner, J. Kuta, *Pure Appl. Chem.* **1984**, *56*, 461–466.

[E58] H. J. Gericke, N. I. Barnard, E. Erasmus, J. C. Swarts, M. J. Cook, M. A. S. Aquino, *Inorg. Chim. Acta* **2010**, *363*, 2222–2232.

[E59] R. F. Winter, *Organometallics* **2014**, *33*, 4517–4536.

[E60] M. Krejčik, M. Daněk, F. Hartl, *J. Electroanal. Chem.* **1991**, *317*, 179–187.

[E61] N. S. Hush, *Electrochim. Acta* **1968**, *13*, 1005–1023.

[E62] M. B. Robin, P. Day, *Adv. Inorg. Chem. Radiochem.* **1967**, *10*, 247–422.

[E63] A. Nafady, W. E. Geiger, *Organometallics* **2008**, *27*, 5624–5631.

[E64] G. M. Sheldrick, *Acta Crystallogr., Sect. A* **1990**, *46*, 467–473.

[E65] G. M. Sheldrick, *SHELXL-97, Struct. Refinement* **1997**, University of Göttingen.

[E66] W. Henderson, S. R. Alley, *J. Organomet. Chem.* **2002**, *656*, 120–128.

[E67] J. D. Masuda, K. C. Jantunen, O. V Ozerov, K. J. T. Noonan, D. P. Gates, B. L. Scott, J. L. Kiplinger, *J. Am. Chem. Soc.* **2008**, *130*, 2408–2409.

[E68] A. H. Cowley, J. E. Kilduff, T. H. Newman, M. Pakulski, *J. Am. Chem. Soc.* **1982**, *104*, 5820–5821.

[E69] Y. van den Winkel, H. M. M. Bastiaans, F. Bickelhaupt, *J. Organomet. Chem.* **1991**, *405*, 183–194.

[E70] Z. Yuan, G. Stringer, I. R. Jobe, D. Kreller, K. Scott, L. Koch, N. J. Taylor, T. B. Marder, *J. Organomet. Chem.* **1993**, *452*, 115–120.

F Zusammenfassung

Das Ziel der vorliegenden Arbeit bestand in der Synthese und Charakterisierung Ferrocenyl-funktionalisierter Phosphole. Der Schwerpunkt lag dabei in der chemischen Modifikation des Phospholsystems, wie beispielsweise durch Komplexierungsreaktionen über das freie Elektronenpaar am Phosphoratom oder das dienische System und der Untersuchung der Auswirkungen auf den Elektronentransfer der Ferrocenyleinheiten in 2- und 5-Position. Die elektronische Flexibilität der Phosphole eignet sich dabei hervorragend, um die elektronischen Eigenschaften gezielt zu verändern und somit einen Einfluss auf die Metall-Metall-Interaktion zu nehmen.

Die erhaltenen Resultate der Arbeit lassen sich dabei in vier Kapitel unterteilen:

Kapitel B: **The Synthesis and (Spectro)electrochemical Behavior of 2,5-Diferrocenyl-1-phenyl-1*H*-phosphole**

Kapitel C: **Transition Metal Carbonyl Complexes of 2,5-Diferrocenyl-1-phenyl-1*H*-phosphole**

Kapitel D: **Electronic Interactions in Gold(I) Complexes of 2,5-Diferrocenyl-1-phenyl-1*H*-phosphole**

Kapitel E: **Influence of P-Bonded Bulky Substituents on the Electronic Interaction in Ferrocenyl Substituted Phospholes**

Im Folgenden werden die wichtigsten Ergebnisse zu jedem Kapitel zusammengefasst.

Kapitel B

In diesem Kapitel ist die Synthese der Ferrocenyl-funktionalisierten Phosphole **B-3**–**B-5** sowie deren spektroelektrochemische Untersuchung zur Klassifizierung der elektronischen Interaktion der Ferrocenylgruppen in 2- und 5-Position über den Phospholring vorgestellt. Weiterhin wurde der Einfluss der Oxidation des Phosphoratoms von P^{III} zu P^{V} auf die Metall-Metall-Wechselwirkung untersucht. Zum Aufbau des Phospholsystems **B-3** wurde eine Cyclisierungsreaktion von Phenylphosphin (**B-1**) mit 1,4-Diferrocenylbutadiin (**B-2**) in Gegenwart von *n*-Butyllithium gewählt (Schema F1). Die chemische Oxidation des

Phosphoratoms erfolgte mit elementarem Schwefel bzw. Selen zu den Verbindungen **B-4** und **B-5**.

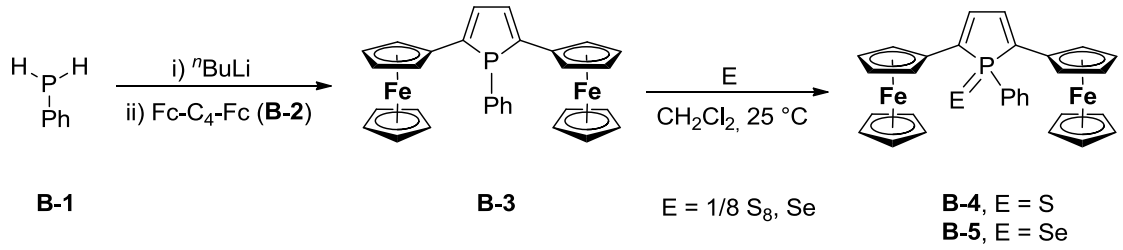

Schema F1. Synthese von 2,5-Diferrocenyl-1-phenyl-1*H*-phosphol (**B-3**) und anschließende Umsetzung zum Sulfid **B-4** bzw. Selenid **B-5**.

Um Informationen über das Redoxverhalten der Verbindungen zu erhalten, wurden zunächst elektrochemische Messungen durchgeführt. Dazu konnten in den Cyclovoltammogrammen der Verbindungen **B-3**–**B-5** zwei separate Redoxprozesse gefunden werden. Dies bedeutet, dass die beiden Ferrocenylgruppen separat voneinander oxidiert bzw. reduziert werden. Durch Vergleich der Größe der Redoxseparation zwischen diesen beiden Redoxprozessen konnten erste Abschätzungen zur Stärke der elektronischen Interaktion getroffen werden. Nach Oxidation des Phosphoratoms mit Schwefel bzw. Selen wurde eine leichte Abnahme der Redoxseparation zwischen beiden Redoxprozessen beobachtet (**B-3**, 280 mV; **B-4**, 240 mV; **B-5**, 235 mV), wodurch eine verminderte elektronische Interaktion der Fc/Fc^+-Gruppen angedeutet wird. Zur genauen Charakterisierung der Stärke der Metall-Metall-Wechselwirkung erfolgte die Aufnahme von UV/Vis-NIR-Spektren. Dabei zeigten die gemischt-valenten Verbindungen $[\mathbf{B\text{-}1}]^+$–$[\mathbf{B\text{-}3}]^+$ Intervalence-Charge-Transfer-Absorptionen (IVCT-Banden) im NIR-Bereich, welche durch den Elektronentransfer zwischen den terminalen Fc/Fc^+-Gruppen zustande kommen. Nach der Oxidation des Phosphors von P^{III} zu P^V nahm die Intensität der IVCT-Bande ab (**B-3**, 1750 $L \cdot mol^{-1} \cdot cm^{-1}$; **B-4**, 1300 $L \cdot mol^{-1} \cdot cm^{-1}$; **B-5**, 1100 $L \cdot mol^{-1} \cdot cm^{-1}$), während die Halbwertsbreite anstieg (3050 cm^{-1} (**B-3**), 4200 cm^{-1} (**B-4**, **B-5**)). Die Änderung der Geometrie der IVCT-Bande zeigte, dass durch Blockieren des freien Elektronenpaares die elektronische Kommunikation über das heterozyklische Brückenfragment leicht abnimmt. Theoretische Berechnungen stützen die Vermutung, dass der Elektronentransfer hauptsächlich über das dienische System erfolgt. Der Einfluss des Phosphoratoms wird allerdings durch die leichte Abnahme der Wechselwirkung nach kompletter Aufhebung der Delokalisation durch Oxidation des Phosphoratoms deutlich. Die untersuchten Verbindungen **B-3**–**B-5** konnten der Klasse II nach Robin und Day zugeordnet werden. Der Phospholring eignet sich sehr gut, um chemische

Modifikationen zur Änderung der elektronischen Eigenschaften am Ringsystem vorzunehmen.

Kapitel C

Um die Auswirkungen gezielter, chemischer Modifikationen am Phosphoratom unter Beibehaltung der Oxidationsstufe und am dienischen System genauer zu untersuchen, wurden die Übergangsmetallkomplexe **C-3a**–**c**, **C-4a**–**c**, **C-6**, **C-7** und **C-9** des 2,5-Diferrocenyl-1-phenyl-1*H*-phosphols dargestellt (Schema F2). Dabei erfolgte die Koordination vom freien Elektronenpaar des Phosphoratoms, vom dienischen System oder von beiden an Fe, Cr, Mo oder W.

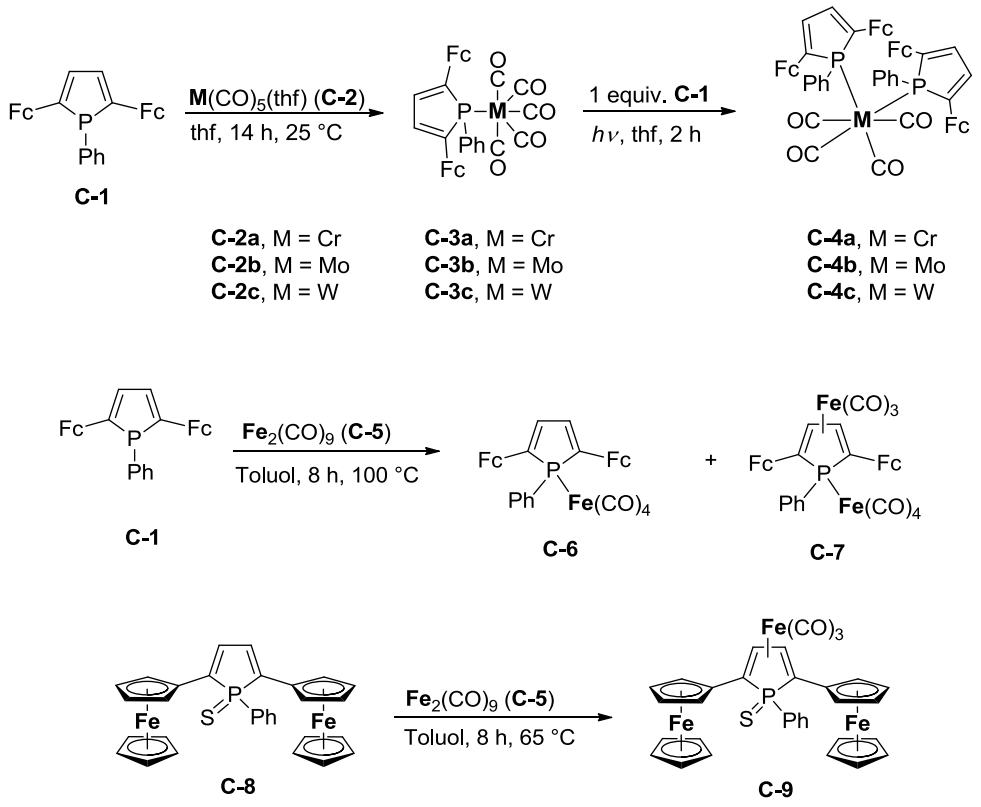

Schema F2. Synthese der Carbonylkomplexe **C-3a**–**c**, **C-4a**–**c**, **C-6**, **C-7** und **C-9**.

Elektrochemische Messungen zeigten, dass die Ferrocenylgruppen getrennt voneinander oxidiert und reduziert werden. Dabei ist die Größe der Redoxseparation ($\Delta E°' \approx 260$ mV) bei Koordination des P-Atoms an $M(CO)_5$ (**C-3a**–**c**) und $M(CO)_4$ (**C-4a**–**c**) ähnlich dem unkomplexierten Phosphol **C-1**. Die Koordination des dienischen Systems an $Fe(CO)_3$ in **C-9** führte allerdings zu einer signifikanten Abnahme der Redoxseparation auf 190 mV im Vergleich zu **C-8** (240 mV). Die Verbindungen **C-6** und **C-7** zeigten während

elektrochemischer Messungen irreversibles Redoxverhalten, weswegen eine spektroelektrochemische Charakterisierung nicht möglich war. Durch UV/Vis-NIR-Spektroskopie konnte der größere Einfluss des dienischen Systems bestätigt werden. Die IVCT-Bande von [**C-9**]$^+$ (ε_{max} = 400 L $\cdot$mol^{-1} $\cdot$cm^{-1}) weist eine deutlich geringere Intensität im Vergleich zu [**C-8**]$^+$ (ε_{max} = 1300 L $\cdot$mol^{-1} $\cdot$cm^{-1}) auf. Dies kann durch die geringere Elektronendichte am konjugierten System erklärt werden. Jedoch könnte auch die „Abwinkelung“ des Phospholrings nach Koordination an $Fe(CO)_3$, welche durch Einkristallröntgentrukturanalyse belegt wurde, ein Grund für die geringere Metall-Metall-Interaktion sein. Spektroelektrochemische IR-Messungen zeigten ebenfalls, dass die Carbonyl-Schwingungsbanden während der elektrochemischen Oxidation stärker beeinflusst werden, wenn das Metallcarbonyl-Fragment am dienischen System anstatt am Phosphoratom gebunden ist. Durch Koordination des Phosphoratoms und des dienischen Systems an Übergangsmetalle konnte gezeigt werden, dass die Veränderungen der elektronischen Eigenschaften am dienischen System einen deutlich größeren Einfluss auf die Metall-Metall-Wechselwirkung haben.

Kapitel D

Zusätzlich zur Koordination des Phosphoratoms an Metall(0)-Komplexfragmente (Kapitel C) wurden die Au(I)-Phospholkomplexe **D-3**–**D-5** synthetisiert und elektrochemisch sowie spektroelektrochemisch charakterisiert.

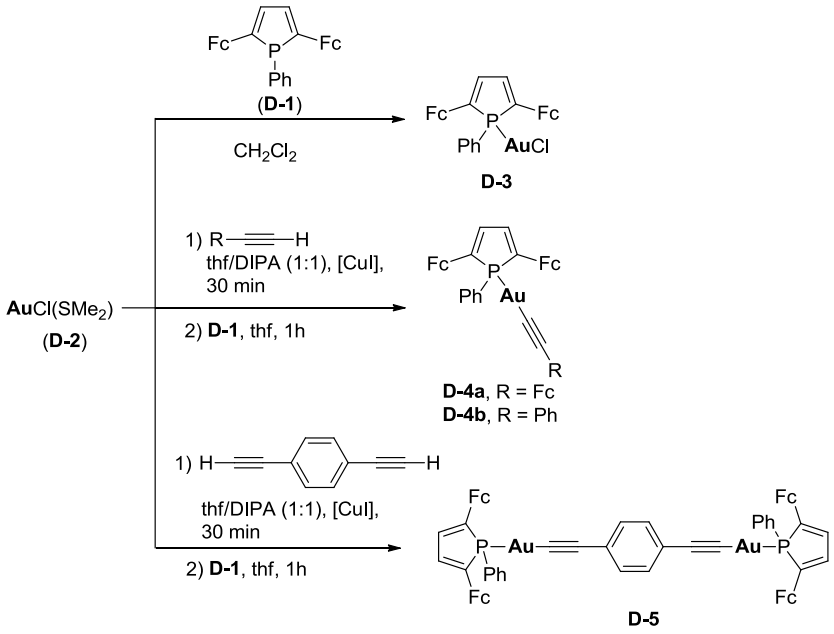

Schema F3. Synthese der Goldkomplexe **D-3**, **D-4a**,**b** und **D-5**.

Dabei sollte die Koordination des 2,5-Diferrocenyl-1-phenyl-1*H*-phosphols an Metall(I)-Komplexfragmente erfolgen, da diese einen deutlicheren Einfluss auf die Elektronendichte des Phospholrings aufweisen sollten. Zur Synthese erfolgte die Umsetzung von 2,5-Diferrocenyl-1-phenyl-1*H*-phosphol (**D-1**) mit $AuCl(SMe_2)$ (**D-2**) (Schema F3) bzw. die Reaktion von **D-2** mit den entsprechenden Arylethinen und **D-1** in Anwesenheit von katalytischen Mengen an Kupferiodid.

In den Cyclovoltammogrammen der Verbindungen **D-3** und **D-4a**,**b** sind jeweils zwei Redoxprozesse für die Ferrocenylgruppen mit Redoxseparationen von etwa 260 mV zu beobachten. Im Vergleich zu **D-1** kam es somit nach Koordination an Au-R zu einer Abnahme der Redoxseparation. Verbindung **D-5** mit vier Ferrocenyleinheiten zeigt in elektrochemischen Untersuchungen ebenfalls zwei Redoxprozesse, welche jedoch eine auffällig hohe Differenz zwischen Oxidations- und Reduktionspotential aufweisen. Nach der Methode von Richardson und Taube konnte eine Separation der nah beieinanderliegenden Prozesse von etwa 65 mV bestimmt werden. Spektroelektrochemische Untersuchungen ergaben eine Abnahme der Intensität (ε_{max} = 1100–1300 $L \cdot mol^{-1} \cdot cm^{-1}$) und eine Zunahme der Halbwertsbreite ($\Delta\nu_{1/2} \approx 3650\ cm^{-1}$) der IVCT-Banden von [**D-3**]$^+$, [**D-4a**]$^+$ und [**D-4b**]$^+$ im Vergleich zu [**D-1**]$^+$. Somit konnte gezeigt werden, dass die elektronische Wechselwirkung der Ferrocenylgruppen nach Koordination des Phosphors an Au(I) abnimmt. Für Verbindung **D-5**, welche zwei Phospholgruppen aufweist, konnte eine Verdopplung der Intensität (ε_{max} = 2700 $L \cdot mol^{-1} \cdot cm^{-1}$) beobachtet werden, da die absorbierende Struktureinheit zweimal im Molekül vorhanden ist.

Die Veränderungen der elektronischen Eigenschaften des heterozyklischen Brückenfragmentes nach Koordination des Phosphoratoms an ein Metall(I)-Fragment haben somit deutlich größeren Einfluss als die Koordination an Metall(0)-Komplexfragmente (Kapitel C).

Kapitel E

In diesem Kapitel ist die Synthese der Phosphole **E-3a**–**e** (Schema F4) mit verschieden sterisch anspruchsvollen Substituenten am Phosphoratom zur Erhöhung der Aromatizität im Phospholring gezeigt. Die Synthese der Phosphole erfolgte analog zur in Kapitel B beschriebenen Synthese mit verschiedenen Arylphosphinen (Ar = Ph, Fc, 2,4,6-Me_3-C_6H_2, 2,4,6-Ph_3-C_6H_2, 2,4,6-$^t Bu_3$-C_6H_2). Mit Hilfe der VT-NMR-Spektroskopie wurden die

Aktivierungsenergien und -enthalpien des Inversionsprozesses des Phosphoratoms bestimmt. Dabei konnte gezeigt werden, dass mit steigendem sterischen Anspruch der Substituenten die Aktivierungsenthalpien sinken. Die experimentelle Bestimmung der Inversionsbarrieren wurde durch theoretische Berechnungen am Beispiel von **E-3c** gestützt. Somit wurden erste Hinweise erhalten, dass es mit steigendem sterischen Anspruch der P-gebundenen Substituenten zu Planarisierung des Phosphoratoms kommt.

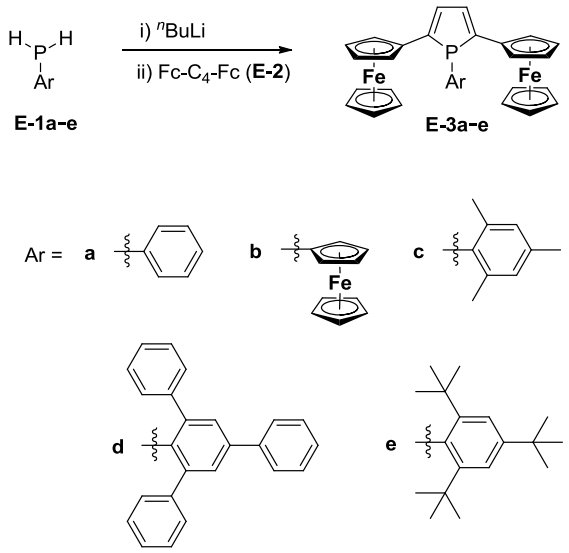

Schema F4. Synthese der Phosphole **E-3a**–**e**.

Der Einfluss der Substituenten in 1-Position des Phospholringes konnte weiterhin mittels Einkristallröntgenstrukturanalyse belegt werden. Dabei konnte eine deutliche Planarisierung für Phosphol **E-3e** im Vergleich zum sterisch ungehinderten **E-3a**,**b** beobachtet werden. Anhand geometrischer Kriterien ließ sich weiterhin der Bird-Index berechnen, welcher eine Abschätzung der Aromatizität einer Verbindung erlaubt. Für die Verwendung des sterisch anspruchsvollen 2,4,6-Tri-*tert*-butylphenyl-Substituenten konnte dieser bis auf 46.6 im Vergleich zum sterisch ungehinderten 1,2,5-Triferrocenyl-1*H*-phosphol (19.5) gesteigert werden, was eine erhöhte Delokalisierung im Ring anzeigt.

Elektrochemische Messungen zeigten, dass die höhere Delokalisierung in den Phospholen **E-3d**,**e** zu einer höheren Redoxseparation der zwei Redoxprozesse der Ferrocenyl-substituenten führte. Die Vermutung, dass der Grund hierfür eine stärkere elektronische Wechselwirkung der Fc/Fc^{+}-Gruppen über den Phospholring ist, konnten mittels *in situ* UV/Vis-NIR-Spektroskopie bestätigt werden. Die stärkste elektronische Kommunikation in der untersuchten Reihe wurde für Verbindung **E-3e** (ε_{max} = 3000 $L \cdot mol^{-1} \cdot cm^{-1}$, $\Delta\nu_{1/2}$ = 2550 cm^{-1}) festgestellt. Theoretische Berechnungen zeigten ebenfalls, dass mit steigendem

sterischen Anspruch der Substituenten die Delokalisation im Ringsystem erhöht wird. Es konnte gezeigt werden, dass durch Verändern der Substituenten am Phosphoratom die elektronische Kommunikation signifikant beeinflusst werden kann.

Danksagung

An dieser Stelle möchte ich mich bei allen bedanken, die mir während der letzten Jahre immer hilfreich zur Seite standen. Zuerst möchte ich meinem Chef Prof. Dr. Heinrich Lang danken, für die Unterstützung und hilfreichen Diskussionen, für die Freiheiten und das Vertrauen während der Bearbeitung des Themas und auch für die Möglichkeit die Ergebnisse auf Tagungen vorzustellen. Bei Prof. Dr. Stefan Spange möchte ich mich für das Anfertigen des Zweitgutachtens bedanken. Ein großer Dank geht an Dr. Alexander Hildebrandt für die großartige Unterstützung und den zahlreichen fachlichen Diskussionen während der gesamten Promotionszeit und der Unterstützung in frustrierenden Zeiten. Bei Dr. Bianca Milde möchte ich mich für die Hilfe besonders am Anfang und am Ende der Promotion, den vielen hilfreichen Diskussionen und der Unterstützung bei Problemen bedanken.

Ich möchte mich bei Dr. Bianca Milde, Dr. Alexander Hildebrandt und Dr. Roy Buschbeck für das Korrekturlesen der Arbeit bedanken. Meinen Laborkollegen und ehemaligen Laborkollegen aus der B113, Frank, Bianca, Carola, Khaled und Sebastian danke ich für die schöne Zeit. Ich möchte der gesamten Arbeitsgruppe der Anorganischen Chemie für das angenehme Arbeitsklima in den letzten vier Jahren danken. Ich danke Marcus Korb und Dr. Dieter Schaarschmidt für das Anfertigen der Einkristallröntgenstrukturanalysen. Bei Ute Stöß, Janine Fritzsch und Katrin Müller möchte ich mich für die Messungen der Elementaranalysen und bei Dr. Roy Buschbeck und Brigitte Kempe für die Aufnahme der Massenspektren bedanken. Bei Jutta Ruder und Natalia Rüffer möchte ich mich für die Unterstützung in allen organisatorischen Angelegenheiten bedanken. Dr. Holm Petzold und Christian Gäbler danke ich für die hilfreichen Diskussionen bei NMR-Auswertungen. Meinen Kommilitonen Ulrike Pfaff und Christian Gäbler danke ich für die gemeinsamen schönen Momente seit Beginn des Chemiestudiums.

Bei Prof. Dr. Paul J. Low und Dr. Duncan A. Wild (The University of Western Australia) bedanke ich mich für die hilfreiche Kooperation und die theoretischen Berechnungen.

Meiner Familie und meinem Freund danke ich für die Unterstützung und den Rückhalt während der letzten Jahre. Nadine, Carola, Katja, Alexander und Susanne danke ich für zahlreiche Aktivitäten außerhalb der Uni.

Anhang A

Organometallics **2013**, *32*, 2993–3002.

The Synthesis and (Spectro)electrochemical Behavior of 2,5-Diferrocenyl-1-phenyl-1*H*-phosphole

Dominique Miesel, Alexander Hildebrandt, Marcus Korb, Paul J. Low[§], and Heinrich Lang*

Technische Universität Chemnitz, Faculty of Natural Sciences, Institute of Chemistry, Inorganic Chemistry, Straße der Nationen 62, 09111 Chemnitz, Germany.

[§] Durham University, Department of Chemistry, South Rd, Durham DH1 3LE, UK

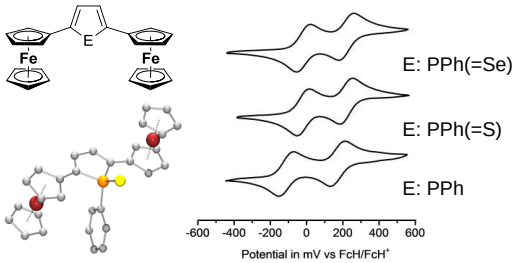

Abstract: 2,5-Diferrocenyl-1-phenyl-1*H*-phosphole (**B-3**) has successfully been prepared by a cyclization reaction of phenylphosphine with 1,4-diferrocenylbutadiyne. Subsequent reaction with elemental sulfur and selenium, respectively, leads to the formation of the appropriate phosphole sulfide (**B-4**) or selenide (**B-5**). Molecules **B-4** and **B-5** have structurally been characterized by single crystal X-ray diffraction. Despite the tetrahedral environment at the phosphorus atom, the $^{c}C_4P$ ring itself is planar and coplanar to the cyclopentadienyl rings of the ferrocenyl termini. Electrochemical measurements revealed that the two ferrocenyl groups could be oxidized at discrete potentials, with separation of the individual redox waves of 280 mV (**B-3**), 240 mV (**B-4**) and 235 mV (**B-5**), respectively. These values agree with other examples of heterocyclic-bridged diferrocenyl compounds such as diferrocenyl thiophene (260 mV) and diferrocenyl furan (290 mV). Compounds [**B-3**]$^+$, [**B-4**]$^+$ and [**B-5**]$^+$ exhibit IVCT absorptions of weak to moderate strength which conforms well to the predictions of the Hush two-state model for weakly coupled mixed-valence systems. These conclusions are supported by DFT and TD-DFT results, which satisfactorily model the observed structural and spectroscopic parameters. The computational work assists in assigning the various low energy (LF, IVCT) electronic transitions and also highlights the key role of the unsaturated *cis*-diene-like C_4H_2 building block of the heterocycle in promoting the Fc → Fc^+ electron-transfer transition.

Anhang B

Organometallics **2015**, *34*, 4293–4304.

Transition Metal Carbonyl Complexes of 2,5-Diferrocenyl-1-phenyl-1*H*-phosphole

Dominique Miesel, Alexander Hildebrandt, Marcus Korb, Dieter Schaarschmidt and Heinrich Lang*

Technische Universität Chemnitz, Faculty of Natural Sciences, Institute of Chemistry, Inorganic Chemistry, D-09107 Chemnitz, Germany

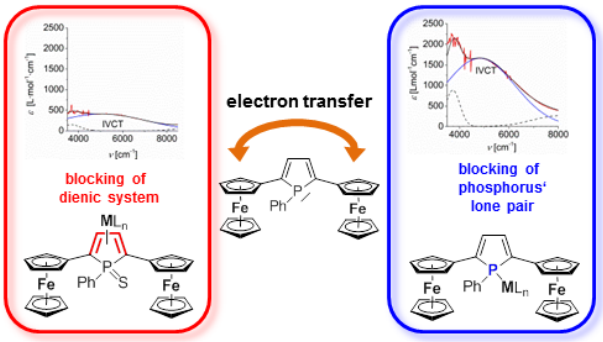

Abstract: Pentacarbonyl-(2,5-diferrocenyl-1-phenyl-1*H*-phosphole) metal complexes **C-3a–c** (**C-3a**, M = Cr; **C-3b**, M = Mo; **C-3c**, M = W) have successfully been synthesized by the reaction of 2,5-diferrocenyl-1-phenyl-1*H*-phosphole (**C-1**) with $M(CO)_5(thf)$ (**C-2a**, M = Cr; **C-2b**, M = Mo; **C-2c**, M = W). Further irradiation of **C-3a–c** with 1 equiv. of **C-1** in tetrahydrofuran leads to tetracarbonyl-bis(2,5-diferrocenyl-1-phenyl-1*H*-phosphole) metal complexes **C-4a–c** (**C-4a**, M = Cr; **C-4b**, M = Mo; **C-4c**, M = W). In addition, the reaction of **C-1** with $Fe_2(CO)_9$ gave tetracarbonyl-(2,5-diferrocenyl-1-phenyl-1*H*-phosphole) iron (**C-6**) and heptacarbonyl-[μ-(2,3,4,5-η)-1-(2,5-diferrocenyl-1-phenyl-1*H*-phosphole) diiron (**C-7**), respectively. Treatment of 2,5-diferrocenyl-1-phenyl-1*H*-phosphole sulfide (**C-8**) with $Fe_2(CO)_9$ afforded tricarbonyl-[(2,3,4,5,-η)-(2,5-diferrocenyl-1-phenyl-1*H*-phosphole 1-sulfide) iron (**C-9**). Complexes **C-3b**,**c**, **C-4c**, **C-7** and **C-9** have been characterized by single crystal X-ray diffraction. Molecules **C-3b**,**c** and **C-4c** exhibit a distorted octahedral geometry, whereas in **C-4c** the two phosphole units are *cis* oriented. Coordination of the dienic system to $Fe(CO)_3$ in **C-7** and **C-9**, respectively, resulted in a deflection of the phosphorus atom from the C_4 plane. Electrochemical measurements of **C-3a–c**, **C-4a–c** and **C-9** demonstrated that the ferrocenyl units can be oxidized separately. The coordination of the dienic system to the $Fe(CO)_3$ building block leads to a decrease of the redox splitting ($\Delta E^{\circ\prime}$ = 190 mV) when

compared to **C-8** ($\Delta E^{\circ\prime}$ = 240 mV). Mixed-valent [**C-3a**]$^{+}$–[**C-3c**]$^{+}$, [**C-4a**]$^{2+}$–[**C-4c**]$^{2+}$ and [**C-9**]$^{+}$ show IVCT absorptions of weak to moderate strengths. The coordination of the phosphorus atom to $M(CO)_5$ in **C-3a–c** has no significant influence on the metal-metal interaction in the mixed-valent species. However, the coordination of the dienic system in **C-9** results in a significantly decreased electronic communication of the Fc/Fc^{+} termini *via* the heterocyclic core.

Anhang C

Journal of Organometallic Chemistry, **2015**, *803*, 104–110.

Electronic Interactions in Gold(I) Complexes of 2,5-Diferrocenyl-1-phenyl-1*H*-phosphole

Dominique Miesel, Alexander Hildebrandt, Marcus Korb and Heinrich Lang*

Technische Universität Chemnitz, Faculty of Natural Sciences, Institute of Chemistry, Inorganic Chemistry, D-09107 Chemnitz, Germany

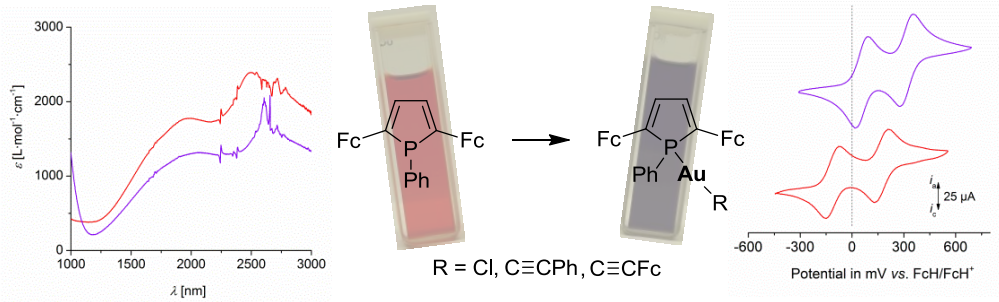

The synthesis of gold(I) complexes of 2,5-diferrocenyl-1-phenyl-1*H*-phosphole (**D-1**) is presented. Chloro(2,5-diferrocenyl-1-phenyl-1*H*-phosphole)gold (**D-3**) has successfully been prepared by the reaction of **D-1** with $AuCl(SMe_2)$ (**D-2**). Treatment of **D-2** with arylethyne (aryl = ferrocenyl, phenyl) using catalytical amounts of [CuI] and 1 equiv. of **D-1** gave arylethynyl-(2,5-diferrocenyl-1-phenyl-1*H*-phosphole)gold **D-4a** and **D-4b** (aryl: **a** = ferrocenyl; **b** = phenyl). Compound [μ-(1,4-phenylenedi-2,1-ethynediyl)]bis(2,5-diferrocenyl-1-phenyl-1*H*-phosphole) digold (**D-5**) could be synthesized by a similar procedure using 0.5 equiv. of 1,4-diethynylbenzene. The electrochemical properties of **D-3**, **D-4a**,**b** and **D-5** were investigated by cyclic and square wave voltammetry. In **D-3**, **D-4a** and **D-4b** each ferrocenyl unit shows one reversible redox event with redox separations of the ferrocenyl moieties in 2,5 position of approximately 260 mV. In **D-5** two redox events for the four ferrocenyl groups were observed. Spectroelectrochemical measurements of **D-3**, **D-4a** and **D-4b** reveal IVCT absorptions with intensities of 1100–1300 $L \cdot mol^{-1} \cdot cm^{-1}$ and a full-width-at-half-height of ≈ 3650 cm^{-1}. In **D-5** two mixed-valent units are present per molecule and therefore, the intensity of the IVCT band is increased to 2700 $L \cdot mol^{-1} \cdot cm^{-1}$. Compounds **D-3**, **D-4a**,**b** and **D-5** can be classified as moderately coupled class II systems according to Robin and Day. The complexation of the gold(I) fragment by the phosphorus atom leads to a decreased metal-metal interaction when compared to **D-1**.

Anhang D

Chemistry – A European Journal, **2015**, *21*, 11545–11559.

Influence of P-Bonded Bulky Substituents on the Electronic Interaction in Ferrocenyl Substituted Phospholes

Dominique Miesel, Alexander Hildebrandt, Marcus Korb, Duncan A. Wild[§], Paul J. Low[§], and Heinrich Lang*

Technische Universität Chemnitz, Faculty of Natural Sciences, Institute of Chemistry, Inorganic Chemistry, Straße der Nationen 62, 09111 Chemnitz, Germany.

[§]School of Chemistry and Biochemistry, University of Western Australia Department, Crawley, Perth, WA 6009, Australia

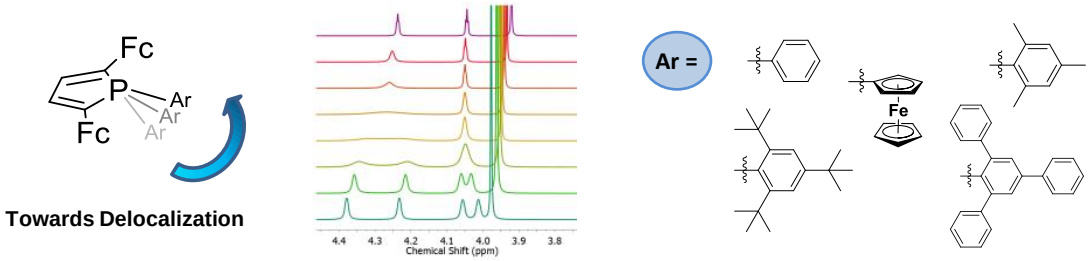

Abstract: 2,5-Diferrocenyl-1-Ar-1*H*-phospholes **E-3a–e** (Ar = phenyl (**a**), ferrocenyl (**b**), mesityl (**c**), 2,4,6-triphenylphenyl (**d**), 2,4,6-tri-*tert*-butylphenyl (**e**)) have been prepared by reactions of $ArPH_2$ (**E-1a–e**) with 1,4-diferrocenyl butadiyne. Compounds **E-3b–e** have structurally been characterized by single crystal X-ray diffraction analysis. The application of the sterically demanding 2,4,6-tri-*tert*-butylphenyl group led to an increased flattening of the pyramidal phosphorus environment. The ferrocenyl units could be oxidized separately, with redox separations of 265 mV (**E-3b**), 295 mV (**E-3c**), 340 mV (**E-3d**) and 315 mV (**E-3e**), which indicates the substantial thermodynamic stability of the mixed-valence radical cations. Mono-cationic $[\mathbf{E\text{-}3b}]^+$–$[\mathbf{E\text{-}3e}]^+$ show IVCT absorptions between 4650–5050 cm^{-1} of moderate intensity and half-height band-width. Compounds **E-3c–e** with the bulky, electron-rich substituents evince a significant increase of the electronic interaction compared to less demanding groups in **E-3a** and **E-3b**.

Anhang E Lebenslauf

Persönliche Daten

Name	Dominique Miesel
Geburtsdatum	17.02.1988
Geburtsort	Karl-Marx-Stadt, jetzt Chemnitz
Staatsangehörigkeit	deutsch

Schulbildung

08/1994 – 06/1998	Grundschule Oberlichtenau
08/1998 – 06/2006	Städtisches Gymnasium Mittweida

Studium

10/2006 – 08/2011	Studium der Chemie an der Technischen Universität Chemnitz, Schwerpunktbereich: Synthese
11/2010 – 08/2011	Diplomarbeit "*Synthese, Reaktivität und Reaktionsverhalten von Ferrocenylphosphan-Übergangsmetallkomplexen*", Lehrstuhl für Anorganische Chemie, TU Chemnitz (Prof. Dr. Heinrich Lang)
08/2011	Diplomverteidigung
seit 15.09.2011	Dissertation, Lehrstuhl für Anorganische Chemie, TU Chemnitz (Prof. Dr. Heinrich Lang)

Anhang F Veröffentlichungen, Vorträge, Poster

Veröffentlichungen

1. **Synthesis and (Spectro)electrochemical Behavior of 2,5-Diferrocenyl-1-phenyl-1*H*-phosphole.**

   D. Miesel, A. Hildebrandt, M. Korb, P.J. Low, H. Lang, *Organometallics* **2013**, *32*, 2993–3002.

2. **Electron-Transfer Studies of *trans*-Platinum Bis(acetylide) Complexes.**

   D. Miesel, A. Hildebrandt, T. Rüffer, D. Schaarschmidt, H. Lang, *Eur. J. Inorg. Chem*. **2014**, 5541–5553.

3. **Synthesis and (spectro)electrochemistry of mixed-valent diferrocenyl–dihydrothiopyran derivatives.**

   K. Kowalski, R. Karpowicz, G. Mlostoń, D. Miesel, A. Hildebrandt, H. Lang, R. Czerwieniec, B. Therrien, *Dalton Trans*. **2015**, 6268–6276.

4. **Influence of P-Bonded Bulky Substituents on Electronic Interactions in Ferrocenyl-Substituted Phospholes.**

   D. Miesel, A. Hildebrandt, M. Korb, D.A. Wild, P. J. Low, H. Lang, *Chem. Eur. J.* **2015**, *21*, 11545–11559.

5. **Transition-Metal Carbonyl Complexes of 2,5-Diferrocenyl-1-phenyl-1*H*-phosphole.**

   D. Miesel, A. Hildebrandt, M. Korb, D. Schaarschmidt, H. Lang, *Organometallics* **2015**, *34*, 4293–4304.

6. **Electronic Interactions in Gold(I) Complexes of 2,5-Diferrocenyl-1-phenyl-1*H*-phosphole.**

   D. Miesel, A. Hildebrandt, M. Korb, H. Lang, *J. Organomet. Chem.* **2015***, 803,* 104–110.

Vorträge

1. **Elektronentransferstudien an ferrocenylfunktionalisierten Phospholen.**

   D. Miesel, A. Hildebrandt, M. Korb, H. Lang, 11. Mitteldeutsches Anorganiker-Nachwuchs-Symposium, 19.09.2013, Dresden.

Poster

1. **Electron Transfer Studies in *trans*-Platinum Bis(Acetylide) Complexes.**

   D. Miesel, H. Lang, 10th Ferrocene Colloquium, 15.–17.02.2012, Braunschweig

2. **Synthesis, Electrochemistry and Spectroelectrochemistry of 2,5-Diferrocenyl-1-phenyl-1*H*-phoshpole.**

   D. Miesel, A. Hildebrandt, H. Lang, 11th Ferrocene Colloquium, 06.–08.02.2013, Hannover.

3. **Transition Metal Complexes of 2,5-Diferrocenyl-1-phenyl-1*H*-phosphole.**

   D. Miesel, A. Hildebrandt, M. Korb, H. Lang, 12th Ferrocene Colloquium, 17.–19.02.2014, Innsbruck.

4. **Influence of Electronic Interactions in 2,5-Diferrocenyl-Phospholes.**

   D. Miesel, M. Korb, A. Hildebrandt, H. Lang, 13th Ferrocene Colloquium, 22.–24.02.2015, Leipzig

Selbstständigkeitserklärung

Hiermit versichere ich an Eides statt, dass ich die vorliegende Dissertation mit dem Titel „Beeinflussung der Metall-Metall-Interaktionen in Ferrocenyl-funktionalisierten Phospholen“ selbstständig angefertigt und keine anderen als die angegebenen Quellen und Hilfsmittel benutzt habe. Die Arbeit hat in dieser oder ähnlicher Form noch keiner anderen Prüfungsbehörde vorgelegen.

Chemnitz, den 29.10.2015